THÈSE de DOCTORAT de l'UNIVERSITÉ PARIS 11
Laboratoire Charles Fabry de l'Institut d'Optique

Spécialité :
Physique Quantique

présentée par

Gaël VAROQUAUX

pour obtenir le grade de DOCTEUR de l'UNIVERSITÉ PARIS 11

sujet de la Thèse :

Sources atomiques pour senseurs inertiels interférométriques à long temps d'interrogation

Atomic sources for long-time-of-flight interferometric inertial sensors

Soutenue le 18 Janvier 2008
devant le jury composé de :

M.	**P. PILLET**	Président du jury
M.	**E. RASEL**	Rapporteur
M.	**C. SALOMON**	Rapporteur
M.	**P. TOUBOUL**	Examinateur
M.	**A. ASPECT**	Directeur de thèse
M.	**P. BOUYER**	Directeur de thèse

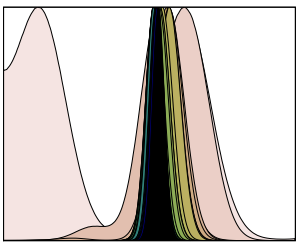

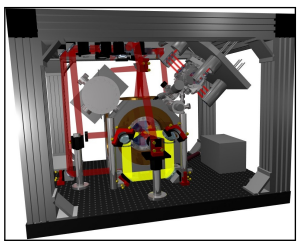
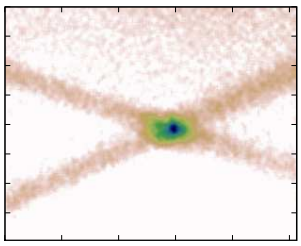

'Tis pleasant, sure, to see one's name in print; A book's a book, although there's nothing in 't.
Byron – English Bards and Scotch Reviewers (1809)

Remerciements

Une thèse, surtout sur les expériences compliquées de physique atomique, s'inscrit dans le travail d'une équipe entière, et j'ai beaucoup de monde à remercier.

Tout d'abord, j'aimerais remercier ceux qui ont dirigé ma thèse, Alain Aspect qui m'a accueilli dans son équipe pour commencer un nouveau projet de recherche et une nouvelle expérience, et Philippe Bouyer, qui a suivi plus directement la construction des montages expérimentaux, les mesures, les projets, les plans sur la comète, et la rédaction des articles.

Je suis particulièrement reconnaissant à Ernst Rasel et Christophe Salomon d'avoir accepté d'être mes rapporteurs et d'avoir pris le temps de lire ce manuscrit, m'apportant leur point de vue de spécialistes des atomes froids en microgravité. Je voudrais aussi remercier Pierre Pillet et Pierre Touboule d'avoir accepté de participer à mon jury de thèse.

Mon travail de thèse s'est déroulé au Laboratoire Charles Fabry de l'institut d'optique, et je voudrais remercier son directeur, Pierre Chavel, pour l'ambiance décontractée et efficace qu'il y fait régner, ainsi que sa disponibilité, même à l'égard de l'un des nombreux doctorants du laboratoire.

L'encadrement de Rob Nyman, ses suggestions, ses critiques, son travail sur l'expérience, ont été sans prix pour l'avancement de ma thèse. Rob et moi sommes très différents, et j'ai beaucoup appris de lui. Je lui suis très reconnaissant pour tous ses apports, ainsi que sa patience. Je le remercie aussi pour sa relecture méticuleuse de ce manuscrit. Le noyau dur de l'expérience "*KRub*" a grandi d'année en année, et je voudrais remercier Jean-François Clément et Jean-Philippe Brantut d'avoir travaillé avec moi sur l'expérience, et de l'avoir fait tourner quand j'étais occupé ailleurs. Jean-François est arrivé à un moment où l'expérience n'était encore qu'un squelette, et il m'a rejoint sur les tâches laborieuses de montage et de construction. Avec lui, Jean-Philippe a fait marcher cet empilement d'équipement et de câbles. De plus ils

ont mené à bien le déménagement de l'expérience, un fardeau supplémentaire pendant leur thèse, et je les remercie de m'en avoir déchargé. Thomas Bourdel a su s'intégrer pour prendre la direction d'une équipe déjà formée et je le remercie d'assumer le lourd héritage de *Krub*. Martin Robert de Saint Vincent est le grand petit dernier sur l'expérience ; je le remercie d'avance pour les fabuleuses expériences qu'il va faire avec ce montage .

Nassim Zazham a travaillé de longues heures avec moi pour terminer le montage de l'expérience "*little-ICE*". Je le remercie pour son ardeur et son efficacité, alors que sa fille, Ambre, était sur le point de naître. "*little-ICE*" a aussi été le fruit d'une collaboration entre trois instituts et de nombreuses personnes. Walid Chaibi et Franc Pereira dos Santos ont fait tourner la chaîne hyperfréquence, Alexandre Bresson, Yannick Bidel et Olivier Carraz ont participé à la construction des lasers, Arnaud Landragin et Linda Mondin ont participé à la campagne de vol.

Frédéric Moron et André Villing, nos talentueux électroniciens, ont été des éléments indispensables à la construction des expériences. Je remercie Frédéric non seulement pour la quantité impressionnante d'appareils électroniques qu'il a construit sur les expériences avec une qualité toujours proche de la perfection, mais aussi pour ses services d'électronicien de l'urgence pour les réparations, les modifications ou les montages improvisés.

Little-ICE a été construit dans des délais très courts, et ceci n'a été possible que grâce aux efforts et à la souplesse du service achats. Je suis très reconnaissant à Christine Avignon-Vérité pour avoir fait l'impossible pour que les commandes arrivent à l'heure dans un contexte de clôture annuelle des comptes ainsi que de déménagement de l'institut.

De nombreuses personnes à l'institut d'optique ont permis la réalisation des expériences. Les services techniques, Jacky Robin, Jean-Luc Cadoret et Éric Vigné nous ont équipé les salles, assuré la maintenance et prêté beaucoup de matériel. Les services de travaux pratiques, en particulier Thierry Avignon, ont été une source précieuse d'équipement spécialisé. Je voudrais prendre le temps de remercier Michel Gaulon à l'atelier de mécanique, qui nous a quitté, bon vivant, bon ami, qui a su quelques fois se montrer très rapide, et le reste de temps m'a donné d'excellents conseils qui ont contribué à ma formation de mécanicien. Aussi à l'atelier de mécanique, Patrick Roth, tourneur, est a l'origine du dicton institutopticien "*Quand c'est rond, ça va plus vite*". Alain Aide m'a souvent conseillé sur les machines outils et m'a parfois dépanné.

"*Krub*" a eu la chance de bénéficier du travail de stagiaires, en particulier Delphine Sacchet et Brice Villier sur les lasers, et Diana García López qui a fait des simulations.

Le groupe d'optique atomique est un groupe plein de vie et de bonne humeur. J'ai eu beaucoup de plaisir a partager des pauses cafés, de nombreux gâteaux, et souvent plus, avec ses membres, Alain, Andrès, Aurélien, Ben, Carlos, Chris, les Davids, Denis, Hai, Hong, Isabelle, Jean-Baptiste, Jean-Félix, Jérome, Jocelyne, Julien, Juliette, Karen, Karim, Laurent, Marie, Martijn, Mathilde, Nathalie, Pierre, Rodolphe,

Ronald, Sebastien, Signe, Simon, Valentina, Vanessa, Vincent William, Yahn, Yannick, Zang-chu. Après trois années de thèse, j'ai côtoyé de nombreux thésards et post-doc inconnus des nouvelles générations, et en faire la liste rappelle de bons souvenirs.

Finalement je tiens à remercier Graça Martin pour les impressions de ce manuscrit, que je lui ai par moment demandé en urgence.

Je voudrais, *last but not least*, remercier Emmanuelle pour m'avoir accompagné pendant ma thèse. Je la remercie d'avoir supporté sans sourciller mes horaires de travails extensibles, mes conversations "boulot", mais surtout je la remercie de m'avoir aidé dans les moments durs.

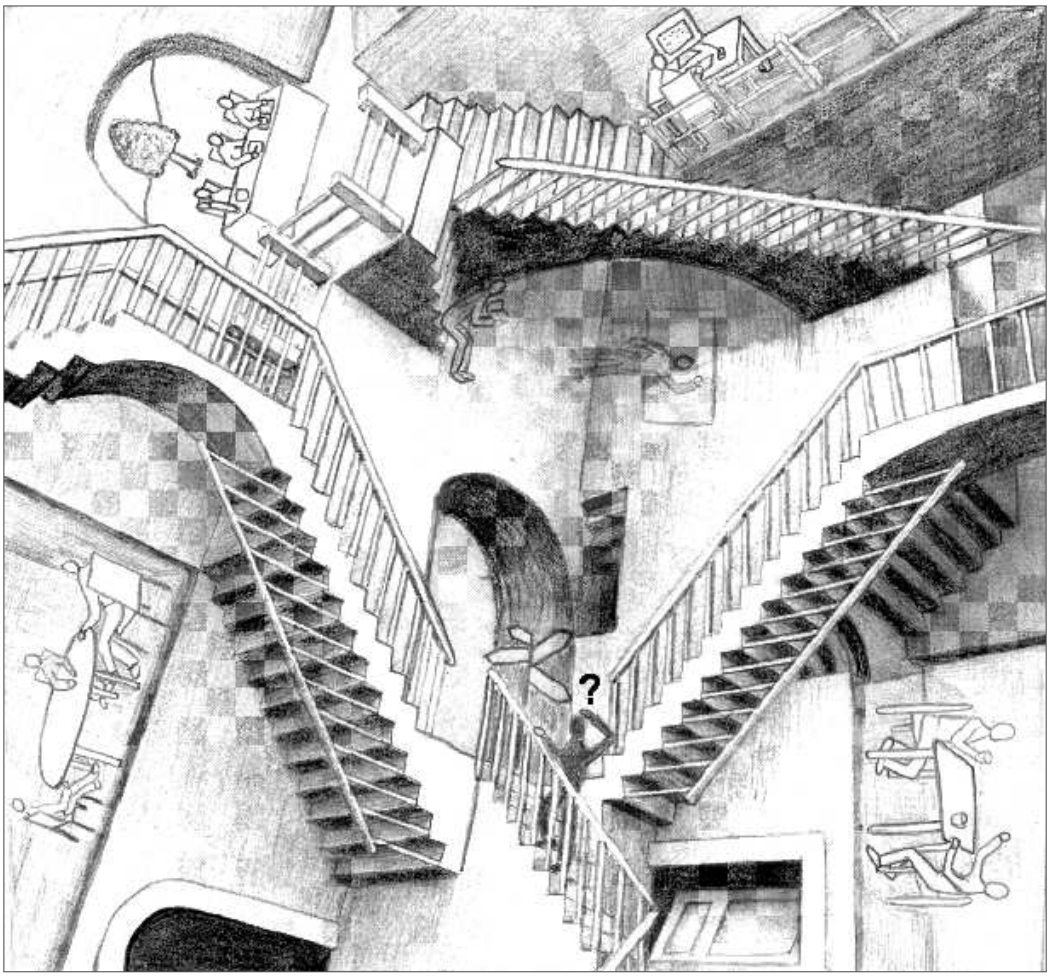

Contents

Introduction

A brief history of atom interferometry

Interferometry: from photons to atoms

In 1655, a gentleman named Francesco Maria Grimaldi observed curious diffraction fringes produced by a narrow slit. These observations, and many others that would follow later, could not fit in the established understanding of light and its propagation. This was the beginning of an scientific revolution, which would mark the transition from a corpuscular description of light to a wave theory.

The wave nature of light was fully established by Thomas Young's double-slit experiment in 1802, which introduced the notions of coherence and superposition by demonstrating that combining two sources of light could lead to an observation of local zeros of light: interference fringes. A hundred years later, in his famous 1905 article on the photoelectric effect, Albert Einstein reintroduced a particle to describe light, the photon. The description of light could not be completed without picturing it both as a particle and a wave.

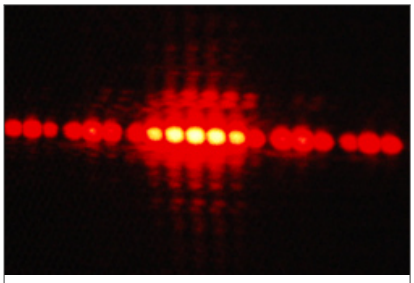

Double-slit interference pattern
Photo: University of Massachusetts

This notion of wave-particle duality played a central role in the birth of quantum mechanics. In his 1924 doctoral thesis [1], Louis de Broglie stated that every particle can be described as a wave. The concept of coherent quantum superposition, which describes a particle as being in several states at once, reconciles the observations of interference with particle theory. A particle, a photon for instance, can propagate through different paths at the same time and, when recombined, its state is a result of the actions of all possible paths.

During the 20^{th} century, interferometry with light evolved from an oddity to a universal high-precision measurement technique. Yet interference patterns can only be observed in special conditions, as interference from many different particles can easily wash out. In 1960, Theodore Maiman demonstrated the first laser: a source of light-emitting photons with strong cross-particle coherence. Photons from a laser are all in the same state, and, as they explore different paths, the interference patterns

add up. With the laser, interferometry became a ubiquitous tool, used for instance to measure distances on construction sites, or rotations in airplanes.

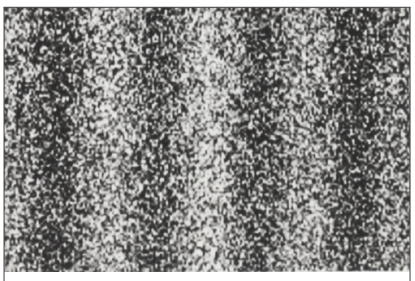

Electronic double-slit experiment
Photo: Dr. Tanamura, Hitachi.

As early as 1927, Clinton Davisson and Lester Germer observed the wave-like behavior of electrons in the pattern made by their diffraction from a crystal. In 1961, Claus Jönsson reproduced Young's double-slit experiment with electrons, extending interferometry techniques from light to matter. The wavelength of room-temperature matter is extremely small, and matter-wave interferometry has remained a technical feat limited to research laboratories only. Laser cooling of atoms, developed in the 1980s by many groups, notably Steve Chu, Claude Cohen-Tannoudji, and William Phillips, has opened the door to atom-interferometric experiments with increased wavelengths, and the hopes of applications. In 1995, Eric Cornell and Carl Wieman [2] achieved Bose-Einstein condensation, a state of matter similar to that of photons in a laser in which all atoms are in the same state, and can interfere together.

Atom optics is the art and science of manipulating atoms as photons, deflecting, splitting and recombining them. Atom interferometry builds upon it to develop interferometric measurement techniques.

From interferometry with beams of particles to macroscopic wave functions

Atoms are sensitive to many different physical effects, due to their internal structure, and interferometry with atoms was quickly used to provide high-precision measurements of these effects.

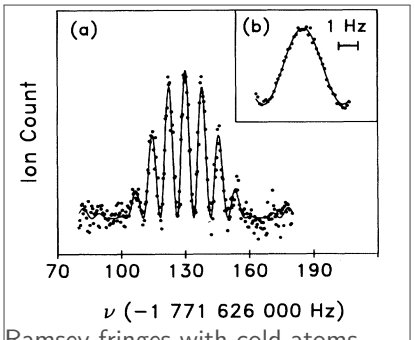

Ramsey fringes with cold atoms
Source: Kasevich *et al.* [3]

Atom-interferometry experiments were pioneered by Norman Ramsey on thermal molecular beams, in the early 1950s, to measure with then-unmatched precision the effect of magnetic fields on the beam. They were quickly used to measure time flow with atomic clocks. These interferometers divide the atoms in the beam in a superposition of two different spin levels using a micro-wave pulse. After a short propagation distance, another micro-wave pulse is applied to recombine the two spin levels. Interference effects appear in the atomic populations after the last pulse.

Atomic clocks based on Ramsey interferometry have been the basis of the definition of the second since 1967, setting the time standard. Their precision was however limited by the short time during which they could interrogate the hot and rapidly-moving atoms. The progress in laser cooling and trapping of atoms has opened the door to

improved atomic clocks, where cold and slow atoms are used for longer interrogation times.

In the 1990s, the field of cold atoms has seen the advent of Bose-Einstein condensation of dilute atomic vapors [2, 5]. This new quantum phase is more than an ultra-cold sample of matter. Atoms accumulate in the same quantum state. As a result, a Bose-Einstein condensate (BEC) both displays strong inter-particle coherence, and behave as a very monochromatic atomic source. A BEC is a macroscopic wave function, a macroscopic state of matter that displays fully wave-like behavior. It is to a thermal atomic source what the laser is to a light bulb: interference is ubiquitous.

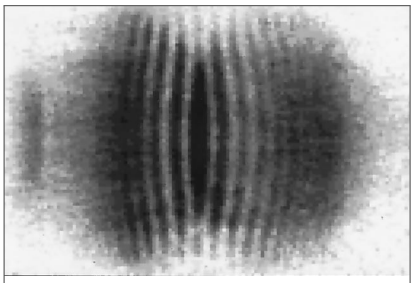

Interference with a BEC
Source: Andrews *et al.* [4]

In photon interferometry, the laser came as a revolution due to its high coherence and collimation. BECs are not currently used in high-precision atom interferometry, but they seem the natural extension of the historical path taken by atomic sources toward slower and colder sources, and their strong coherence makes it possible to observe interference in a wide range of situations.

Photons and atoms to measure gravito-inertial fields

Interferometric measurements have been crucial for the development of inertial and gravitational theories, and are used in today most-precise gravito-inertial sensors.

In 1887, Albert Michelson and Edward Morley performed an interferometric experiment to detect the aether, the medium in which light was thought to propagate through its movement. This experiment, probing for anisotropy of light propagation, became what might be called the most famous failed experiment to date. Its negative results pushed Hendrik Lorentz to introduce in 1899 the Lorentz transformations, describing how motion contracts space and time. They were used by Albert Einstein to establish the foundations of special relativity.

In 1913, Georges Sagnac set a ring-shaped interferometer in rotation, measuring the effect of rotation through the difference in propagation time for light pulses traveling in opposite directions on a revolving platform. Ironically, he interpreted his results as a contradiction of Einstein's theory of relativity, while it is now recognized that they cannot be properly explained without it. Nowadays the Sagnac experiment is the basis of the high-precision gyrometers used for inertial navigation on airplanes.

Interferometry with light is also used in high-precision gravimeters, by measuring the acceleration of a freely-falling test mass. But maybe the most impressive interferometer deployed is LIGO [6], the Laser Interferometer Gravitational-Wave Observatory, a four-kilometer-long Michelson-like interferometer used to monitor space-time

deformations in an attempt to detect gravitational waves predicted by general relativity.

The first inertial-sensing interferometric experiments with matter waves were performed by Zimmerman and Mercereau [7] in 1965 using electron Cooper pairs within a superconducting loop. Interferometric experiments with beams of particle sensitive to inertial fields were pioneered with neutron beams [9] using Bragg diffraction in crystals to physically split and recombine the beam in a Mach-Zehnder-like geometry. They were later followed by atomic [10, 11, 12] and electronic [13] beam experiments also using Mach-Zehnder geometries.

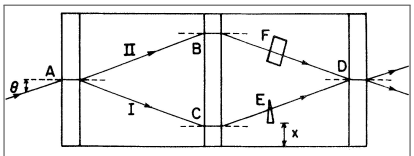

Neutron Mach-Zehnder geometry
Source: Greenberger [8]

With the progress in laser cooling and trapping of atoms, modern atom interferometers operate on cold atomic samples released from a trap [14, 15]. These low-velocity samples offer high monochromaticity and can be precisely manipulated with laser-light pulses, creating the atom-optic equivalent of the beam splitters and mirrors used in photon interferometry.

Atoms, unlike photons, have a non-zero rest mass, and are thus much more sensitive to gravito-inertial effects. Given two Sagnac interferometers with the same geometry, one using photons, the other using atoms, the atom-interferometric one will have a sensitivity eleven orders of magnitude higher. Unfortunately it is currently impossible to build atom interferometers as large as photon interferometers.

Advances in inertial sensing with atoms

State-of-the-art sensors

The accuracy and precision of current atom-interferometric inertial sensors rival state-of-the-art conventional devices. Using atom interferometry, the two groups of Steven Chu and Mark Kasevich were able to measure Earth gravity acceleration with a precision of $2 \cdot 10^{-9}\,\mathrm{m}\cdot\mathrm{s}^{-1}\cdot\mathrm{Hz}^{-1/2}$ [14], Earth gravity gradient with a precision of $4 \cdot 10^{-9}\,\mathrm{s}^{-1}\cdot\mathrm{Hz}^{-1/2}$ [16], and rotations with an angular resolution better than $10^{-9}\,\mathrm{rad}\cdot\mathrm{s}^{-1}\cdot\mathrm{Hz}^{-1/2}$ [17].

Atom-interferometric inertial sensing is rapidly developping. The BNM (Bureau National de Metrologie) has selected atom-interferometric gravimetry has the local acceleration reference measurement for the Watt balance project [18] that aims to establish a new mass reference. Metrology experiments using atom interferometry have started or are starting in many different groups ([19, 16, 20, 15, 21, 22, 23]).

State-of-the-art atom-interferometric inertial sensors make use of laser-cooled atomic clouds as atomic sources. A confined atomic cloud is first prepared and cooled, then

released to propagate freely in the interferometer. The interferometer itself is created by shining a succession of light pulses on the cloud.

Increasing the scale factor for atom interferometers

While the sensitivity of a photon interferometer increases with its arm length, the relevant parameter for an atom interferometer is the flight time for the atoms, called the interrogation time. Indeed, in an inertial-sensing atom interferometer, atoms are left freely falling as they propagate through the interferometer that probes their flight. Thus the available flight time is limited by the fall of the atoms, unlike with light rays, that can be bounced hundreds of times across LIGO's four-kilometer-long baseline. For long-interrogation-time atom interferometry, a long free fall path or a gravity-less environment is required.

Apart from its high degree of coherence, the laser brings to long-baseline interferometers its very well collimated beams that do not expand significantly across the interferometer. A freely-falling cloud of laser-cooled atoms expands quickly. To push interrogation times above the second, the use of a Bose-Einstein condensate, the atomic equivalent to the laser, as a source of atoms seems a promising candidate, as long as it is released into its free flight with a well-controlled initial velocity.

In atomic clocks, the most advanced high-precision atom interferometers, interrogation times have increased from milliseconds to fractions of seconds, thus gaining several orders of magnitude on the precision of the clocks. This progress has been achieved by mastering both the divergence of the atomic cloud, and its global movement. Zacharia, in the early 1950s, tried to perform Ramsey interferometry on a fountain, by launching atoms upward, and waiting for their fall in the Earth gravity field, but failed because the large velocity spread of his hot samples. His proposition was implemented in 1991 with laser-cooled atoms [3, 24]. Already in 1970, Ramsey and coworkers [25] were envisaging an orbital clock to escape from gravity. Today, a cold atom clock for space project is nearing readiness [26]. While the precision of atomic clocks is directly limited by the time during which atoms can be interrogated, atom-interferometric inertial sensors are limited by the physical separation between the different beams, and their sensitivity increases faster with atomic flight time than for clocks.

Thesis outline

During my PhD, I have investigated atomic sources for long-interrogation-time inertial-sensing interferometry. I have started the construction of two atomic sources, one operating in a micro-gravity environment for long free-fall times, the other aiming to use ultra-cold quantum-degenerate gases to achieve a high collimation. This manuscript will present the design and the construction of the two atomic sources,

as well the scientific and technical motivations for our choices. These two sources constitute the atomic sources for the ICE (Interférométrie atomique Cohérente pour l'Espace) project, the French collaboration to bring atom-interferometric inertial sensing to space.

In a first chapter, I present a reflection on atom interferometry inertial sensing and atomic sources. I study which properties of atomic sources are important for long-time-of-flight interferometry in order to draw a figure of merit for cold atom sources, and how the measured phase shift relates to the gravito-inertial fields, introducing a formalism useful for comparing sensitivity to gravito-inertial fields for different types of interferometers.

After this general chapter, part 1 of this thesis covers atom interferometry in a microgravity environment. This environment was achieved through atmospheric ballistic flights. I was in charge of assembling a micro-gravity-compatible cold atom source for testing in ballistic flights. In the first chapter of this part (chapter 2), I discuss the suitability of this microgravity environment for long-interrogation-time atom interferometry, and present scientific goals for this project. I introduce a new experimental protocole that enables to perform a measurement of the universality of free fall in this noisy environment. Chapter 3 covers the design of the atomic source, as well as the results of the flight campaign that we conducted.

Part 2 presents the apparatus for producing degenerate atomic gases for atom interferometry, built during my thesis. It has been designed as a prototype for degenerate micro-gravity atomic sources. Chapter 4 presents the new semiconductor laser sources that we developed for laser cooling potassium and rubidium. The particularity of these sources is their 20 nm tunability range that makes them unique semiconductor lasers useful for both atomic species. Chapter 5 presents the design and construction of the atom-optics apparatus. I give scaling laws and simple models to dimension the different elements of the apparatus. A compact apparatus has been designed for precise control of the atomic interactions via a large and homogeneous magnetic field and a compressible optical trap. Chapter 6 outlines our strategy for loading the optical trap with laser-cooled atoms. First results for the loading are presented. Using a novel imaging technique we image the shape of the trapping potential, as well as the potential energy distribution of the atoms during the first instants of the loading process. Using simple models, I discuss several scenarios for laser cooling in the optical trap, as well as the limits for trapped atom number in these scenarios.

Synthèse des travaux effectués

Le travail présenté dans cette thèse s'inscrit dans les deux axes qui ont historiquement fait progresser les temps d'interrogation dans les interféromètres atomiques : s'affranchir de la chute des atomes, et fournir des sources mieux collimatées. Les sources construites cherchent à repousser ces limites à l'extrême.

Ainsi, pour allonger le temps de chute des atomes, nous avons réalisé une source atomique pouvant les accompagner dans leur chute, grâce à la manœuvre de vol parabolique dans un avion. Cette démarche avait été initiée dans la fin des années 1990 par le projet d'horloge atomique PHARAO (Laurent *et al.* [27]). L'enjeu actuel est de développer une telle source pour des senseurs inertiels, pour lesquels le gain en sensibilité lorsque le temps d'interrogation augmente est encore plus marqué que dans les horloges. Toutefois les mesures sont difficiles à utiliser à cause des variations des champs inertiels eux-mêmes.

Par ailleurs, pour s'attaquer au problème de l'expansion des sources atomiques, nous avons commencé la construction d'un montage qui vise à étudier les sources atomiques limitées par la diffraction. Ce montage servira à l'obtention d'un condensat de Bose-Einstein, souvent qualifié d'équivalent atomique du laser, mais il permettra aussi d'étudier les limites de cette approche dues aux interactions atomiques, ainsi qu'une source atomique collimatée qui n'a pas d'équivalent photonique : les gaz dégénérés d'atomes fermioniques.

Mesures inertielles interférométriques en microgravité

Une source atomique en microgravité : un défi technique

L'interférométrie atomique avec des atomes froids est un domaine à la pointe de la technologie. Les expériences sont généralement réalisées dans l'environnement bien contrôlé d'un laboratoire, occupent une salle à elles-mêmes, et demandent un entretien constant de la part des expérimentateurs. Pour embarquer une telle expérience dans un avion qui effectue des chutes libres de deux kilomètres, il est nécessaire de la concevoir

avec soin. Les deux programmes d'atomes froids qui ont volé dans les avions à vols paraboliques du CNES constituent, au dire des opérateurs de ces vols, les expériences les plus compliquées à y avoir été menées.

Nous avons dû adapter les techniques expérimentales aux exigences de sécurité d'un tel exercice, rendre l'expérience suffisamment robuste et automatique pour pouvoir fonctionner avec un minimum d'intervention humaine malgré les vibrations, les variations brutales de température et de gravité, et les sautes de courant, tout en ne sacrifiant pas la polyvalence et la possibilité de faire de changements rapides et imprévus qui caractérisent un montage de recherche. Cette démarche est détaillée dans le troisième chapitre de ma thèse.

Donner un sens à des mesures inertielles en microgravité

A quoi des mesures d'un champ de pesanteur peuvent-elles bien servir, si elles sont effectuées en apesanteur ?

Des applications pratiques Tout d'abord, les applications de la gravimétrie et de l'accélérométrie sur Terre sont aussi valable en apesanteur. En effet la géophysique demande une cartographie précise et complète du champ de pesanteur de la Terre, qui peut se faire entre autre en orbite, par gradiométrie. De plus la navigation inertielle spatiale repose sur des mesures de très faibles accélérations. Les senseurs inertiels en microgravité sont donc utiles pour mesurer les faibles champs inertiels auxquels sont soumis les appareils sur lesquels ils sont embarqués.

Un intérêt fondamental Par ailleurs, comme je le souligne dans le premier chapitre de ma thèse, le déphasage inertiel de l'atome peut-être directement lié au tenseur métrique, en ne faisant intervenir que des grandeurs bien contrôlées théoriquement et expérimentalement. Pour vérifier, ou infirmer, les théories gravitationnelles modernes, il est nécessaire de mesurer les effets inertiels d'ordre supérieur qu'elles prédisent, tel que l'effet Lens-Thirring, ou une accélération différentielle entre deux corps différents, signe d'une violation du principe d'équivalence.

Je m'attache par ailleurs dans le premier chapitre de ma thèse à montrer le lien entre des interféromètres expérimentalement très différents, qui peuvent tous être rapportés à une mesure du tenseur inertiel, afin de bien souligner qu'ils mesurent les mêmes effets fondamentaux, et de pouvoir confronter leurs résultats.

Distinguer l'effet recherché des déplacements du senseur De par les déplacements de la plate-forme expérimentale, ses vibrations, le mouvement des masses qui l'entoure, le champ inertiel mesuré varie constamment. Sa mesure interférométrique ne peut se faire qu'à l'aide de plusieurs points expérimentaux, et la précision de la mesure augmente avec le nombre de points. Il faut donc savoir corréler les différentes mesures instantanées pour dégager l'effet recherché des différentes sources de bruit et

de dérives. Dans le cas d'un avion en chute libre, les variations d'une réalisation de la chute libre à l'autre sont importantes. Dans le deuxième chapitre de ma thèse, je dégage une méthode permettant de corréler les résultats expérimentaux de différentes chutes pour en extraire une mesure de l'accélération différentielle de deux atomes.

Des sources collimatées : les gaz atomiques dégénérés

Augmenter la densité dans l'espace des phases pour des sources plus cohérentes et plus collimatées

Pour qu'un nuage atomique puisse être utilisé pour observer des interférences après un long temps de vol, il doit former une source atomique bien monochromatique et collimatée.

Cohérence Le contraste des franges d'une expérience interférométrique est donné par la cohérence de la source. Ce concept, introduit aussi bien en mécanique quantique qu'en optique classique, est difficile à cerner et je fais une brève revue de différents sens qui lui sont donnés dans le premier chapitre. L'interférométrie atomique avec des gaz ultra-froids est en effet à la frontière entre optique et mécanique quantique car elle fait intervenir la mécanique ondulatoire et les statistiques quantique. Cependant, même avec des condensats de Bose-Einstein, seule la cohérence telle qu'elle est comprise en optique est importante pour les senseurs inertiel par interférométrie atomique. On peut donc comparer différentes sources atomiques uniquement par leur longueur de cohérence.

Collimation Un nuage atomique lâché d'un piège s'étend à cause de sa dispersion en vitesse. Cette distribution en vitesse des atomes en vol libre est liée à la distribution en énergie des atomes dans le piège et, par cet intermédiaire, à la longueur de cohérence de la source atomique. Cette longueur, que je calcule pour différentes sources dans le premier chapitre de ma thèse, apparaît donc comme une mesure importante de la qualité d'une source atomique.

Densité dans l'espace des phase Pour maximiser le nombre d'atomes détectés, il convient de maximiser le nombre d'atomes dans l'échantillon. Produire des nuages atomes à grande longueur de cohérence avec un grand nombre d'atomes revient à maximiser la densité dans l'espace des phases. Pour produire des sources à grand flux cohérentes et collimatées, nous proposons donc d'utiliser des gaz atomiques dégénérés, tels que les condensats de Bose-Einstein. Une grande partie de mon travail de thèse à été de démarrer la construction d'un montage permettant de refroidir des atomes pour créer des gaz quantiques dégénérés. Ce travail est exposé dans les chapitres 4, 5 et 6 de mon manuscrit.

Le problème des interactions dans les échantillons denses

Les interactions dans les gaz atomiques dégénérés élargissent leur distribution en vitesse et nuisent à la cohérence et à la collimation de la sources. De plus elles sont la source d'erreurs systématiques dans les interféromètres. C'est pourquoi nous avons conçu notre expérience de gaz quantiques dégénérés afin de pouvoir contrôler les interactions atomiques par des champs magnétiques. Par ailleurs, notre piège optique devrait nous permettre de réduire la densité du nuage atomique en augmentant la taille du piège avant de lâcher les atomes pour limiter l'influence des interactions sur l'échantillon en vol libre. Finalement, notre expérience a la possibilité de refroidir des atomes fermioniques, dont la densité dans l'espace des phases est limitée par le principe d'exclusion de Pauli. La distribution en vitesse d'un gaz dégénéré de fermions est plus large que celle d'un condensat de Bose-Einstein sans interactions, mais cet élargissement est comparable à l'effet des interactions. Il peut aussi être réduit en augmentant la taille du piège.

La conception et la construction d'un montage expérimental pour explorer en détail les sources atomiques dégénérées et valider ces considérations préliminaires sont décrites en détails dans la deuxième partie de ma thèse.

Chapter I

Interferometric inertial sensing with cold atoms

Physics is like sex. Sure, it may give some practical results, but that's not why we do it.

Richard S. Feynman

This chapter presents a general discussion of atomic sources and interferometry for inertial sensing. I introduce here a few considerations to motivate and guide experimental work on long-interrogation-time inertial sensing. In the first section, I try to define what properties of the atomic sources we are interested in. In particular, after discussing coherence and collimation of the source, I propose a figure of merit for these features. In the second section, I focus on how the interferometric phase shift relates to inertial effects and introduce a novel formalism that can be applied to all inertial-sensing interferometers.

In an interferometer, a wave packet is separated in a superposition of two or more distinguishable states by a first beam-splitting process, propagated, and recombined by a second beam-splitting process. The readout of the resulting interference pattern gives information on the fields which the wave packet was exposed to during its propagation through a very sensitive measurement of the phase difference accumulated between the different possible paths (see Figure I.1).

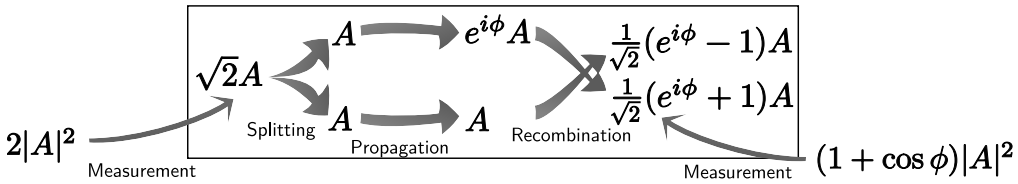

Figure I.1 – **2-wave interferometric process**
An initial state is split in a superposition of two distinguishable states that are propagated separately. During their propagation, they can acquire a differential phase shift ϕ. They are then recombined into indiguistible state. The propagation phase shift appears as modulation of the final measurement result. The measurement ranges from zero to twice the value of a measurement without interference; the contrast of the interference is 1.

1 Coherent sources and atom-interferometry

Classical optics introduces the notion of coherence to measure the ability of two waves to combine and produce more, or less, observed intensity than the sum of the two separate waves, in other words, their ability to interfere. In this section I look at the properties of cold atom sources which make them suitable for long-interrogation time atom interferometry: coherence and collimation. I introduce a figure of merit to compare one source to another.

1.1 Coherence of an interferometric source

The physical concept of coherence is intimately linked to the ability of two waves to be combined and display interference. It is a quantification of the contrast of the modulation of the interferometric measurement as the phase difference is varied. However, coherence is in the eye of the beholder: the amount of coherence of a given wave depends on the interferometric experiment. The tools used in photon optics to quantify the coherence of a source can be used in atom optics, but only with some care. To quantify the coherence of the sources required for atom-interferometry, let us first look at the different aspects of coherence.

1.1.1 Quantum coherence between two states

According to quantum mechanics, a system can be split into a superposition of several distinguishable states: a measure can yield different results and only the probably of these different outcomes can be predicted. This unknown is not due to an incomplete description of the system[1] and the system can evolve from a system with quantum superposition to a system without in a reversible way. Moreover, in a coherent superposition, there exists a well-defined phase difference between these the different states.

Recombining these states into indistinguishable states and performing a measurement on the resulting recombination can show an interferometric term: the outcome of the experiment can depend on the phase difference accumulated during the separation. In Ramsey interferometers, the observation of interference is due to coherence between the two atomic spin states. If we write the atomic states corresponding to the two spin levels $|0\rangle$ and $|1\rangle$, the interferometric process can be described using the convention of Figure I.1 by:

$$|0\rangle \begin{cases} |1\rangle \to e^{i\phi}|1\rangle \\ |0\rangle \to |0\rangle \end{cases} \begin{cases} (1+e^{i\phi})|0\rangle \\ (1-e^{i\phi})|1\rangle \end{cases} \tag{I.1}$$

[1] This has been the source of a historical controversy that has been resolved through a theoretical prediction by John Bell [28] thoroughly verified experimentally (see Aspect [29] for a review).

As soon as the system we are interested in is coupled to the environment, our knowledge of its state and its evolution is limited. The environment has a very large amount of microscopic degrees of freedom, and is described by macroscopic variables, giving the most probable values of the microscopic quantities, as introduced by statistical physics. It introduces some uncertainty in our description of our system. If the phase ϕ in the interferometric experiment described in I.2 depends on a fluctuating parameter of the environment, it will fluctuate too, becoming a random variable ϕ_n. When repeating the experiment several times, or doing the experiment at once with a large number of particles, as in an atomic beam, the measurement will be averaged over many realizations. After the recombination, the final state is written $(1+\exp(i\phi_n))\,|0\rangle$, and when averaging, if the random values of ϕ_n spread over a span on the order of 2π, the interference term will disappear. Overall, the coherence of the atomic beam has been lost: it shows no interferometric effect[2].

However, if the $|0\rangle$ state also undergoes a phase shift ψ_n during propagation, the final state will be $\Big(1+\exp(i(\phi_n-\psi_n))\Big)\,|0\rangle$. If the fluctuations of this phase shift are identical to those of ϕ_n, they will cancel each other, and the difference will not vary. Thus correlations in the fluctuations can prevent the loss of coherence.

Quantum coherence between two states is the existence of a well-defined phase between the quantum mechanical representations of these states[3]. It is a signature of quantum superposition and can be destroyed by fluctuations. It has been shown (Magyar and Mandel [31], Andrews *et al.* [4]) that two states can be coherent without sharing a common history. Coherence is a property of the states, brought to light by measurements performed on their superpositions.

1.1.2 Coherence of quantum fields

In many interferometric experiments, the physical extension of the particles embodying the quantum states has to be considered. The particles are described as waves, or, in modern quantum formalism, fields. If the propagation lengths in the different arms of the interferometers are different, the superimposed fields on the detector are shifted relatively to one another. In such a situation, the interference measurement is a comparison of the phases of the different fields at different positions. Coherence is then a signature of spatial and temporal correlations in the original field.

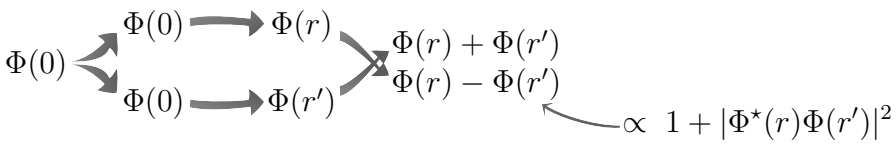

(I.2)

[2] If the effect of the fluctuations on the phase of each atom can be reversed, for instance using a spin-echo technique, the contrast of the interference pattern can be restored. This return of coherence underlines the fact that coherence cannot be defined without considering a particular experiment.

[3] A more formal description of coherence, in statistical quantum mechanics, is the existence of non-zero off-diagonal terms in the density matrix representation of the system (Penrose and Onsager [30]).

In 1955, Hanbury Brown and Twiss [32] performed an experiment that revealed interference in photon-counting statistics with light deemed as incoherent. This observation prompted Roy Glauber to introduce a new definition of coherence (Glauber [33]), that unifies the quantum understanding of coherence and the optical concept for quantum fields. He defined coherence of a quantum field through its n^{th}-order spatial and temporal quantum-statistical correlation functions. A quantum field in a pure state, with no phase fluctuations, is fully coherent: the absence of statistical unknowns means that the field is correlated to any order over its propagation distance. Glauber's criterion for n^{th}-order coherence of a field is that its n^{th}-order quantum correlation function must reduce to products of its first-order correlation function: knowing the relation between the phases of two points at varying distance is enough to fully describe the field.

A measurement of the square of the field probes only the first-order correlations. Standard optical coherence can thus be defined as a first order coherence, as long as it only measures the intensity of the field, that is, the probability of finding a particle. Such experiments do not really probe the interparticle quantum coherence of the field. Measuring correlations of the intensity, as Hanbury Brown and Twist did, measures a quartic, or higher-order observable of the field, and thus probes higher-order coherence. These experiments are hard to describe accurately using classical fields, as the measured observable involves products of the field operator that do not commute. For proper descriptions of the experiments, the quantum commutation relations have to be used.

1.1.3 Optical coherence of a source

Interference of intensity, as in classical optics, only probes first-order coherence. By itself, optical coherence imposes much less stringent requirements than full quantum coherence. A statistical ensemble of photons can form a coherent source, as long as they are monochromatic. They do not need to share a well-defined phase, each photon only interferes with itself[4]. Quantum coherence between different particles is not important for observing interferometric fringes, as long as coherence between the different arms of the interferometer is not lost. The source can be considered as emitting independent particles. This is also true for Bose-Einstein condensates: the interference pattern comes from a single particle effect.

Temporal coherence If the interferometer introduces a delay between its arms, it probes the time correlation function of the field. The Wiener-Kinchin theorem links the correlation time of the signal to the spectral width $\Delta\nu$ of the source: $t_c \sim 1/\Delta\nu$.

[4] Dirac stated [34] this famous phrase: " Each photon ... only interferes with itself. Interference between different photons never occurs.". This is true for all interferometric experiments involving only intensity measurements. Two-photon interference can appear in correlation measurements or higher-order effects, but these do not probe first order coherence. For a review on this subject, see Ou [35].

For particles in a beam propagating at a velocity v we can define a length over which the beam is coherent:

$$l_c = \frac{v}{\Delta\nu} \tag{I.3}$$

For a perfectly monochromatic source, this length is infinite.

Spatial coherence Spatial correlations of the field can be probed by an interferometer inducing a lateral spatial separation in the different arms. This introduces the notion of lateral coherence length: the maximum distance the fields can be laterally shifted before its correlation drops and the interference pattern is washed out.

If the source has a physical width, particles originating from different points of the source will propagate through the interferometer with different trajectories before arriving to the detector, therefore giving rise to different phase shifts. We can define a coherence area A_c that gives the area over which waves originating from all statistically-independent points of the source produce the same interferometric shift (see Mandel and Wolf [36]):

$$A_c = \frac{\lambda^2}{\Omega} \tag{I.4}$$

where λ is the wavelength of the source, and Ω is the source solid angle as seen by the detector at the output of the interferometer. For a surface smaller than this area, the source can be considered as a point source.

Coherence volume The coherence length gives the propagation length over which a field with statistical noise can be considered as a single coherent wave packet. The coherence area gives the lateral section over which this wave extends. The volume defined by the coherence area extruded along the coherence length is called the coherence volume of the field:

$$V_c = A_c \cdot l_c = \frac{v^3}{\nu^2 \Delta\nu \Omega} \tag{I.5}$$

Any two points in this volume can give rise to interference[5]. It can be pictured as the spatial extension of the wave-packets of the particles constituting the field.

Quantum mechanics tells us that a particle of momentum spread $\Delta p_x \Delta p_y \Delta p_z$ has a spatial spread of $\hbar^3/(\Delta p_x \Delta p_y \Delta p_z)$. With a source of spectral width $\Delta\nu$, the longitudinal momentum spread of the particle is $\Delta p_z = 2\pi\hbar\Delta\nu/v = 2\pi\hbar/l_c$, according to the de Broglie relation. The lateral momentum spread is given by the width of the source: $\Delta p_x \sim p_z \sin\theta = 2\pi\hbar/\lambda \sin\theta$, with θ the angle subtended by the source. Therefore $\Delta p_x \Delta p_y = (2\pi\hbar)^2 A_c$. The coherence volume introduced in the previous paragraphs from classical arguments indeed corresponds to the spread of a particle originating from a source of a given spectral and physical width[6] as given by quantum

[5] Formally, the coherence volume is the volume in which the first-order spatial correlation function is non-zero.

[6] The factor of 2π difference between the two formulas comes from the fact that the Heisenberg relation holds for r.m.s width, whereas the coherence volume in optics is defined for large bounds.

mechanics. It is therefore the region of space throughout which two otherwise identical particles of the field are indistinguishable from each other.

It should be noted that the discussion about the area of coherence assumes that the phase shift probed by the interferometric experiment is only due to free propagation. In the case of a more complex situation the formulas given are inexact, but the resulting interpretation of the coherence volume still holds. The coherence volume and the lateral coherence area are thus concepts that have a broader application than for a physically large source: as long as there is some statistical spread in the lateral momentum distribution of the particles, there is an associated coherence area.

The coherence volume gives the maximum displacement over which the different paths of the interferometer can operate on the particles without the interference pattern being washed out. In the case of an interferometer with no physical displacement, as with a Ramsey interferometer, it is irrelevant.

In conclusion, coherence is a highly overloaded concept that is difficult to pinpoint. It can be measured through correlation functions of the field. For interferometers with a physical displacement between the different arms (or in other terms, a different propagation shift), a good quantity to qualify the coherence of a beam is its coherence volume, which can be interpreted as the size of the wave packets or of the particles associated with the field.

1.2 Maximizing signal-to-noise in interferometric experiments

With enough frequency filters and spatial filtering, any optical source can be made coherent-enough for a given experiment. Similarly, with strong velocity selection, atomic sources can be made coherent. However this filtering comes at the cost of a large loss in particles. Coherence by itself is not enough to qualify the suitability of a source for interferometry, the fraction of its flux usable for interferometry also is an important parameter to maximize the interferometric measurement signal-to-noise.

1.2.1 Degeneracy

In optics the source degeneracy parameter, δ, is defined as the number of particles emitted by the source per coherence volume, or alternatively, the flux of particles going through an section of the lateral coherence area during the coherence time. For an interferometric experiment, the detector used must be no larger than the lateral coherence area[7], or the interference effect will be washed out. The degeneracy δ is thus the proper quantity to measure the suitability of a source for interferometry: by limiting the source to a unique coherence volume, it can be made coherent-enough for

[7] It is a common trick in interferometric experiments to extend vastly the coherence area by placing the source at the focal point of a lens, thus making it a point source ($\Delta\Omega = 0$) for the detector.

the purposes of the experiment, the amplitude of the useful signal is then given by the number of particles in this volume.

For a atomic gas trapped in a parabolic potential, the degeneracy parameter corresponds to the phase-space density, and is given by:

$$\delta = n_0 \, \lambda_{\mathrm{dB}}^3 \tag{I.6}$$

where n_0 is the density at the center of the trap. Degeneracy is a constant of the free evolution.

1.2.2 Collimation of the source

For long propagation times, the coherence volume of the beam increases and detection volume cannot be made large-enough to match the coherence volume. To be used in large interferometers a source should be well collimated to avoid signal loss through expansion of the beam. For photonic sources, the collimation of the source is measured by its divergence angle. For atomic sources, there is no clear direction of propagation: atoms at rest have no velocity. We can measure the collimation of an atomic source by measuring its expansion: given a detection volume V_{D}, how will the number of atoms contained in this volume decrease?

This number is directly related to the width of the velocity distribution of the atomic source, Δv, which is itself related to the de Broglie thermal wavelength of the source, λ_{dB}, for a thermal source:

$$\Delta v \sim \frac{\hbar}{m \, \lambda_{\mathrm{dB}}} \tag{I.7}$$

The number of atoms N_{D} in the detection volume scales for long propagation times as:

$$N_{\mathrm{D}} \;\sim\; V_{\mathrm{D}} \, n_0 \, (\Delta v \, t)^{-3} \;=\; V_{\mathrm{D}} \, n_0 \left(\frac{m \, \lambda_{\mathrm{dB}}}{\hbar \, t} \right)^3 \tag{I.8}$$

where n_0 is the initial atom density.

It is interesting to note that for a thermal atomic gas released from a trap, collimation and coherence volume are related[8]. Indeed the coherence volume of an atomic gas is given by λ_{dB}^3. Moreover, the number of detected atoms (given by equation I.8) can be expressed as a function of the degeneracy parameter of the source, the detection volume, and a constant prefactor:

$$N_{\mathrm{D}} = \left(\frac{m}{\hbar \, t} \right)^3 V_{\mathrm{D}} \, \delta \tag{I.9}$$

[8] There is no relation between coherence and collimation for photonic sources in general, as has been demonstrated by Collett and Wolf [37], as incoherent Gaussian sources can be superimposed to generate a diffraction-limited beam with arbitrarily small coherence.

For long-propagation atom interferometry, the degeneracy of the source appears as the critical parameter, as the signal-to-noise ratio of the interferometric measurement is limited by the number of atoms in the detection volume, which is greatest for highly degenerate sources. Although this is not true in general in photon optics, these considerations are similar to the ones met in the design of synchrotron sources (see Shen [38]), as, with these sources also, all the wave-packets are centered on the same point.

1.3 Interferometry with degenerate atomic sources

1.3.1 Atomic gases in the degenerate regime

As the degeneracy of a field increases, quantum statistics come into play. Indeed a highly degenerate field has several indistinguishable particles in the same coherence volume, or in other words, several quanta in the same mode.

Bose condensates

Due to bosonic attraction, for a degeneracy parameter above one[9] in a Bose gas, a phase transition occurs and the single-particle ground state becomes macroscopically occupied. The atomic gas can then be considered as a two-component gas made of a thermal cloud, and a Bose condensate, the macroscopically-occupied ground state wave-function. The Bose condensate is often described as the atom-optics equivalent of the laser: even though it is not created by amplification in a resonator, all particles have the same wave-function. As a result the coherence volume of a condensate is the volume of the complete condensate[10], just as the transverse coherence area of a laser is the total area of the beam. As far as collimation goes, a Bose condensate is a diffraction-limited source, although the trap-release process can increase the divergence (Le Coq *et al.* [41]).

Fermi seas

On the contrary, due to Pauli blocking, a Fermi gas cannot have a degeneracy parameter higher than one: there cannot be more than one fermion per mode. At low temperature, the momentum width of the cloud is not given by the thermal momentum distribution but by the Fermi momentum: the energy levels at small momenta cannot be occupied by more than one particle, and the maximum momentum of the atomic cloud increases with the number of particles. The coherence volume is given by the inverse of the volume occupied in momentum space: $V_c = (\hbar/\Delta p)^3$. The corresponding

[9] More precisely, the transition occurs at $\delta = 1.202$, for a non-interacting Bose gas in a harmonic trap.

[10] For reduced dimensionality (Gerbier *et al.* [39]), or at temperature close to the transition (Donner *et al.* [40]), the phase fluctuations across the condensate reduce the coherence volume.

length scale (given by the de Broglie thermal wavelength in the case of a thermal cloud) is, for a cloud in a trap of frequency[11] ω (see Butts and Rokhsar [42]):

$$\lambda_{\mathrm{F}} = \frac{2\pi}{k_{\mathrm{F}}} = \sqrt{\frac{\hbar}{m\,\omega}}\left(\frac{1}{48\,N}\right)^{1/6} \tag{I.10}$$

The coherence volume, given by λ_{F}^3, decreases with the number of atoms in the atomic cloud, contrarily to bosonic sources.

1.3.2 Interactions in degenerate gases

Degenerate atomic gases are most often dense[12] samples and two-body collisions must be taken into account in the description of the cloud.

Pauli blocking inhibits collisions at low temperature

At ultra low temperature, the only possible collisions are s-wave collisions. Indeed, colliding particles have little kinetic energy and collisions occur with zero centrifugal energy: the wave functions are spherically symmetric in the center-of-mass frame[13]. For s-wave collisions, the probability amplitude of the collision is proportional to the probability of the two particles to be at the same point. It follows that collisions between identical fermions are suppressed at low temperatures. An interacting Fermi gas mostly behaves as an ideal Fermi gas.

Broadening of the velocity distribution in BECs

In a Bose gas, the collisions are not suppressed at low temperature, and they can be accounted for in the energy by a mean-field term. The energy to add an extra particle, that is the chemical potential, for an interacting Bose condensate in a harmonic trap, in the Thomas-Fermi regime (when the kinetic energy is negligible) can be written as (Dalfovo *et al.* [43]):

$$\mu = \frac{\hbar\,\omega}{2}\left(15\,N\frac{a}{a_{\mathrm{ho}}}\right)^{2/5} \tag{I.11}$$

where a is the scattering length of the atoms, and a_{ho} is the size of the ground state of the harmonic oscillator of same frequency as the trap: $a_{\mathrm{ho}} = \sqrt{\hbar/(m\,\omega)}$. If we assume that all the energy of the trapped condensate is transformed into kinetic energy when

[11] The trap frequencies express the stiffness of the trap: the trapping potential can be parabolized and expressed as $U = (1/2)\,m\,\omega^2\mathbf{r}^2$

[12] The typical density of an atomic vapor BEC is $10^{14}\,\mathrm{At}\cdot\mathrm{cm}^{-3}$. Such a sample can be called dense because many-body effects are present.

[13] The proper description of the problem is done using the wave function of the reduced particle, and not the wave function of the particles themselves. This wave function is spherically symmetrical for s-wave collisions, but not the wave function of the real particles, if the two particles are not identical.

the condensate is released from the trap, the momentum width of the atomic source can be derived from the chemical potential. The corresponding length-scale (given by $\lambda_{\mathrm{BEC}}\,\Delta p = \hbar$) gives the length of the wave packets, or, in other words, the cubic root of the coherence volume:

$$\lambda_{\mathrm{BEC}} = \sqrt{\frac{\hbar}{m\,\omega}}\left(\sqrt{\frac{\hbar}{m\,\omega}}\frac{1}{15\,N\,a}\right)^{1/5} \tag{I.12}$$

As with Fermi gases, we find that the coherence volume decreases with the number of atoms in the cloud. Interactions in Bose-condensed clouds have an impact on momentum distribution, coherence volume, and collimation similar to quantum pressure in Fermi gases.

Collisional shifts in interferometers

An atom interferometer measures difference in atomic phase shift accumulated between the branches of the interferometer. Collisions between atoms contribute to this phase shift. In a mean-field description, this shift can be interpreted as a change in the atomic frequency, given by $\Delta\omega = \mu/\hbar$. This frequency shift gives rise to an unwanted phase difference measured at the output of the interferometer.

First of all, it can introduce systematic errors in the measurements if the phase shift is repeated from one experimental run to another. These systematics are well-known with atomic clocks. They are directly interpreted as a collisional shift of the frequency of the clock transition as this is the frequency probed by the clock measurement (Gibble and Chu [44], Sortais *et al.* [45]). These systematic shifts can be calibrated as a function of atom number and, being reproducible, they can be accounted for and subtracted (Pereira Dos Santos *et al.* [46]). With inertial-sensing interferometers, the origin of the systematic phase-shift is more subtle: the two wave packets are physically separated and, if the beam splitters are really 50/50 beam splitters[14], the collisional phase shift is the same for both arms of the interferometers. However, during the beam splitting process, the two wave packets overlap, and this gives rise to a systematic phase shift (Le Coq *et al.* [47]).

A second issue with collisional shift in interferometers arises from the fact that as both the total atom number and the splitting ratio between the different arms, fluctuate, the phase shift is not repeatable. This can be interpreted as a phase diffusion (Castin and Dalibard [48]) in the relative phase in the two arms, the diffusion process appearing as a spread of the RMS value of the phase difference over repeated experiments[15].

[14] In actual interferometer setups, as I will expose in the next section, the beam-splitters and mirrors are not perfect, and there is indeed a systematic imbalance in the atom number on the different segments of the interferometer.

[15] This is a good example of loss of coherence through averaging over a statistical ensemble, as mentioned earlier. The phase difference between the two condensates is always well-defined, but it fluctuates from one experiment. If the fluctuations are larger than 2π, the ensemble of condensates have lost coherence: although each individual experiment shows a phase between the condensates, when averaged the phase disappears, and the interference signal washes out (see Jo *et al.* [49] and references within for a discussion of this decoherence process).

Ultra-cold Fermi gases behave as ideal gases, as collisions are suppressed. As a result, they have no collisional shift and both the unwanted systematic errors observed in clocks and the reduction of the coherence time due to phase diffusion are suppressed Gupta *et al.* [50], Roati *et al.* [51]).

Comparison of an interacting BEC and a Fermi sea as atomic sources

As we have seen, the coherence length of an atomic cloud is a very important parameter for an atomic source, both in regard of its coherence and its collimation. We can consider it as a figure of merit for the suitability of a source for long-interrogation-time atom interferometry. Let us compare the orders of magnitude accessible for the coherence length for an interacting BEC and a Fermi sea, using equations I.10 and I.12.

The experimentally accessible parameters are N, the number of atoms in the cloud, and ω, the trap frequency, higher for tightly confining traps. Typically, in current ultra-cold atom experiments, N is on the order of 10^6. Increasing N gives a better signal-to-noise ratio in the experiments and leads to higher quantum-projection noise limit (Wineland *et al.* [52], Santarelli *et al.* [53]), but, for a degenerate source, decreases the coherence length. ω ranges between Hertz and kiloHertz[16]. The scattering length, a, is equal to 5 nm for rubidium.

The values of the coherence lengths for different trapping frequencies are:

	$\omega = 2\pi \cdot 20\,\mathrm{Hz}$	$2\pi \cdot 1\,\mathrm{kHz}$	$\omega = 2\pi \cdot 20\,\mathrm{kHz}$
λ_{BEC}	300 nm	18 nm	4.8 nm
λ_{F}	130 nm	29 nm	4.0 nm

We can see that for both types of degenerate gases a weak confinement yields more coherent and collimated atomics sources. In addition, the orders of magnitude of coherence length for Bose gases and for Fermi gases are similar (see Figure I.2 for a graph comparing coherence lengths for different experimental parameters).

[16] The lower limit for the trapping confinement is set by the trapping force required to maintain the atoms in the trap. In the case of atoms in an gravity field g, such as on Earth, the smallest possible value for ω is $\sqrt{2\,g\,r} \sim 2\pi \cdot 20\,\mathrm{Hz}$ for a trap size of $r = 1\,\mathrm{mm}$.

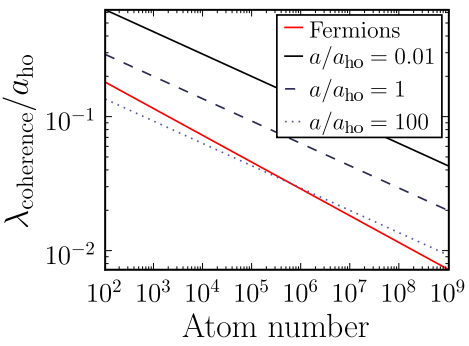

FIGURE I.2 – **Coherence length of degenerate clouds**
Typically, for rubidium, $a_{\mathrm{ho}} < 2.5\,\mu\mathrm{m}$ ($\omega > 2\pi \cdot 20\,\mathrm{Hz}$) and $a_{\mathrm{ho}} > 75\,\mathrm{nm}$ ($\omega > 2\pi \cdot 20\,\mathrm{kHz}$). The scattering length for rubidium is $a = 5\,\mathrm{nm}$. Therefore, unless the scattering length is enhanced using a magnetically tunable-Feschbach resonance, $a < a_{\mathrm{ho}}$.
Thus, typical experimental conditions for BECs are represented by the solid and the dashed lines; the coherence length of a Bose condensate is always larger than that of a Fermi gas.

The scattering length a can be decreased via magnetically-tunable Feschbach resonances. This can yield increased coherence in Bose gases, as recently demonstrated by Fattori *et al.* [54], as well as diffraction-limited atom-optic sources as observed in Cornish *et al.* [55]. The limits of this technique are that the magnetic field has to be very well controlled and homogeneous in order for interactions to cancel over the entire sample, and also to avoid additional magnetically-induced phase shifts in the interferometer leading to systematic errors.

1.3.3 Cooling to quantum degeneracy

Degenerate atomic sources are promising candidates for atom interferometry. These atomic sources have been experimentally observed only recently. The technical challenge of cooling a dilute atomic vapor to a BEC, a quantum degenerate gas, involves the combination of laser-cooling techniques, for which Steve Chu, Claude Cohen-Tannoudji, and William Phillips were awarded the Nobel prize in 1997 (Chu [56], Cohen-Tannoudji [57], Phillips [58]), and the evaporative cooling techniques pioneered on spin-polarized hydrogen by Harold Hess (Hess [59]).

A dilute atomic vapor is first trapped and cooled using the radiation pressure of near-resonance lasers (see e.g. Metcalf and van der Straten [60]). This first stage creates an atomic cloud in a Magneto-Optical Trap (MOT) at a sub-milliKelvin temperatures and densities around $10^{10}\,\mathrm{at}\cdot\,\mathrm{cm}^{-3}$. Further cooling in optical molasses can bring the temperature of the cloud[17] to $10\,\mu$K.

To reach the BEC critical temperature, the phase space density ($n\lambda_{\mathrm{dB}}^3$, with n the atomic density and λ_{dB} the de Broglie wavelength) must be above 1, six orders of magnitude above the phase-space density of optical molasses. Phase-space densities achievable through laser cooling are ultimately limited by photon scattering. More fundamentally, the relationship between fluctuations and dissipation limits the temperature achievable through a dissipative process: any dissipative process will bring in some fluctuations[18], these fluctuations will limit the lowest temperature achievable. The fluctuation-dissipation theorem relates the fluctuations to the dissipation: the fluctuations can be reduced only by reducing the amount of dissipation. An arbitrarily low temperature can theoretically be reached through dissipative processes by reducing the amount of dissipation as the temperature decreases, but the time required to lower the temperature increases exponentially[19].

[17] Figures quoted here are given for ^{87}Rb. They vary from a laser-cooled species to another.

[18] The fundamental laws of physics are conservative. Dissipation, whether it be in quantum mechanics, or in classical mechanics, can only occur when considering the system of interest as coupled to a reservoir with a large number of degrees of freedom. Averaging the equations over the external degrees of freedom, to remove the reservoir from the description of the system, introduces dissipation in the averaged values. It also means that fluctuations from these mean values have to be added to the description of the system.

[19] This strategy has been attempted with some success with laser cooling of atoms, by developing sub-recoil cooling techniques in which atoms are accumulated in dark states free of dissipation as they are cooled down. The amount of coupling to the environment was never reduced enough to reach Bose-Einstein condensation. It was limited by multiple scattering of photons in the cooled cloud.

This is why the final cooling stage to reach BEC, evaporative cooling, is done in a conservative trap. The atomic gas is kept at thermal equilibrium with itself, but decoupled from any other system[20]. Energy is removed from the atomic cloud by removing the atoms in the high-energy tail of its thermal distribution, by lowering the trap depth. As time is left for the gas to rethermalize, the temperature of the cloud, given by the peak of its velocity distribution, is lowered. In this process, atom-atom collisions are critical, as they rebuild the Maxwell-Boltzmann velocity distribution after its tail has been removed. As the cloud is trapped, decreasing its energy makes it settle down at the bottom of the trap, its density increasing. This increase in density is important for reaching BEC, but it is also important for the success of the evaporation: if density increases enough to compensate for the loss of atoms, collision rate also increases.

A historical review of atom-interferometric experiments shows that the sources used have progressively converged to slower and denser sources as the atom-cooling techniques progressed. Indeed a close look at the important parameters of an atomic source shows that they can be summarized by the coherence volume and the expansion rate of the cloud. Optimizing a source according to these parameters while imposing a high flux on the detector maximizes the source degeneracy. Degenerate sources have limitations when used for atom-interferometry: quantum-pressure in the case of fermions, and interactions in the case of bosons reduces their coherence volume. In the case of bosons, collisions induce unwanted terms in interferometry. A close study of the collimation and coherence of both fermionic and bosonic sources shows that the relevant characteristic length scales (given by equations I.10 and I.12) are similar for both gases. The interparticle quantum coherence present in BECs is not required for atom interferometry. BECs are not needed for classical schemes used in current atom-interferometry experiments. They woud be preferred over thermal clouds or fermi gases only for signal-to-noise considerations[21].

2 Inertial sensing with atoms

The goal of this section, is to establish the link between the phase shift measured in inertial-sensing atom interferometers and the gravito-inertial fields. In particular I discuss a general-relativistic description of the interferometer as one of the important

It is however worth noting that with these techniques a phase-space density of $1/2$ was achieved (Mukaiyama *et al.* [61]).

[20] The trap has to be created with very little noise or fluctuations.

[21] Non classical states such as squeezed states can be used to push the limits of quantum projection noise on atomic phase measurement. In this case BECs may be required to perform the experiment (Bouyer and Kasevich [62]).

application of atom-interferometric inertial sensing is testing general relativity. These calculations have been performed in details with different formalisms in numerous previous publications, and the reader is invited to refer to Bordé [63] or Wolf and Tourrenc [64] for other examples of derivations.

Current state-of-the-art inertial sensors use photon-interferometry for absolute measurements: Sagnac-effect fiber-optics gyrometers or gyro-lasers, and interferometrically-tracked free fall of test masses for absolute gravity measurement[22]. However, due to their non-zero rest mass, atoms are much more coupled to the gravito-inertial fields. For the same interferometer dimensions, an atom interferometer displays eleven orders of magnitude more of sensitivity to an inertial field than the equivalent photon interferometer. Indeed the scale factor for an inertial-sensing interferometer is given by a geometrical factor, and the Compton angular frequency, $\omega_{\text{Compton}} = mc^2/\hbar$, for an interferometer using particles of mass m, or the angular frequency ω of the light, for a photon interferometer[23]. For rubidium atoms, $\omega_{\text{Compton}} \sim 10^{26}\,\text{rad}\cdot\ \text{s}^{-1}$, whereas for a helium-neon laser, $\omega \sim 3 \cdot 10^{15}\,\text{rad} \cdot \text{s}^{-1}$.

Atoms thus seem to be very good candidates for high-precision measurements of small rotation and acceleration. Atom-interferometric inertial sensing is still in its youth, whereas photon interferometry is a mature technique, but the progress in controlling the systematic errors, the noise, and increasing the size of the interferometers has led to very promising results with cold-atomic sensors, with a sensitivity comparable to other kinds of sensors, for both rotation (Gustavson *et al.* [66, 17], Canuel *et al.* [15]) and for acceleration (Peters *et al.* [14], Peters *et al.* [19]).

In this section, I use an interferometer geometry commonly-used in inertial sensors as an example to derive the inertial phase shift. I first give the simple textbook[24] derivation of the phase shift measured in this interferometer that does not require relativity, and only a semi-classical view of quantum mechanics. I then refine the description of this interferometric process by repeating the calculation in the reference frame of the apparatus to underline how the phase-shift can be interpreted as an inertial phase shift on the atom. Next, I reformulate the calculations using relativistic expressions. Finally, I consider the wave nature and spatial extent of the particle used in the interferometer and introduce a more general formalism valid for all interferometers. One of the goals of this progression is to make the link between the purely non-relativistic description of the interferometer, often used in atom-optics, and the relativistic derivation of the phase shift used in photonic inertial-sensing interferometers.

[22]The best absolute gravimeter is currently the FG5, from Micro-g solutions, that tracks a corner-cube mirror falling in a vacuum tube with a laser. See Vitushkin [65] for a study of their precision and accuracy.

[23] This can easily be seen by comparing the phase-shift for a Sagnac-effect gyrometer of area $\mathbf{S}$ rotating with a rotation $\mathbf{\Omega}$: $(m/\hbar)\, 2\mathbf{\Omega}\cdot\mathbf{S}$ for a massive-particle interferometer, and $4\pi\,\mathbf{\Omega}\cdot\mathbf{S}/(\lambda\, c)$ for a photon interferometer. A more general formula useful for comparing interferometers is derived in §I.26.

[24]This derivation is present in many articles or theses dealing about atom interferometry. See Storey and Cohen-Tannoudji [67] for an introduction to the methods used, Peters *et al.* [14] and Wolf and Tourrenc [64] for an application of these methods to a specific experimental configuration.

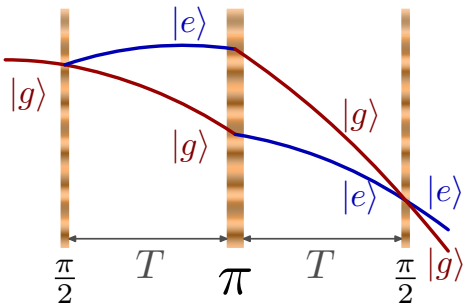

FIGURE I.3 – **Light-pulse interferometer**
Raman transitions between hyperfine levels $|e\rangle$ and $|g\rangle$ with momentum transfer create a Mach-Zehnder interferometer:

1. **Beam splitter**: a $\frac{\pi}{2}$ pulse splits the wave packet into a superposition of different momentum states
2. **Mirror**: a π pulse inverts the two states
3. **Output beam splitter**: a second $\frac{\pi}{2}$ pulse recombines the wave packet

2.1 Mach-Zehnder geometry

An interferometer to be sensitive to gravito-inertial fields if it has physically separated paths. Unlike in atomic clocks relying on Ramsey interferometry, the beam-splitting processes used in inertial-sensing interferometers communicate momentum to the atoms. A common scheme uses two-photon transitions to coherently transfer momentum from laser beams to atoms (Kasevich and Chu [11]). Laser pulses of appropriate duration and intensity can contribute two photon momenta and be used as mirrors or beam splitters to form what is called a light-pulse interferometer, for instance with a Mach-Zehnder geometry (see Figure I.3).

Two hyperfine levels $|g\rangle$ and $|e\rangle$ of an atom can be coupled via two counter-propagating laser beams with a Raman transition. Unlike simple Bragg scattering, the different output states of a beam-splitter are distinguishable not only by their momentum, but also by their internal degree of freedom. The output of the interferometer can thus by read as in Ramsey interferometry, by measuring atomic populations (see Bordé [68] for the initial proposition), for instance with resonant laser light, which is much easier than measuring momentum.

A Raman laser pulse induces Rabi oscillations between $|g, \mathbf{p}\rangle$ and $|e, \mathbf{p} + \mathbf{\Delta p}\rangle$, where $\mathbf{\Delta p}$ is the momentum contributed by the two photons: $\mathbf{\Delta p} = \hbar(\mathbf{k_1} - \mathbf{k_2})$ with $\mathbf{k_1}$ and $\mathbf{k_2}$ the wave-vectors of the two counter-propagating lasers. By adjusting the duration of the pulse to half a Rabi period[25], the atomic population can be fully transfered from one state to another, thus deflecting the beam and creating the equivalent of a mirror, called a π pulse, in atom interferometry jargon, inherited from NMR parlance. Similarly, a laser pulse of duration one quarter of a Rabi period (a $\pi/2$ pulse) creates a superposition of the two states, forming a beam-splitter.

2.2 Calculation of the phase shift in an inertial reference frame

The quantum-mechanical description of an atom is that of a wave, or a partially localized wave packet, rather than a particle. Its evolution is given by a propagation equation, the Schrödinger equation, equivalent to the Maxwell equations in photon optics. However, the coherence volume of an atom is most often small compared to

[25] See appendix A for the full expressions of the Rabi angular frequency and the transition probability.

the dimensions of the interferometer, and a semi-classical picture is well-adapted to the description of atom interferometer: the atom can be considered as a point-like particle, propagating along a trajectory given by its classical equation of motion, the equivalent of a light ray in optics, with a phase, taken as the phase of the wave at the center of the wave packet. This phase is modified by propagation of the particle. The phase-shift of a particle traveling along a path $\mathcal{P}$ can be calculated using the semi-classical approximation of Feynman's path integral formalism (see Storey and Cohen-Tannoudji [67] for a tutorial article on this approach):

$$\Delta_{\mathcal{P}}\phi = \frac{1}{\hbar} S_{\mathcal{P}} = \frac{1}{\hbar} \int_{\mathcal{P}} \mathcal{L}\, dt \tag{I.13}$$

where $S_{\mathcal{P}}$ is the classical action along path $\mathcal{P}$, that is the integral of the Lagrangian $\mathcal{L}$. In light-pulse interferometers, most of the time, the atom is on an inertial trajectory: no forces are applied to it and it is in free fall. We can decompose the phase shift into a free-propagation term $\Delta_{\text{free}}\phi$, and a term due to the interaction with the lasers, $\Delta_{\text{lasers}}\phi$.

Free propagation If we carry the calculations in an inertial reference frame, during free propagation there are no forces applied to the atoms: $\mathcal{L}_{\text{free}} = H_0 + p^2/(2m)$, with H_0 the Hamiltonian of the internal degrees of liberty of the atom, and p the momentum of the atom. During a free flight both H_0 and p are constant (the internal state is not changed, and, in an inertial reference frame, p is constant during free flight), the phase shift between two light-pulses is thus proportional to the time between the pulses.

The Mach-Zehnder interferometer is symmetrical: atoms spend the same amount of time in each state $|g, \mathbf{p}\rangle$ and $|e, \mathbf{p} + \mathbf{\Delta p}\rangle$ in one arm or the other. Therefore the phase shift due to free propagation is the same through both arms:

$$\Delta_{\text{free}}\phi = 0 \tag{I.14}$$

Interaction with the lasers Solving the Schrödinger equation describing the interaction of the atom with the light pulses (Moler *et al.* [69]) shows that during the interaction with a Raman pulse, the wave packet acquires a phase shift that is given by the effective phase of the Raman process: $\phi_{\text{eff}} = \phi_1 - \phi_2$, where ϕ_1 and ϕ_2 are the phases of the two counterpropagating Raman lasers at the center of the atomic wave packet:

$$\Delta_{\text{lasers}}\phi = \phi_{\text{eff}}(A) - \phi_{\text{eff}}(B) - \phi_{\text{eff}}(B') + \phi_{\text{eff}}(C) \tag{I.15}$$

with points A, B, B' and C as given by Figure I.4.

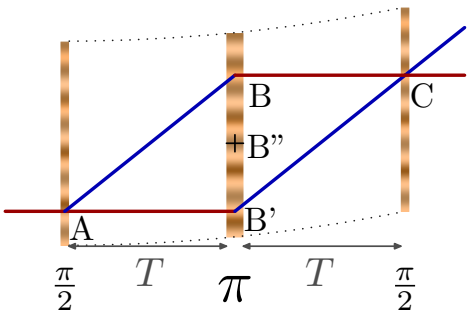

FIGURE I.4 – **Interferometer in an inertial reference frame**
Free propagation segments are symmetrical in both arms and do not yield any differential phase shift. Effective phase of the Raman process ϕ_{eff} changes as the apparatus is accelerated and the laser beams are displaced relative to the inertial reference frame. The difference in ϕ_{eff} in points A, B", and C creates an atomic phase difference at the output of the interferometer.

The phase shift measured at the output of the interferometer can thus be written[26], B" being the midpoint between B and B':

$$\Delta\phi = \Big(\phi_{\text{eff}}(A) - \phi_{\text{eff}}(B'')\Big) - \Big(\phi_{\text{eff}}(B'') - \phi_{\text{eff}}(C)\Big) \tag{I.16}$$

If the interferometer is in a constant acceleration, or equivalently in a gravitational field $\mathbf{g}$, its movement relative to the inertial reference frame can calculated. Inserting the values of the ϕ_{eff} in this formula yields the expression of the phase-shift as a function of the local acceleration:

$$\Delta\phi = \mathbf{k}_{\text{eff}} \cdot \mathbf{g}\, T^2 \tag{I.17}$$

The interferometer then performs as an accelerometer/gravimeter.

The interferometric process can be seen as measuring the classical position of freely-falling atoms on the optical ruler made up by the two Raman lasers beating together with a wavevector given by the difference of their wavevectors. Its sensitivity to inertial effects comes from the interferometric measurement of the position of the atoms used as test masses. The Mach-Zehnder geometry can perform as a gravimeter, but also a gyrometer, or a sensor for any inertial effect that appears on three successive readings of a free-fall trajectory.

2.3 Atomic phase shift in the reference frame of the apparatus

In the case of a rotation, the calculation of the previous paragraph yields an expression for the atomic phase shift at the output of the interferometer: $\Delta\phi = (2m/\hbar)\,\mathbf{\Omega}\cdot\mathbf{S}$ where $\mathbf{\Omega}$ is the rotation vector of the apparatus, and $\mathbf{S}$ is the vector area encircled by the atomic path. This formula is that of the Sagnac effect, which gives the phase shift of a light wave propagating in a closed trajectory in a rotating frame[27]. The importance of the Sagnac effect, that is, of a shift on the phase of the atoms due to

[26] This expression can be generalized: for any symmetric interferometer made of n light-pulses, the phase shift is given by the difference in the effective phases of the successive middle points. Even more generally, any symmetric interferometer described by quadratic Hamiltonians can be seen as a line of classical midpoints with effective interactions, see Antoine and Bordé [70].

[27] see for instance Post [71] for a historical review on this matter.

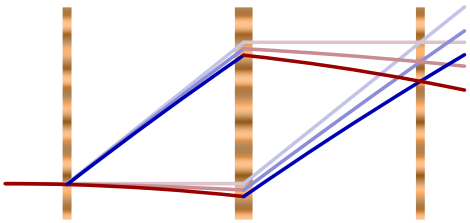

Figure I.5 – **Trajectories in the reference frame of the apparatus**
In the presence of an acceleration, the classical trajectories in the reference frame of the apparatus deviate from a straight line.
The perturbation approach we use consists in using the Lagrangien with the inertial forces and the non-deflected trajectories.

a rotation, is not obvious in our derivation of the interferometric shift. Let us revisit this calculation in the rotating reference frame of the measuring apparatus to make the connection with the Sagnac effect, or, in case of an acceleration, an inertial effect on the atom in the accelerated frame, by opposition to the movement of the lasers in the inertial frame.

Rotation as a perturbation term

In the reference frame of the apparatus, let us consider the rotation as a small perturbation of the atomic Lagrangian. If the apparatus is not turning, the trajectories are straight lines, and the interaction points with the Raman lasers are symmetrical and do not yield any phase shift, as introduced in the previous paragraph. For small angular velocities we can treat the trajectories as unmodified, but we need to add a rotational energy term to the Lagrangian, following Hasselbach and Nicklaus [13] and Storey and Cohen-Tannoudji [67]:

$$\mathcal{L}_{\text{free}} = H_0 + \frac{\mathbf{p}^2}{2m} + \mathbf{\Omega} \cdot (\mathbf{r} \times \mathbf{p}) + \frac{m}{2}(\mathbf{\Omega} \times \mathbf{r})^2 \tag{I.18}$$

The total interferometric shift is given by the integration of this Lagrangian over the unmodified trajectories. Neglecting the term in $\mathbf{\Omega}^2$, the difference in the phase of a wavepacket through each arm involves the area S subtended by the closed contour $\mathcal{P}$:

$$\Delta\phi = \frac{m}{\hbar}\mathbf{\Omega} \cdot \oint_{\mathcal{P}} \mathbf{r} \times \mathbf{p}\, dt = \frac{1}{\hbar}\mathbf{\Omega} \cdot \oint_{\mathcal{P}} \mathbf{r} \times d\mathbf{r} = \frac{2m}{\hbar}\mathbf{\Omega} \cdot \mathbf{S} \tag{I.19}$$

Thus the Sagnac phase shift appears if we consider trajectories going straight in the rotating frame, and not bent by the effect of the rotation, as the real classical trajectories in the inertial frame are. In this case, the trajectories cross the Raman lasers at the intersection points explored in the case with no rotation, and no phase shift arises from the lasers. The phase shift lies entirely in the inertial effect on the atoms.

Calculation for an accelerated frame

In the case of an acceleration, or a gravitational field, the Lagrangian in the reference frame of the apparatus is $\mathcal{L}_{\text{free}} = H_0 + \mathbf{p}^2/(2m) + m\,\mathbf{g} \cdot \mathbf{r}$. Let us suppose

that the acceleration $\mathbf{g}$ is parallel to the propagation of the Raman pulse[28], $\mathbf{k}_{\text{eff}}$. The phase shift is calculated along the unperturbed trajectories, the AB and B'C segment explore the same potential energy, and bring the same phase shifts. On the contrary, the AB' and BC segments are at different altitudes, and the phase shifts along them are different:

$$\Delta\phi = \Delta\phi_{\text{AB}} - \Delta\phi_{\text{B'C}} \tag{I.20}$$

$$= T\, m\, g\, \Delta z \tag{I.21}$$

with Δz the altitude difference between B and B',

$$= T\, g\, k_{\text{eff}}\, T \tag{I.22}$$

The phase shift in a gravimeter can thus be interpreted as the difference in potential energy explored by the two arms.

Generalization to non-perturbative treatment for the inertial effect

As show above, the phase shift can be understood as an atomic phase shift when the calculation is not performed in the inertial frame of reference, whereas it appears as a phase shift in the lasers when reasoning in the inertial frame of reference. I have performed the calculation using Feynman path integrals as the formalism, and the intuitive understanding, can easily be linked to optics. As the phase shift of a freely propagating particle along its propagation path is always zero, I had to use a perturbation approach to show inertial effects on the atom and to calculate the effect of the inertial forces on the phase of the atom along a path different from the classical path of the atom. This approach is discussed in details by Greenberger and Overhauser [72] in the context of inertial forces in neutron interferometry experiments. They show in particular the validity of this approach when the additional forces bend the classical trajectory of the particle.

More generally, the interferometric term is given by the comparison of the phase of the laser beams and the position of the atomic wave-packet in a term $\propto \mathbf{k}_{\text{laser}} \cdot \mathbf{r}_{\text{atom}}$. We can see that, in this term, the inertial effect can lie either in the displacement of the atom or in a phase shift in the laser. Depending on where the phase reference is taken, the inertial effects lie in the phase of one wave, or the other.

Using the Schrödinger equation rather than a path-integral formalism to calculate the phase shift both the contributions the laser and the free propagation can be expressed in the same equation (Antoine [73]). The Schrödinger equation holds only in an inertial reference frame, as all fundamental laws of physics do. The effects of rotation lead to a time-dependent laser wave vector in the atom-laser interaction Hamiltonian. A change of basis for the representation of the wave function can be used to express it in the rotating reference frame: $|\Phi'\rangle = U\,|\Phi\rangle$, where U is the unitary operator for the reference frame change, $|\Phi\rangle$ is the wave function in the inertial reference frame, and $|\Phi'\rangle$ the wave function in the rotating frame. The Schrödinger

[28] As the unperturbed trajectories are fully symmetrical in the other directions, components of the acceleration along these directions do not add a phase shift.

equation can thus be expressed in the rotating frame using the relation between $|\Phi\rangle$ and $|\Phi'\rangle$. This change of representation introduces the rotation in the wave function and the additional terms cancel the rotation terms in the laser interaction expression (Antoine [73]). This demonstrates formally without a perturbation approach that the effect of gravito-inertial fields can be seen either as an atomic phase shift, or a phase shift in the lasers. Indeed the phase of a wave (or a quantum state) has no physical meaning by itself, only the physical results, such as phase differences measured at the output of the interferometer, have a meaning. Thus they cannot depend on the choice of the reference frame. They are said to be *gauge invariant*.

2.4 Relativistic interpretation of the phase shift

The Sagnac effect is often said to be a purely relativistic effect, but all the calculations presented above above make no use of relativity, whether special or general. In the following paragraph, I depart from the formalism of Storey and Cohen-Tannoudji [67] and use the relativistic Lagrangian to introduce a relativistic expression of the phase shift. This formulation is more general as it can describe new inertial effects (Lense-Thirring, gravitational waves) or establish a link with photon-interferometric inertial sensing[29].

Relativistic expression of the Lagrangian

In relativity, the free propagation Lagrangian can be written, in the low velocity limit, $L_{\text{free}} = m(-c^2 + \frac{1}{2}v^2)$. The phase shift due to the internal energy of the atom is included in the rest mass[30]. The expression of the kinetic energy is only a low velocity expansion. The fully relativistic expression of the Lagrangian can be written in terms of the proper time τ of the atom:

$$\frac{d\tau}{dt} = \sqrt{1 - \frac{v^2}{c^2}} \sim 1 - \frac{1}{2}\frac{v^2}{c^2} \tag{I.23}$$

Thus the phase shift during free propagation of the atom is given by:

$$\Delta\phi_{\text{propagtion}} = -\frac{1}{\hbar}\int_{\mathcal{P}} mc^2 \frac{d\tau}{dt}\, dt \tag{I.24}$$

$$= -\omega_{\text{Compton}}\Delta_{\text{free}}\tau \tag{I.25}$$

where $\omega_{\text{Compton}} = m\,c^2/\hbar$ is the Compton angular frequency of the particle. The inertial effects are included in the expression of the Lagrangian: $L_{\text{free}} = -mc^2 d\tau$,

[29] It is impossible to describe a photon-interferometric inertial sensor without using relativistic kinematics as photons travel with a speed close to the speed of light.

[30] mc^2 is the internal energy of the atom which depends on its internal state. Classical (non-relativistic) quantum mechanics does not impose an origin for energy, whereas relativity does, this is why the jump from the mass to the energy of a state appearing in the Hamiltonian is not obvious, but the energy differences can easily translate to mass difference: $\Delta m\, c^2 = \hbar\,\Delta\omega$.

with $d\tau^2 = g_\mu{}^\nu ds^\mu\, ds_\nu$ (we use the convention that a relativistic interval is a time interval). The metric tensor $g_\mu{}^\nu$ contains all the description of the gravito-inertial effects as local curvatures of phase space:

$$\Delta\phi_{\text{propagation}} = -\omega_{\text{Compton}} \int_{\text{Atomic path}} \sqrt{g_\mu{}^\nu\, ds^\mu\, ds_\nu} \tag{I.26}$$

The scale factor of an inertial-sensing interferometer to a particular inertial effect is thus given by a geometrical factor, and the Compton angular frequency of the particle. This formula shows that the relevant quantity for the sensitivity to inertial fields of a massive particle is its Compton angular frequency.

Interpretation of the interferometric phase shift as proper time differences

Using this expression of the phase shift during free propagation, the total interferometer process can be reinterpreted in terms of proper time shifts:

In a gravity field, the gravitational red shift, or more accurately the gravitational time dilation, changes the rate at which the proper time flows as a function of the altitude: clocks that are far from massive bodies run faster; clocks close to massive bodies run slower. If the gravity field is oriented along the axis of the Raman lasers, the phase shift can be interpreted as a difference in the proper time spent along the AB and B'C segments. As D. Greenberger states very clearly in his review of the neutron interferometer ([8], sec. IX):

> *"So the phase shift [...] is seen to be caused by the different rates at which a clock ticks along each of the two beams."*

In the case of a rotation, the Sagnac phase shift arises from the fact that clocks cannot be synchronized in a rotating reference frame. The time delay between the reading of the transported clock and that of the clock standing still on the rotation platform lies at the root of the Sagnac effect (this point of view has been held long ago by P. Langevin [74] and L. Silberstein [75], a modern discussion can be found in Anandan [76]).

2.5 Spatial extent of the wave-packet

Up to now, we have neglected the spatial extent of the wave-packet. However, in certain situations, for instance when the interferometer is set into rotation, the interferometer is no longer closed: at the instant of the last recombining pulse, the centers of wave-packets are not in the same place (see Figure I.6). If this displacement is larger than the width of the wave-packet, no interference is observed. If the wave-packets do overlap, the interferometric phase measured has to be calculated taking into account the spatial variation of the phase across the wave-packet.

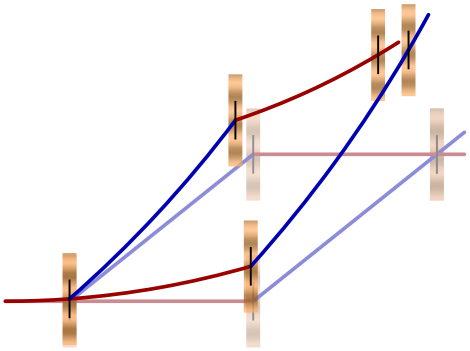

Figure I.6 – **Trajectories in a rotating frame**
When the apparatus is rotating, the momentum kicks communicated by the Raman lasers no longer add up to close the interferometer: at the instant of the last recombining pulse the centers of the wave-packets are not at the same point. Indeed the phase measurement event is defined by its time, the instant at which the recombining $\pi/2$ is sent, and not by a specific position of the atoms.

Contribution of the separation to the interferometer phase difference

The simplest possible description of the spatial extent of the atomic wave is a plane wave. Let us study the propagation of plane waves in the interferometer[31] to have an estimation of the phase shift due to the separation of the wave-packets on the output beam-splitter.

For a plane wave, the phase shift between two spatially separated points $\mathbf{r}_1$ and $\mathbf{r}_2$ is given by:

$$\Delta\phi = \frac{1}{\hbar}\mathbf{p}\cdot(\mathbf{r}_2 - \mathbf{r}_1) \tag{I.27}$$

It can be expressed in a fully covariant way using $\mathbf{P}^\mu$, the energy-momentum four-vector and $d\mathbf{s}^\nu$ the elementary interval. This expression gives the difference between the phase at the center of mass[32] of a particle and the phase measured at another position of its wave packet. Thus the phase difference measured between two wave packets with separated center-of-mass positions r_1 and r_2 is given by[33]:

$$\Delta\phi_{\text{separation}} = \frac{c}{\hbar}\int_{r_1}^{r_2} g_\mu{}^\nu\, \mathbf{P}^\mu d\mathbf{s}_\nu \tag{I.28}$$

Effect of Raman pulses on a plane wave

For a particle with no spatial extent, the deflection by a Raman pulse induces a phase-shift equal to the effective phase of the Raman transition. We have already seen that this phase shift can be accounted for either in the propagation phase shift, in which case the phase of the lasers is considered as unmodified by the inertial fields,

[31] A wave-packet is a superposition of plane waves. For the calculations performed here to be complete, it would be necessary to apply the results derived for a plane wave to each spectral component of the wave-packet, and sum the resulting phase shifts. Exact calculations for Gaussian wave packets have been performed by Bordé [77] using a different formalism. None of the formulas presented here differ when calculations are performed with complete wave-packets rather than plane waves.

[32] A plane wave has no center of mass. In our calculations on plane waves, the phase acquired through propagation can be seen as the phase of a reference position in the plane wave, this position moving along the trajectory defined by the classical equations of movement of the particle.

[33] We use the convention that the relativistic interval is a time-like quantity, thus the spatial quantity is given by $c\,ds$.

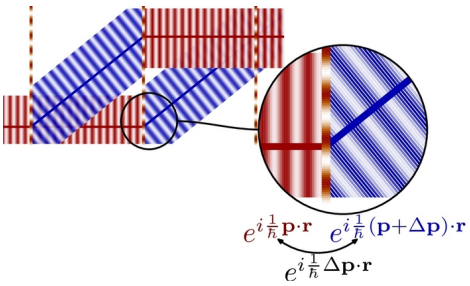

FIGURE I.7 – **Effect of Raman pulses on plane waves**
The Raman pulse acts as a phase mask on a plane wave, contributing the phase required to deflect it between $|\mathbf{p}\rangle$ and $|\mathbf{p}+\mathbf{\Delta p}\rangle$.
This diagram should be taken with a pinch of salt as it suggests that the beam splitters operate at a given position, whereas they actually operate at given instant.

or in the phase contribution of the Raman pulses, in which case propagation of the atom between beam-splitters and mirrors is described as inertial and yields no phase shift.

For a plane wave, this phase shift can be interpreted as the difference between the local phases of the incoming and the outgoing waves, before and after deflection by a beam splitter or a mirror (see Figure I.7). The phase shift occurs because the phase planes are not parallel.

The Raman pulse can thus be seen as a phase mask acting on the atomic wave function, just like in photon optics diverging light rays can be focused back together using a phase mask to compensate for the differences in the propagation times for the different rays. A Fresnel lens is a clear example of this effect, but all thin lenses can be understood as operating similarly, and, closer to our situation, the same is true for mirrors. In our atom-optic interferometer, the π-pulse beams play the role of mirrors bringing the beams back together, it is thus not surprising to find that the different phases contributed by the Raman pulses account for the same effect as a free propagation phase factor while constraining the atom on a trajectory: the Raman lasers act to deviate these trajectories.

Complete expression for an interferometer with spatial separation and propagation

Thus two different phenomena contribute to the phase shift: propagation, and physical separation of the wave packets at the output of the interferometer. Combining the formulas for both contributions (I.26 and I.28), the phase difference between the two waves traveling through each arm of the interferometer, at a given point $\mathbf{r}$ on the output beam splitter, can be expressed as:

$$\Delta\phi = \left(\int_{\mathcal{P}_1} - \int_{\mathcal{P}_2}\right)\omega_{Compton}\sqrt{g_\mu{}^\nu\, ds^\mu\, ds_\nu} + \left(\int_{\mathbf{r}_1}^{\mathbf{r}} - \int_{\mathbf{r}_2}^{\mathbf{r}}\right)\frac{c}{\hbar}g_\mu{}^\nu\,\mathbf{P}^\mu d\mathbf{s}_\nu \qquad \text{(I.29)}$$

where $\mathcal{P}_1$ and $\mathcal{P}_2$ are the classical trajectories of the atom through each arms, $\mathbf{r}_1$ and $\mathbf{r}_2$ are the two classical exit points on the output beam splitter:

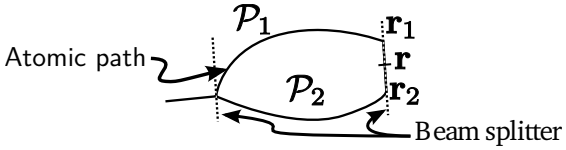

Application to pure acceleration and rotation cases

Using the expression of $g_{\mu\nu}$ for an accelerated frame or for a rotating platform, we can use formula I.29 to recover the results for an accelerometer or a gravimeter, taking in account the separation of the wave packets. I outline the calculations below for low velocity particles to show how this expression transforms into the more familiar expressions.

For small accelerations or rotations, $g_{\mu\nu}$ can be written $g_{\mu\nu} = \eta_{\mu\nu} + h_{\mu\nu}$, where $h \ll 1$, and η is the flat metric tensor, giving Minkowski's metric.

Accelerated frame $h_{00} = -2\mathbf{g}\cdot\mathbf{r}/c^2$

The tensorial sum is limited to the index 0: time. For the propagation term, we expand the square root to first order in h_{00}; this expansion gives rise to a term in $\frac{1}{2}h_{00}\,ds_0$ in addition to the propagation terms in absence of acceleration. As $ds_0 = -dt$, the integral boils down to $\Delta\phi = 1/\hbar \int m\,g\,r\,dt$ (care has to be taken to factor the time component out of the square root before expanding it). Inserting the classical equations of motion for the atom (segments in the inertial frame) in this integral yields the sum of the altitude difference: $\Delta\phi = 1/\hbar \int_0^T k_{\text{eff}} T\, m\, g\, dt = m\, g\, k_{\text{eff}} T^2$.

In an accelerated frame, there is no separation of the wave packets on the output beam splitter, and there is no need to take in account the separation term. However, if another effect is present, such as a gravity gradient, or a rotation, the separation integral brings along the sum of the potential energy difference along the world line of the recombining beam splitter: $\Delta\phi_{\text{separation}} = \Delta t\, m\, g\, \Delta z$, where Δt and Δz are the difference in time and altitude between the measurement events for each wave packet.

Rotating platform $\mathbf{h} = \{h^{0m}\} = \boldsymbol{\Omega}\times\mathbf{r}/c$

In the case of a rotating platform, the calculation is a bit more tedious, as the wave packets are separated on the output beam splitter. Both propagation of the wave packet and separation contain a term in the integrals in $\boldsymbol{\Omega}\times\mathbf{r}\cdot d\mathbf{r}$. This term is integrated over the closed line $\mathcal{P}$ defined by the path of each wave packet and the portion of beam splitter separating the two output positions, and the integration yield a Sagnac-like formula: $2m/\hbar\,\boldsymbol{\Omega}\cdot\mathbf{S}$, with $\mathbf{S}$ the area enclosed by $\mathcal{P}$. However, the separation also introduces terms due to the different velocity of each wave packet on the output beam splitter. I have not been able to find a general expression for these end-point terms and they must be calculated specifically for each interferometer geometry. They are due to the difference is wavelength of the recombining wave packets due to their different speed; they have no equivalent that I know of in optical-Sagnac interferometers. Similar end-point terms are derived more precisely in Antoine and Bordé [70].

2.6 Atom-interferometric inertial sensing and other interferometric sensors

Formula I.29 for the phase shift in an inertial field is very general and provides a unified formalism not only for atom interferometry, but also for photon interferometry, or other types of matter-wave interferometry, as well as various geometries. This allows us to draw parallels; and clarify the differences between different interferometers.

Space-domain and time-domain interferometers

The general formula takes into account the spatial extent of the wave packet[34] and the phase shift due to separation rather than propagation. It can be applied in the case of a fully delocalized wave packet, such as a gyrolaser, or a condensate in a torus (or a superfluid gyrometer[35], which is a theoretically similar situation, see Varoquaux and Varoquaux [79]). In such a geometry, the dividing and recombining beam splitters are separated by a space-like interval, and there is no propagation term, unlike in an interferometer where the beam splitting and recombining events are separated by a time-like interval. We can call these interferometers space-domain interferometers.

Light beams have the peculiar property that propagation and separation yield the same phase shift: the phase difference while following the equation of motion of a photon is the same as the phase difference in the light field between the different space-time positions of the photon propagating in vacuum. This can be seen as an expression of the fact that the internal clock of a photon does not tick. Indeed, the interval following a photon is always zero, thus the propagation phase shift of a photon is zero (using equation I.26), the phase of the field at the second position of the photon is the same as the phase of the field at the initial position of the photon. As long as the photon travels in vacuum, this phase difference is the same as the phase difference due to separation, given by equation I.28. This is why no discussion of light interferometers mentions a difference between propagation and spatial separation[36]. Moreover, light propagates in vacuum along a world line that is neither space-like, nor time-like; there

[34] The derivation performed in the previous paragraph only calculates the phase difference and does not discuss the contrast of the interferometric signal. If the separation is larger than the extent of the wave packets, the interferometric signal will disappear. This is measured in terms of correlation functions of the source, or in other words coherence volume of the field (see §I.1.1.3).

[35] A superfluid gyrometer is made of a superfluid sitting in a loop-shaped container. The loop is interrupted at one point by a Josephson junction. If the apparatus rotates, a Sagnac phase shift appears between both sides of the Josephson junction. The Josephson junction allows to perform the readout of the interferometric signal: interference between the wave function on both sides of the junction appear as a time-modulated super-current through the junction (see Avenel *et al.* [78] for a introduction to superfluid gyrometry).

[36] When light is propagating in material media, this distinction can make sense. The propagation appears through the refractive index of the medium, and can yield an additional phase shift, unrelated to inertial effects. In fiber-optic gyroscopes, for instance, it is necessary to consider both the wave propagating in the corotating direction and that in the counterrotating direction to eliminate the refraction properties of the medium (see Arditty and Lefevre [80] for a discussion).

is no real space-domain light interferometer, although a gyrolaser is the equivalent of a superfluid gyrometer, as it is a standing wave in a circular cavity interfering with itself[37], while a fiber optic gyrometer is closer to an atom interferometer.

Time-domain and space-domain interferometers have access to different physical effects. This is well illustrated by the calculation of the phase shift for a purely accelerated frame, or on a rotating platform. Indeed acceleration can only be probed by the propagation term, as it appears as a difference in the proper time accumulated by the particle in each arm of the interferometer. It is a measure of the differential gravitational red shift (i.e. relativistic time dilatation), and the particles probing the field have to spend some time at a different altitude. The scale factor of a gravimeter is given by the time spent at different altitudes in each arm; a gravimeter does not need a spatial area and can be a purely time-domain interferometer.

On the contrary, the Sagnac effect is only related to the area swept along the arms of the interferometer, and not the speed at which the particle propagates through these arms, if they propagate at all. A Sagnac interferometer can be a purely space-domain interferometer. The measured phase shift is an expression of the purely topological phase induced by the rotation on Lorentz-invariant scalars, such as the phase of a wave. This phase difference is not created by the propagation of the particle, but an is expression of the fact that coordinate time cannot be defined in a univalued global way in a rotating frame (see Ashby and Allan [81] or Varoquaux and Varoquaux [79] and references within).

Necessity of relativity in Sagnac effect derivations

The final formula for the phase shift derived in this section that is applicable for all interferometers is expressed within the formalism of general relativity. A unique feature of photons is that their rest mass is zero and their speed is c. Approximations of the above formulas to non-relativistic formulas cannot be performed. This has led to the claim that inertial effects such as the Sagnac effect can only be explained in the frame of relativity (special, and general), using relativistic kinematic. Moreover, confusion, arising most probably from the lack of a common description of interferometers, has led to arbitrary distinctions made between superfluid gyrometers and other Sagnac-effect gyrometers[38].

As illustrated by the calculation performed in the first paragraph of this section for a light-pulse atom interferometer, or in Varoquaux and Varoquaux [79] for superfluid gyrometers, the correct formula (to the first order in $\mathbf{\Omega} \times \mathbf{r}/c$) can be derived using non-relativistic arguments (no Lorentz transformations, no covariant or contravariant

[37] Unlike in a superfluid gyrometer, the wave vectors of the modes of a gyrolaser are not imposed but free to adapt to the rotation. There is no need for an equivalent to Josephson junction to relax the phase continuity condition, as in a superfluid gyrometer, and the effect of a rotation is the splitting of the mode of the cavity into two counter-rotating modes of different energies.

[38] See Malykin [82], Nandi and Zhang [83], Rizzi and Ruggiero [84], for examples of this distinction between superfluid gyrometers and Sagnac-effect based gyrometers, and Varoquaux and Varoquaux [79] for an answer.

notations), as long as the phase of the various waves is expressed in an inertial reference frame[39].

The necessity for a relativistic description of the Sagnac effect is often illustrated[40] by the flawed classical derivation of the effect, first performed by Sagnac himself: if the phase shift is estimated using the velocity of the two counter-propagating objects in the interferometer, the right formula can be derived ($\Delta\phi = 4\pi\,\mathbf{\Omega}\cdot\mathbf{S}/(\lambda\,c)$), but with the wave phase velocity, instead of c. The error here is not to use non-relativistic kinematics but rather, either to discuss a Sagnac effect for the phase of a wave propagating in a medium, or to write the propagation equation for a particle in a non-inertial reference frame, when the Sagnac effect comes from the very fact that the propagation equation only holds in an inertial reference frame.

In a relativistic picture of the interferometric process, the interferometer can be seen as a comparison of the reading of two clocks transported along the different paths. Physically transporting very accurate clocks along macroscopic paths (see Ashby and Allan [81] and references within) displays the same effects. There is a striking similarity between a clock transportation experiment performed with atomic clocks, in which the time flow is measured continuously during the transport by reading the evolution of the phase of an atom, and an inertial sensing interferometer, in which the phase evolution of an atom along two different path is compared by an interferometric process. The picture of inertial-sensing interferometry as a comparison of clocks is very robust and can apply universally to all inertial sensing interferometric processes, whether they be with atoms, photons, or superfluids, and whatever may be the geometry of the interferometer.

For interferometric experiments not involving correlation measurements, the relevant coherence measurement appears to be the coherence volume, that is the size of the wave-packet. In the case of strongly diverging sources, such as atomic sources, another important quantity is the divergence, or the expansion of the source. In the case of atomic sources, these two quantities are directly linked as the inverse of the momentum width gives the size of the wave-packet, for dilute samples. If signal-to-noise considerations are taken in account, the number of particles in one coherence volume becomes the relevant quantity for the quality of the interferometric measurement. In cold-atom

[39] It is impossible to find a gauge field that maps the phase of a wave between two reference frames, one rotating relative to the other, and that transforms the observable quantities of the wave related to the phase, such as the velocity, proportional to the gradient of the phase. Indeed the velocity field in a rotating frame is given by $\mathbf{\Omega}\times\mathbf{r}$, and no gauge field can be added to the phase of the wave function that would generate such a velocity field, as its vorticity is non-zero. The fundamental propagation equation of the wave, giving the evolution of its phase, only holds in an inertial reference frame, as all fundamental laws of physics. It can be transformed to other reference frames through the addition of inertia-related terms, but this requires care, especially if both quantum and relativistic effects are to be taken in account. In this case the proper theoretical framework is that of the Dirac equation.

[40] See Malykin [82], §5.2 and references within for a discussion claiming that classical kinematics cannot explain the Sagnac effect, whether it be with light waves or with matter waves.

terms, this quantity is the phase-space density. The high-phase-space-density atomic sources are the degenerate gases, BEC and Fermi seas. Due to Pauli blocking, Fermi seas have a broadened velocity distribution and a reduced coherence volume However, interactions in Bose gases induce similar effects. Moreover, these interactions give rise to systematic shifts and reduced coherence in interferometers.

These atomic sources used in interferometric inertial-sensing experiments can probe the gravito-inertial fields by exploring the metric tensor in different paths. The results of these experiments can thus be directly related to the metric tensor. We have developed a novel expression for the phase shift that unifies the effects of propagation and of physical separation, and can describe experiments in which a very delocalized wave-packet is used. Similar, and yet unpublished, work has been conducted by C. Bordé, using a propagation equation approach and with no approximations. An interesting outcome of this formalism is that the effect of the rotation is, both for propagation and separation phase shifts, related to clock synchronization in a rotation frame. Similarly, sensitivity to acceleration is related to the gravitational time dilatation. A unified, relativistic, picture of inertial sensing interferometry is offered by clock transportation and Einstein synchronization: massive quantum particles, waves, and actual clocks all carry their own time reference, and the values of the phase of a delocalized wave-packet at different positions in this wave are related by clock synchronization. Although this formalism will not be used in the remaining of this thesis, it underpins the relationship between the quantity measured, the phase read-out of the interferometer, and the fundamental effects at stake, which lie in the metric tensor.

This calculation shows clearly that the scale factor of an acceleration-sensing interferometer is given by the altitude separation achieved by the wave packets, but also by the time spent at the different altitudes. On the contrary, for a rotation-sensing interferometer (or for any other topological effect, such as the Lense-Thirring effect), only the area of the interferometer is relevant, and the interferometer can be purely spatial, e.g. a delocalized wave-packet in a torus.

Part 1

Microgravity atom interferometry

Part contents

Résumé de la première partie

Introduction to part 1

In an atom interferometer, the longer the time the atoms spend between the beam splitters, the greater the scaling factor between the accumulated phase shifts and the effect they probe. The same is true in photon interferometry, and the record-setting photon-interferometric inertial sensors are very large interferometers, such as the three-meter-wide ring laser in Christchurch, NZ (Stedman *et al.* [85]), or the four kilometers-long Michelson interferometers of the LIGO project.

However, unlike light beams, atoms that are not trapped by external forces fall in a gravity field. The available free-fall height limits interrogation times in Earth-based interferometers. Indeed, in order to avoid uncontrolled residual phase-shifts in the interferometer, it is best not to apply fields other than that which is probed during the phase accumulation period. In the case of inertial sensing this implies that atoms must be in free fall between the beam-splitting processes. Atom interferometry in micro-gravity allows for longer free fall and thus promises increased precision.

In this part, I study the use of an airplane to achieve short-duration micro-gravity for atom-interferometric inertial-sensing experiments. First, I study the airplane as an experimental platform and show that scientifically-relevant high-precision inertial measurements, namely a test of the universality of free fall, can be performed in the airplane, detailing a procedure to extract pure free-fall measurements in a jittering airplane. In the second chapter, I describe a transportable cold-atom source suitable for operation in the airplane, built and tested in micro-gravity during my thesis.

Résumé de la première partie

L'un des facteurs limitant pour le temps d'interrogation des senseurs inertiels interférométriques est la distance parcourue par les atomes en chute libre entre les impulsions lasers utilisées pour séparer le paquet d'onde en deux, ou le recombiner. En effet, augmenter le temps d'interrogation conduit, sur Terre, à la construction de fontaines de plus en plus grandes, et contrôler l'environnement (tel que l'homogénéité des champs magnétiques) sur de grandes distances pour garantir l'exactitude de la mesure devient un défi expérimental, et une véritable limite à la qualité de la mesure elle-même.

Les senseurs inertiels par interférométrie atomique gagneraient donc fortement en sensibilité en étant utilisés en apesanteur, ce qui permettrait de limiter la taille de la zone explorée par les atomes à quelques centimètres cubes, tout en bénéficiant de longs temps d'interrogation. Les mesures inertielles à grande précision en microgravité ont un enjeu double : d'une part des applications comme la navigation inertielle spatiale, ou la cartographie du champ de pesanteur terrestre par des satellites nécessitant des mesures d'accélération très sensibles au voisinage de zéro ; d'autre part, des tests fondamentaux des théories gravitationelles peuvent être menés en mesurant des courbures de l'espace-temps très faibles.

Dans cette première partie de ma thèse, je présente la source d'atomes lents refroidis par laser que j'ai construit en vue de faire de mesures d'interférométrie atomique dans un avion effectuant des vols paraboliques de 20 secondes de chute libre, ainsi que sa validation expérimentale lors d'une première campagne de vol que nous avons menée. De plus j'étudie la possibilité de l'utiliser pour réaliser un test de l'universalité de la chute libre dans l'avion.

Un Airbus : des conditions expérimentales propices à des mesures de précision ?

Jusqu'à quatre secondes de temps d'interrogation possible

Des vols suivant une trajectoire parabolique permettent de réaliser de courtes périodes de microgravité. Cependant cette microgravité n'est pas une réelle apesanteur :

l'avion est encore soumis à la friction de l'air que les pilotes doivent compenser. Dans le premier chapitre de cette partie, nous commençons par analyser des données d'accéléromètres classiques acquises lors de la campagne de vols paraboliques. Il en ressort qu'une accélération résiduelle de quelques $10^{-2}\,g$, ainsi que du bruit d'accélération, impose de découpler l'expérience de l'avion pour obtenir des temps d'interrogation supérieurs aux fontaines dans une enceinte compacte. En utilisant une expérience lâchée en vol libre dans la cabine, nous estimons que des mesures avec des temps d'interrogation allant jusqu'à quatre secondes peuvent être menées.

Précision d'un test de l'universalité de la chute libre en vol

Chaque période de microgravité se fait avec des paramètres expérimentaux non répétables : l'altitude, la rotation de l'appareil, et même l'écart à la chute libre, fluctuent. Ces variations rendent difficile toute étude systématique d'un effet inertiel, mais ne déteriorent pas une mesure différentielle. C'est pourquoi nous proposons un test de l'universalité de la chute libre effectué à l'aide de la comparaison dans un même interféromètre atomique de l'accélération subie par des atomes de rubidium et des atomes de potassium lors de paraboles. Les mesures interférométriques nécessitent plusieurs points expérimentaux dans les mêmes conditions expérimentales, afin de déduire la phase à partir d'un interférogramme. Pour pouvoir étaler ces points expérimentaux sur différentes paraboles, et avoir une bonne estimation de l'incertitude sur la phase mesurée, nous construisons un modèle statistique de l'expérience interférométrique, et nous donnons un exemple d'utilisation d'un estimateur Bayesien pour extraire la valeur de l'accélération différentielle à partir de mesures bruitées.

Vol d'une source d'atomes froids en microgravité

Le deuxième chapitre de cette première partie détaille la construction et la validation d'une source d'atomes pour une expérience d'interférométrie atomique en vol. Cette source atomique a été testée en microgravité lors d'une campagne de vol en mars 2007, que j'ai coordonnée, constituant la première validation grandeur nature des composants du projet ICE. Les résultats de ce travail ont été publiés dans Varoquaux *et al.* [86].

Pendant l'hiver 2006-2007 nous avons construit une expérience d'atomes froids pour la campagne de vols paraboliques de mars 2007, en assemblant des lasers montés par l'ONERA, une référence micro-ondes montée par l'observatoire de Paris (SYRTE) ainsi qu'une chambre à vide que j'ai conçue pour l'occasion. Les contraintes sur la robustesse et le budget encombrement, poids, puissance d'une expérience embarquée sont lourdes et j'ai développé une configuration expérimentale modulaire pour ne pas

sacrifier de flexibilité, et cependant assurer le fonctionnement de l'expérience en vol. Les lasers utilisés sont une technologie nouvelle pour l'interférométrie atomique : des sources télécom fibrées à 1560 nm, doublées.

L'expérience a très bien résisté au transport, aux fortes variations journalières de température, ainsi qu'aux vibrations et aux changements de pesanteur en vol. Nous avons obtenu un piège magnéto-optique en vol de manière fiable et reproductible. Les prochaines étape du programme sont de réaliser un interféromètre atomique en effectuant des transferts Raman. De plus, il faudra monter un blindage magnétique, afin que le mécanisme de refroidissement laser ne soit pas déséquilibré par le champ magnétique de la Terre tournant au cours de la parabole. En effet, ce déséquilibre limite le contrôle sur la vitesse de lâcher des atomes, et nous n'avons pu accéder pendant les paraboles à des temps de vols supérieurs aux temps de vols sur terre.

Cette partie résume ma contribution au lancement d'un programme d'études et de développement de senseurs inertiels par interférométrie atomique en microgravité à l'aide de vols paraboliques. Les procédés expérimentaux développés aux cours des campagnes de vol peuvent non seulement aboutir à des expériences de métrologie ou d'atomes froids en vol, mais aussi fournir de bases pour développer des techniques spatiales.

Chapter II

An Airbus as an experimental platform

'There is no use trying', said Alice, 'one can't believe impossible things.'
'I dare say you haven't had much practice', said the Queen. 'When I was your age, I always did it for half an hour a day. Why, sometimes I've believe as many as six impossible things before breakfast.'

Lewis Carroll

In this chapter, I examine the possibility of using ballistic flights in an airplane to perform high-precision atom-interferometric inertial-sensing experiments. In a first section I look at the potential increase in sensitivity through longer interrogation times and give an estimation of the maximum free-fall times accessible in the plane. In a second section I discuss the difficulties of performing high-precision measurements in the airplane and describe an experimental scheme for a test of the universality of free fall, giving special attention to the detrimental effect of acceleration noise.

Experiments in micro-gravity can be conducted in space, on the international space station or on a satellite, for instance. The PHARAO project (Laurent *et al.* [26]) has been working on a space-compatible cold-atom clock designed for the international space station. Such a project requires a large effort, as, not only is the launch very costly, but it also sets very strict requirements on the robustness of the apparatus, and its weight, size, and energy budget. Moreover it is impossible to operate on the experiment once it has been launched.

Short periods of micro-gravity can be achieved on Earth through free fall. The longest free-fall time in a ground-based facility is reached in the Fallturm Bremen, a drop tower at the ZARM (Center of Applied Space Technology and Microgravity) at the University of Bremen. It has a 123-meter-high drop tube (actual drop distance is 110 m), in which for 4.74 seconds (with release of the drop capsule), or for over 9 seconds (with the use of a catapult) weightlessness can be produced. The entire tower is 146 meters high. The drop tube is pumped down prior to every free-fall experiment to about 10 Pa. Evacuation takes about 1.5 hours, only a two to three launches per day are possible. The drop capsule can accommodate experiments up to 0.8 m diameter, and 2.4 m height. Acceleration on landing is up to 50 g. Residual acceleration during

free fall is 10^{-5} g. A cold-atom experiment currently under construction for the ZARM (Vogel *et al.* [87]) will open the door to atom interferometry in drop towers.

Free fall can also be achieved in ballistic atmospheric flights. A modified A-300 Airbus, called the Zero-G Airbus, operated by Novespace, is the biggest parabolic aircraft flight in the world. It provides near weightlessness during 20 s-long parabolas. We use it as a platform for developing techniques and conducting experiments using micro-gravity atom-interferometric inertial sensing.

1 Long interrogation times through ballistic flights

1.1 Increasing atom interferometry sensitivity with longer interrogation times

The sensitivity of an atom-interferometric inertial sensor increases with interrogation time. The dependence on interrogation time is different for different light-pulse sequences[1], but it scales at least as the square of the interrogation time, in contrast with Fourier-transform-limited measurements in atomic clocks (see Laurent *et al.* [27]). The maximal resolution on the read-out of the phase is due to shot-noise in the quantum projection during the measurement of the atomic populations (Wineland *et al.* [52], Santarelli *et al.* [53]). For a projection-noise-limited phase read-out, sensitivity of a measurement scale as $\sqrt{N}$ where N is the number of detected atoms. Overall, the ideal sensitivity of an atom-interferometric inertial sensor scales as:

$$\frac{\Delta\phi}{\Delta\phi_{\min}} = \sqrt{N}\,T^{\alpha} \qquad \text{with} \quad \alpha \geq 2 \tag{II.1}$$

In a gravity field, interrogation time is limited by the fall of the atoms, itself limited by the height of the vacuum chamber. This has motivated the use of atomic fountains, in which the available interrogation time for a given fall height is increased by a factor of two by launching the atoms upward so that they cross the vacuum fall tube twice during their ballistic flight.

In micro-gravity, the atoms do not fall, and the whole interferometry sequence can take place in a compact apparatus. As the detection region has a finite size, atoms moving relatively to the apparatus eventually escape detection. This loss of atoms will lower the sensitivity of the interferometer, according to II.1. It can be due to a non-zero average velocity, or a finite momentum-distribution width.

[1] The sensitivity of a four-light-pulse gravimeter scales as T^3. More generally, the sensitivity of a rotation-sensing interferometer scales as the area enclosed by the atomic trajectories, whereas the sensitivity of an gravitation-sensing interferometer scales as the time-indexed integral of the altitude (see §I.2.6).

Drift of the cloud Residual acceleration in a micro-gravity environment, or, in other words, displacement of the apparatus relative to free-fall trajectory, is a possible source of drift. In this case, after the center of the cloud has left the detection volume, the number of atoms scales as the tail of the cloud position distribution. As the cloud has a finite extension, it falls to zero on the time scale it takes for the cloud to drift across the detection region, and the sensitivity of the interferometer falls to zero on this time scale.

Cloud expansion In the case of a finite momentum-distribution width, the atoms escape the detection volume in all directions. After a time T_i required for the escaping atoms to reach the limits of the detection volume, the number of atoms decreases as[2] $N \propto (T - T_i)^{-3}$. As a results, the sensitivity of a measurement scales as $T^{\alpha-3/2}$ for flight times larger than T_i. As α is greater [3] than 2, the loss in atom number is compensated by the increase in the scale factor for longer interrogation times.

In a gravity field, for modern experiments, the movement of the atoms relative to the apparatus is by far the limiting factor, whereas in micro-gravity experiments, both situations will arise. Atoms can be laser cooled down to velocities of a few $\mathrm{cm}\cdot\mathrm{s}^{-1}$, and released with a initial velocity of a fraction of this figure. If the drift of the cloud is smaller than its spread, longer flight times for longer interrogation times yield increased sensitivity. This is especially true as long as the flight time is smaller than the time T_i required for atoms to reach the limits of the detection volume, in which case the sensitivity scales as T^{α}.

One should note that, as interrogation time goes up, repetition rate of the measurement goes down. The precision[4] of a repeated measurement decreases as the inverse square root of the number of measurements. For continuous probing, the precision of a sensor is thus proportional to the square root of its repetition rate. The above discussion only holds for single shot sensitivity; the gain in sensitivity with the increase in interrogation time will be scaled down for a repeated measurement if the repetition rate is determined by the interrogation time[5].

[2] I have described the cloud density has a ball, rather than a spherical Gaussian, which is more realistic. With a more accurate description, the results, especially considering long interrogation times, are similar.

[3] The sensitivity of the interferometer scales at least as the square of the interogation time.

[4] The precision of a repeated measurement is often evaluated by its Allan variance (Allan [88]), that, unlike the standard variance, does not diverge with a constant drift in the measurement. The definition of the Allan variance of a m repeated measurement x_n is:

$$\sigma^2(m) = \frac{1}{2}\lim_{n\to\infty}\left(\frac{1}{n}\sum_{k=1}^{n}\big(X_{k+1}(m) - X_k(m)\big)^2\right)$$

where $X_k(m)$is the mean value of k groups of m measurements: $X_k(m) = \frac{1}{m}\sum_{i=m(k-1)+1}^{mk} x_i$

[5] In the case of repeated parabolas, or dropped experiments, it is most likely that the repetition rate will be the repetition rate of the micro-gravity phases, unless several measurements can be carried out during one micro-gravity phase.

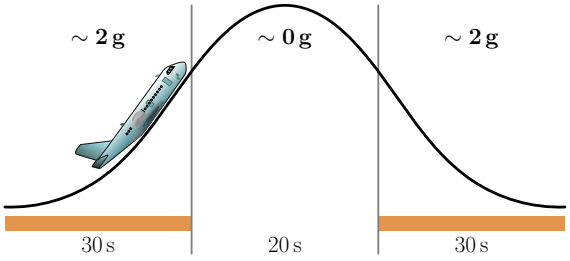

Figure II.1 – **Parabola sequence**
A 30 s-long pull-up phase is required to bring the pitch of the airplane to 45°. The airplane then follows a 20 s long parabola that brings it to a negative pitch of 45°. 30 s are required to bring the aircraft back to normal horizontal flight.

The optimal choice of interrogation time for a given velocity distribution is thus conditioned by the quality of the micro-gravity: as long as the drift of the atomic cloud does not yield heavy losses, increasing flight time increases the projection-noise-limited sensitivity of the measurement. In the next few paragraphs we will take a close look at the interrogation times achievable on the Zero-G Airbus.

1.2 Ballistic flights for micro-gravity

A parabolic flight campaign provides 90 parabolas in a total of three days. During a flight, the airplane executes six sequences of five parabolas, separated by two minutes. There is a break of several minutes between two sequences.

Starting from a steady normal horizontal flight, the aircraft takes a 2 g load factor, nosing up to 45° and climbing to 7 000 m over an interval of about 30 seconds. This is the entry pull-up phase. The 2 g load factor is the centrifugal acceleration due the curvature of the trajectory.

Then the engine thrust is considerably reduced, to the point where it just overcomes the aerodynamic drag, and the pilot kills the lift. This transitory phase of "injection" separating the 2 g pull-up from the micro-gravity parabola lasts less than five seconds.

The aircraft is then in micro-gravity phase for some 20 seconds. A symmetrical 2 g pullout phase is executed on the down side of the parabola to bring the aircraft back to its steady horizontal flight in about 30 seconds.

During the parabola, the pilots steer the airplane on a free-fall trajectory by canceling acceleration as measured by accelerometers in the center of the plane. Drag is canceled with the engines, the curvature of the trajectory is adapted to cancel out gravity, and lateral motion is kept as small as possible. Residual acceleration is a few 10^{-2} g.

1.3 Deviation from free-fall trajectories

To achieve long interrogation times, the residual acceleration is not the only relevant parameter. What we are interested in is the trajectory of a freely-falling object in the Airbus frame. Does the object drift away at a constant velocity? Is it accelerated? How repeatable is this motion? This information can be extracted by measuring the

absolute acceleration in the Airbus and integrating it twice to recover its movement in an inertial frame of reference.

Such data was collected during the March 2007 campaign in which we participated, using conventional accelerometers (see Figure II.2). As the weather was poor during this campaign, we also processed data from another campaign, with more favorable conditions. Integration of all the trajectories is shown on Figure II.4. Histograms of displacements after different flight times are shown in Figure II.5. The quality of a parabola depends strongly on the success of the injection. Once the parabola is injected, the pilots will try to correct as little as possible, for fear of overreacting and causing large oscillations[6]. However for a given campaign, pilots always seem to err on the same side, and trajectories show a mean acceleration in a constant direction of a few 10^{-2} g that varies from a flight campaign to another. Both this mean behavior, and the spread, vary noticeably between the two campaigns for which we have data to process.

Atomic detection volume is limited to, at most, a few centimeters radius, as not only is the size of the chamber limited for practical reasons but also the size of the detection optics. Histograms on Figure II.5 show that, for a reasonable probability of keeping the atomic cloud in this volume, the flight time should be limited to a fraction of a second. In this regime, the interrogation time will not be limited by the thermal expansion of a laser-cooled atomic cloud.

1.4 Canceling residual drift

Damping of acceleration noise is necessary

We have recorded acceleration noise up to acoustic frequencies during a test campaign (see Figure II.3). Acoustic noise is lower during a parabola than during normal cruise conditions, as the thrust of the engines is reduced.

[6]Many experiments in the Airbus need a low absolute value for the acceleration. For long time of flights, we need a zero mean value.

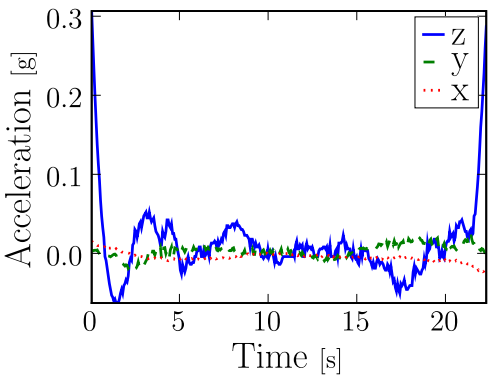

FIGURE II.2 – **Residual acceleration during a parabola**
Acceleration along the z axis (the vertical of the plane cabin) is perturbed in the beginning of the parabola, as the pilots balance the plane. At the end of the parabola, the plane is flying fast downward, and z acceleration is also perturbed. Acceleration along y (transverse) oscillates as the pilots try to keep the plane on a course as straight as possible. Along the x axis (longitudinal direction), acceleration in the parabola is small and smooth. This direction is controlled via the thrust of the engines.

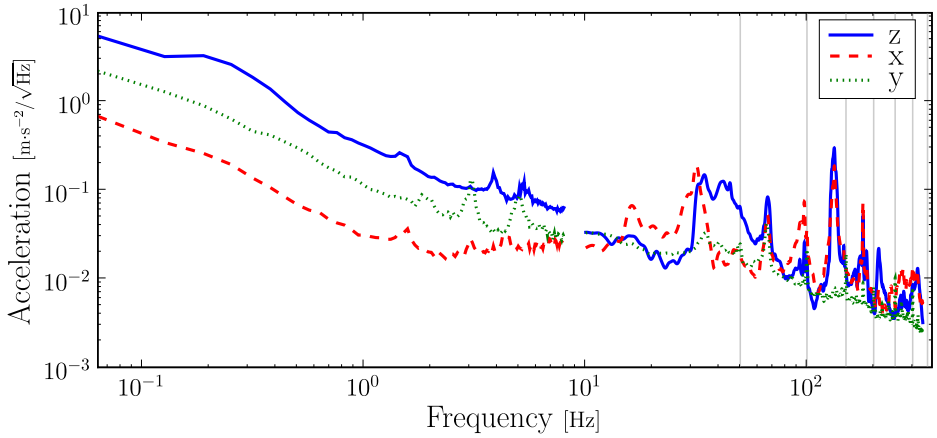

Figure II.3 – **Acceleration noise spectrum during a parabola**
The acceleration noise spectrum was recorded on an optical breadboard during a parabola. Different accelerometers where used for high and low frequency. The lower amount of noise on the y axis at high frequency can be attributed to the use of a less sensitive accelerometer in this direction.
The vertical light gray lines represent 50 Hz harmonics.

Acceleration noise is not only detrimental to atomic motion in the apparatus, it can also set the Raman-beam mirrors into vibration and limit the precision of the measurement. The apparatus, or at least the Raman-beam mirrors, need to be isolated from the airplane. A mechanical low-pass filter can be used to cut high frequency noise. Damping material such as Sorbothane cuts acoustic frequencies. Lower frequencies can be damped using springs or torsion bars[7]. The motion of the apparatus in the inertial reference frame is smoothed-out on time scales above the inverse cutoff frequency. If this frequency is low enough, the drift of the apparatus relative to the atomic cloud can be reduced during the cloud's expansion time, allowing for longer interrogation time.

The stiffness of torsion bars or springs can be made low enough for a very loose attachment between the apparatus and the airplane and the apparatus can be effectively free-floating in the cabin. However, as the analysis of the cabin acceleration shows, a free-floating object will travel several meters in a few seconds. If the apparatus is initially released with the springs in their mid-travel, linear, position, it will drift until it compresses or stretches the springs in their non-linear regime, increasing their stiffness to the point where they no longer help extending available atomic flight time.

A freely-flying apparatus

For good compensation of drift, the stiffness of the restoring mechanism should be as weak as possible, ideally zero. In other terms, the best solution would be a floating apparatus, not attached to the cabin. This is not possible as the > 100 kg apparatus

[7]Torsion bars are used in high-end vibration isolation platforms developed by MinusK (http://www.minusk.com)

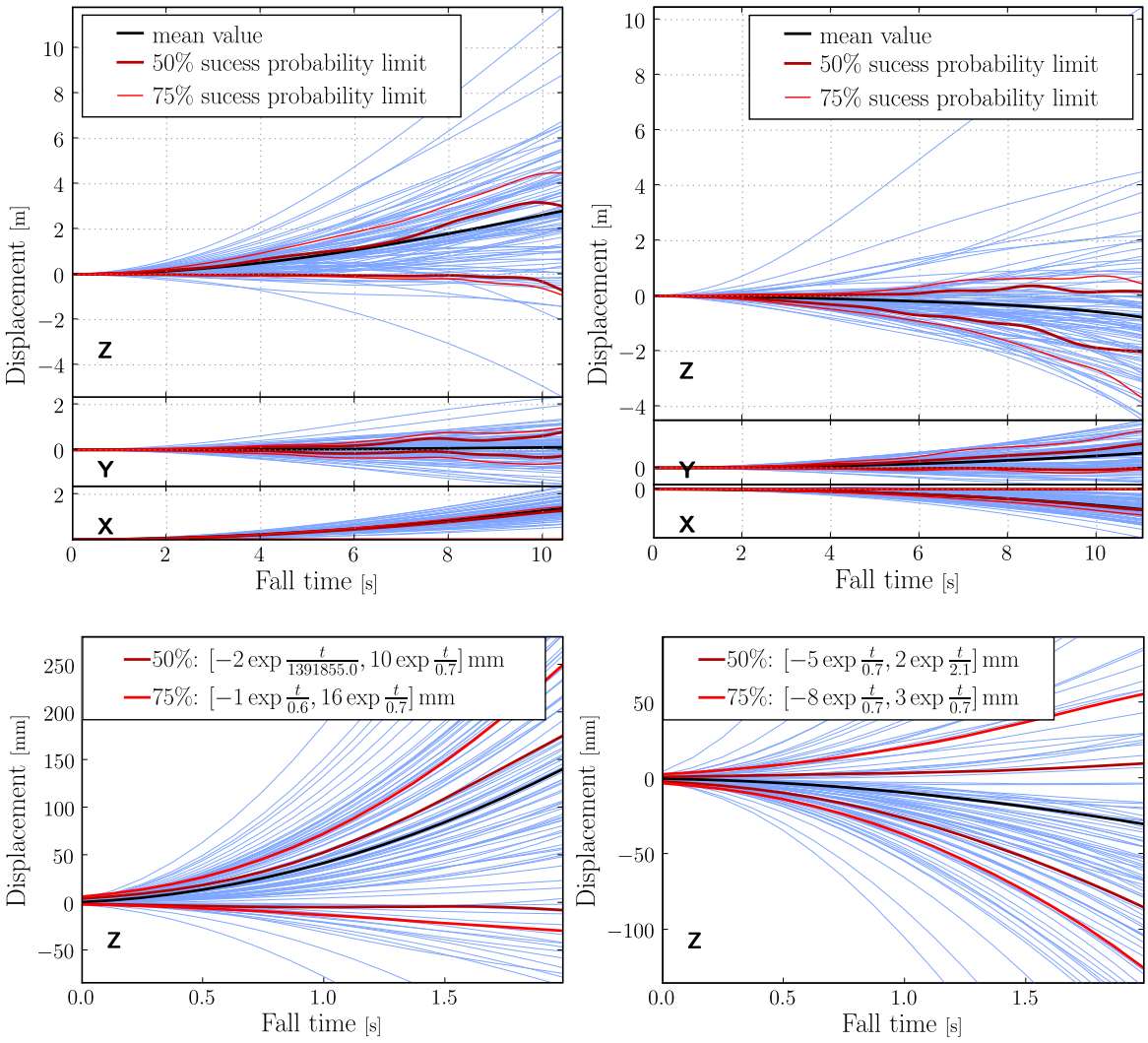

FIGURE II.4 – **(a) Displacement as a function of free-fall duration. Left – recorded during the March 2007 campaign**

The displacements are calculated for a free-flight time centered on the middle of the parabola. Lines corresponding to the maximum extension of 50% (and 75%) of the trajectories are plotted in red.

The displacement plotted is not directly an integration of the acceleration, as the initial time has been chosen, for each fall time, to position the free flight at the center of the parabola, where the conditions are best, as can be seen in Figure II.2.

The bottom plot is a zoom of the first two seconds. The 50% and 75% probability fit very well with exponential curves.

(b) Right – recorded during good atmospheric conditions

Data kindly provided by Novespace.

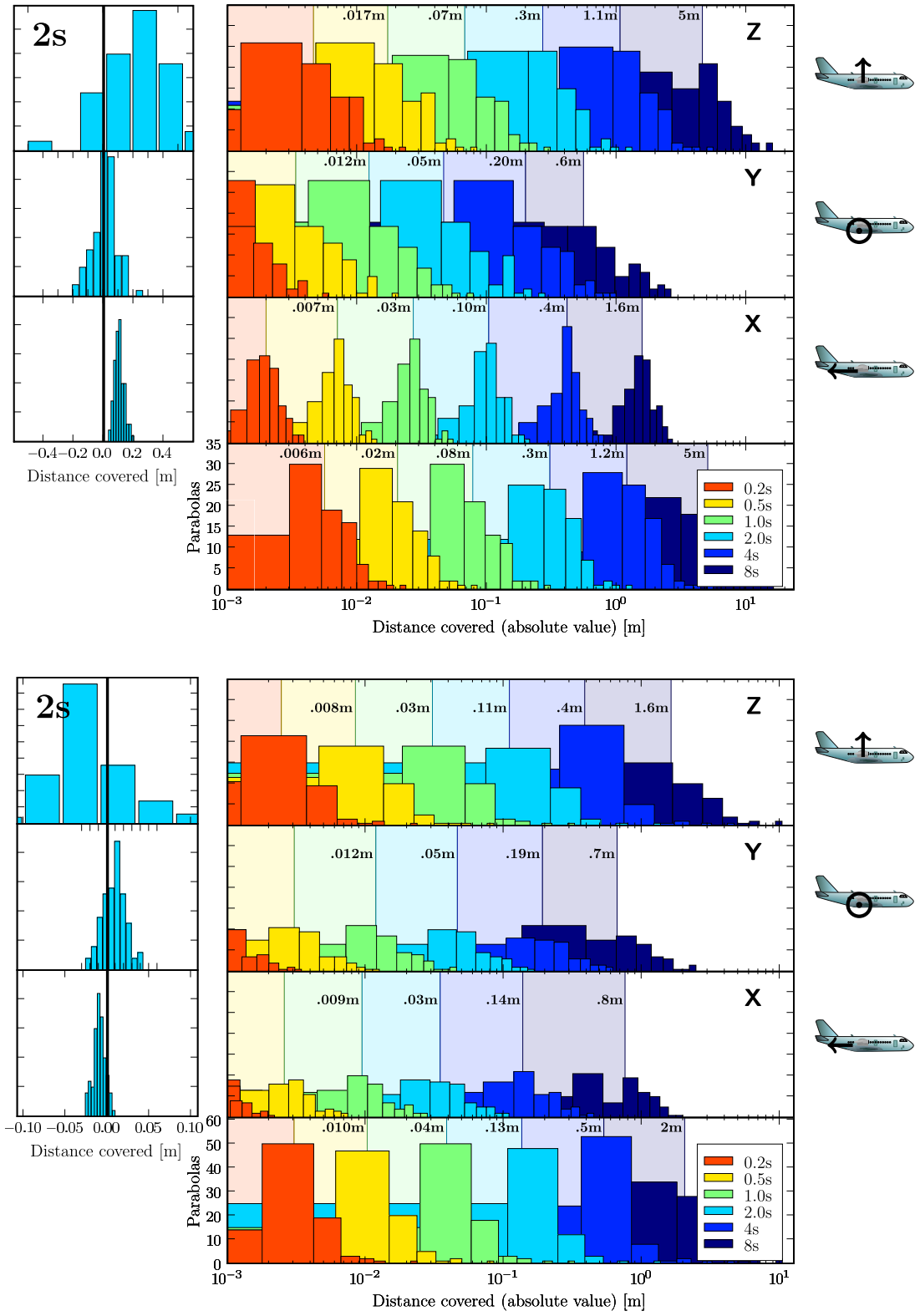

Figure II.5 – **(a) Displacement histogram. Top – recorded during the March 2007 campaign**

Histograms of the displacement of a truly free-falling object, relative to the airplane. Center: logarithmic scale, for varying fall time, the median of the absolute value is displayed for each fall time. Left: linear scale, 2 s fall time.

(b) Bottom – recorded during good atmospheric conditions

must be slowed down before it hits the walls of the cabin, and cannot be allowed to cross the cabin uncontrolled. However, ropes, or loose elastic bands, do provide zero stiffness when not under tension. A frame in which the apparatus would be tied by elastic bands or ropes with a controllable tension can be designed. Free travel could be up to 1.5 m in the vertical direction. As can be seen in Figure II.4, this would give at least a 75% chance of achieving 4 s of unperturbed free flight, even under poor weather conditions, and up to 8 s with a 50% chance of success in good weather conditions. It can be technically difficult to make use of the full 1.5 m available travel. For flight times less than 2 s, the travel required to have a good chance of success scales as:

$$d \sim 20\,\mathrm{mm} \cdot \exp \frac{t}{0.7\,\mathrm{s}} \tag{II.2}$$

As the travel of a free floater cannot be made large enough to compensate for drift during a complete parabola, (the cabin is only two meters high), it has to be designed to be recentered and released for each experimental run.

Once is the apparatus released and freely flying in the cabin, it is no longer subject to the mechanical vibrations created by the airbus. If the release process of the apparatus is well-controlled, acceleration noise on the Raman-beam mirrors can be made similar to ground-based experiments.

In summary, the micro-gravity achieved during parabolic flights in the Zero-G Airbus is of rather poor quality but several seconds of high-quality micro-gravity environment can be achieved by releasing a freely-flying apparatus in the cabin. The increase in interrogation times should lead to an increase in sensitivity of the inertial sensors, even though the expansion of the cloud leads to a loss of atoms.

2 Conducting high-precision experiments in the Airbus

2.1 Inertial sensing in free fall: technical challenges and scientific perspectives

Atom-interferometric inertial sensing is most often presented as a tool to measure the absolute acceleration or rotation of the reference frame of the apparatus. In the case of a freely-falling experimental platform, whether it be a dropped capsule, or a airplane in a ballistic paraboa, this information is of little scientific or technical interest.

There is, however, strong interest in implementing these techniques in space-borne missions. The goal is two-fold. Accelerometers with a high precision in the low

acceleration regime can be used as new-generation sensors for very weak gravity fields, with applications e.g. in the geodesic mapping of the Earth gravity field, drag-free navigation, or deep-space measurement of gravity in an effort to resolve the Pioneer anomaly (Anderson *et al.* [89]). Additionally, the well-controlled accuracy and error budget of high-precision atom-interferometric inertial sensing can also serve as the basis for local tests of gravitational theories.

Developing and improving sensors in a freely-falling experimental platform is a good way to pave the road for high-precision space-borne sensors, but as we will see, these platforms may also be suited to fundamental gravitational-physics experiments.

Atmospheric free fall versus outer-space weightlessness?

For ultra-precise tests of gravitational theories, space is the perfect laboratory, as attested by the recent Gravity Probe B experiment (Buchman *et al.* [90]) and the ongoing work on the next-generation experimental tests (Dittus *et al.* [91]). However there is no fundamental difference between an atmospheric freely-falling platform and a satellite test. Indeed, the Einstein equivalence principle states that physics in a freely-falling reference frame, in a gravitational field, is locally equivalent to physics without any gravito-inertial fields[8]. An atom interrogated during its free fall in an interferometer on Earth behaves like an atom interrogated in deep space, as long as tidal effects are neglected.

However, an experiment carried out nearby a massive object is not equivalent to a deep space experiment if the curvature of the metric is probed: the variation of the metric appears as tidal terms. Atom-interferometric inertial sensors have a physical extent, and can be sensitive to tidal effects; they have been proposed as a measure of the Lense-Thirring effect (Bingham *et al.* [93]), although detailed calculations have later shown that the contribution of this effect would be hard to measure (Angonin *et al.* [94]).

There is no difference between an experiment carried out in a freely falling airplane and one on a satellite orbiting around the Earth or the Sun: orders of magnitude of the tidal effects may vary[9], the physical processes are the same. An airplane is a perfectly valid frame for fundamental tests of gravitational theories, as long as quantities of general interest can be measured.

Interesting inertial measurements in micro-gravity

As pointed out in §I.2.5, the phase shift of an inertial-sensing interferometer relates directly to the local metric tensor. By choosing the shape and the type of the

[8]For gravitational physics, this is illustrated by the fact that for any given metric tensor there exists a Lorentz transform that reduces the metric tensor at a given point to its Galilean form (Landau and Lifshitz [92], §82).

[9]For one given experimental platform, be it a atmospheric one, as an airplane, or an orbital one, tidal effects can vary, as the altitude of the platform varies, however with a satellite on a well-chosen orbit, these effects can be very restricted, limited only to the effect of the moon.

interferometer, different components of the tensor can be probed. Inertial-sensing interferometers have a non-zero physical size and can probe the gradients of the metric (the Christoffel symbols, that give the force applied on an atom – see Landau and Lifshitz [92], §86).

An inertial measurement is either made with reference to a particular frame, or is a differential measurement. Ultra-precise weak gravity measurements relative to the apparatus frame can be used in experiments similar to Gravity Probe B, or the Pioneer anomaly, where the local inertial measurement is compared to a frame defined by distant objects. For these experiments atom interferometry can act as a conventional, but very precise, inertial sensor.

Running experiments with non-repeatable parameters

Atom-interferometric inertial sensing has been proposed (Dimopoulos *et al.* [95]) to push the limits of conventional inertial sensors and measure, for instance, the post-Newtonian parameters[10] using the ballistic fall of atoms in the Earth gravitational field. Repeatingly measuring the free fall of atoms in the Earth gravity field while changing the launch velocity gives access to the post-Newtonian parameters. In order to improve the current uncertainty on the parameters, interrogation times have to be larger than one second. The proposed experiment uses a 10 m-high fountain for 1 s interrogation times and plans for a 100 m-high fountain for 3 s interrogation times are discussed. The technical challenge of metrology-quality fountains of such a height should not be under-estimated. Ultra-high vacuum needs to be maintained in the entire tube, and the magnetic field should be well-controlled, in order to avoid interferometric shifts.

One would like to replace the 100 m-high fountain with ballistic flight. Unfortunately, this experiment cannot be realized in the Airbus, as it requires precisely repeatable experimental conditions. Launch velocity relative to the Earth is a critical parameter, so is altitude. In the Airbus, the initial parameters and the movement of the apparatus are not controlled or repeatable.

As the movement of the measuring instrument in the Airbus is not controlled or reproducible, fundamental measurements can only be made of quantities independent of this movement. Measuring the differential movement between two freely falling

[10] A gravitational theory gives relations between the matter distribution and the fields and metric it creates. The response of matter to the metric gives rise to the equations of motion. Thus the metric and the equations of motion for matter become the primary entities for calculating observable effects, and all that distinguishes one metric theory from another is the particular way in which matter and possibly other gravitational fields generate the metric.

The comparison of metric theories of gravity with each other and with experiment becomes particularly simple when one takes the slow-motion, weak-field limit. In this approximation, known as the post-Newtonian limit, the equations giving the metric and the equations of motion are expanded and characterized by a small number of parameters, the so-called post-Newtonian parameters. Not all gravitational theories can be expressed in this formalism and described in terms of post-Newtonian parameters, but a large number of theories, including general relativity, called the PPN theories (Parametrized Post-Newtonian theories), can be described in such a way and experimentally tested by their post-Newtonian parameters.

atoms does not require any reference frame, and the Airbus is thus suited for such experiments.

In conclusion, the Airbus is a convenient development platform for next-generation, long-interrogation-time, inertial sensors, but it is only suited for experiments measuring differential inertial quantities. We will study in detail in the next paragraphs such an experiment aiming to test the Universality of Free Fall (UFF) by comparing the acceleration of two atoms in free fall in the Airbus.

2.2 The importance of a test of the Universality of Free Fall (UFF)

Before proposing to conduct an experimental test of general relativity in the Airbus, I wish to detail the position of the measured effect (the UFF) in the current theoretical framework.

The first formulation of an equivalence principle for gravitational theories comes from Galileo who showed experimentally that the acceleration of a test mass due to gravitation is independent of the amount of mass being accelerated. These findings led to a gravitational theory, which concludes that inertial and gravitational masses are identical. Albert Einstein went one step further, stating that the physics is described by the same laws in an accelerated reference frame and a gravitational field:

"we [...] assume the complete physical equivalence of a gravitational field and a corresponding acceleration of the reference system." (Einstein [96])

General relativity elevates this observation to the status of a principle: free fall in a gravitational field is identified to inertial motion.

2.2.1 Different equivalence principles

Modern gravitational physics distinguishes three different forms of equivalence principles[11] (see Dicke [99] for a historical discussion, or Clifford [98] for a contemporary review):

The weak equivalence principle, (most often called the **Universality of Free Fall** – UFF) is the assumption that inertial and gravitational masses are equal. In other words, all bodies at the same space-time point in a given gravitational field will undergo the same acceleration.

[11] It has been pointed out to me that the phrasing of the different principles in this paragraph is very similar to that of the relevant Wikipedia article. This should not be a surprise, as many discussions of the equivalent principles use similar and sometimes identical wording, see for instance Harvey [97], p. 130, or the definitions of the principles scattered in Clifford [98]. These principles can be considered as theorems, and thus are often defined using the same words. The original wording most probably comes from Dicke [99].

The Einstein equivalence principle (EEP) states that the physical laws in a reference frame in free fall in a gravitational field are equivalent to the physical laws in an inertial reference frame. In other words, the result of a local experiment (not involving gravitational forces) in an inertial frame of reference is independent of the velocity or location of the experiment in the universe.

The strong equivalence principle states that the result of any local experiment is independent of the velocity or location of the experiment in the universe. Unlike the EEP, it includes experiments with involving gravitational forces and bodies with self-gravitational interactions.

Distinguishing three equivalence principles allows to differentiate gravitational theories depending on which equivalence principles they hold as true[12]. General relativity is the only known theory that satisfies the strong equivalence principle.

2.2.2 The Einstein equivalence principle as a foundation of general relativity

The EEP can be broken down into three statements:

- The UFF.
- The universality of gravitational red shift, which follows from the assumption that the laws of physics are the same independently of location.
- The local validity of Lorentz invariance, which follows from the assumptions that the laws of physics do not depend on the velocity of the reference frame in which they are expressed.

One can show from these three principles that the gravitational field has to be described by a space-time metric. The Dirac and Maxwell equations follow from the application of the EEP to quantum mechanics and electromagnetism (Lämmerzahl [101]). General relativity can be constructed from these postulates solely by adding Einstein field equations for the space-time metric.

The on-going quest for a new gravitation theory, unifying quantum physics and general relativity, tries to find guidance from an experimental refutation of general relativity. This refutation can come either from contradictions of its predictions[13] or a contradiction of its postulates. Different theories for quantum gravitation predict violations of different postulates (see Lämmerzahl [102] for a review). Good experimental tests of these postulates are a major challenge in current research (Chhun *et al.* [103], Sumner *et al.* [104]).

[12] It might not be completely true that these postulates can be all considered separately, as Schiff conjectured that any complete, self-consistent theory of gravity that embodies UFF and special relativity necessarily embodies EEP (Schiff [100]).

[13] The Gravity Probe B satellite experiment (Buchman *et al.* [90]) is an ongoing attempt to verify the Lens-Thirring effect to an unmatched precision.

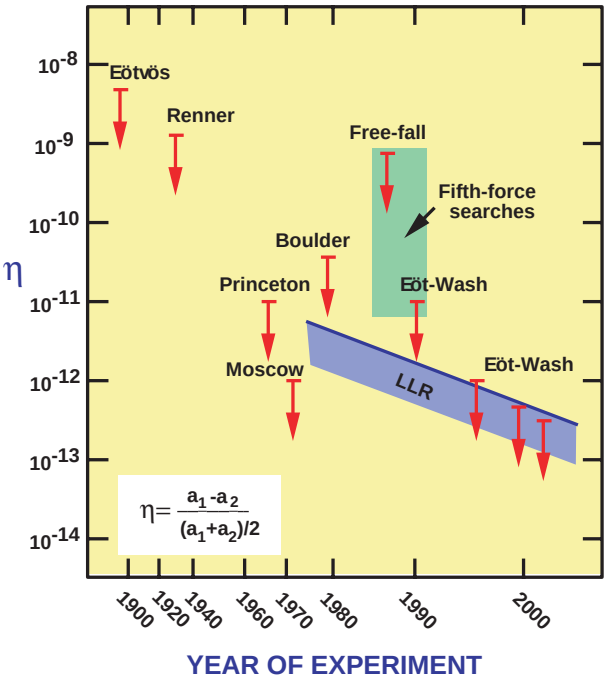

Figure II.6 – **Experimental tests of the UFF**

The figure of merit most often used in an experiment probing for violations of the UFF is the η parameter:

$$\eta = \frac{2\,(a_1 - a_2)}{a_1 + a_2}$$

where a_1 and a_2 are the accelerations of two bodies falling in the same gravitational field. The historical Eötvös experiment is a torsion balance experiment, where the gravitational traction of the Earth on test masses is balanced by the centripetal force due to the rotation of the Earth, thus probing the difference between gravitational and inertial masses. Similar experiments (the Eöt-Wash experiments, for instance) set the best limit to UFF violations in lab environment. The best test of the UFF is however performed by the Lunar Laser Ranging (LLR).
Figure from Clifford [98].

2.2.3 Atomic inertial-sensing test of the UFF: a keystone experiment

The universality of gravitational red shift and the local validity of the Lorentz invariance are both local properties and can be very well tested with clocks (Lämmerzahl [102], Clifford [98]). Earth-based atomic clocks currently set the record for tests of Lorentz invariance (see Wolf *et al.* [105], for instance), and the comparison between atomic clocks in different gravitational potentials should, in the near future, push the limits of testing gravitational red shift (Cacciapuoti *et al.* [106]).

However, the UFF can only be tested through free-fall tests. Current limits on the validity of the UFF are set by pendulum experiments, involving macroscopic test masses[14], and the lunar laser ranging experiment, where the test mass is the moon itself (see Figure II.6 and Clifford [98] for a review). The validity of tests of the UFF for macroscopic objects in complex motion is harder to link to fundamental principles than tests on simple, well-described, objects such as atoms. A test of the UFF using atoms as test masses is thus a central experiment in the current landscape. In such a test, atom interferometry is the best way to read out atomic trajectories.

A possible major contribution of atom-interferometric inertial sensing to advances in fundamental physics is therefore to compare the accelerations of two atoms of different masses falling freely in a gravitational field.

[14] Fray *et al.* [107] have preformed an atom-interferometric test of the UFF to $\Delta g/g \sim 10^{-7}$.

2.3 Experimental scheme for testing the UFF in the Airbus

2.3.1 Atom-interferometric free-fall comparison of rubidium and potassium

Principle of the experiment

An atom-interferometric inertial sensor can be understood as, in a very simplified picture, a device comparing the position of single-atomic test masses on an optical ruler formed by the Raman lasers (see §I.2.2). When performing an experiment in the Airbus, the movements of this ruler are not well-controlled. However in a test of the UFF, we are only interested in comparing the displacement of two different atomic test masses on the ruler, and not the absolute measurement. The Zero-G Airbus is thus well suited to perform such an experiment.

Ideally the free-fall comparison should be realized on atoms with a large mass difference. Potassium and rubidium differ by a factor of two in atomic mass and can be manipulated with lasers of similar wavelengths: 767 nm and 780 nm, which simplifies the experimental procedures.

Ideal experiment sensitivity

The acceleration phase shift for a 4 second total flight time (interrogation time $T = 2\,\mathrm{s}$, as given by equation I.17):

$$\Delta\phi = a_1\, k_{\mathrm{eff}}\, T^2 \sim \frac{g}{10^{-8}\,\mathrm{m}\cdot\,\mathrm{s}^{-2}} \tag{II.3}$$

In the best possible scenario, the knowledge of the phase is limited to the quantum-projection limit by the finite number N_{at} of atoms in the sample, for 10^6 atoms:

$$\Delta\phi_{\mathrm{min}} = \frac{1}{\sqrt{N_{\mathrm{at}}}} \sim 10^{-3} \tag{II.4}$$

The acceleration for each specie can thus be known to $10^{-11}\,\mathrm{m}\cdot\mathrm{s}^{-1}$. For an acceleration of $g = 9.81\,\mathrm{m}\cdot\,\mathrm{s}^{-1}$, the error on the η parameter, defined as $\frac{2\,(a_1-a_2)}{a_1+a_2}$, is a few 10^{-12}. This is comparable to the error bars imposed by the best experiments (see Figure II.6). However, as we will see, the quantum-projection noise limit on the phase measurement cannot be reached in a noisy environment such as the Airbus.

2.3.2 Quantitative measurements in a noisy environment

From interferometric measurements to phase differences

The phase shift $\Delta\phi$ is not directly measured in the experiments, only the relative atomic populations are. Each interferometer run yields an observable quantity m, the ratio of the measured number of atoms in the two output states, such that:

$$m = a + b\sin\Delta\phi \tag{II.5}$$

a and b are parameters depending on the experimental conditions. a is due to the imperfections in initial atomic-state polarization, and b deviates from 1 because of non-complete Raman transitions. As parameters a and b vary from one experimental run to another, one measurement of m is not sufficient to measure $\Delta\phi$. Typically, at least three measurements are needed, varying $\Delta\phi$ by $\frac{\pi}{2}$. In interferometry jargon, this is called "scanning a fringe". As with most estimation of a statistical unknowns, the statistical root-mean-square error on the determination of $\Delta\phi$ decreases with the inverse square root of the number of measurements performed.

These different measurements have to be done with repeatable experimental conditions. First of all, the phase shift $\Delta\phi$ to be determined needs to be constant, second the experimental conditions should not vary from one shot to another.

The easiest solution to take several data points in the same experimental conditions is to perform these measurements during one single flight of the freely-flying apparatus. As this flight is limited to two seconds, both the available interrogation time for the interferometric experiment and the number of measurements will be strongly limited[15].

Isolation of a repeatable phase shift

The inertial phase shift is given by (see: I.2.2):

$$\Delta\phi = \mathbf{k}_{\text{eff}} \cdot (\mathbf{g} + 2\,\boldsymbol{\Omega} \times \mathbf{v}_{\text{launch}})\, T^2 \tag{II.6}$$

where $\boldsymbol{\Omega}$ is the rotation vector of the apparatus and $\mathbf{v}_{\text{launch}}$ is the launch velocity of the atoms in the inertial frame. This launch velocity, in our case mostly given by the velocity of the airplane, gives a physical area to the interferometer[16], making it sensitive to rotations. Both this launch velocity and the rotation of the apparatus, given by the rotation of the plane, and the rotational momentum communicated to the freely-flying apparatus when it is released, can hardly be controlled and repeated from a parabola to another. On the other hand, if the apparatus is really freely flying during the interferometric measurement, the acceleration g is well-controlled and repeatable (although it varies with altitude and position).

Using classical inertial sensor to measure rotation and acceleration, we can compensate the inertial phase on the atoms by feed forward on the Raman laser [108, 109] and keep each atomic phase-shift close to zero[17]. In the 0.25 Hz range, the rejection can be up to 20 dB.

Thus with a free-flyer and a feed-forward on the Raman lasers, we can achieve a inertial-effect-related phase shift that is repeatable from one parabola to another.

[15]The duty cycle of the experiment is much longer than the interrogation time as, between two interferometric runs, a new sample of cold atoms has to be prepared. This sample needs to be large for long interrogation times, to compensate for losses due to cloud expansion.

[16] The resulting area is given by $\mathbf{A} = \mathbf{k}_{\text{eff}} \times \mathbf{v}_{\text{launch}}\, T^2$.

[17]As the lasers for both species are phase-locked, modifying the phase of the lasers does not modify the measurement of the differential phase shift.

Measuring the differential phase shift

In laboratory experiments, the largest source of noise comes from the vibrations of the return mirror of the Raman beams (Le Gouet *et al.* [110]), which introduces a random component to the phase shift. If this phase noise is too high it washes-out the interferometric fringes and the value of the phase cannot be deduced from the atomic-population measurement. The interesting phase information is lost if the amplitude of the displacement of the mirror between different measurements exceeds $\lambda/4 \sim 200\,\mathrm{nm}$ for rubidium or potassium. In the case of measurements performed during different free-flying sequences this means that the difference between the trajectory of the apparatus and a ballistic trajectory should be less than 200 nm. This seems hard to achieve, but the reason why a test of UFF is conceivable in the Airbus is that it is a differential measurement: only the differential phase-shift between the potassium interferometer and the rubidium one must thus be extracted from the interferometric measurements.

For these different atomic phase shifts to be correlated, the phase shifts communicated by the Raman transitions (i.e. the positions of the optical rulers) need to be also correlated, which means that the different lasers involved in the transitions must all be phase-locked. This can be achieved either by deriving all frequencies from the same laser, with a wavelength located in between both transition frequencies, or by using a frequency comb to phase lock two lasers near the atomic transition of each species.

Using the same laser for both species is ideal, as the position of the freely falling atoms are measured relative to the same optical ruler, but it requires a detuning of at least[18] 5 nm. With such a large detuning, for limited laser power, the Raman pulses have to be long, and therefore very selective in velocity (see §A). An optical power of one Watt in each Raman laser is required to achieve a momentum width large-enough to operate on a Bose-condensed cloud, and ten Watts are sufficient for a laser-cooled cloud. Lasers with such powers are not technically impossible with the current technology, but building sources suited for the harsh environment of the Airbus would be a technical challenge.

When using two lasers, each close to an atomic resonance for a different species, the phase shift for each species is given by:

$$\begin{cases} \Delta\phi_{\mathrm{K}} & = k_{\mathrm{K}}\left(g_{\mathrm{K}}T^2 + X_{\mathrm{mirror}}\right) \\ \Delta\phi_{\mathrm{Rb}} & = k_{\mathrm{Rb}}\left(g_{\mathrm{Rb}}T^2 + X_{\mathrm{mirror}}\right) \end{cases} \tag{II.7}$$

Where X_{mirror} is the position of the mirror retro-reflecting the Raman beam. The fluctuation of the phase of the Raman transition is the same for both species as the two lasers are phase-locked. This expression can be written in terms of the acceleration difference between the two species:

$$\Delta\phi_{\mathrm{K}} = k_{\mathrm{K}}\left(\delta x + \widetilde{X}_{\mathrm{mirror}}\right) + \Delta\phi_{\mathrm{Rb}} \tag{II.8}$$

[18] Using the potassium D1 transitions (770 nm), and the rubidium D2 (780 nm) yields very close transition wavelengths.

where: $$\delta x = T^2 \delta g = T^2 (g_{\mathrm{K}} - \frac{k_{\mathrm{Rb}}}{k_{\mathrm{K}}} g_{\mathrm{Rb}}) \tag{II.9}$$

and $$\widetilde{X}_{\mathrm{mirror}} = X_{\mathrm{mirror}} \left(1 - \frac{k_{\mathrm{Rb}}}{k_{\mathrm{K}}}\right) \tag{II.10}$$

The interferometric measurements are thus given by:

$$\begin{cases} m_{\mathrm{K}} & = A + B \sin\Big(\Delta\phi_{\mathrm{Rb}} + k_{\mathrm{K}}(\delta x + \widetilde{X}_{\mathrm{mirror}})\Big) \\ m_{\mathrm{Rb}} & = C + D \sin \Delta\phi_{\mathrm{Rb}} \end{cases} \tag{II.11}$$

where the capital letters (including $\Delta\phi_{\mathrm{Rb}}$) are random variables and δx can be understood as the difference in free-fall displacement between atoms of each species. Testing the UFF implies measuring δx, which should be 0. The phase $\Delta\phi_{\mathrm{Rb}}$ is treated as a fluctuating variable as the exact acceleration may vary from one parabola to another, due to deviations from free fall. A, B, C, and D have the same meaning as the a and b variables introduced for a single-species measurement model, in equation II.5. k_{K} and k_{Rb} are the effective Raman laser wave-vectors for potassium and rubidium. The main source of noise comes from the fluctuations of $\widetilde{X}_{\mathrm{mirror}}$ and $\Delta\phi_{\mathrm{Rb}}$, as the relative fluctuations of A, B, C, and D are small. The distribution of the different fluctuating variables can be measured separately or inferred from the knowledge of the experiment.

If k_{K} and k_{Rb} are identical, as when using a single laser instead of two phase-locked near-resonance lasers, or for coupled measurements in a gradiometer setup using only one species instead of two, $\widetilde{X}_{\mathrm{mirror}}$ is zero, and all the data points plotted in the $(m_{\mathrm{K}}, m_{\mathrm{Rb}})$ plane lie near an ellipse of ellipticity δx. In this case, the differential phase information can be extracted from the noisy signal for any amount of noise on the position of the mirror, X_{mirror}, and on the inertial phase shift, $\Delta\phi_{\mathrm{Rb}}$, by fitting the experimental points to an ellipse, as described by Foster *et al.* [111]. One should note that if the single species phase-shift varies too much, for instance if the inertial phase-shift is not controlled, the contrast of the interferometric signal will also vary, as the coherence length of the atomic beam is finite, and the two interferometers can operate only for small phase shifts.

However, in the case of two near-resonance lasers[19], $k_{\mathrm{K}} = 4\pi/767\,\mathrm{nm}$ and $k_{\mathrm{Rb}} = 4\pi/780\,\mathrm{nm}$, and the fluctuations of the mirror position blur out the ellipse (see Figure II.7). As $\widetilde{X}_{\mathrm{mirror}}$ relates to the physical displacement of the mirror, X_{mirror}, by a factor of $1 - \frac{k_{\mathrm{Rb}}}{k_{\mathrm{K}}}$: the closer the two wave-vectors are, the less significant the vibrations of the mirror are.

Statistical inference of the phase difference

We are faced with the problem of estimating the internal state of a process given only a sequence of noisy observations and a model of the process, including a statistical model of the random variables. Using this model, we can estimate the probability

[19]We use here worst-case scenarios, by using the D2 transition wavelengths for the potassium. The Raman effective angular frequency is twice the transition angular frequency.

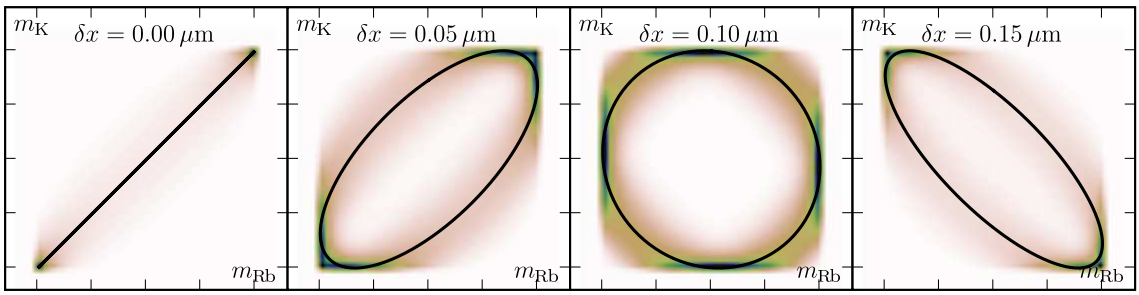

FIGURE II.7 – **Locus of the measurements in the (m_K, m_{Rb}) plane**
The locus of the interferometric measurements in the (m_K, m_{Rb}) plane, varying only $\Delta\phi_{Rb}$ is represented with a solid line for different value of δx.
In addition, the broadening of this line is shown by the color plot of the probability density of a measurement, taking in account a Gaussian probability distribution for $\widetilde{X}_{mirror}$ of a half width at half maximum of $0.2\,\mu$m.

distribution for the different values of the parameter δx we are interested in, as shown in Figure II.7. If the different probability distributions are distinguishable in a finite number of measurements, the information on the value of δx is not lost. I will introduce an algorithm to estimate δx given a set of data points, and use it to determine the level of noise acceptable for a test of the UFF.

Recursive Bayesian estimators The problem, stated in Bayesian statistical language, is to evaluate the probability[20] for a hidden parameter, the position difference, to take the value δx, given the results m_K and m_{Rb}: $p(\delta x|m_K, m_{Rb})$. This problem is well suited to the use of a recursive Bayesian estimator (Stockton *et al.* [112] introduced for the first time Bayesian estimators in atom interferometry).

After n repeated measurements, our knowledge of the value taken by δx is described by the probability distribution of δx, given the results of all the previous measurements. As the outcome of these measurements are statistically independent, this joint probability is given by the product of the successive conditional probabilities:

$$\begin{aligned} p(\delta x|m_K(n), m_{Rb}(n),\, m_K(n-1), m_{Rb}(n-1), \dots) \\ = p(\delta x|m_K(n), m_{Rb}(n))\; p(\delta x|m_K(n-1), m_{Rb}(n-1) \dots \end{aligned} \quad \text{(II.12)}$$

Given a set of experimental results, we can use this formula to evaluate the most probable value of the δx parameter, its mean value, and the root mean square error, quantifying the amount of knowledge these measurements have given us about the value of the parameter. The Bayesian estimator can be understood and implemented as a recursive refining of the probability density function of the δx parameter. Given

[20] In the following paragraphs, I shall talk about probability of a continuous variable taking a given value while the right concept to use is the probability density function: the function p associating to a value x the probability of the variable X to be in the neighborhood $[x, x + dx]$: $p(x)\,dx = P(X \in [x, x + dx])$. I shall use P and p alike, and I shall not make a distinction between X and x.

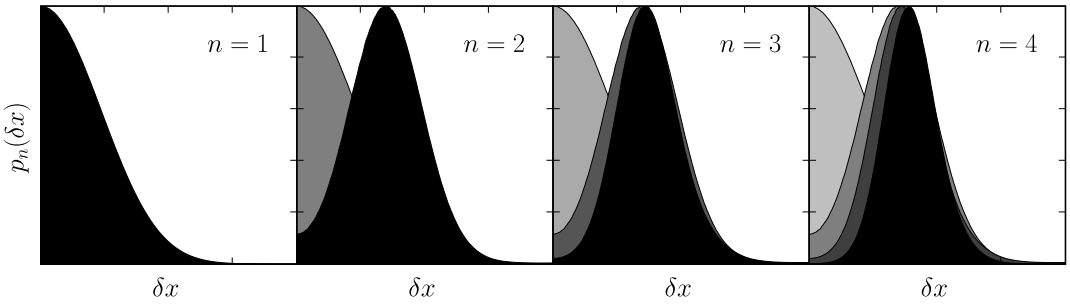

Figure II.8 – **Narrowing of the probability density function for δx**
As a new measurement is made, the conditional probability $p(\delta x|m_{\mathrm{K}}(n), m_{\mathrm{Rb}}(n)$ is multiplied with the previous probability distribution $p_n(\delta x)$ to obtain the updated probability distribution. Successive multiplications leave only areas for which the probability of δx was high for every measurement.

an initial distribution $p_0(\delta x)$ quantifying our a priori knowledge on the possible values of δx we apply the following steps for each measurement:

1. Calculate the conditional probability knowing the results of the n^{th} measurement: $p(\delta x|m_{\mathrm{K}}(n), m_{\mathrm{Rb}}(n))$
2. Update the probability density function for δx:

$$p_n(\delta x) = p(\delta x|m_{\mathrm{K}}(n), m_{\mathrm{Rb}}(n))\; p_{n-1}(\delta x)$$

3. Renormalize the resulting $p_n(\delta x)$.
4. Perform a new measurement and recurse the algorithm.

The iterative narrowing of the probability density function $p(\delta x)$ is illustrated in Figure II.8.

Implementation of a Bayesian estimator for the phase difference We have implemented a Bayesian estimator for the model II.11 and use it to estimate the limits on the knowledge of δx that we can acquire through experiments in the Airbus.

An analytical expression for $p(\delta x|m_{\mathrm{K}}, m_{\mathrm{Rb}})$ can only be derived for simple models. The probability usually derived in Bayesian estimators is the reversed conditional probability, $p(m_{\mathrm{K}}, m_{\mathrm{Rb}}|\delta x)$, linked to the forward conditional probability by Bayes' theorem: $p(a|b) \propto p(a)\, p(b|a)$. This probability is simpler to calculate, and can be used similarly in the estimator algorithm, using Bayes' theorem. We have derived an expression for a simplified model, assuming $A = C = 0$ and $B = D$ (see appendix B).

$$p(m_{\mathrm{K}}, m_{\mathrm{Rb}}|\delta x) = \int \sum_{\substack{x \text{ such as} \\ m_{\mathrm{Rb}} \sin(\delta\phi + k_{\mathrm{K}}(x+\delta x)) \\ = m_{\mathrm{K}} \sin\delta\phi}} p(x)\, \frac{\sin^2 \delta\phi}{m_{\mathrm{Rb}}\, k_{\mathrm{K}} |\cos\Big(\delta\phi + k_{\mathrm{K}}(x+\delta x)\Big)|} \; p_b\left(\frac{m_{\mathrm{Rb}}}{\sin\delta\phi}\right) p(\delta\phi)\, d\delta\phi \quad \text{(II.13)}$$

where p_b is the probability density function for B.

The difficulty in calculating the conditional probability of model II.11 comes from the non-linear coupled terms, whereas the contribution of A and C are trivial[21]. We can evaluate these terms using a numerical Monte Carlo sampling of the state space (see Appendix A for a description of the implementation). The result of this numerical calculation is a large three-dimensional lookup table giving $p(m_{\mathrm{Rb}}, m_{\mathrm{K}}|\delta x)$, made by a two-dimensional histogram of the values of m_{Rb} and m_{K} for different values of δx, or conversely the reverse probability, $p(\delta x|m_{\mathrm{Rb}}, m_{\mathrm{K}})$ by inversing the lookup direction of the table. This calculation is numerically heavy, as it involves several billion samplings to avoid aliasing noise in the histogram, but once it is done, running the Bayesian estimator is almost costless, as it consists only of multiplying pre-calculated arrays[22], the estimator can thus be used to process experimental data on the fly.

Convergence rate for the phase difference estimation Simulations[23], as, for example, displayed in Figure II.9, show that large variations of the inertial phase shift, expressed in the term $\Delta\phi_{\mathrm{Rb}}$, do not lead to a loss of information on the measurement of the differential phase. This means that different measurements can indeed be performed across several parabolas, with non-repeatable ballistic trajectories[24].

Moreover, the estimator still converges when the variations of the position of the Raman mirror, due to mechanical deformation of the freely-flying apparatus, largely exceed $\lambda/4 \sim 200\,\mathrm{nm}$, the length scale of the phase change of the light-pulse accelerometer. Indeed, $\widetilde{X}_{\mathrm{mirror}}$ is linked to the displacement of the mirror by a factor $1-k_{\mathrm{Rb}}/k_{\mathrm{K}} \sim 0.017$, therefore a simulation with displacements of the mirror of $1.2\,\mu\mathrm{m}$, as on Figure II.9, top figure, corresponds to $\sigma_{\widetilde{X}_{\mathrm{mirror}}} = 0.02\,\mu\mathrm{m}$. However the convergence rate of the estimation, and thus the precision achievable in a small number of measurements (there are only 30 parabolas during one flight), is much higher for narrow distributions of $\widetilde{X}_{\mathrm{mirror}}$, as can be seen in Figure II.9, bottom figure.

A systematic study of the convergence rate as a function of $\sigma_{X_{\mathrm{mirror}}}$ shows the RMS error on the δx parameter that we are trying to estimate decreases as $\sigma_{\delta x} \sim n^{-1/2}$ with n the number of measurements, for $\sigma_{\widetilde{X}_{\mathrm{mirror}}} \sim 1\,\mu\mathrm{m}$. Under this value for $\sigma_{\widetilde{X}_{\mathrm{mirror}}}$, it decreases faster than $n^{-1/2}$ at small number of measurements, whereas the opposite is true for $\sigma_{\widetilde{X}_{\mathrm{mirror}}} > 1\,\mu\mathrm{m}$ (see Figure II.10).

[21] They appear as convolutions: $p_x(a+b) = \int p_x(a)\,p(b)\,db$.

[22] On the contrary, the use of the analytical expression for the simple model II.13 is numerically expensive, as it involves finding numerically all roots of an equation, and it is hard to express in highly-optimized operations on arrays, or in other words, CPU-cache-optimized operations.

[23] The simulations are run with a value of $0.1\,\mu\mathrm{m}$ for δx corresponding to a phase shift of $\pi/4$, as this is the optimal point for the estimator (δx and $-\delta x$ cannot be distinguished, therefore $\delta x \sim 0$ is a very bad working point). This can be achieved experimentally by adding a phase difference between the two species through a jump of the phase of the lasers for one wavelength.

[24] The inertial phase shift must remain close to zero, for the interferometer contrast to be repeatable. This is why a freely-flying apparatus, and a rotation-insensitive interferometer, as mentioned earlier, are necessary.

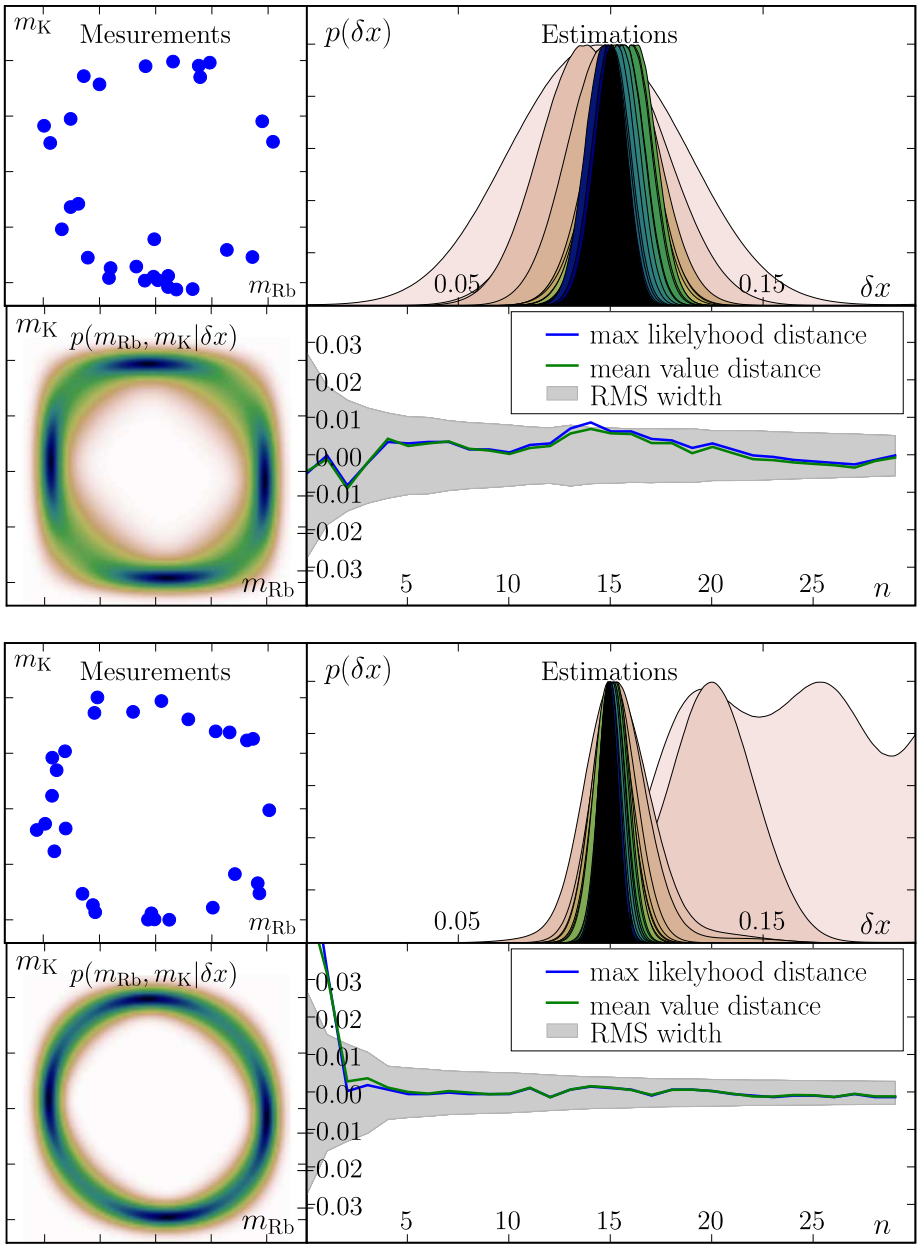

Figure II.9 – **Simulations of Bayesian recursive estimator runs**

The model II.11 is simulated both to build the estimator kernel with a Monte Carlo sampling of the state phase and to draw random measurements.

For each simulation are displayed: the different measurements drawn, the successive estimations for δx, the probability of the measurements knowing δx, and the distance between estimated values of δx and the actual value.

Top: The distributions used for the random variables are:

$\Delta\phi_{Rb}$	Uniform in $[0, 2\pi]$
X_{mirror}	Normal, $\sigma = 1.2\,\mu$m
A, C	Normal, $\sigma = 0.05$, center: 0
B, D	Normal, $\sigma = 0.05$, center: 1

Bottom: Same parameters, but with $\sigma_{X_{mirror}} = 0.6\,\mu$m.

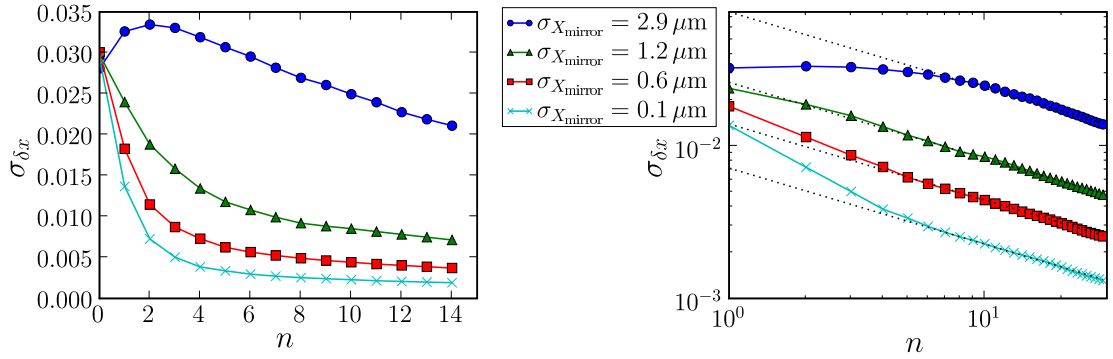

FIGURE II.10 – **Decrease in RMS error as a function of number of experimental points**
The error between the estimated mean value, and the real value of δx was computed on a large amount of simulations for different normal distribution for the position of the mirror X of varying width.
Right : Linear plot.
Left: Log-log plot. The dotted line is the $1/\sqrt{n}$ long-term behavior of the RMS of the error.

Choosing the interrogation time to maximize sensitivity

With a small number of points, in a noisy environment such as the Airbus, the shot-noise-limited sensitivity on the measure of the phase given in the beginning of this section cannot be reached. Armed with a correct noise model we can find the optimum interrogation time, which gives a large scale factor but enough measurements to reach a good accuracy on the phase.

To perform more than one measurement per parabola we need either to be able to release the freely flying apparatus more than once, or to perform several experimental cycles during a flight. In this last case, the fluctuating inertial phase is constant for each free flight, and an optimized Bayesian estimator with a faster initial convergence rate can be calculated[25].

If the vibrations of the mirror are small enough, for more than ~ 6 points the error on δx decreases as $\sqrt{n}$, therefore as $T^{-3/2}$, if we squeeze several interferometer runs of interrogation time T in each ballistic flight of the apparatus. As $\delta x \sim T^2 \delta g$, the precision that can be reached on δg scales as $T^{3/2}$, as long as the loss of atoms does not lead to a loss of precision of the measurement, as discussed in §II.1.1. In this situation it is more favorable to extend the interrogation time, rather than to multiply the number of measurement. We should note that the formulas discussed in §II.1.1 do not apply to a small number of noisy measurements, as these will not be shot-noise limited. The limit to the interrogation time achievable because of atomic loss is mainly due to classical signal-to-noise loss in the measurement and not to quantum-projection noise.

[25] Calculating the optimized Bayesian estimator will be slightly more tedious as the number of relevant parameters is higher. It can be modeled either as multiple set of non-independent measurements, which increases the dimensionality of the measurement plane, or as a problem with two fixed unknown parameters δx and $\Delta\phi_{\mathrm{Rb}}$, the probability density function for δx after a set of correlated measurements being obtained by tracing the 2 dimensional $(\delta x, \Delta\phi_{\mathrm{Rb}})$ probability density over the $\Delta\phi_{\mathrm{Rb}}$ parameter.

We can now review the predictions for the sensitivity of the experiment given at the beginning of this section: if the amplitude of vibrations of the mirror is below $0.1\,\mu$m, the resolution achievable on δx after 30 measurements is 1 nm. Supposing that we are not limited by loss of atoms and that we can fully use the available four seconds of ballistic flight, the corresponding resolution on δx is $0.25\,\mathrm{nm}\cdot\mathrm{s}^{-2} \sim 2.5\cdot10^{-11}\,\mathrm{g}$. This sensitivity corresponds to a parameter η of $5\cdot10^{-11}$. The number of atoms required to reach this sensitivity without being limited by quantum-projection noise is 10^5.

Using a statistical description of the noise and fluctuations of the parameters in the Airbus as well as an apparatus released to float freely in the cabin, we can envisage a precise test of the universality of free fall using two different atomic species released in ballistic flights in the Zero-G Airbus, rather than in tall fountains or drop towers. Total flight times could be up to 4 seconds, which corresponds to a fall height of 80 meters. Although such an experiment will not push the limits of experimental tests of the universality of free fall, it would be important as it is performed with very simple test masses that can be unambiguously described theoretically. Moreover technological advances achieved on the Airbus can later on be transferred to orbital platforms. However, the Airbus is an interesting technological solution to achieve micro-gravity only if it imposes weaker experimental constraints than its alternatives, as it is an intrinsically noisy environment. The following chapter will explore the experimental challenges of operating an atom interferometer in the Airbus.

Chapter III

Test flight of a cold atom source

I love deadlines.
I like the whooshing sound they make as they fly by.
Douglas Adams

This chapter describes the cold-atom apparatus that was built during my PhD for micro-gravity operation, as well as the results of the first test flight. Assembling novel laser sources with a compact and robust atomic-physics, we have built a source of laser-cooled atoms suitable for atom-interferometry in a freely-falling airplane.

The ICE (Interférometrie atomique Cohérente pour l'Espace) project[1] is a collaboration between ONERA (Office National d'Études et Recherches Aérospatiales), SYRTE (SYstèmes de Référence Temps Espace), and our group at Institut d'Optique) for the development of atom-interferometric inertial sensors for space.

At the end of November 2006, the project was approved by CNES for a test flight campaign on the zero-G Airbus, scheduled in March 2007. The initial goals of this campaign were to test the laser sources developed by the ONERA and explore the requirements for embarking an atom-interferometer on the airplane. To do this we decided to assemble a cold-atom apparatus with a Magneto-Optical Trap (MOT), while keeping the possibility to add Raman-pulse beam splitters to pave the way to an interferometer setup.

Work between the institutes was divided as such:

SYRTE Ultra-stable hyperfrequency reference source at 6.8 GHz, agile in frequency; as well as the software for its computer control.

ONERA Laser sources, namely Doppler-cooling lasers, and Raman pulses laser, including frequency servo-locking and control.

Institut d'Optique Atom-optics chamber with vacuum and optics. Global infrastructure for the experiment, including flight-suitable racks, electric system, computer and sequencing electronics.

[1] http://www.ice-space.fr/

I was in charge of coordinating the work, planning the flight, as well as assembling the contribution of Institut d'Optique. The schedule planned for assembly of the different parts in Palaiseau at Institut d'Optique in the end of January 2007. This project was mainly constrained by its tight time frame, as most of the components were to be built from new equipment to be purchased. It was nicknamed *Little-ICE*, as it is the smallest of the two atom-optics apparatuses in the I.C.E. project.

1 A ballistic-flight-compatible atom interferometry apparatus

1.1 In-flight lab infrastructure

Operating in the Zero-G Airbus places severe requirements on the apparatus. First of all, standard lab infrastructure is not present, the environment is not well-controlled. Second, flight safety imposes drastic constraints on the apparatus and the experimental procedures. Thirdly the on-board resources are limited. And last, experimental procedures have to be adapted to the rapid alternation of micro-gravity and hyper-gravity phases.

1.1.1 Rack arrangement

Airbus experimental area The experiments are arranged in a large padded test area in the center of the Airbus (see Figure III.1). All the experiments share this space and apparatuses of different shapes and sizes are bolted to eight rails running on the floor of the cabin (see Figure III.2). This is a very crowded area, both in flight, and during flight preparation. Large empty spaces are therefore left between the experiments. We extensively used these for diagnostic equipment that did not fly and was disembarked before each flight.

Structural requirements We were assigned a $2 \times 2\,\mathrm{m}$ footprint for the experiment. We were not limited in absolute weight, but in the end weight was limited by the structural strength of the apparatus. The apparatus should not break apart during an emergency landing. This imposes drastic constraints on its resistance to accelerations. More specifically, the entire structure has to be able to withstand $9\,\mathrm{g}$ accelerations oriented towards the front of the plane, $3\,\mathrm{g}$ lateral accelerations, and $7\,\mathrm{g}$ downward. As the apparatus is bolted from below on to the cabin rails, the $9\,\mathrm{g}$ forward acceleration limit is the hardest to meet. Given that the rails have a limited strength, they have a maximum linear load. The experiment is attached to the rails at a small number of points that transmit the frontward torque to the rails. The weight of the experiment is limited by the torque it can develop on the rails. To maximize

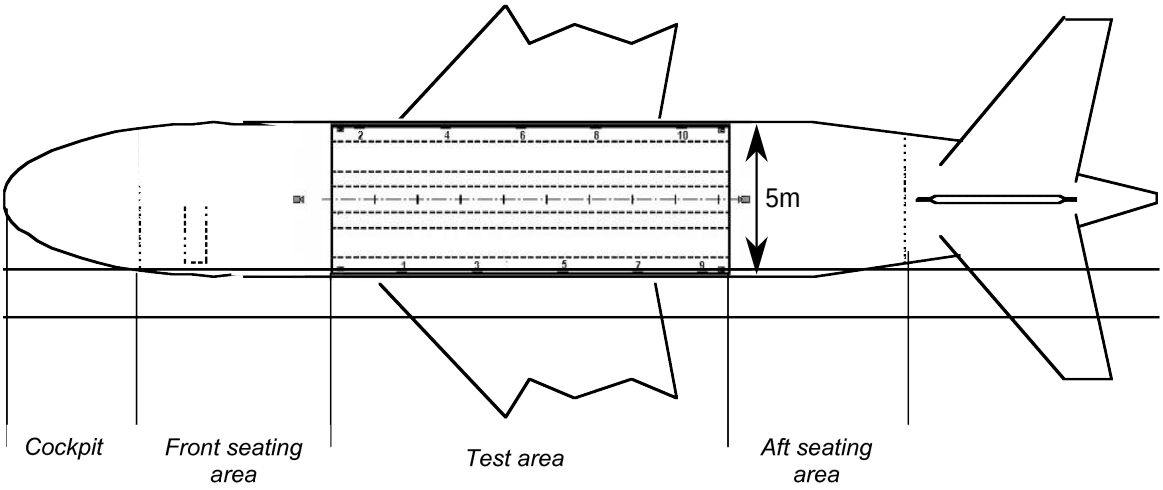

FIGURE III.1 – **Layout of the test area in the airbus**

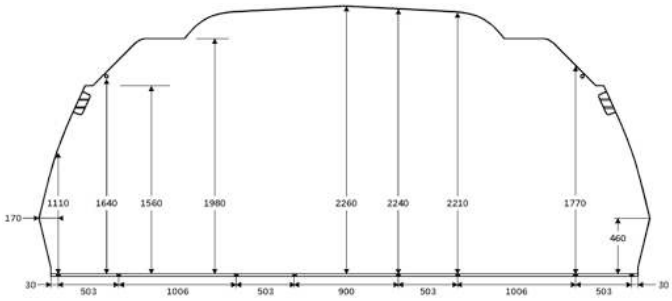

FIGURE III.2 – **Cabin cross section**
The eight rails for attaching the experiments can be seen on the floor of the cabin.

the on-board weight, the experiment should be as long a possible in the longitudinal direction, and with a center of mass as low as possible.

Stacking equipment To minimize the moment of inertia of the experiment, we pack as much equipment as we can, in as little room as possible. Devices have to be stacked one upon the other, but each should be firmly held to a rigid structure to insure the strength of the overall arrangement. Off-the-shelf racks cannot be used as even earthquake-proof equipment (e.g. Knür Maxload series, www.Knuerr.com) is not certified for these high lateral loads.

For each experimental rack, we have built a structure from strut profiles and adapted components used for machine building[2]. These components can be ordered with a large amount of accessories and complex assemblies can be built without machine shop access. But most importantly, the structural strength of profiles is well specified and we can make an estimation of the strength of the assembly without resorting to finite-element analysis. The structure is assembled using Nylon lock nuts and oversized angle brackets. Only fireproof materials can be used; this specifically excludes plywood and plexiglass for trays and panels.

[2]ITEM, http://www.itemamerica.com

Figure III.3 – **Experimentalist hovering above the interferometer**
Arnaud Landragin, from SYRTE.

We arrange uprights with a 19" space between them and mount instruments using standard 19" rack equipment. This strategy has been extremely successful: it defines a set of standard sizes (1U, 2U) which helps communication between institutes[3], it makes mounting instruments very easy[4], and allows a very compact arrangement[5].

1.1.2 The experimentalist in micro-gravity

During the flights the experimental area is packed with many operators for the experiments and flight attendants in charge of safety. This is why there are large empty spaces between the experiments, and a 1 m-wide central corridor. Between parabolas and during micro-gravity there is many movement and we build the experiment to protect it from others experimentalists, especially since it may be difficult to control one's movements in micro-gravity. Unprotected connections and control knobs are all located on sides facing the cabin wall, whereas the equipment facing the corridor is protected with aluminum plates.

The hyper-gravity phases ($2\,g$) can be very uncomfortable as the increased gravity tends to drain blood from the brain. This can surprisingly easily lead to a gray-out (the first step in the so-called g–induced loss of consciousness) as even though the hyper-gravity is small, it lasts for thirty seconds. Moreover moving one's head during this phase quickly induces dizziness and can lead to sickness. The best way to spend these thirty seconds is to lie on one's back, fixing a point on the ceiling. In this position, one barely feels the hyper-gravity.

To my surprise and relief, the micro-gravity parabola does not feel like a free-fall. The switch from hyper-gravity to micro-gravity is disorienting, but not brutal. Movements in micro-gravity have to be slow and well-controlled, as any push on an object induces a displacement in the opposite direction. In the beginning we were

[3]Care must be taken to respect these standards. Half a day can easily be lost if a single protruding screw head prevents mounting a device in its bay.

[4]There is an order of magnitude difference in the amount of work between bolting an rack-mounted device, and clamping a box-shaped instrument with attachment hardware that will inevitably be partly homemade.

[5]The game of Tetris has no solution with box-shaped objects of arbitrary dimensions.

held near the floor with loose and adjustable straps around our knees. This makes it possible to use both hands on the experiment. As we grew accustomed to micro-gravity we progressively released the straps. The end of the micro-gravity phase is progressive, but it is better to have one's feet closer to the floor than one's head[6].

1.1.3 Layout of the experiment

The experimental apparatus is made of three rack structures. Rack number 1 contains the atomic-physics chamber, rack number 2 the control electronics and the laser sources, and rack number 3 the electrical equipment. The layout of rack 1 is described in §III.1.4.

Control rack The control rack (rack number 2) is the nerve center of the experiment. It is highly packed with instruments and the number of instruments we could add to it was limited by its vertical moment of inertia[7]. Detailed listing of the components it houses can be found in §C.1, on page 207. The main components are:

- Lasers sources for MOT and Raman beams, with their servo-locks.
- Computer, input/output, and sequencing interfaces.
- Hyper-frequency source.
- Control oscilloscopes.
- Power supplies for the rack.

This rack is where the operators control the experiment. Sequences are entirely automatic and a run of several experimental sequences is manually started at the beginning of a parabola[8]. During the March 2007 test flight, there were three operators. One was in charge of entering the parameters of the experimental run in the computer and starting the sequence, one was in charge of monitoring the laser locking system and relocking the lasers if they jumped out of lock, the third was a backup, to be able to modifying wiring, if required. It is awkward, during the flight, to change wiring to monitor different signals. It is therefore convenient to have many oscilloscopes (four channels) and hand-held multimeters. These weigh very little and require little electrical power. Operators sit on the floor of the cabin, loosely strapped to it. They can lie back during hypergravity phases, to reduce discomfort.

[6] This is not the equilibrium position in micro-gravity, as a push with the feet on the floor sends them flying to the ceiling, and pushing with the hands on the ceiling sends one's head down.

[7] We could not measure precisely its center of mass height. We resorted to calculations to estimate it and had to include a safety factor. We were forced to remove an 18 kg electronic spectrum analyzer, that was occupying 5U. This allowed us to lower the center of mass. At 9 g forward acceleration, the torque on the uprights is 1.5tonne$\cdot$ m and the force on the rear attachment points in 15 kN per attachment point.

[8] The duration of a sequence is mainly limited by the loading time of the MOT, on the order of 1 s. We do as many sequences as possible during one parabola.

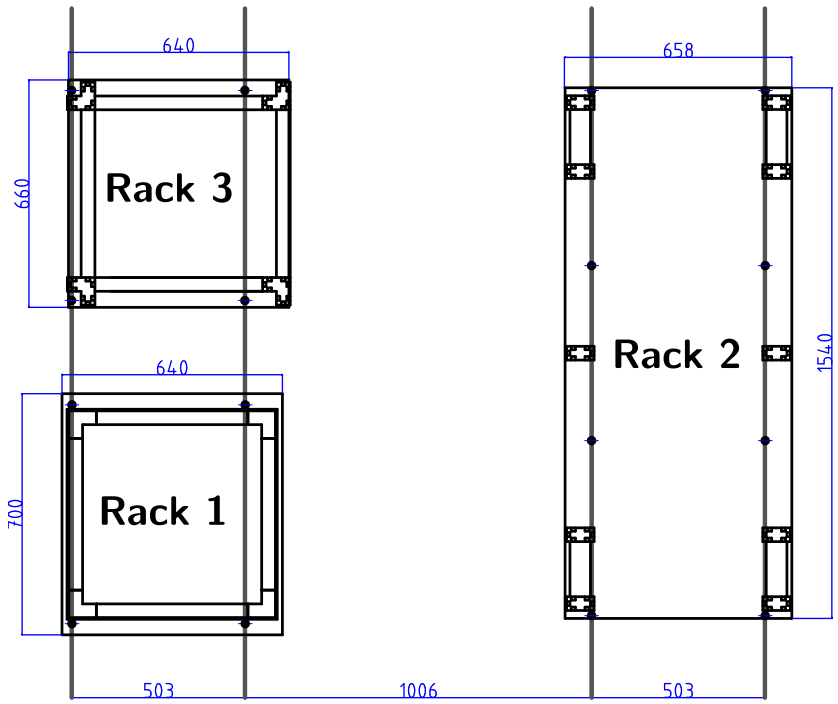

Figure III.4 – **Experimental racks**
The experimental apparatus is divided in three experimental racks attached to two pair of cabin rails. Rack 1 is the atom-optic chamber. Rack 2 holds control electronics and laser sources. Rack 3 holds the electrical equipements and power supplies.

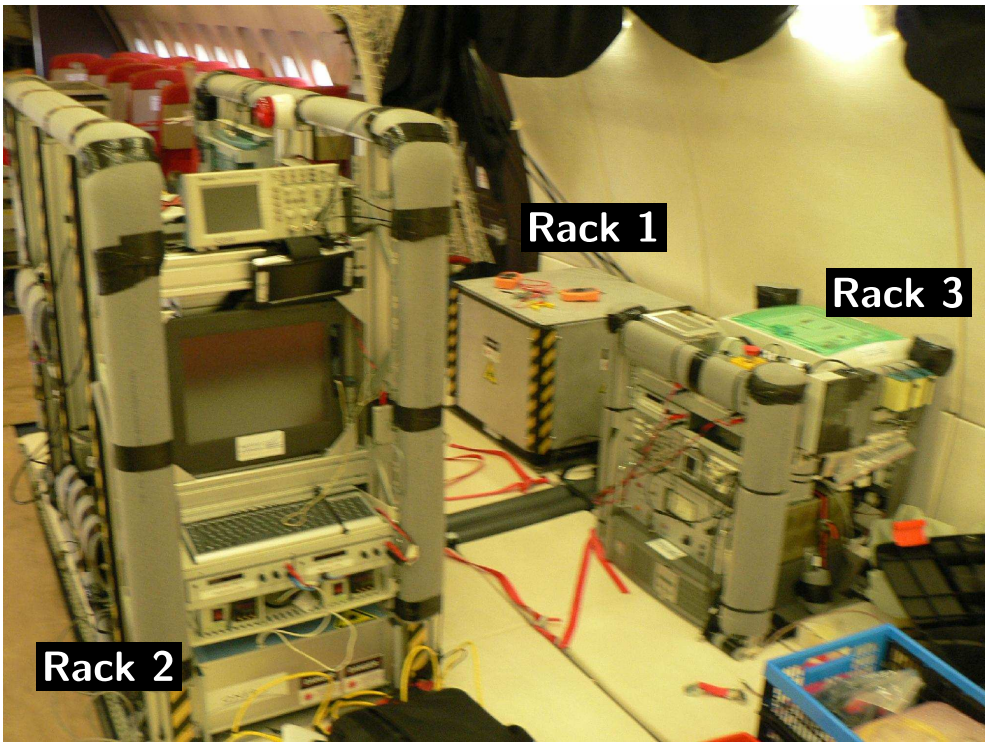

Figure III.5 – **Picture of the experiment installed in the airplane.**

Electrical rack The rack number 3 houses the electrical power system. The on-board power (220 V AC) is connected to an electrical distribution board where standard safety equipment (trip-switches, ...) is mounted. An Uninterruptible Power Supply[9] (UPS) is connected to the board and powers part of the equipment. An emergency switch turns off both the main trip-switch and the UPS via its *enable* input. A delayed-turn-on power distributor divides the power between different power lines to the equipment. The lines are turned on successively with an interval of a fraction of a second. This avoids current surges when the experiment turns on when the power comes on. A power consumption of 800 VA has been measured for typical use, but it varies a lot with the amount of work of the different servo locks (it can go up to 1200 VA). Detailed listing of the components on this rack can be found in §C.2, on page 208.

We use switching power supplies for all our voltage needs. Unlike standard lab power supplies, which are linear power supplies, they can generate high frequency noise (switching noise), but they are much lighter due to the absence of a metallic core in the transformer, and much more efficient. All home-made electronic devices and many commercial ones require low DC voltage. In order to avoid proliferation of power supplies we limit the different voltages used to 5 V and ±15 V, but a number of devices require adjustable voltages. For fixed voltage we use compact eurorack-mounted power supplies (Schott) and for adjustable power voltage we use rack-mounted Delta ES-series power supplies, that have a display of the current and voltage, and that can be controlled both by a knob on the front-panel and a remote-controlled analog set-point.

1.2 Novel integrated laser sources

The laser sources were developed at ONERA. They were adapted to compact 19" rack mounts compatible with flight safety requirements for this campaign.

Design

Laser cooling and manipulation of atoms requires frequency-stable, narrow-linewidth laser sources. The laser systems most often used in ultracold atom experiments are neither transportable nor reliable and robust enough for our application. Indeed, free-space optical benches with macroscopic cavities often need regular re-alignment. Moving away from the standard semiconductor-laser based design (see e.g. Laurent *et al.* [26]), we use laser sources at 780 nm, suitable for atom interferometry with ^{87}Rb, created by frequency-doubled fiber lasers and other telecom components at 1560 nm. These novel laser sources have been described in length elsewhere (Lienhart *et al.* [113], Lienhart [114]), in this section we will limit ourselves to outlining the successful design choices in light of the test flight.

[9] MGE Pulsar, 2000 VA

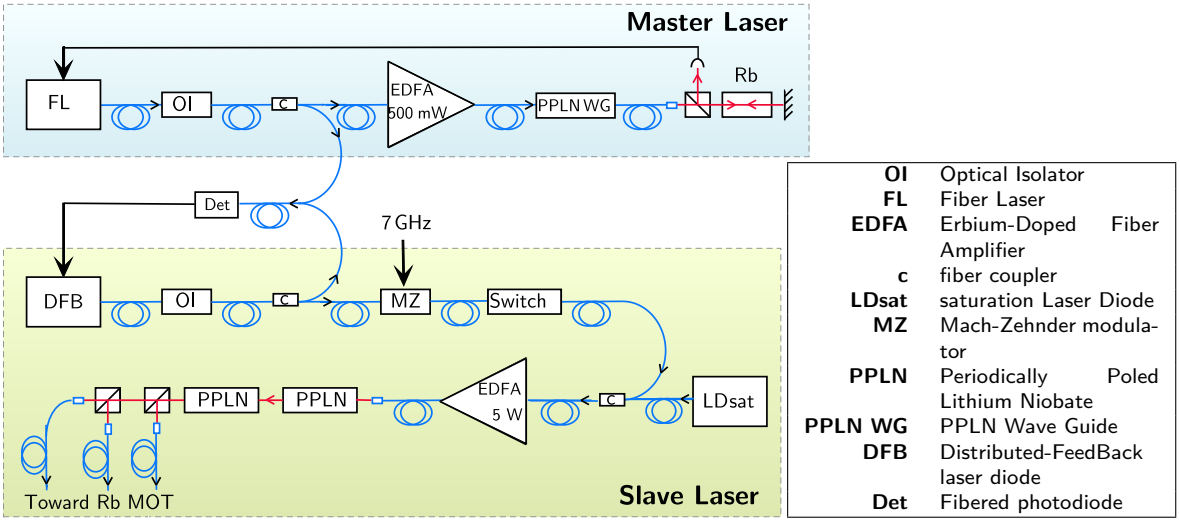

Figure III.6 – **Diagram of our laser system**
The master laser is pictured on top, the slave below.

To achieve a frequency-agile configuration, we use a master laser locked on a rubidium transition and slave lasers which are frequency-locked to the master laser with an arbitrary frequency difference (see figure III.6).

The master laser (linewidth of 10 kHz) is a monolithic semiconductor element: a 1560 nm Distributed Feed-Back (DFB) fiber laser, amplified in a 500 mW Erbium-doped fiber amplifier and frequency doubled in a PPLN waveguide. The resulting 780 nm light is then sent into a saturated-absorption spectroscopy setup for frequency locking to a rubidium transition. An error signal is obtained by modulating the frequency of the master laser for phase-sensitive detection[10]. Control of the frequency is achieved via a piezoelectric transducer (acting on the DFB laser) but we also change the temperature of the DFB fiber when the piezoelectric voltage approaches its maximum range[11].

The slave lasers are 80 mW 1560 nm DFB laser diodes (line-width of 1.1 MHz). After amplification through an Erbium-doped fiber amplifier, they are frequency doubled in free space with two 4 cm bulk PPLN crystals in cascade (similar to Thompson *et al.* [115]). With a 5W fiber amplifier, we obtain ~ 0.3 W at 780 nm at the output of a fiber. The slave lasers are frequency-locked to the master laser by measuring the frequency of a beat-note between the two 1560 nm lasers recorded on a fibered fast photodiode. Control of the frequency of the slave lasers is achieved via feedback to their supply current.

[10] We modulate the piezoelectric element of the Bragg fiber at a frequency of 1.3 kHz. Noise up to 1.6 Hz is attenuated. The r.m.s. excursion of the laser frequency in the 0-20 Hz band is less than 200 kHz.

[11] An integrated circuit based on a PIC 16F84 micro-controller was developed: the output voltage of the piezoelectric regulator is monitored by the micro-controller, and, when fixed boundaries are exceeded, the set temperature of the laser controller is adjusted to shift the frequency of the laser.

The power of the cooling laser can be adjusted by switching off the 1560 nm input laser of the fibered amplifier with an optical switch after saturating it with a laser source at 1556 nm. The 1556 nm light is not frequency doubled by the PPLN crystals and is filtered by the single-mode 780 nm fibers. A very good extinction is obtained, limited by the amplified spontaneous emission of the fibered amplifier that is frequency-doubled. Mechanical shutters are used to completely extinguish the lasers over long timescales (they have a 7 ms dead time), but the use of the saturation diode allows for quicker switching times ($\sim 50\,\mu$s).

In order to laser cool ^{87}Rb, an additional frequency (called the repumping laser), located 7 GHz away from the cooling laser, is required. Instead of using another laser, we use a 1560 nm fiber Mach-Zehnder modulator to generate two sidebands 7 GHz apart. One sideband is for repumping and the other is off-resonance, so causes no adverse effects.

To drive Raman transitions, we use a similar slave laser. The two Raman frequencies are also created by modulation of the laser at the frequency difference. This actually creates two side-bands and a carrier frequency, therefore opening a second Raman transition. This second transition is further away from resonance than the first and is less probable. Moreover, the beam-splitters it creates do not lead to a closed interferometer: the atomic wave packets do not overlap on the output beam-splitter, thus no unwanted signal appear on the read-out of the interferometer.

Transportable implementation

The laser system is separated into several 19" rack mounts, connected by polarization-maintaining fibers:

Master laser The master laser diode is mounted in a separate box, along with its fiber amplifier and wave-guide doubling crystal, as well as a free-space rubidium saturated-absorption spectroscopy setup.

Slave laser sources Four slave laser sources[12] are contained in the same box. The pigtailed laser diodes are connected to fibered components (optical isolators, switches, modulators...) by non-polarization-maintaining fibers coiled on dedicated supports. Despite large temperature changes we have not noticed any perturbation due to polarization drift.

Controllers The lasers diodes and their thermo-electric cooler are driven by a rack of integrated and highly compact dedicated power supplies (Tektronix Profile Pro).

Servo-locks The servo-locking rack comprises beat-note electronics, for frequency-locking the slaves on the master, a lock-in regulator for locking the master laser on the saturated-absorption signal (Toptica LIR 110), and the electronics for adjusting the temperature set-point of the master laser to follow frequency

[12] We use only two sources, the two others are backups.

drifts. The photodiodes for the beat-note locking sit next to the lasers-diodes themselves.

Optical amplifiers Each slave laser is injected in a separate Koheras fiber amplifier. Only one of the two fiber amplifiers used for the test-flight was polarization-maintaining.

Doubling stage The output of the fiber amplifier is frequency-doubled in a free space optical setup made of standard lab components mounted on a 10 mm-thick duraluminium breadboard. The two doubling crystals are not phase-matched, as the propagation required would be greater than a meter. We do not use a build-up cavity to increase the doubling efficiency, as previous experience has shown this was prone to mis-alignment with temperature changes. After frequency-doubling, the beam passes through mechanical shutters and is injected in a 780 nm mono-mode fiber. In the Raman-pulse laser doubling, stage we use an AOM for pulse shaping.

The fibers connecting the different components protrude from their front face. We use Velcro tape to press them against the racks as, during the flight, operators may not control well their movements. For the same reason, we prefer angled connectors for electrical connections.

The laser sources have proven remarkably robust during the test flight, surviving pressure changes of 200 mPa, temperature changes of 15°C, and remaining frequency-locked in spite of the noisy environment. It is worth noting that an amplifier was damaged during flight operations, its output power dropping by a factor of 10. This failure did not prevent the MOT from functioning. Later diagnosis has shown that a pump diode module was dead. This might be due to a diode failure, or to a mechanical misalignment of the pig-tailing.

1.3 Hyperfrequency source

The frequency difference between the Raman beams needs to be locked to a very stable microwave oscillator, whose frequency is close to the hyperfine transition frequency, $f_{MW} = 6.834\,\mathrm{GHz}$ for ^{87}Rb. The reference frequency is delivered by a frequency chain, which transposes an RF source into the microwave domain, retaining the low level of phase noise. With degradation-free transposition the phase-noise power spectral density of the RF oscillator, of frequency f_{RF}, is multiplied by $(f_{MW}/f_{RF})^2$.

The hyperfrequency source has been design and built by SYRTE, based on their knowledge of microwave references.

The RF primary source is an ultra-stable quartz crystal oscillator specially designed for low acceleration sensitivity (we use the quartz oscillator developed originally for the test-flights of the PHARAO project, see Besson and Mourey [116]. Its relative frequency shift due to acceleration is of a few 10^{-11} for one g). The source is first sent to a set of mixers that multiply its frequency by 10; the 100 MHz output is filtered,

amplified, and sent to a non-linear transmission line which generates a frequency comb at multiples of 100 MHz. One of the harmonics (close to 7 GHz) is filtered and mixed with a Direct Digital Synthesizer[13] (DDS) for an adjustable offset frequency control. A tunable microwave source is thus generated which transposes the 10 MHz reference, and its phase noise, to the desired frequency. Mixing operations generate little noise, but some high-frequency phase noise generated could be filtered by using phase locks (see e.g. Nyman *et al.* [22]). However, in a noisy environment such as an airplane, phase lock loop can unlock. As the high-frequency noise added by the mixers and the DDS is small compared to the high-frequency noise of the crystal[14] we decided not to work on robust hyperfrequency phase locks. The crystal oscillation frequency is temperature-sensitive. For better temperature stability, the crystal is held in a well thermally isolated chamber with a temperature servo. Equilibrium times are very long and the servo-loop can be powered on batteries during the night.

The hyper-frequency source has two DDSs for two different output frequencies. One is used to generate the repumping frequency, the other for the Raman beams. The DDSs are programmed by a computer via a parallel port and frequency changes or sweep can be trigged by TTL signals.

1.4 Design of the atomic-physics chamber

A ^{87}Rb vapor is created from commercially-available alkali-metal dispensers, and is collected in a single-chamber Magneto-Optical Trap (MOT) apparatus. After Doppler-cooling in the MOT, the magnetic field is turned off and optical molasses the atoms are released into ballistic flight. Their expansion is monitored by a camera and a photo-diode for atom-number estimations.

The atomic-physics part of the interferometer was built using off-the-shelf lab equipment with few custom-built parts. The apparatus is enclosed in a $600 \times 600 \times 500$ mm rigid frame[15] bolted through an optical breadboard. The frame supports the stainless-steel Ultra-High Vacuum (UHV) chamber to meet the flight security requirements for structural strength and optical confinement. While operating the atomic source, the dispensers are run continuously at a current of 3.9 A and a dilute ($< 10^{-8}$ mBar) rubidium vapor fills the chamber. There are two pumps: an ion pump and an activated-alloy getter pump, maintaining the required vacuum even during night power cut. The chamber is an octagon with ten ports (two CF100, eight CF40), one of which is used for the dispensers, while the others are available for optical access (see Fig.III.7). We dedicate separate windows for incident laser beams and observation. The six MOT beams enter the chamber through four lateral CF40 viewports and the two longitudinal CF100 viewports. Horizontal Raman beams for a light-pulse interferometer can also be added in the large longitudinal viewports. The

[13]The DDS is clocked by a signal generated from the quartz oscillator signal.

[14]Standard high-precision experiments use several crystals, with low-noise spectra in different bands, but we do not have low-acceleration-sensitivity crystals available for different bands.

[15] Also made of ITEM components.

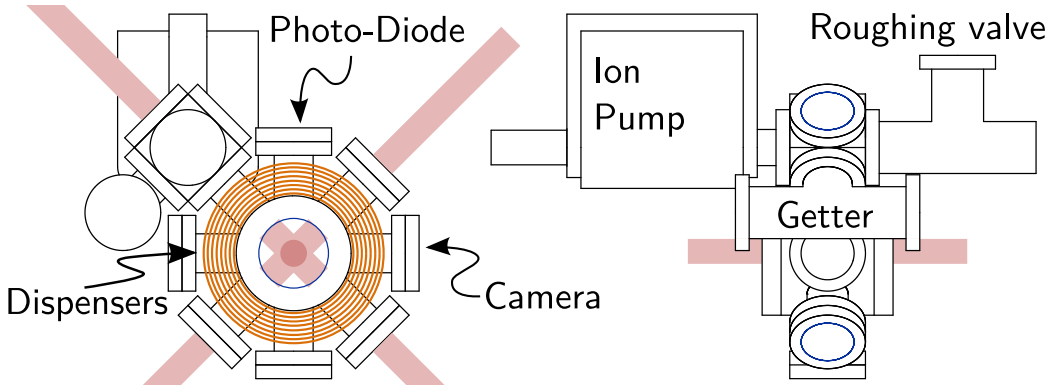

Figure III.7 – **Diagram of the vacuum chamber.**
The pumps are on top, to leave access for optics bolted on the breadboard. The MOT beams (drawn in light colors), angled at $45°$, leave access for vertical Raman-pulse beams.

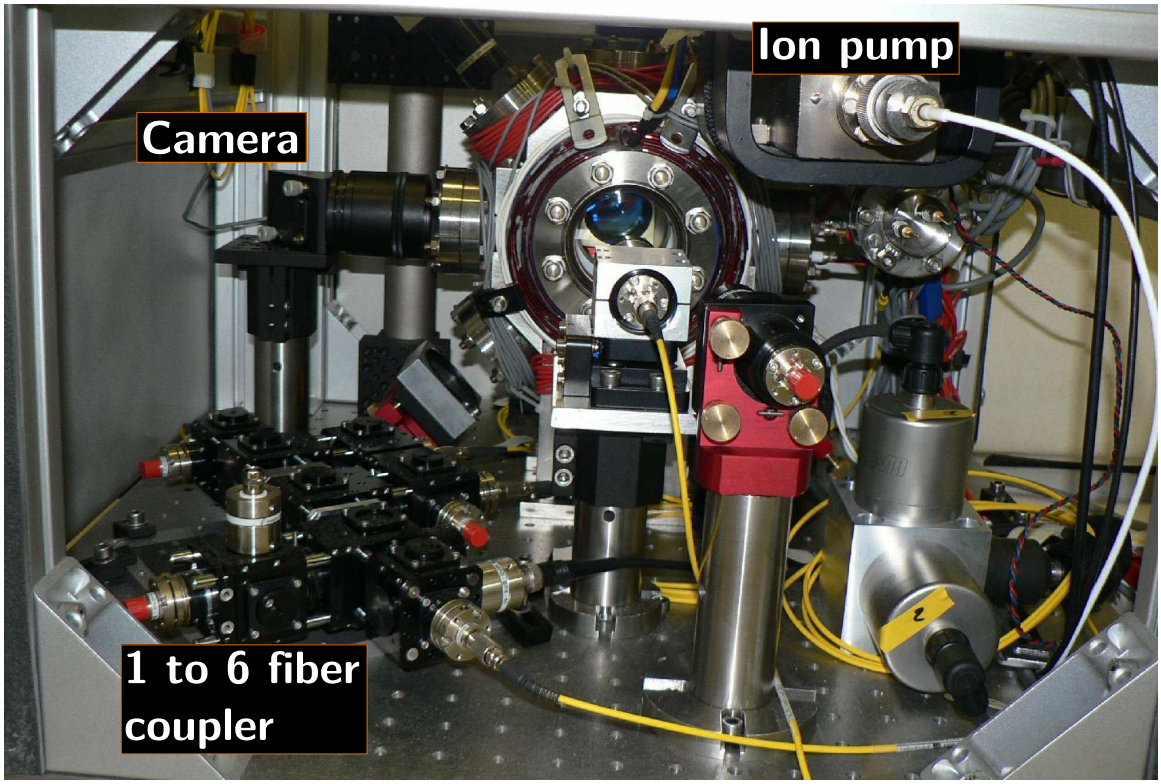

Figure III.8 – **Picture of the atomic physics apparatus.**
The view is from the other side than the diagram on the left of Figure III.7.

camera and the photodiode collect the light from the atomic cloud via lenses positioned close to a free lateral viewport. By shifting imaging to a longitudinal port, we can free access for vertical Raman beams for future experiments. MOT and compensation coils are directly wound onto the chamber. The vacuum chamber is slightly magnetic, and the ion-pump is not shielded. We rely solely on the compensation coils to cancel out the magnetic fields in the surroundings of the atoms. The dispensers are bolted onto the rods of an UHV electrical feedthrough. We have three dispensers in the vacuum chamber for redundancy in case of an electrical connection failure.

The light coming from the fibered laser sources is split into three separate fibers by a fiber beam-splitter (*Schäfter + Kirchhoff*) based on miniature polarizing optics. The beam-splitter is factory-aligned and stable against temperature changes and vibrations. Although it is possible to re-align, or to tune the power balance between the different outputs, this was never required. The six counter-propagating lasers beams of the MOT are made of three retro-reflected beams. Each beam is expanded out of a fiber by an out-coupler (*Schäfter + Kirchhoff*) producing a 24 mm full-aperture diameter, Gaussian (14 mm $1/e^2$ diameter), circularly-polarized, beam, and positioned on a 4-axis kinematic mount (*New Focus* 9071). Retro-reflection mirrors are 38 mm wide, mounted on kinematic mirror mounts (*Radiant-Dyes*), with a quarter-wave plate glued and clamped to their surface. Optics are held on 38 mm posts bolted and glued on the breadboard. Flight-compatible vibration and shock absorbers (*Enidine* WR8 series wire-rope isolators) can be used to attach the 120 kg apparatus to its baseplate.

A security CCD camera (*Conrad electronics* finger camera) is connected to a portable multimedia player (*Archos* AV700) to monitor and record the flight of the atoms during the optical molasses. A photo-diode with 0.1 numerical aperture collection optics is connected to hardware-triggered fast DAQ for quantitative signals of time of flight or atom-interferometric sequences.

The components making up the interferometer are modular and independent of each other. The atom-optics chamber has been used to test other laser sources, and the laser sources used during the flight are currently used on another experiment. The system is "plug and play": all the MOT needs to operate is a fiber with the proper frequencies and power.

2 In-flight demonstration of a cold atom source

2.1 Micro-gravity operation of the MOT

The setup was optimized in our lab in Palaiseau, then carried on a truck 500 km away to Bordeaux and loaded into the airplane with no particular precautions. In the airplane, every day, the temperature cycled from 6°C to 20°C. We did not notice any misalignment and the laser sources reliably operated at the required frequency. The only readjustment performed during the campaign was tweaking the injection of the

output fiber of the frequency-doubling stages after the transportation. The apparatus cannot operate below 15°C, as the signal-to-noise ratio in the saturated-absorption spectroscopy is too low[16]. Above 15° the system is very robust, the lasers stay locked and deliver sufficient power to obtain a MOT, whether in hyper-gravity, or in micro-gravity. Operation of the MOT is perturbed neither by take off or landing, nor by the repetition of micro-gravity and hyper-gravity phases No broadening of the lasers due to acoustic noise has been observed[17] in the noisy flight environment.

In normal operational conditions, we send a total of 75 mW of laser light in the chamber. We load 10^9 atoms of ^{87}Rb in the MOT in one second. With the disfunctioning amplifier we lost almost two orders of magnitude in number of atoms, and we operated with a two second loading time to retrieve a higher number of atoms and resume data acquisition.

2.2 Time-of-flight sequences

In order to have an estimation of the available interrogation times with our setup, we perform time of flight sequences. The MOT coils are abruptly turned off, and the detuning of the cooling and repumping lasers is ramped from $2\,\Gamma$ to $10\,\Gamma$ in 20 ms. After a variable wait time, we suddenly tune the lasers back to resonance and observe the fluorescence peak to measure the number of atoms still in the MOT region (see Figure III.9(a)). The mechanical shutters are not reliable-enough on these short time scales and we cannot extinguish the lasers as would have been preferable for real free propagation of the atoms. Instead we use a large detuning to reduce the effect of the laser on the atoms during their flight. We will install AOMs to address this issue in the next flight campaign.

This sequence is similar to the actual detection scheme we plan to use for the atom interferometer: atoms are released from the MOT and after a brief optical molasses sequence, they undergo free ballistic expansion during which the light-pulse sequence is applied to perform the atomic beam-splitters and mirrors. The atoms can be selectively prepared in the lower hyperfine state by turning off the repumping light. Similarly, detection can be state sensitive by first probing the atoms in the higher hyperfine state using a laser light without the repumping frequency. As we are interested by the population ratio between the two hyperfine states, the total number of recaptured atoms is then measured by turning on the repumper, thus addressing all atoms.

During this first flight campaign, the measured accessible interrogation time was of the order of 40 ms (see Figure III.9(b)), not any longer than laboratory experiments. Indeed, our interrogation time was not limited by gravitational acceleration of the atoms. Our preliminary setup had no magnetic shield[18] and the rotation of the Earth's

[16] This is mostly due to the low rubidium pressure in the vapor pressure cell, but the output power of the laser sources setup also drops by a factor of two at low temperature.

[17] No quantitative data has been taken to back this observation. Our observation only relies on frequency spectrum of the beat note signal between laser monitored during flight.

[18] Magnetic shield material had been ordered but could not be delivered on time for the flight.

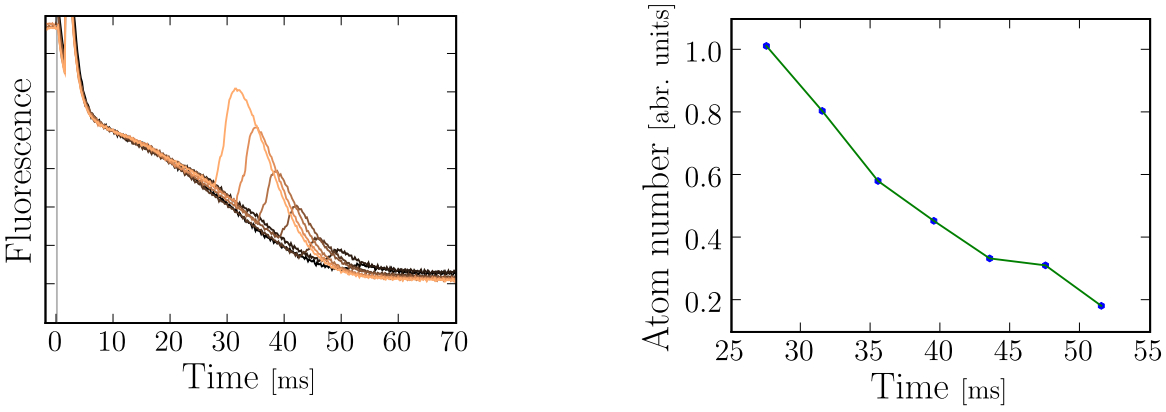

FIGURE III.9 – **(a) Time of flight sequences**

The magnetic field is switched of at $t = 0$. This causes stray e.m.f.s that are picked up by the photodiode amplifier (located close to the coils). As the lasers are detuned from the resonance, the fluorescence decreases, but when they are tuned back on resonance, a fluorescence peak reveals the atoms still in the MOT region. This data has been taken in micro-gravity, for variable flight time, and the decrease of the area in the peak shows the decrease in atom number in the detection volume.

(b) Atom number decay

The number of atoms decays linearly with time. This indicates an escape by a systematic drift of the cloud in one direction, rather than a ballistic expansion, which would yield a decay in $\sim t^{-3}$, as the atoms leave the detection volume in all directions (see §II.1.1).

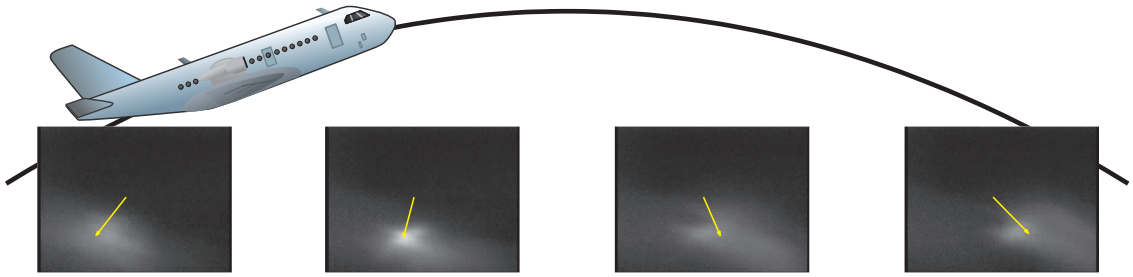

FIGURE III.10 – **Images of molasses at different airplane angles**

The tilt in the Earth's magnetic field produces an imbalance in the radiation pressure during the molasses phase, and alters the direction in which the atoms escape. The arrows connect the positions of the initial trapped cloud to the escaping atoms. The escape direction does not directly relate to the pitch angle of the airplane, as its bearing also changes the direction of the magnetic-field.

magnetic field created uncompensated Zeeman shifts. These shifts imbalance the radiation pressure during molasses, limiting the atomic escape velocity (see figure III.10). They cannot be compensated for by compensation coils: the rotation of the Earth magnetic field is not repeatable for one parabola to another, as the bearing of the plane changes.

This flight campaign has demonstrated that the Airbus provides an environment suitable for micro-gravity atom-optics experiments. The quick setup, with standard laboratory equipment, of a cold atom source shows that laboratory experiments can be adapted for this new experimental platform. Indeed this apparatus uses less custom-made equipment than a standard metrology experiment, as run for instance at SYRTE. The time frame to assemble this prototype was very short ($\sim$ 3 months, two full time persons). Unlike drop towers, and moreover orbital platforms, development cycles can be sufficiently short to allow for the rapid technological evolution for future sensors. The accessible long interrogation times can serve for new fundamental inertial-sensing experiments and push the technology, each flight campaign bringing better understanding of the limitations of the apparatus and the systematics in the measurements that can be incrementally improved between campaigns.

Conclusion to part I

In this part, I have shown that the Zero-G Airbus is a promising platform to conduct atom-interferometric experiments. Indeed, although parabolic flights are not real free fall, with an apparatus freely floating in the cabin they open the door to four-second-long atomic flight times in a compact vacuum chamber. Moreover, by comparing the fall of two different atoms in the Earth gravity field, an experimental test of the universality of free fall is possible. In addition, we have demonstrated the operation of a laser-cooled source of slow atoms, thus validating our technological choices for atom optics in the Airbus, and showing that this platform does not impose heavy design constraints on the experiments.

The lessons to be learned from the test flight are that 780 nm laser sources created by frequency doubling telecom laser sources are solid and reliable, and that a small lab-quality atom-optics chamber can be made transportable and ballistic-flight-compatible. For long interrogation times, the requirements on the source are the same in the Airbus than in a laboratory: low temperatures and small release velocities. The experimental challenges are the same, namely, for laser-cooled atoms, good optical molasses.

I have outlined a protocol to test the universality of free fall on an experimental platform with a motion that is neither well-known, nor well-controlled. The key elements are:

- two inertial-sensing atom-interferometers, for potassium and rubidium, phase-coupled by using either phase-locked lasers or the same laser for the Raman transition,
- isolation of repeatable experimental situations by releasing the measuring apparatus in a free flight only for the time of the experiment, and by using a rotationally-insensitive interferometric scheme,
- a statistical description of the contrast and phase noise of the interferometers, and the use of a Bayesian estimator to infere the differential inertial measurement for the interferometric measurements.

This protocol has broader applications than performing an experiment on the Airbus. Indeed, even on orbital platforms, the acceleration of the platform is difficult to control. Propositions for satellite tests of the universality of free fall most often lay out the need for a drag-free satellite. The protocol described above can be used to address some of the difficulties of a test of the universality of free fall on orbital platforms. The η parameter, figure of merit of such a test, scales as the square of the interferometric interrogation time and the square root of the number of measurements performed. With ultra-cold atoms and large interrogation regions, free-flight times longer than a minute are possible, leading to an increase for shot-to-shot sensitivity of two to three orders of magnitude. On top of that, the number of measurements

can be increased by many orders of magnitude so that the measurement is quantum-projection-noise limited. This would result in η parameter of down to 10^{-16}. This is not competitive with propositions of satellites tests of the equivalence principle using macroscopic objects[19]. To increase further sensitivity, longer interrogation times can be used, at the cost of loss of signal due to the expansion of the atomic cloud.

All in all, developing atom-interferometric inertial sensors for the Zero-G Airbus appears as a test-bed for new techniques and protocoles for eventual orbital missions.

[19]The STEP program should achieve $\eta \sim 10^{-18}$ (Worden *et al.* [117]).

Part 2

Degenerate gases for a collimated atomic source

Part contents

Résumé de la deuxième partie

IV Tunable semi-conductor laser system

V Building a transportable boson-fermion coherent source

Introduction to part 2

In long-interrogation-time atom-interferometric inertial sensors, expansion of the cloud leads to a loss of signal, as the atomic cloud grows bigger than the detection volume. As detailed in §I.1.2, for atomic sources, collimation and first-order coherence are directly linked, as the typical length scale for coherence is the De Broglie wavelength associated to the momentum spread of the cloud. Collimated atomic sources are thus also coherent atomic sources, obtained for ultra-cold atomic clouds.

Maximizing collimation and coherence, for a high atomic flux, leads to producing degenerate sources, for which the momentum spread is given by the quantum statistics of the atomic gas. In a non-interacting Bose gas with a degeneracy parameter greater than 1, Bose-Einstein condensation occurs, and the ground state becomes macroscopically occupied, in which case the momentum width is limited by the size of the

wave-packet, through the Heisenberg uncertainty principle. However, interactions in Bose condensates lead to a broadening of the momentum distribution and systematic errors in interferometers. As for ultra-cold Fermi gases, the degeneracy parameter is cannot be greater than one because two fermions cannot occupy the same state. This appears in a Fermi gas through the suppression of collisions, but also a broadening of the momentum width due to Pauli pressure. In typical experimental situations, the orders of magnitude of the broadening due to interactions in Bose gases, and the broadening to to Pauli pressure in Fermi gases are similar.

In the second part of my thesis, I describe the design and construction of an apparatus to cool atomic gases to degeneracy. In order to have a versatile apparatus to compare the effects of Pauli pressure and interaction in an atomic sources, we have designed the apparatus to allow simultaneous cooling of bosonic rubidium, to create a Bose-Einstein condensate, and potassium, for which a fermionic isotope can be cooled to degeneracy, as well as a bosonic isotope with precisely-tunable interactions. Moreover, we have designed the apparatus to create the atomic source in an optical trap that we can both turn off quickly in a well-controlled way, to release the atoms from the trap with no initial velocity, or expand adiabatically, to lower the density of the atomic cloud and reduce the effects of interactions and quantum pressure.

In its current status, the apparatus has been successively used to laser cool rubidium atoms, and to load them in the dipole trap. Although the laser sources were demonstrated on potassium atoms, no work on cooling and trapping of potassium has yet started.

An ultracold-atom apparatus is a complex machinery and in this part I discuss in detail various components of the apparatus whose performance will condition the experiments and measurements that can be perform with the resulting atomic source.

I successively present the tunable laser sources that we developed for laser cooling of potassium and rubidium, the atom-optics apparatus itself, and the first dipole-trap-loading results.

Résumé de la deuxième partie

Dans un interféromètre atomique où de longs temps de vol sont accessibles, tel qu'un appareil en chute libre ou en micro-gravité, l'expansion du nuage atomique peut être une limite aux temps d'interrogation. Un nuage refroidi par laser a une dispersion en vitesse typique de $0.1\,\mathrm{m}\cdot\mathrm{s}^{-1}$, et il est difficile d'envisager des temps d'interrogation supérieurs à quelques secondes. De plus la dispersion des trajectoires atomiques dans l'interféromètre peut limiter la précision des senseurs inertiels.

C'est pourquoi les sources atomiques denses et ultra-froides créées par refroidissement évaporatif d'un nuage refroidi par laser sont des sources idéales pour l'interférométrie atomique à long temps de vol. Le refroidissement évaporatif permet de créer un condensat de Bose-Einstein, c'est à dire une source d'optique atomique limitée par la diffraction.

Comme souligné dans le premier chapitre, la cohérence du premier ordre d'un nuage atomique est directement liée à sa dispersion en vitesse. Il peut donc être intéressant d'utiliser des gaz de Fermi comme source pour l'interférométrie atomique, plutôt que des condensats de Bose-Einstein pour lesquels les interactions atomiques élargissent la distribution vitesse et peuvent introduire des erreurs systématiques.

Dans la deuxième partie de ma thèse, je présente la construction d'une deuxième source atomique, élaborée en vue de produire des gaz dégénérés. L'expérience a été conçue pour pouvoir fonctionner simultanément avec des atomes de rubidium 87, pour lesquels l'obtention d'un condensat de Bose-Einstein est une technique bien maîtrisée, et des atomes de potassium. En effet, le potassium peut être refroidi sympathiquement par le rubidium, et possède un isotope fermionique et un isotope bosonique pour lequel les interactions sont contrôlables très précisément par des résonances de Feschbach.

Pour produire une bonne source pour l'interférométrie atomique à long temps de vol, il est nécessaire de bien contrôler le lâcher du nuage atomique ainsi que les interactions. Nous avons choisi d'utiliser un piège optique pour le refroidissement évaporatif, car cela nous donne la liberté de contrôler les interactions magnétiquement. De plus, la coupure du piège n'est pas gênée par des courants de Foucault. Par ailleurs nous pouvons contrôler dynamiquement la taille de notre piège, ce qui permettra l'ouverture adiabatique du piège, pour se placer dans de bonnes conditions pour le lâcher des atomes.

Les travaux expérimentaux présentés dans cette partie ne constituent qu'une partie du chemin à accomplir pour créer une source de nuages atomiques dégénérés. Pendant ma thèse, nous avons développé des sources laser pour refroidir le potassium et le rubidium, nous avons construit une expérience d'atomes froids conçue en vue de

l'obtention de gaz dégénérés, nous avons obtenu des nuages de rubidium refroidis par laser, et nous avons chargé ces atomes dans le piège optique. Il reste encore à évaporer dans le piège optique pour obtenir la condensation du rubidium, tandis que pour le potassium, l'étape de refroidissement laser est encore à maîtriser avant même que l'on puisse s'attaquer au refroidissement sympathique.

Lasers semiconducteurs accordables pour le refroidissement du potassium et du rubidium

Les longueurs d'onde de refroidissement laser du potassium et du rubidium sont proches : 767 nm pour le potassium et 780 nm pour le rubidium. Pour le rubidium, il est possible d'utiliser un montage de diode laser en cavité étendue avec des semiconducteurs produits en masse pour obtenir le rayonnement nécessaire au refroidissement laser. Mais pour le potassium, il n'existe pas sur le marché actuel de diode laser dont la plage de gain permette de laser à 767 nm à température ambiante. Afin de ne pas dépendre d'une technologie non-embarquable comme un laser titane-saphir, il nous a paru important d'utiliser pour notre expérience des sources laser à semi-conducteur.

En utilisant comme milieu à gain des diodes laser traitées anti-reflet, que l'on réinjecte avec un élément sélectif en longueur d'onde, nous avons créé des diodes laser accordables en longueur d'onde sur une plage de 20 nm et utilisables pour le rubidium tout comme pour le potassium. Cette plage d'accordabilité nettement supérieure aux diodes laser en cavité étendue non traitées anti-reflet est due à la présence d'une seule cavité au lieu de deux, ainsi qu'à un plus large gain du milieu semi-conducteur dû à sa moindre saturation, car la cavité laser est d'une faible finesse.

Nous avons utilisé des amplificateurs semi-conducteurs pour produire une intensité lumineuse suffisante pour le montage de refroidissement laser. Nous avons mesuré la qualité spectrale des différentes étapes de la chaîne laser qui est bien compatible avec les exigences du refroidissement Doppler.

Une expérience d'atomes froids compacte, avec des technologies embarquables

Nous avons conçu et réalisé un montage de refroidissement laser et de piégeage optique, en cherchant des solutions nouvelles, au minimum pour le laboratoire, pour que l'expérience puisse un jour être rendue compacte et embarquable. Cependant, nous ne nous sommes pas engagés dans un processus de miniaturisation ou de développement technologique.

Le montage exploite le volume complet d'un cadre de 90 cm × 90 cm × 120 cm ; il regroupe un piège magnéto-optique bidimensionnel qui sert de source d'atomes lents, un piège magnéto-optique tridimensionnel pour refroidir les atomes par laser, des bobines pour créer un champ magnétique intense (0.12 T) en vue de contrôler les interactions atomiques, ainsi que l'optique nécessaire à la mise en forme du faisceau pour le piège dipolaire ainsi qu'au contrôle dynamique de sa taille.

Dans le chapitre de ma thèse décrivant le montage expérimental, je m'efforce d'expliquer les démarches qui ont conduit aux choix techniques lors de la conception de l'expérience, souvent à l'aide de petits modèles simplifiés dégageant des lois d'échelle. Beaucoup de contraintes que nous nous sommes imposés sont en vue d'étapes futures pour l'obtention de la source atomique, et tous les choix ne sont pas encore validés.

Chargement du piège optique

Nous avons obtenu, en septembre 2007, les premiers résultats sur le chargement d'atomes dans la pince optique compressible. Dans le dernier chapitre de ma thèse, je présente une analyse de ces résultats préliminaires, en m'intéressant plus particulièrement à la caractérisation du piège optique, ainsi qu'aux mécanismes limitant l'efficacité de chargement. L'utilisation d'une technique nouvelle d'imagerie permet d'accéder à la distribution atomique pour différentes énergies potentielles.

De plus, j'étudie la possibilité de superposer un refroidissement Doppler au piégeage dipolaire. Le décalage des transitions atomiques par le piège dipolaire perturbe fortement le refroidissement dipolaire ; on ne peut donc combiner piégeage dipolaire et refroidissement laser que sur des petites régions du piège, où la diffusion de photons limite le nombre d'atomes piégés.

Cette partie présente donc la construction d'un montage dont on peut voir les premiers résultats expérimentaux. Ce montage est un moyen, et non une fin ; nous avons tenté de lui donner les outils nécessaires pour mener à bien des expériences liées à l'interférométrie atomique avec des gaz dégénérés.

Chapter IV

Tunable semi-conductor laser system

Improvement makes strait roads,
but the crooked roads without Improvement, are roads of Genius.
William Blake – The Marriage of Heaven and Hell

This chapter describes the tunable laser sources developed for laser cooling potassium and rubidium. By using a single-cavity design for extended cavity diode lasers we were able to achieve 20 nm of tunability range with a fully semi-conductor, compact laser system. The work presented in this chapter has been published in Nyman *et al.* [118].

Atomic-physics experiments have strict demands on the quality of the laser systems used for the manipulation of atoms. Laser cooling and trapping requires laser linewidth smaller than the natural linewidth of the relevant atomic transitions, and the ability to servo-lock the laser frequency close to the transition. Atom interferometry experiments using stimulated two-photon transitions to induce coherent population transfer are highly sensitive to laser frequency noise (Le Gouet *et al.* [110]).

For the degenerate gas apparatus, we use fully semi-conductor laser systems, as they are both well-tried and scalable laser sources for atomic physics. Semi-conductor lasers are planned for use on space-borne atomic clock missions (as described in Laurent *et al.* [26]). They can be mass-produced and fit in a compact volume.

Rubidium has a cycling transition close to 780 nm (Sheehy *et al.* [119]), used for cooling and trapping, e.g. optical molasses and magneto-optical traps, and coherent manipulations. For this wavelength, semiconductor laser-diode systems have been available for some time, due to their use in compact disc players and recorders. Potassium laser trapping and cooling is achieved via its cycling transition at 767 nm (Williamson and Walker [120], Williamson [121]).

The use of diode lasers for atomic physics experiments has been made possible by the development of extended-cavity diode lasers (ECDL) (see Wieman and Hollberg [122] for a review). These take advantage of the available laser diodes and use frequency-selective feedback and high photon numbers to achieve tunability and narrow linewidth, typically via a diffraction grating in either the Littrow (Arnold *et al.* [123]) or Littman configuration (Littmann and Metcalf [124]). Using the temperature

dependence of the semiconductor gain medium has allowed use of mass-produced diode lasers, whose room temperature wavelength is controlled to within a few nanometers, for a rich variety of atomic species. In particular, diode lasers centered around 785 nm are commonly used for rubidium trapping (780 nm) when used at room temperature. However, for these readily-available diodes, the semi-conductor medium gain curve does not extend far to the blue, and, for operation at the 767 nm potassium transition, the ECDLs have to be cooled to sub-zero temperature. Consequently, diode-lasers so far developed that present the capability of tuning across the full spectra of the two species without significant changes in temperature, alignment, or even the laser diode are only of low power, suitable for spectroscopy[1]. So far, most groups working with atomic potassium produce light at this wavelength using either Titanium-Sapphire lasers (for instance Cataliotti *et al.* [126], Prevedelli *et al.* [127]) or by cooling diode lasers designed for 780 nm below zero degrees Celsius (Demarco [128], Fletcher and Close [129]). In both cases, the result is a complex, and sometimes expensive, set-up.

Since ECDLs do not usually deliver more than a few milliwatts of useful light, amplification is required for atomic trapping and cooling, by injection locking (Wieman and Hollberg [122]), through a broad-area laser (Shvarchuck *et al.* [130]) or via a tapered amplifier (Voigt *et al.* [131], Goldwin *et al.* [132]). An alternative is to put the high-power semiconductor element in a cavity, resulting in either a tapered laser (a commercial example is used in Catani *et al.* [133]), or an external-cavity broad-area laser diode (Cassettari *et al.* [134]). These alternatives have the drawback of requiring complex mechanical engineering, cooling and beam-shaping.

We have developed a novel system of semiconductor Master Oscillators (MOs) and Optical Power Amplifiers (OPAs), which can be tuned anywhere in the range $760-790$nm close to room temperature and is thus useful for simultaneous cooling and trapping of rubidium and potassium. The master oscillators in our system are Littrow-type ECDLs using antireflection-coated laser diodes with gratings chosen for weak feedback in the semiconductor medium. We have verified that our optical amplifiers do not appreciably degrade the spectrum of our laser sources.

1 Master Oscillators: ECDL with Anti-reflection-coated Diode Lasers

1.1 Construction of an Extended Cavity Diode Laser (ECDL)

Design The ECDLs follow the design of Arnold *et al.* [123] modified by C. Aussibal [135] (see Fig. IV.1(a)). Briefly, the diode is mounted in a collimation tube

[1]Very low power commercial ECDLs are available at 767 nm (New Focus Vortex series, using a modified Littmann-Metcalf configuration), but, for laser trapping and cooling, they need to be amplified using two stages: an injection-locked slave diode, then a tapered amplifier, as used in Aubin *et al.* [125].

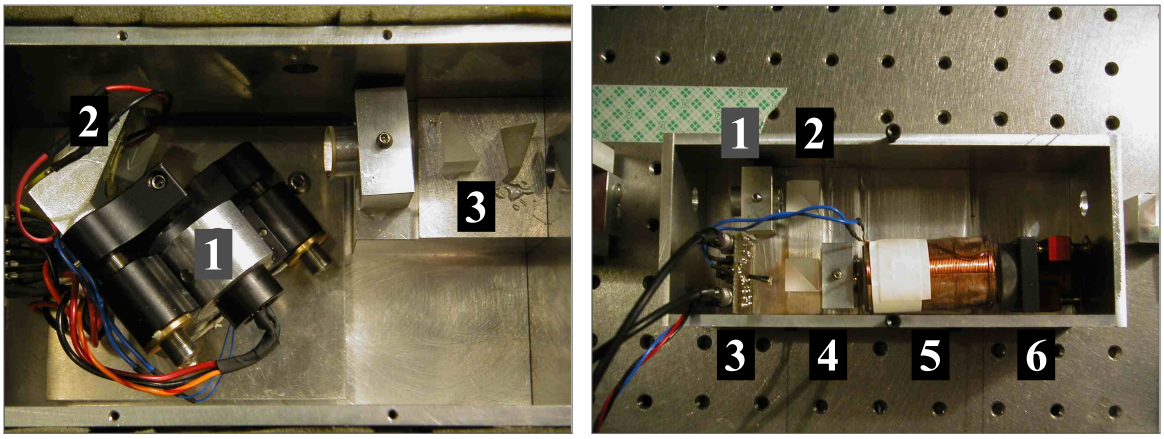

FIGURE IV.1 – **(a) Picture of the ECDL (Littrow configuration)**
(1) Diode laser mount (*Thorlabs* LT240P-B) which also acts as a mount for the collimation lens. (2) Holographic grating. (3) Anamorphic Prisms.
(b) Saturated absorption spectroscopy module
(1) Half-wave plate. (2) Polarizing beam-splitter cube. (3) Photodiode. (4) Quarter-wave plate. (5) Atomic vapor cell, surrounded by electromagnet. (6) Mirror.
The box is about 17 cm long, by 7 cm wide by about 6 cm deep. It and can be closed to reduce background light.

(*Thorlabs* LT240P-B) with an aspheric collimation lens. The tube is then mounted into a modified, high-precision mirror-mount, which is held on a thermoelectric cooling device (TE cooler). A holographic diffraction grating is glued onto a piezoelectric element which is itself fixed on the moving part of the mirror mount, putting the ECDL in the Littrow configuration: the first diffraction order is retro-reflected and the zero order is output. The orientation of the grating with respect to the diode can be changed by adjustment of the modified mirror mount. The cavity length can be finely adjusted by altering the voltage across the piezoelectric element.

Implementation The long-term stability, the sensitivity to acoustic noise, and the power output of the ECDL vary from one to another. First of all, not all diodes are born and made equal. We keep a small stock of diodes (< 5) in the lab and we select each diode for a given purpose based on the emission spectrum provided by the manufacturer, as their center frequency varies. The good quality of the collimation is very important for high optical power output: for the extended cavity to be well closed, the retro-reflected beam needs to be precisely collimated. The grating used for the extended cavity is glued on a low-voltage piezoelectric electronic buzzer that bends as its driving voltage is varied. The quality of the glue used, and the exact position of the spot of glue between the grating and the buzzer is paramount for the long-term stability of the ECDL. It also determines the mechanical resonances of the cavity. These need to be higher than a few kiloHertz to avoid pickup of the acoustic noise in

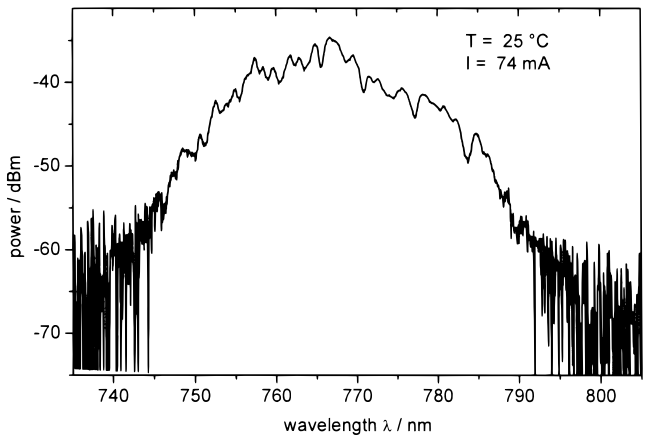

Figure IV.2 – **Spectrum of a free running diode**
As the diodes are AR coated, there is no lasing effect. The spectrum of the free running diode corresponds to the spontaneous emission of the semiconductor gain medium, thus also to its gain spectrum. Shown above is a typical spectrum. The center wavelength of the gain curve can vary by up to 5 nm depending on the diode. (Source: Eagleyard specification sheet)

the frequency of the laser[2]. Finally the distance between the thermistor sensor for the temperature servo loop and the laser diode itself has a great impact on the long-term thermal stability of the diode, and thus on its operation wavelength stability.

1.2 Anti-reflection-coated diodes for shorter operational wavelengths

Most ECDL designs employ standard diode lasers (Wieman and Hollberg [122]), which thus create a coupled-cavity system. This coupling can result in collapse of coherence (Sacher *et al.* [136]) that increases the linewidth of the laser and can make the mode-hop-free continuous scanning range much less than the free-spectral range of the extended cavity. In our ECDLs, we use *Eagleyard*, Ridge-Waveguide Laser (SOT03 package), nominally specified for laser emission at 790 nm (reference EYP-RWE-0790-0400-0750-SOT03-0000). The diodes have been anti-reflection coated on the output facet, to about 0.1% reflectance, which shifts the gain spectrum of the semiconductor medium to the blue. This shift allows us to use these diodes on the 767 nm potassium transition.

Extending the tuning range to the blue To understand this effect, one notes that the gain curve of a semiconductor laser depends on the photon density in the medium. The gain medium used in many of the commercially-available diode lasers specified for emission at 780 to 790 nm actually extends further to the blue (see Fig. IV.2). However, in diode laser heterojunctions, the region where free electrons and holes exist simultaneously, the active region, is confined to a thin middle layer. The

[2]Some of our laser diode setups have a peaked resonance around 1.2 kHz. This is due to the vibration of the NewPort mirror mounts, which vary from one batch to another.

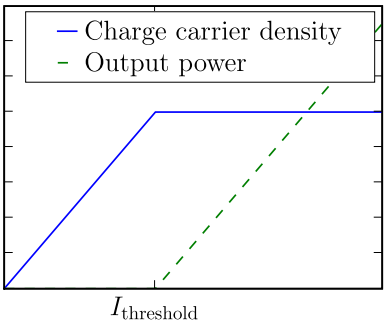

FIGURE IV.3 – **Output optical power and carrier density as a function of drive current**

light is also confined to this region, where the amplification takes place, leading to a high photon density in the junction. The higher the optical density, the more the semiconductor bands are depleted, and therefore the lower the gap between the quasi-Fermi levels (Chow and Sargent III [137]). Therefore, when the semiconductor medium is inserted in a high optical-density cavity (as in a diode laser), its high-energy transitions are no longer available; the blue end of its gain spectrum is not usable for laser emission.

Above the laser threshold, the carrier density is given by the balance between the injection of charge carriers due to the current through the junction, and the loss of carriers through stimulated radiative transitions. The number of intra-cavity photons is given both by their life-time in the cavity and the rate of radiative transitions between the semiconductor bands. The number of carriers in the junction reaches a limit at the lasing threshold. At the threshold, the rate at which photons are created by electron-hole recombinations balances the loss of photons by intra-cavity dissipative processes. Above threshold, extra carriers injected in the junction via the driving current yield photons that exit the cavity, the laser radiation; the carrier density is independent of driving current and given by the threshold carrier density (see Figure IV.3):

$$N_{\text{th}} = N_0 + \frac{1}{\beta\,\tau_{\text{cavity}}}, \tag{IV.1}$$

where N_0 the charge carrier density required to render the medium transparent, β is a factor characterizing the probability that an electron-hole recombination creates a photon in the cavity mode, and τ_{cavity} is the photon lifetime in the cavity[3].

ECDLs achieve narrow linewidth lasers by increasing the photon lifetime in the cavity. Their intra-cavity frequency-selective element (the grating) makes it possible to tune the laser and produce a wavelength other than the center wavelength of the gain medium, but the blue-end of the naked semiconductor gain spectrum is not usable due to the high photon lifetime.

We use AR-coated diodes in ECDLs. The above-threshold carrier density is reduced in comparison with a non-antireflection-coated diode laser as the photon cavity

[3]This formula assumes that the semiconductor medium entirely fills the cavity, as in a diode laser. If it is not the case the ratio of the photon densities inside the cavity and inside the semiconductor medium appears as a correcting factor to τ_{cavity}.

lifetime τ_{cavity} is reduced. We observed this experimentally by the reduction of the threshold current from 27 mA (non AR-coated ECDL) to 24 mA (AR-coated ECDL). As a result the total tuning range of diode lasers is extended to the blue (Hildebrandt *et al.* [138]). We can, by adjusting the angle of the grating, tuning the lasing wavelength of one diode from 765 nm to 785 nm.

Choice of the grating The choice of the grating is crucial for optimal operation. Compared to standard ECDLs, since there are no coupled-cavity dynamics, the cavity mode is stable for a lower grating-reflectivity in our system. Low finesse is required to avoid high in-cavity optical intensity, which could damage the semiconductor. In particular, the grating has to be chosen so as best to match the reflectance of the surface of a non-AR-coated diode laser, namely about 7%. We chose for a (cheap) grating a 1 200 lines/mm holographic grating, optimized for UV light (*Edmund Optics* T43-772), which diffracts roughly 10% of light into the first order[4] and sends the remaining light into the zero-order output beam. The photon lifetime in an AR-coated ECDL with a low-reflectivity grating is lower than in a normal ECDL, but it is greater than in a normal diode laser where it is limited by the short cavity length (see appendix D).

The orientation of the grating with respect to the diode laser controls the wavelength and optimizes the output intensity, by diffracting the first-order light into the semiconductor medium, and reflecting the remaining light into the output beam (the zeroth order). Since the diode sits in a cavity of very low finesse (around 1), the intensity of light in the semiconductor element is scarcely greater than the intensity of the output beam.

The extended cavity has a free spectral range of roughly 5 GHz (0.01 nm). Thus continuous scans can be performed of up to 5 GHz around a wavelength in the range $765 - 785$ nm, by changing the length of the cavity using the voltage across the piezoelectric element. The central wavelength is chosen by turning the screws on the mirror mount, adjusting the angle of the grating with respect to the diode (changing the voltage on the piezoelectric element scans the wavelength on a range of 0.3 nm with mode-hops of 0.09 nm).

1.3 Performance of ECDL

The AR-coated diode laser is specified to operate with a typical free-running center wavelength of 780 nm at 25°C ($d\lambda/dT \sim +0.3\,\text{nm}/^\circ\text{C}$), with a spontaneous emission spectrum between 750 and 790 nm (see Figure IV.2). For our 1 200 line/mm grating, the angle between the grating and the optical axis of the cavity is 27.9° for 780 nm and 27.4° for 767 nm, a range achievable by adjusting the mirror mount orientation. Although mode matching via fine-tuning the temperature is required, we found that

[4]Standard ECDL design (Aussibal [135])uses 40% reflectance gratings.

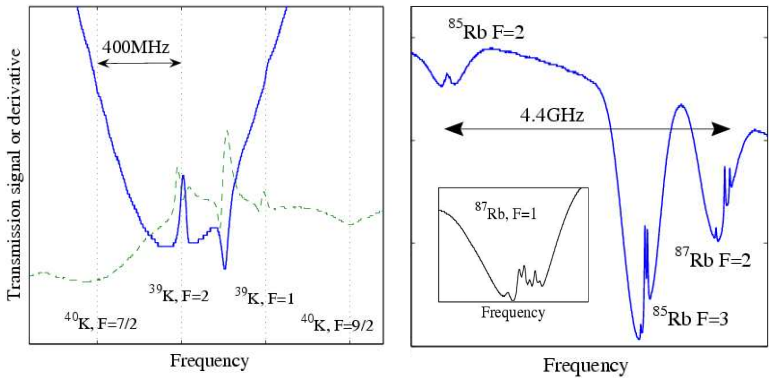

FIGURE IV.4 – **Saturated absorption spectra**

On the left: the spectrum of natural abundance potassium (93% ^{39}K), heated to about 60°C. The dashed curve is derivative of the saturated-absorption signal (solid curve). On the right: Natural abundance rubidium saturated-absorption signal (at room temperature). The free spectral range of the extended cavity is 5 GHz. Inset: narrow scan of ^{87}Rb, $|F = 1\rangle \rightarrow |F' = 0, 1, 2\rangle$ transitions. Each peak has a natural linewidth of 6 MHz.

the desired wavelengths can consistently be found between 18 and 25°C. Operating at 90 mA, the output power is about 40 mW.

The power output from the cavity can be up to 50 mW, more than 50% of the nominal power of the free running laser (when not AR coated). Running continuously at an output power between 30 and 50 mW, for the first 42 diode-months (30 000 hours) we have seen no spontaneous failures of the laser diodes and in the three years of operation, only one diode out of five died spontaneously.

Frequency locking For use in laser cooling, the MOs are frequency-locked to the corresponding atomic transitions using sub-Doppler saturated-absorption spectroscopy (Schawlow and Townes [139]). The spectroscopy module is designed to be compact and stable (Fig. IV.1(b)) and allows monitoring of the spectra of natural-abundance potassium and rubidium as shown in Fig. IV.4. The hyperfine lines have widths of order 6 MHz for both species, but the excited state energy levels of potassium are too close to be resolved (Santos *et al.* [140]). As expected, scans of more than about 5 GHz are interrupted by mode hops of the extended cavity. Longer continuous scans would be made possible by matching the change in cavity-length with a change in the grating angle, to adapt the frequency selective element to the center wavelength of the cavity.

For Zeeman-effect-modulation locking, a magnetic field directed along the optical path and oscillating at 60kHz is applied, shifting the m_F sub-levels. The error signal (derivative of spectroscopic signal) is generated using phase-sensitive detection, and then fed back via a proportional-integral loop to the master oscillator. The proportional signal is added to the laser diode current, and the integral signal to the voltage across piezoelectric element. The feedback loop has a bandwidth of roughly 1.5 kHz. In terms of long term use, we find that the ECDLs can be kept frequency-locked for many hours, and locking is limited by drifts of the room-temperature that are not

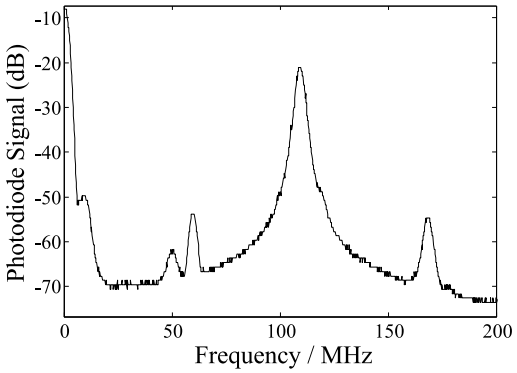

Figure IV.5 – **Beam-beating experiments, averaging of 64 measures during one minute**

The two beams are passed twice through acousto-optic modulators at 59.5 MHz and 114 MHz (taking the first diffraction order each time), giving a beat note at 109 MHz, plus some weaker beat notes due to unwanted diffraction orders in the double-pass AOM, or due to harmonics in the RF-driving electronics.

entirely compensated by the temperature lock, or external acoustic noise. Locking is consistently more stable on the potassium line since the spectrum contains broader features, so the capture range is larger for K than for Rb.

We also use a beat-note lock to frequency lock two lasers at a fixed frequency difference. We superimpose the two lasers on a fast photodiode. The resulting beat note is sent in a frequency to voltage converter. The output voltage is compared with a reference and the resulting signal is used for the proportional-integral locking loop.

Spectral width We have measured the linewidth of the MOs using a heterodyne measurement between two systems at 780 nm. The outputs of the two MOs were locked to the same atomic ^{87}Rb transition, then shifted by a few MHz with AOMs, and superimposed on a fast photodiode (see Fig. IV.5). The beat-note of two non-AR-coated ECDLs (with gratings which reflect about 40% into the first diffraction order) has a full width at half-maximum of 600kHz, i.e. each ECDL has a linewidth around 300 kHz (Le Coq [141], p39), if we assume that the line shape is Lorentzian. The beat note of one AR-coated and one non-AR-coated ECDL, was recorded using a multi-channel spectrum analyzer, as shown in Fig. IV.5. The full width at -30 dB was (22.3 ± 0.2) MHz, corresponding to a Lorentzian full width at half maximum of (706 ± 6) kHz. We therefore deduce that the frequency width of the ECDL with anti-reflection coated diode is around 400 kHz. We conclude that AR coating the diode and changing the grating does not significantly increase the linewidth. It is worth noting that in both cases, the linewidth of the laser is not limited by spontaneous emission (modified Schawlow-Townes limit, Schawlow and Townes [139], Henry [142]), but by additional technical noise (a detailed calculation of the modified Schalow-Townes limit for ECDLs is performed in appendix D).

2 Broadband Optical Power Amplifiers

The laser light coming out of the MOs is amplified by optical power amplifiers (OPAs). We use tapered amplifiers[5] (Ferrari *et al.* [143]), that offer significant gain in the same wavelength range as the master oscillators, $760 - 790\,\mathrm{nm}$. The OPAs are mounted in a compact self-contained mechanical housing (almost no adjustable parts) that allows very good temperature control of the chip and very good mechanical stability.

2.1 Construction

The mechanical supports hold the lenses to focus incoming light, to collimate the output light, and also to fix the position of the tapered amplifier chip. Our compact design places the chip in the middle of a copper block, which helps control the chip temperature (see Fig. IV.6). Technical drawings of a second-generation design are available[6]. Up to 10 W of heat from the amplifier are dissipated to the water-cooled copper base plate via a TE-cooler. An un-calibrated thermistor is used as a temperature sensor by the temperature control unit (see Fig. IV.7). Since the magnitude and wavelength variation of the gain vary significantly with temperature, the temperature of the amplifier is servo-locked. In addition, a calibrated thermometer is used for fault detection. The copper block also holds the contacts for the amplifier current supply. A lid can be bolted onto the base plate (of the second-generation

[5] *Eagleyard*, EYP-TPA-0780-00500-3006-CMT03, C-Mount 2.75 mm package
[6] http://atomoptic.iota.u-psud.fr/research/KRub/KRub.html

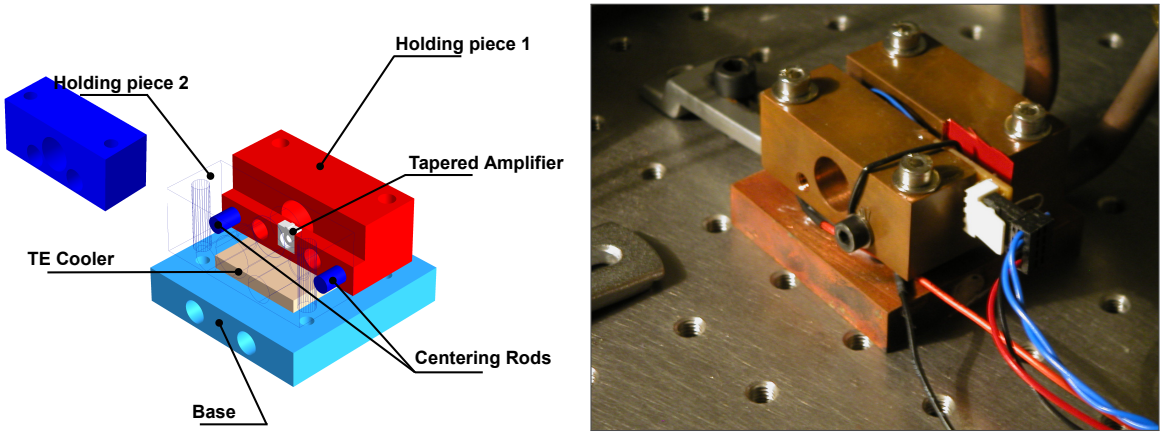

FIGURE IV.6 – **Mechanical and thermal housing for the tapered amplifier (First-generation design)**
Left: exploded diagram. The blocks are made of copper (the centering rods are of steel). Right: photograph of the assembled system.

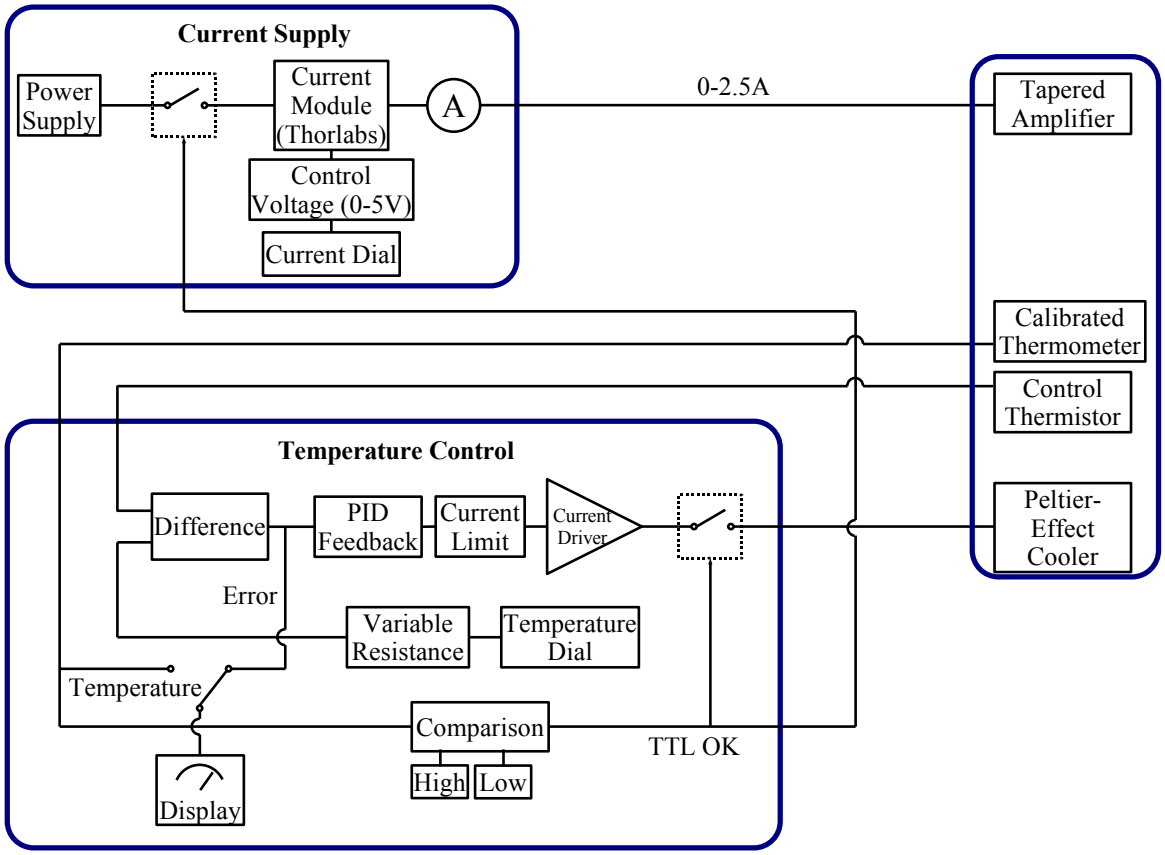

Figure IV.7 – **A Schematic diagram of the Electronics for the tapered amplifier**
If the temperature leaves a pre-defined range, the TTL-OK signal is cut, and both temperature control and current supply are switched off. The desired temperature and current are can be changed during operation, using dials outside the electronics boxes. Other adjustable parameters (e.g. PID gain, acceptable temperature) are optimized before operation. Circuit diagrams are available on http://atomoptic.iota.u-psud.fr/research/KRub/KRub.html.

design) to hold the chip under a water-free environment, so as to prevent condensation on the chip when it is cooled.

The electronic systems for the OPAs consist of a home-made current supply and a temperature stabilization unit, as shown schematically in Fig. IV.7. The power supply is based around a low-noise, 2.5 A current-supply module (*Thorlabs* LD3000). The temperature-control unit is based around a proportional-integral-derivative feedback loop, the output of which drives the TE-cooler. If the temperature of the chip is outside a defined range, both units shut down, leaving the block to return slowly to ambient temperature; the current-supply unit has a soft-stop mechanism to protect the amplifier; manual restart is required.

The output of the tapered amplifier is highly divergent and astigmatic. One axis is collimated using the lenses built into the copper mounting block; the other axis is corrected using a cylindrical lens. The beam is then passed through a telescope to produce a collimated beam of around 2 mm diameter, then sent through an optical

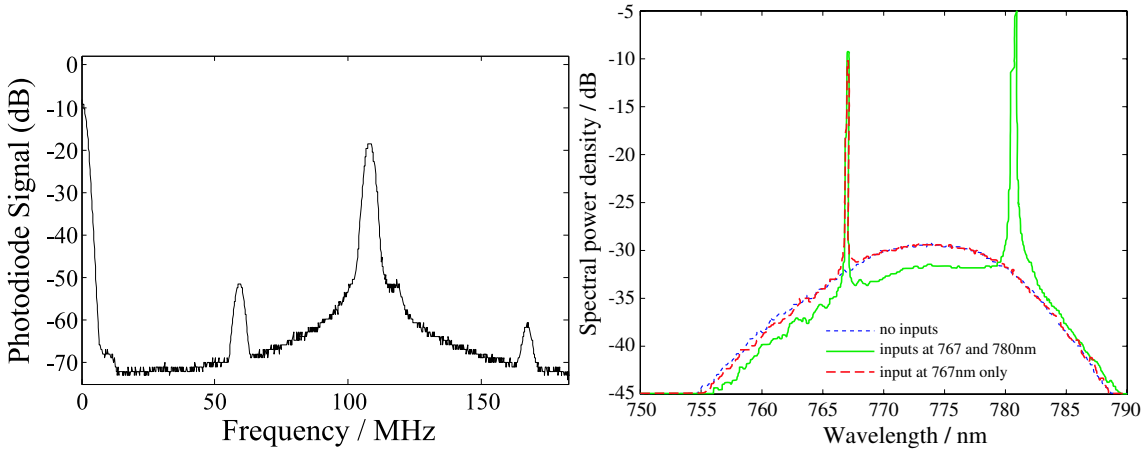

FIGURE IV.8 – **(a) Modulation of output-beam of tapered amplifier**
The same two beams used for the demonstration of the laser linewidth Fig. IV.5 were amplified, and the signal recorded. The spectrum is the average of 64 measurements during one minute.
(b) Output spectrum of tapered amplifier after an optical fiber
Two amplifiers were injected into the same fiber, one with an MO at 767 nm and one with an MO at 780 nm, each amplifier was stabilized at a temperature optimal for output power. Three curves show the total ASE (black, solid), the amplified MO at 767 nm with the ASE at 780 nm (red, dashed) and the sum of two amplified MOs at 767 nm and 780 nm (blue, solid). Linewidths and peak heights of amplified MOs are limited by the detector resolution of 0.1 nm. The ASE covers the region of high gain: 755 – 790 nm.

isolator. The light can be injected into one or more single-mode optical fibers with up to 60% efficiency (see Fig. IV.9(c)).

2.2 Performance of the amplifier

The amplified spontaneous emission (ASE) of the OPA is indicative of the gain spectrum, typically extending between 755 and 790 nm (Fig. IV.8(b), thick black line). For 5 mW of input power to an OPA, we observe around 400 mW of output power (19 dB amplification)[7]. In this range, the amplifier is below saturation intensity. However, when two beams of similar wavelength are injected into the same OPA, the output power is less than the sum of the outputs given when each beam is input individually (evidence of non-linear behavior).

When the same two beams used for measuring the linewidth of the MOs (Fig. IV.5) were injected, the amplified beat-note was not broadened: see Fig. IV.8(a).

[7]Tapered-amplifier chips are rapidly becoming more powerful. We have recently injected 3 mW of light and achieved output of 600 mW (23 dB amplification) at 780 nm. With the same chip we also managed fiber-coupling efficiency of 70%, i.e., more than 400 mW out of a monomode, polarization-maintaining fiber.

The spectrum is shown in Fig. IV.8(b). After injection in a fiber, the typical transmitted spectral power density of the background amplified spontaneous emission (ASE) is less than 2 mW per nm (equivalent to 4nW/MHz, or 24 nW per Γ). For rubidium with a beam of 1 cm^2, this corresponds to 10^4 scattered photons per second per atom for 200 mW of useful light. Much of the suppression of unwanted light is due to spatial filtering, particularly on entry to the fiber: the ASE has a different divergence to the amplified injected light. This background light may have some unwanted effects on certain atomics physics experiments (e.g. coherent atomic manipulation) but will be of negligible effect when near-resonance light is used (e.g. for laser-cooling experiments). The ASE can of course be cut off completely using shutters, when the amplified light is not desired. For far-off-resonance light (e.g. for optical-dipole traps) a warm rubidium cell can be used to filter the resonant light.

We have observed an average lifetime of our tapered amplifiers of approximately one year. This small compared to the two years life span often observed (Demarco [128]). We attribute this reduced life span to both the use of a 30 dB isolator at the output of the OPA (most groups use 60 dB isolators), and the cycling of the input power as we used the AOMs of the MOs to rapidly vary the optical power for our experimental needs. These shortcomings have been addressed in a second generation design.

3 Potassium-rubidium laser cooling bench

The MOs and OPAs described in the previous paragraphs are assembled to generate laser trapping and cooling light for potassium and rubidium (see Fig. IV.9).

3.1 First-generation design

In a first generation design, MOs are frequency-locked to an atomic transition using saturated-absorption spectroscopy, then shifted using an acousto-optical modulator (AOM). The AOM permits rapid control of the amplitude of the MO beam. We inject two MO beams of similar frequencies in an OPA chosen for its maximum gain frequency to match the injected frequencies. After appropriate beam shaping (see Fig. IV.9(c)), the output of the amplifier can be injected into one or more single-mode optical fibers with efficiencies up to 60% (typically 50%). Different MO beams are mixed using non-polarizing beam-splitters and the light injected in the fibers is multi-frequency. When necessary, we use first order waveplates specified for 773 nm to adjust the polarization of a bichromatic 767/780 nm beam. This design is very versatile, as the frequency-shifting of the MOs is independent from the amplification stage with the OPAs, and several MOs can be used to inject the same OPA. However, the limited efficiency of the AOMs and the division of optical power between several

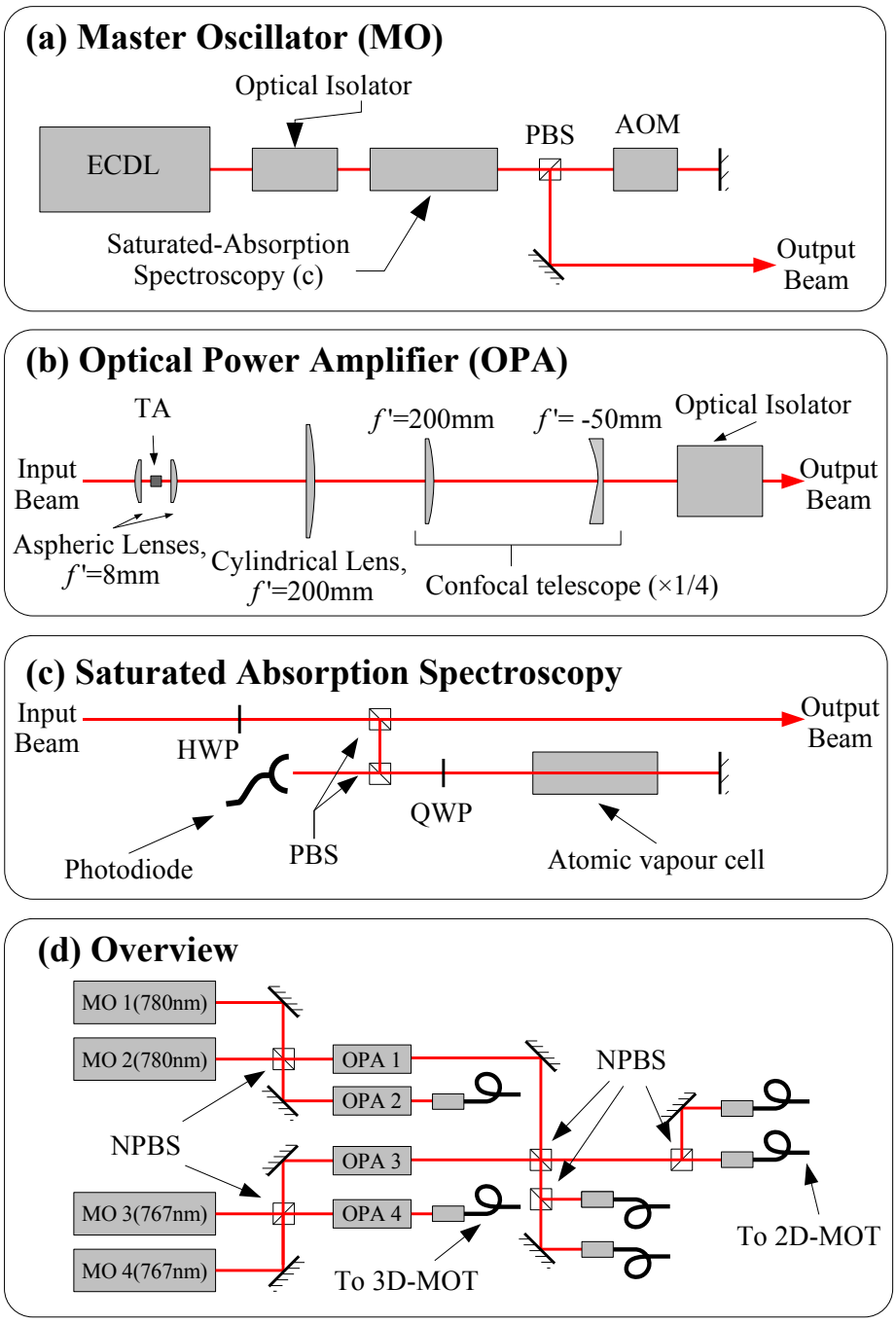

Abreviations used:

ECDL: extended cavity diode laser

PBS: polarizing beam splitter cube

NPBS: non polarizing beam splitter cube

AOM: acousto-optical modulator

TA: tapered ammplifier chip

HWP: half wave plate

QWP: quarter wave plate

FIGURE IV.9 – **Schematic of the laser sources for simultaneous trapping and cooling of rubidium and potassium (first-generation design)**

We use four MOs and four OPAs. For each species two separate MOs generate the trapping and repumping light. Both frequencies are mixed in a non-polarizing beam-splitter cube and injected in two OPAs, one for the 2D-MOT and the other for the 3D-MOT.
AOMs are used for rapid frequency and amplitude control. Small mechanical shutters in addition to the AOMs provide complete extinction. Each MO is equipped with the specific AOM required to shift its frequency from the saturated absorption feature to which it is frequency-locked, to the target atomic transition.
MOs and OPAs are suitable for both wavelengths (767 or 780 nm), but, as the gain spectrum varies from one chip to another, we cherry pick chips for the desired wavelength.
Adjustments made to this design in the second generation are discussed in §IV.3.

OPAs do not yield enough input power to the OPA to saturate it[8]. In such a situation, the overall output power is very sensitive to small mis-alignments in the MO. It varies from day to day as the angle of the grating of the ECDL is fine-tuned to compensate for small room-temperature drifts.

3.2 Second-generation design

In a second-generation design, out of two MOs injecting an OPA, only one is frequency-shifted, the repumping laser, and the other is sent directly to an OPA[9]. An AOM after the OPA shifts both frequencies. Part of the resulting beam is used to inject a second OPA. The frequencies of the two AOMs can no longer be chosen separately, but we strongly saturate the OPAs and we achieve more power with less maintenance. The second AOM is used for rapid control of the amplitude of the beam. The input powers of OPAs are not modulated. This should contribute to extending their life span.

We have found that the OPAs' mechanical supports are very stable: OPA injection only needs re-adjusting when the MO beam has been moved. The beam path after the OPA, including injection of a second OPA, or a fiber, very seldom needs re-optimization. Once the OPAs input-focusing and output-collimation lenses are in place, they never need to be moved.

A separate MO can be used to create a versatile low-power beam. For rubidium absorption imaging we use a MO frequency-locked to the trapping and cooling light via a beat-note lock. The laser frequency can be scanned over a few hundred MHz, e.g. for imaging in a strong magnetic field. We also use a non-amplified portion of the cooling laser for optical pumping.

The use of anti-reflection-coated diode lasers in an extended cavity has allowed us to extend the tuning range of ECDLs to the blue by several nanometers without significant broadening of the spectrum. Amplified with semiconductor optical power amplifiers, they form fully semiconductor room-temperature laser sources suitable for laser cooling of both potassium and rubidium.

[8] Even when not saturated, the OPA outputs 400 mW of optical power with 6 mW of input power. Saturation requires > 15 mW

[9] This scheme can be further improved by frequency-shifting the MO light in the saturated absorption spectroscopy beam path, and sending directly the main beam path to an OPA. We plan to implement this in the laser sources dedicated to potassium trapping and cooling.

Chapter V

Building a transportable boson-fermion coherent source

C'était une de ces machines d'express, à deux essieux couplés, d'une élégance fine et géante, avec ses grandes roues légères réunies par des bras d'acier, son poitrail large, ses reins allongés et puissants, toute cette logique et toute cette certitude qui font la beauté souveraine des êtres de métal, la précision dans la force.

La Bête Humaine – Émile Zola

This chapter describes the apparatus built during my PhD to cool atoms to degeneracy, and motivates the technical decisions made.

We built the apparatus, from the ground up, in an empty lab, and moved it from Orsay to Palaiseau half way through the construction. Technical choices on the experiment have been guided by the scientific goal of the project: pave the road to long-interrogation-time atom interferometry with degenerate atomic sources. Our first step was to develop scalable and robust laser sources suitable for laser cooling both species, a fully-semiconductor room-temperature laser system described in the previous chapter. In the atom-optics apparatus, care has been taken in the design and the construction to choose robust and compact solutions to make it possible to adapt the apparatus to an experiment in the Zero-G Airbus. We use a 2D-MOT as an atomic source and a fiber laser for the optical dipole trap. The large science chamber, very homogeneous magnetic field, wide field of view imaging have been designed with large expanding clouds in mind.

In this chapter, I go into the technical details of the design choices and the performance of the implementation. First, I discuss the design and performance of our laser-cooling stages: a 2D-MOT loading a 3D-MOT. Then I describe the compressible optical-dipole trap, and the coils used for Feshbach resonances. Finally I present how these components are assembled in a compact atom-optic apparatus, while leaving as much flexibility as possible.

Although the experiment has been designed to cool to quantum degeneracy a mixture of bosonic ^{87}Rb and fermionic ^{40}K, no work has been started on ^{40}K, and, at the time of the writing of this manuscript, Bose-Einstein condensation of ^{87}Rb has not yet been reached.

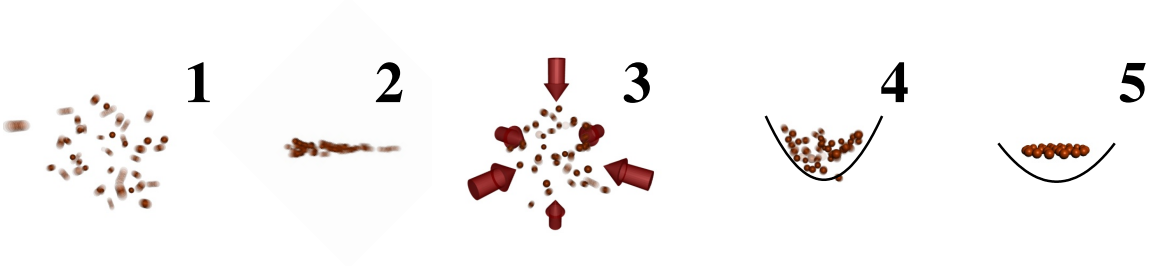

Figure V.1 – **Cooling to quantum degeneracy: the different steps**

1 A dilute atomic vapor is created in the collection chamber using alkali-metal dispensers.
2 A 2D-MOT transversally cools atoms to send a slow and collimated atomic jet in the science chamber.
3 A 3D-MOT captures the atoms in the jet and further cools them to $50\,\mu$K.
4 The atoms are transferred to a conservative optical-dipole trap.
5 Evaporative cooling is performed in the optical-dipole trap by lowering the depth of the trap to remove the most energetic atoms and waiting for rethermalisation.

Steps 1, 2 and 3 are described in §V.1, step 4 is described in §VI.1, and step 5 has not yet been experimentally achieved.

1 A 2D-MOT loading a 3D-MOT

We use the near-resonance semiconductor laser sources to laser cool the atoms and, from a dilute high-temperature vapor, prepare a dense and cold atomic cloud in a Magneto-Optical Trap (MOT). After this laser-cooling stage, the atoms are evaporatively cooled to degeneracy. Evaporative cooling is an atom-consuming process; it requires a high initial number of atoms to be efficient. This is more easily achieved when loading the MOT from a relatively high-pressure background atomic vapor. Evaporation is also a time-consuming process; evaporation time is limited by the rethermalization of the trapped cloud. However lifetime of the cloud in the trap is limited by collisions with the background vapor. These opposite constraints have lead to two-chamber designs in which a first, low-vacuum, chamber serves as a source of slow atoms to load a MOT in a second, high-vacuum, chamber.

In our apparatus, atoms are collected from dilute vapor and pre-cooled in a first low-vacuum chamber, then sent in a slow beam to a second ultra-high vacuum chamber (the science chamber) where they are captured by a MOT and will be evaporatively cooling to degeneracy (see Figure V.1).

To load our MOT in the science chamber, we need a high-flux collimated beam of atoms below the capture velocity of the MOT. A Zeeman slower (Metcalf and van der Straten [60]) is a proven solution that has been successfully used at the Institut d'Optique for many years on previous experiments. However, it is a bulky solution, as a tube long enough for the atoms to be slowed down from hypersonic velocities to MOT-capture velocities is needed. It is not suited for our compact design. Moreover, we plan to use an isotopically-enriched source of fermionic potassium. Such material

is very expensive[1]. An oven-based setup, such as a Zeeman slower, consumes a lot of material, and would be too costly to run.

Double-MOT systems are also widely used. In these apparatuses a high-background-pressure collection MOT allows fast accumulation of a high number of atoms, which are then transferred to the high-vacuum MOT in the science chamber. As the transfer process should not perturb too strongly the operation of the collection MOT, the achievable flux is limited. We chose to use a third solution: a 2D-MOT set-up to collect atoms from a background vapor and load the science chamber MOT. Unlike 3D-MOTs, 2D-MOTs are purposely unbalanced and do not aim to trap atoms, but simply to collimate an atomic jet. They have been demonstrated for ^{87}Rb to produce a flux of $9 \cdot 10^9\,\mathrm{atoms}\cdot\mathrm{s}^{-1}$ with low velocities (Dieckmann *et al.* [144]).

In this section I develop simple models for the capture process of an atom in a 3D-MOT and the collimation in the 2D-MOT to estimate the capture velocity of the 3D-MOT and the velocity distribution of the atomic jet loading it. Then I discuss the dependence of the number of atoms captured in the 3D-MOT on the experimental parameters. I will mainly base my discussion of the laser-cooling stages of the apparatus on Doppler cooling and trapping of the rubidium atom, as we have not yet worked with potassium on the experiment. The physical processes involved are similar, although a few constants like the mass of the atom change.

1.1 Estimation of the capture velocity of a MOT

In a MOT, atoms are trapped using the radiation pressure of near-resonance lasers. Briefly[2], the lasers communicate momentum to the atoms via photon scattering. As the scattering cross-section depends strongly on frequency near an atomic resonance, this radiation pressure force is rendered velocity-dependent through the Doppler effect, and position-dependent by the Zeeman shift created by a magnetic gradient. In a 3D-MOT, the total force resulting from six laser beams coming from all principal directions damps and traps the atom.

Several different experimental parameters come into play when designing a MOT with the goal to capture as many atoms as possible from an atomic beam:

- $\boldsymbol{r_c}$ the radius of the laser beams. It defines the size of the region in which the atoms are subject to the MOT force, we use 1.25 cm.

- $\boldsymbol{I}$ the laser intensity. The relevant dimensionless parameter for the atoms is the saturation parameter: $s_0 = I/I_{\mathrm{sat}}$ where I_{sat} is the atomic transition saturation

[1] Roughly $3000 per 100 mg, available from Trace Sciences

[2] Laser cooling and trapping of atoms has been reviewed in many theses. I will not discuss the physics and processes involved. The reader is invited to refer to Metcalf and van der Straten [60] or Dalibard [145] for a lecture on the subject.

intensity, $I_{\mathrm{sat}} = 1.6\,\mathrm{mW}\cdot\mathrm{cm}^{-2}$ for the rubidium laser cooling transition. We have a 25 mW of laser light per beam[3], and $s_0 \sim 3$.

$\boldsymbol{B_x}$ the magnetic gradient, typically $15\,\mathrm{G}\cdot\mathrm{cm}^{-1}$ in MOTs.

$\boldsymbol{\delta_0}$ the laser detuning to the atomic transition. The relevant parameter is $\Delta_0 = 2\delta_0/\Gamma$, with Γ the linewidth of the transition. Typically $\Delta_0 \sim 2.5$.

B_x and δ_0 can be easily tuned experimentally to the optimum value, but the choice of the beam size is more of an a priori decision as it determined by the size of the optics used. In real-world experimental situation, the available total power is limited and the choice of beam size determines the intensity. It is well known that increasing the beam size can strongly increase the number of trapped atoms (Lindquist *et al.* [146]), but day-to-day observations in the lab show that decreasing the laser intensity is detrimental to the number of atoms. Where does one strike the balance? Given our experimental parameters, will adding an OPA to the experiment to double the available power also double our number of atoms?

The literature on MOTs is abundant (Chu [56], Metcalf and van der Straten [60] amongst many others) and their loading process has often been discussed (Lindquist *et al.* [146], Muniz *et al.* [147], Aubin *et al.* [148], Rapol *et al.* [149]). However, the increase in available laser power has drawn modern experiments in a regime that has not, to my knowledge, been explored in published systematic studies[4]; moreover I have not found a simple analytic model for the capture process that gives the dependence of the capture velocity in laser intensity. Using a minimalistic Doppler model of our MOT and numerical simulations as a guide, the scaling laws can be estimated.

Steady-state number of trapped atoms

The trap can be described by both a loading process, in which ballistic atoms are slowed and captured in the MOT, and loss processes. The steady-state number of trapped atoms is given by the balance between those two processes.

The loading process is characterized by a capture velocity: an atom is captured if its velocity is small enough for it to be slowed to a near stop as it passes through the MOT region. The loading rate is then given by the number of atoms entering the MOT region with a low enough velocity. As we load from a beam, it is then the fraction of the beam with a velocity below the capture velocity.

Loss processes consist of collisions, both with background vapor pressure, and between trapped atoms. They are characterized by an escape velocity: after a collision, an atom will be lost if it has gained enough momentum to leave the trap.

[3] An aging OPA and a worn-out AOM have reduced the power per beam to 5 mW at the time of the writing. This is temporary, but is an illustration of the degree to which laser power can vary as components grow old or mis-aligned.

[4] Bagnato *et al.* [150] have studied trapping processes (specifically capture velocity) with high laser intensities, but their experimental conditions do not relate to most experiments (beam diameter of ~ 12 mm and detuning of $\sim \Gamma$).

If we suppose the escape velocity and the capture velocity are equal, a high capture velocity is critical to achieve both high loading rates, and low losses. However, loss-inducing collisions between trapped atoms are mainly due to light-assisted collisions, and the collisional cross-section depends on the laser light characteristics. For a large number of trapped atoms, the highest steady-state number of atoms is not achieved for the maximum capture velocity as many-body effects (multi-atomic photon scattering, light-assisted collisions) dominate.

The Doppler model of the force

An atom captured in a MOT experiences opposite radiation-pressure forces from counter-propagating lasers. In a simple one-dimension two-level-atom Doppler-cooling model, the expression of the resulting force is (see e.g. Dalibard [145] for a derivation of this model):

$$F_{\mathrm{MOT}} = \frac{\hbar\,\Gamma\,k_{\mathrm{MOT}}}{2}\left(\frac{s_0}{1+s_0+\Delta_+^2} - \frac{s_0}{1+s_0+\Delta_-^2}\right) \tag{V.1}$$

with

$$\Delta_\pm = \frac{x}{x_0} - \frac{v}{v_0} \mp \Delta_0$$

where x_0 and v_0 are a typical position and velocity scale given by the magnetic field gradient and the Doppler shift:

$$x_0 = \frac{\Gamma}{2}\frac{1}{\mu\,B_x} \qquad\qquad v_0 = \frac{\Gamma}{2}\frac{2\pi}{k} \tag{V.2}$$

Simple picture of the dynamics in the MOT

The behavior of a MOT can be understood by separating it in two different spatial regions:

The central region At the center of the trap (the zero of magnetic field), the opposite radiation pressures of counter-propagating lasers cancel out for an atom standing still. For small atomic velocities ($v \ll v_0$), the position and velocity dependencies of the total force can be linearized, and the motion of the atoms can be described as that of a damped harmonic oscillator. The MOT behaves as optical molasses with a small restoring force.

The outer region Away from the center of the trap, the MOT behaves as a Zeeman slower. In this region, the detunings $\Delta_\pm$ are large for atoms with small velocities. In a first approximation, it can be said that these atoms do not see any force. The interesting dynamics happen when moving atoms come into resonance with a laser, for $\Delta_\pm \sim 0 \Leftrightarrow v \sim v_0\frac{x}{x_0}$. Atoms can be deflected by the laser. They are then slowed as in a Zeeman slower: their velocity decreases, but they stay close to resonance as they move in the magnetic field (see figure V.2). Their

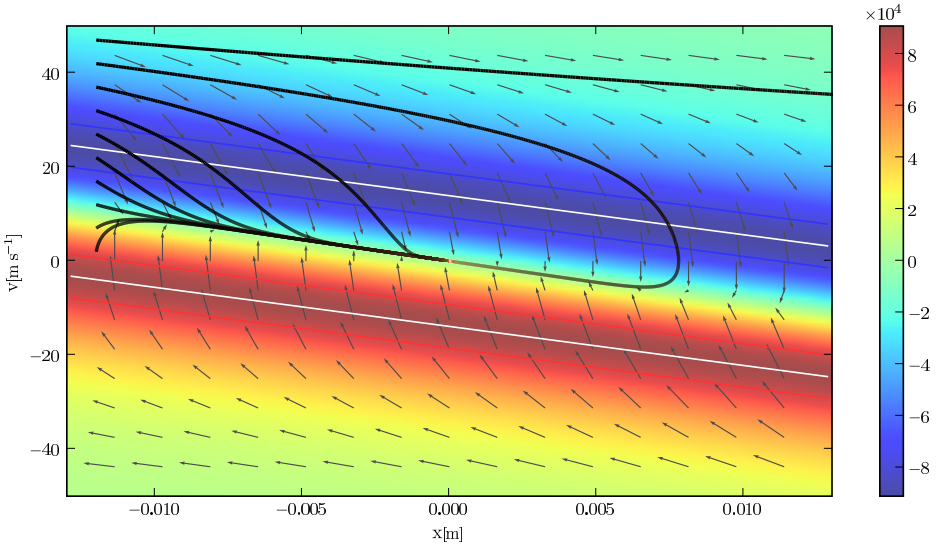

Figure V.2 – **Phase portrait of some trajectories of atoms captured by the MOT**
The color scale represents the intensity of the MOT force directed along the x axis. The two resonance lines (one for each laser) are plotted in white. A sample of numerically integrated trajectories is plotted in black. The dynamical flow[a] is represented by arrows.
Along the diagonal, between the two resonance lines, lies the zone where the radiation pressure forces of the two lasers balance each other. The force is zero there and the atoms entering the MOT region with a low enough velocity are captured in this region and brought to the center of the MOT. Atoms that have a high enough initial velocity do not cross the resonance line of the laser facing them. They are not trapped and escape the MOT at the other end.

[a]The flow is the function that computes the time-derivative of the phase-space vector, as a function of position in phase-space. When looking at the evolution of the system in phase-space, the flow can be viewed similarly to the hydrodynamical flow, carrying particles with it.

dynamics is given by: $v \sim v_0 \frac{x}{x_0}$, and they follow the line of resonance in the (x, v) plane until they enter the central region where they are trapped and cooled (see Figure V.2).

Capture velocity

Capture when resonant with the counter-propagating laser An incoming atom can be captured, if, when it crosses the resonance line of the counter-propagating laser, it is deflected and slowed enough for its changing Doppler shift to compensate the changing Zeeman shift as it move in the magnetic field gradient. This condition can be written $dv \leq \lambda \mu B_x \, dx$. If the atom is not slowed enough, it will escape from the resonance with the laser, the radiation pressure force will decrease, and it cannot be slowed down to be trapped. Using $m \, v \, dv = F \, dx$, we find that the force has to be at least $F_{\text{deflect}} = m \lambda \mu B_x \, v$. On the resonance line, the force is given by $F_{\max} \sim \frac{1}{2} \hbar \Gamma \, k_{\text{MOT}} s_0$.

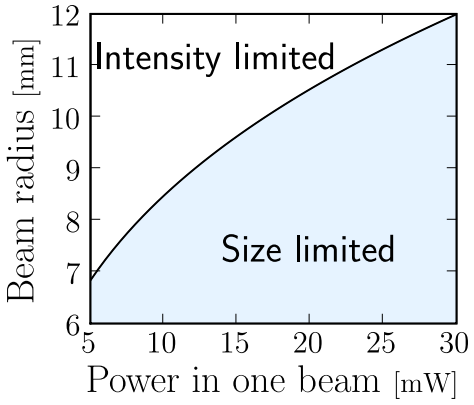

FIGURE V.3 – **Limiting factor for the capture velocity**
Numerical parameters describing our experimental setup have been used for this plot. In the intensity-limited region, the intensity is not large enough and atoms can cross a resonance line on the border of the trapping region without being deflected enough to be trapped. In the size-limited region, all the atoms crossing a resonance are trapped and the capture velocity is limited by the maximum Zeeman shift achieved in the trapping region. The line delimiting the two regions is given by the condition $F_{\text{deflect}} = F_{\text{max}}$

The highest velocity the resonance condition $\frac{v}{v_0} = \frac{x}{x_0} + \Delta_0$ can be achieved at the edge of the trapping region, for $x = r_c$. In most current setups, the intensity of the lasers is sufficiently high, and the trapping region sufficiently small[5], for the radiation pressure at resonance to deflect these atoms (see Figure V.3); the capture velocity is limited by the size of the trapping region and not by the maximum possible deceleration.

This leads to a commonly accepted (Metcalf and van der Straten [60]) expression of the capture velocity:

$$v_c \sim \lambda(\mu\, B_x\, r_c + \delta_0) \tag{V.3}$$

This expression is a good model to evaluate the capture velocity for an experimental situation and gives the right orders of magnitude. However, it cannot be used to tune δ_0 or B_x for optimum atom numbers, or even capture processes, as it does not reflect the breakdown of the damping process in the central region of the MOT for large B_x and δ_0.

Power broadening In most experimental conditions, the capture velocity is not limited by the intensity: the acceleration communicated by the lasers to the atoms at resonance is more than enough to capture them. At intensities higher than the saturation intensity, the resonance is broadened (power broadening) and the resulting width, expressed in corresponding Doppler shifts, is not negligible compared to v_c (as illustrated by four of the capture trajectories shown in Figure V.4). The deflection condition can be met for atoms not strictly resonant with the counter-propagating laser, but with velocities above the resonant velocity (see Figure V.2). This condition gives a more precise expression for the capture velocity, that we shall call v_C. v_C is given by the solution to:

$$F_{\text{MOT}}(r_c, v_C) = F_{\text{deflect}}(v_C) \tag{V.4}$$

No simple analytical expression can be derived from this third-order equation, but a graphical resolution, shown in Figure V.4, gives a good understanding of the dependency on the experimental factors.

[5] Achieving large beam-sizes is impractical as large mirrors are expensive, and the size of the quadrupole coils limits the extent of the magnetic field gradient.

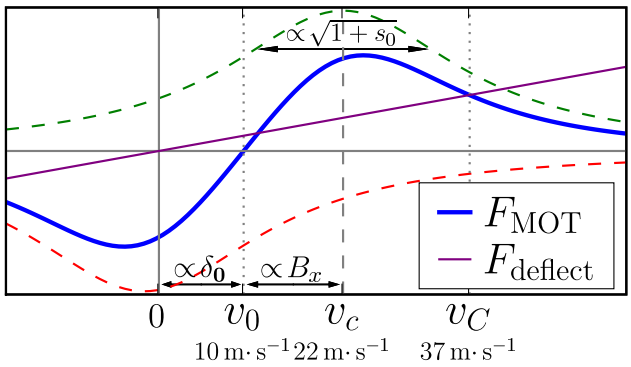

Figure V.4 – **Velocity dependence of the MOT force**
The forces due to the co- and counter-propagating lasers are plotted with dashed lines. The forces are plotted at $x = r_c$. The force F_{deflect} required to deflect and capture an atom is the solid straight line. The capture velocity as we define it, v_C, is given by the largest intersection of F_{MOT} and F_{deflect}. Numerical values are given for our MOT parameters.

The velocity dependence of the MOT force is given by the two Lorentzian-shaped resonances of the two counter-propagating lasers. First of all, the detuning δ_0 should be taken on the order of $2\Gamma\sqrt{1+s_0}$, twice the width of the broadened resonance, in order for the counter-propagating lasers to be shifted enough for their forces not to cancel each other. The optimum value of the magnetic field gradient is dictated by dynamics and collisions in the inner region of the MOT, the cloud itself, and cannot be explained by this simple approach. Finally, the dependence in intensity, all other parameters constant, adds to equation V.3 a factor due to power broadening of the atomic resonance close to $\Gamma\sqrt{1+s_0}$ as long as the detuning is large enough to consider that the Lorentzian of one laser is only weakly affected by the opposite laser. Numerical results given by this toy model are confirmed by our simulations. They also correspond to experimental estimations found in the literature.

Assuming the detuning optimized to follow the power broadening, an estimate of the capture velocity is given by:

$$v_C = \lambda(\mu\, B_x\, r_c + K\,\Gamma\sqrt{1+s_o}) \tag{V.5}$$

with $K \sim 3$, a numerical factor given by the impact of the power broadening on both the optimal detuning and the deflection of off-resonance atoms. This expression suggests that to maximize capture velocity, with a given laser power, the optimum between intensity and beam-size lies for large beams and low intensity, most probably at the limit of the intensity limited regime (see Figure V.3). However, large beams can only be achieved through bulky expansion and free propagation. For our 3D-MOT, we can use beam sizes up to a diameter of 22 mm.

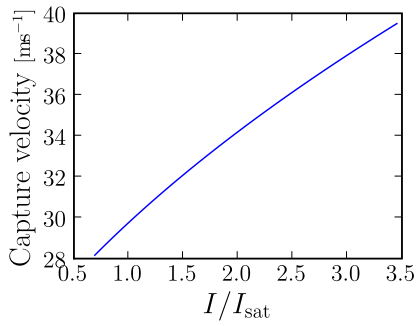

Figure V.5 – **Capture velocity,**
estimated as a function of the intensity in one beam of the MOT. The values for $I < I_{\mathrm{sat}}$ should be considered with caution, as the model does not reflect the breakdown of the cooling process at the center of the MOT for low saturation intensity.

It should be noted that the simplifications made to the atomic level scheme do not account for depumping mechanisms and hence lead to an overestimation of the absolute value of the radiation pressure force. The overestimation for the capture velocity is however small, as, in the regime discussed here, the main limit for the capture velocity is not the force maximum value but its variation with the Doppler shift.

This small model shows why increasing the intensity, even if it is well above the saturation intensity, can still have a significant influence on the capture velocity of a Doppler-cooling process (see Figure V.5): with intensity above saturation intensity, power broadening relaxes the resonance condition which can be matched for atoms with larger Doppler shift. As the number of incoming atoms with a velocity v can go up quickly[6] with v, even a small variation in capture velocity can make a big difference on the number of trapped atoms. As we load our MOT from an atomic beam, we need an estimation of the velocity distribution of the beam to evaluate the variation of the number of captured atoms as the capture velocity changes. The model shows that, at high intensities, the relevant intensity is not the mean intensity over the beam nor the maximum intensity, but, for limited-size beams, the intensity on the edge. The $1/e^2$ diameter of the Gaussian beam should thus be chosen to maximize this intensity, as long as the intensity in the center is kept above saturation intensity, as the cooling process in the center of the trap is inefficient at low intensities for high numbers of atoms.

1.2 Estimation of the velocity distribution of the atomic beam

A 2D-MOT uses laser cooling and trapping in two (lateral) directions to collimate a beam of atoms in the center of the collection chamber. The atoms are not cooled in the third (longitudinal) direction and escape the cloud. A small tube between the collection chamber and the science chamber allows the escaping atoms with a slow enough lateral velocity to reach the science chamber and form the atomic beam (see Figure V.6).

[6] For a thermal distribution, at low velocities, the number of atoms scale as v^3.

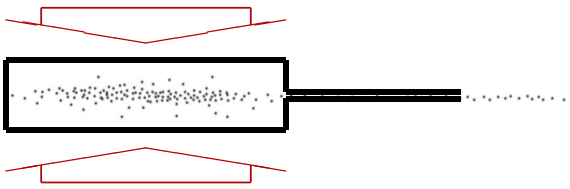

FIGURE V.6 – **Principle of a 2D-MOT**
Transverse Doppler cooling collimates a beam of atoms. Thermal background is filtered by a differential-pumping tube.

Collimation and filtering process

Even though the escaping atoms are not cooled longitudinally, the small exit tube operates a selection on the longitudinally slow atoms. Indeed, for the atoms to go through the tube without hitting a wall, they need to be both well centered on the axis of the tube and to have a velocity collinear to the axis. In the case of atoms transversally trapped and cooled, these conditions are achieved for atoms having spent enough time in the cooling region interacting with the lasers. As the cooling region has a finite length, this requires that the escaping atoms longitudinal velocity is be small enough.

A model of the force can be used to integrate the trajectory of atoms in the 2D-MOT region. The output beam can be described by selecting the atoms entering the exit tube with low enough transverse velocity. This approach underlies the theoretical description introduced in Schoser *et al.* [151] and further explored in Schweikhard [152], Petelski [153].

Briefly, the exit conditions through the output tube are expressed in terms of a condition on the initial transverse velocity of atoms captured in the 2D-MOT, thus defining a critical transverse initial velocity. The flux is then deduced by integrating over a thermal distribution and the scaling laws describing its dependence on several experimental parameters are derived. Although the authors do not calculate explicitly the integral, the exact calculation is possible with the model they use. However the resulting longitudinal velocity distribution of the output beam does not match the experimental curves. Moreover the model does not predict the dependence of the mean velocity in the exit tube dimensions. The analytic scaling laws for the mean velocity as a function of the 2D-MOT parameters are hard to extract from the exact result. A more detailed study shows that they do not depend on the details of the model used to describe the trapping and cooling in the laser field. On the other hand, numerical simulations have been performed that give good agreement with experiments (Chaudhuri *et al.* [154]).

We have observed on our setup a strong dependence on the flux of atoms captured by the 3D-MOT in the intensity of the 2D-MOT lasers. Experimentally we note a threshold at $I/I_{\text{sat}} \sim 1$. We would like to understand this behavior, in order either to improve the design, or to set the requirements on the lasers.

I will describe a simple model of the 2D-MOT cloud and of the output beam, trying to bring into light the dependence of the velocity distribution of the output beam in 2D-MOT geometrical parameters, output tube dimensions, and laser intensity.

1.2.1 Collection in the 2D-MOT chamber

Due to its elongated shape and to the absence of trapping in the longitudinal direction, the 2D-MOT cloud is loaded from the sides. Atoms escape at both ends. The flux of atoms exiting at one end is given by the flux of atoms captured by the transverse cooling process.

Capture conditions An atom with a non-zero longitudinal velocity v_z entering the laser-cooling region at a position z spends a time z/v_z in this region. It can be captured by the Doppler-cooling mechanism only if its initial transverse velocity v_r is below the capture velocity, as defined in §V.1.1. If we suppose the capture process takes a time τ independent of the initial transverse velocity, the atom is captured if $z/v_z < \tau$. This assumption holds both for a critically damped oscillator model, as used in previous models, or for an exponential damping of position and velocity as arises if the atoms follow the resonance line as described in §V.1.1. In both cases, $\tau \sim \frac{x_0}{v_0} \sim 1\,\mathrm{ms}$.

Velocity distribution For a given longitudinal velocity class, the flux of atoms coming out of one end of the cloud is given by:

$$\Phi(v_z) = \int_{z=0}^{l} \int_{v_r=0}^{v_c} \underbrace{v_r\, n\, B_T(v_r, v_z)}_{\substack{\text{flux per surface} \\ \text{element}}} \cdot \underbrace{\begin{cases} 1 \text{ if } z/v_z < \tau \\ 0 \text{ otherwise} \end{cases}}_{\text{Capture condition}} \cdot \underbrace{2\pi v_r dv_r}_{\substack{\text{polar} \\ \text{coord.}}} \underbrace{2\pi\, r_c}_{\substack{\text{2D-MOT} \\ \text{perimeter}}} \; dz \qquad \text{(V.6)}$$

where B_T is the Maxwell-Boltzmann distribution[7] and l is the length of the cooling region. As the range of transverse velocities explored is small ($v_c \sim 30\,\mathrm{m}\cdot\,\mathrm{s}^{-1}$), the variation of the Maxwell-Boltzmann pre-factor over the integral can be neglected.

Collisions in the cloud have been neglected in expression V.6. Not all atoms entering the 2D-MOT cloud reach the end of the cloud. The simplest model for adding collisions is to assume a velocity-independent collision rate, Γ_{coll}. Following Schoser *et al.* [151], we assume collision losses are mainly due to light-assisted collisions between an atom in the beam and an atom in the background vapor: $\Gamma_{\text{coll}} \sim n\langle v\rangle\sigma$ where n is the background vapor density, $\langle v\rangle$ is the mean thermal velocity, and σ is the light-assisted collision cross section, inferred from 3D-MOT lifetimes, $\sigma \sim 2 \cdot 10^{-12}\,\mathrm{cm}^2$. At $10^{-7}\,\mathrm{mBar}$, $\Gamma_{\text{coll}}(n) \sim 0.12$. This yields a correction to the flux going as $\exp(\Gamma_{\text{coll}}(n)\frac{z}{v_z})$. The flux integral can be written:

$$\Phi(v_z) = 2\pi\, r_c\, n\, B_T(v_z) \int_{z=\tau v_z}^{l} \exp\left(\Gamma_{\text{coll}} \frac{z}{v_z}\right) \int_{v_r=0}^{v_c} 2\pi v_r^2 dv_r dz \qquad \text{if } v_z < l/\tau \qquad \text{(V.7)}$$

and $\Phi(v_z) = 0$ if $v_z > l/\tau$.

Thus:

$$\Phi(v_z) = 4\pi^2\, v_c^3\, r_c\, n\, (\pi v_{\max}^2)^{-3/2} e^{-v_z^2/v_{\max}^2} \left(e^{-\Gamma_{\text{coll}}\tau} - e^{-\Gamma_{\text{coll}} l/v_z}\right) \frac{v_z}{\Gamma_{\text{coll}}} \qquad \text{(V.8)}$$

Neglecting the variation of the Maxwell-Boltzmann distribution over $v_z \in [0,\, l/\tau]$, assuming $\Gamma_{\text{coll}}\tau \ll 1$, this expression can be described by a linearly decreasing dependence on v_z: $\Phi(v_z) \sim (l - \tau v_z)$ for $v_z > \Gamma_{\text{coll}} l$, and $\Phi(v_z) = 0$, for $v_z < \Gamma_{\text{coll}} l$ and $v_z > l/\tau$ (see Figure V.7). The low velocity gap is due to the collisional thickness of the cloud: atoms with too slow a velocity cannot go through the cloud. The linearly decreasing tail is due to the finite length of the cooling region.

[7] $B_T = (\pi v_{\max}^2)^{-3/2} \exp\left(-\frac{v_r^2 + v_z^2}{v_{\max}^2}\right)$ with $v_{\max} = \sqrt{2kT/m}$.

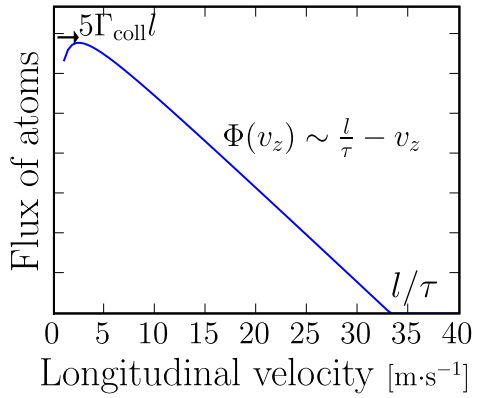

Figure V.7 – **Velocity distribution for atoms exiting the cloud**
The small longitudinal velocity of the atoms exiting the cloud is only due to the finite cooling length. As this is before the exit hole, there is no velocity selection by the output tube.

If $\Gamma_{\text{coll}}l$ is small compared to the mean longitudinal velocity[8], equation V.8 can be simplified to ($e^{-\Gamma_{\text{coll}}\tau} \ll 1$):

$$\Phi(v_z) \propto v_z - \frac{l}{\tau} \tag{V.9}$$

1.2.2 Output atomic beam

Filtering by the exit tube

Divergence of the beam We can assume that the transverse velocity distribution of the atoms captured in the 2D-MOT is given by a thermal distribution at the Doppler limit temperature. This assumption neglects any relationship between the transverse velocity and the time spent in the cooling region, as long as the atom is captured. We suppose that the cooling time is small compared to the trapping time. This holds because the trapping time $\tau \sim 1\,\text{ms}$ (as both suggested by the capture model and observed experimentally in Schoser *et al.* [151]) is dominated by the time required to bring an atom from the periphery of the 2D-MOT to the center, whereas, once the atoms is in the central region, the cooling time is due to the scattering of photons, with a frequency $\sim \Gamma/(2\pi) \sim 6\,\text{MHz}$. Even though many photons need to be scattered for the Doppler limit to be reached, the time scales are very different.

The width of the beam after a propagation on a distance d is given by:

$$w(d) = \Delta v_r \int_{v_z} \frac{d}{v_z} \Phi(v_z) dv_z \tag{V.10}$$

where $\Delta v_r \sim 0.3\,\text{m}\cdot s^{-1}$ is the Doppler-limit velocity width. This expression yields an angular beam divergence (defined as the *full* angle of the cone made by the beam) of:

$$\delta\alpha = \frac{\tau}{l}\Delta v_r\Big(-1 - log(\Gamma_{\text{coll}}\tau)\Big) \tag{V.11}$$

Using numerical values from Schoser *et al.* [151], we find a beam divergence of 26 mrad, in good agreement with the 32 mrad measured on the experiment. One can note that, as in a Zeeman-slower, the slowest atoms contribute most to the divergence.

[8]This assumption breaks down for long setups, or with a high background pressure

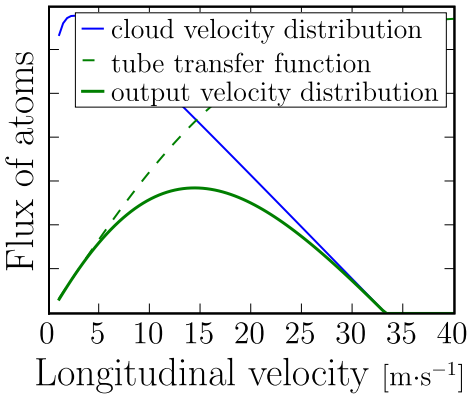

FIGURE V.8 – **Velocity distribution of the output beam**
The output tube filters the atoms with a low longitudinal velocity that spread more transversally over a given propagation distance. Parameters describing our setup were used in these plots.

Velocity distribution of the output beam As the output tube has a limited acceptance angle[9] of α, it filters out the wings of the lateral thermal distribution that extend past its acceptance. The lateral position distribution for atoms with a longitudinal velocity v_z, after a propagation of d, is given by a Gaussian of width $\Delta v_r d/v_z$. The transfer function of the tube is thus:

$$T(v_z) = \mathrm{erf}\Big(\frac{\alpha}{2}\frac{v_z}{\Delta v_r}\Big) \underset{v_z\to 0}{\sim} \frac{\alpha}{\sqrt{\pi}}\frac{v_z}{\Delta v_r} \tag{V.12}$$

The velocity distribution of the atoms coming out of the tube is given by the product of the input flux $\Phi(v_z)$ and the transfer function $T(v_z)$ (see Figure V.8).

As the cloud has a finite size, the limited entrance size of the output tube can also filter atoms from the jet. If we assume that the position of an exiting atom is not correlated to its velocity, neither transverse not longitudinal, we can assume that the size of the entrance hole of the tube limits the flux if it is smaller than the size of the cloud ($\sim 1.5\,\mathrm{mm}$). In this regime the loss of atoms can be approximated to the ratio of the areas of the hole and the cloud[10]. We use a 1 mm-diameter hole, and probably over-filter the atoms.

Effect of a deflection Atoms are subject to spurious forces on their output trajectory. These include the effect of gravitation but also magnetic gradients, and any imbalance in the radiation pressure forces near the entrance of the tube. Supposing that the effects of these forces after a propagation over a distance d can be described by both a transverse velocity kick v_0 and an acceleration g, the expression of the tube transfer function is:

$$T(v_z) = \frac{1}{2}\left(\mathrm{erf}\Big(\frac{\alpha}{2}\frac{v_z}{\Delta v_r} - \frac{v_0}{\Delta v_r} - \frac{1}{2}\frac{g\,d}{v_z\,\Delta v_r}\Big) - \mathrm{erf}\Big(-\frac{\alpha}{2}\frac{v_z}{\Delta v_r} - \frac{v_0}{\Delta v_r} - \frac{1}{2}\frac{g\,d}{v_z\,\Delta v_r}\Big)\right) \tag{V.13}$$

[9] The acceptance angle that we consider is defined by the angle of the cone of straight trajectories going through the output tube and starting from the tip of the atomic cloud, and not from the entrance of the tube. The further away from the tube the 2D-MOT region stops, the smaller this angle.

[10] A better description could approximate the shape of the cloud as being Gaussian. This would yield an dependence in $1 - \mathrm{erf}(r_{\mathrm{cloud}}/r_{\mathrm{hole}})^2$.

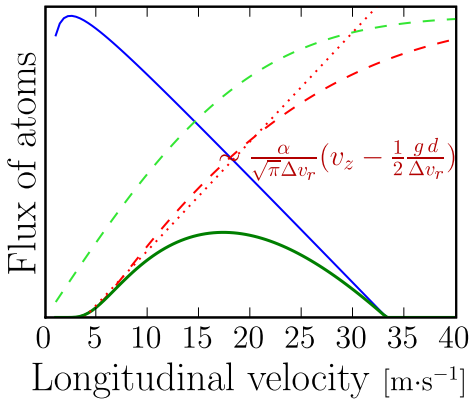

Figure V.9 – **Effect of an acceleration**
The red dashed curve is the transfer function for the output tube of our setup, taking in account the deviation due to gravity. The blue curve is the 2D-MOT velocity distribution, the green dashed curve the transfer function with no deflection, and the thick green curved the output flux, taking into account the effect of gravity.

As can be seen on figure Figure V.9, an uncontrolled deflection out low-longitudinal-velocity atoms, thus reducing the flux and increasing the mean velocity.

Dependence on intensity

Variation of the capture time It seems reasonable to suppose that the time required to trap an atom depends on intensity: the higher the intensity, the higher the radiation pressure force, thus the quicker the atom is brought to the center of the trap. At high saturation parameter, the capture mechanism, as discussed in §V.1.1, relies on capturing the atoms near a resonance line. Following the resonance line imposes $v \sim \frac{v_0}{x_0}x$, therefore $\tau \sim \frac{x_0}{v_0}$, which is independent of the intensity. Indeed, this capture process does not involve resonant forces, but mainly the balance between the two counter-propagating lasers (see Figure V.10).

However, at low saturation parameter, the capture process of a MOT resembles that of a strongly damped harmonic oscillator. The forces involved are too weak to stop the atom in its first pass; it can cross the center region before being slowed enough to be trapped (see Figure V.11(a)). For a damped harmonic oscillator close to the critical regime, the relaxation rate of the envelope of the trajectories is half the damping time: $\tau = \frac{1}{2\gamma}$. In our case the damping factor is given by the expansion of the Doppler force (see eg Dalibard [145], Metcalf and van der Straten [60]):

$$\frac{1}{\gamma} \sim \frac{m}{\hbar\, k_L^2}\frac{1}{s} \tag{V.14}$$

It is inversely proportional to the saturation parameter, therefore in this regime we can assume $\tau \sim 2t_0/s$ where t_0 is derived from equation V.14. For rubidium, $t_0 \sim 20\,\mu$s.

If the intensity is too low, the lasers cannot transfer enough momentum to the atom to stop it in the $2r_c$-long region where the force applies. A simple energy-balance calculation yields the saturation parameter s_{crit} for which atoms no longer can be stopped:

$$s_{\text{crit}} = \frac{m\, v_c^2}{2\, r_c\, \hbar\, k\, \Gamma} \tag{V.15}$$

$s_{\text{crit}} \sim 0.1$ for our 2D-MOT setup.

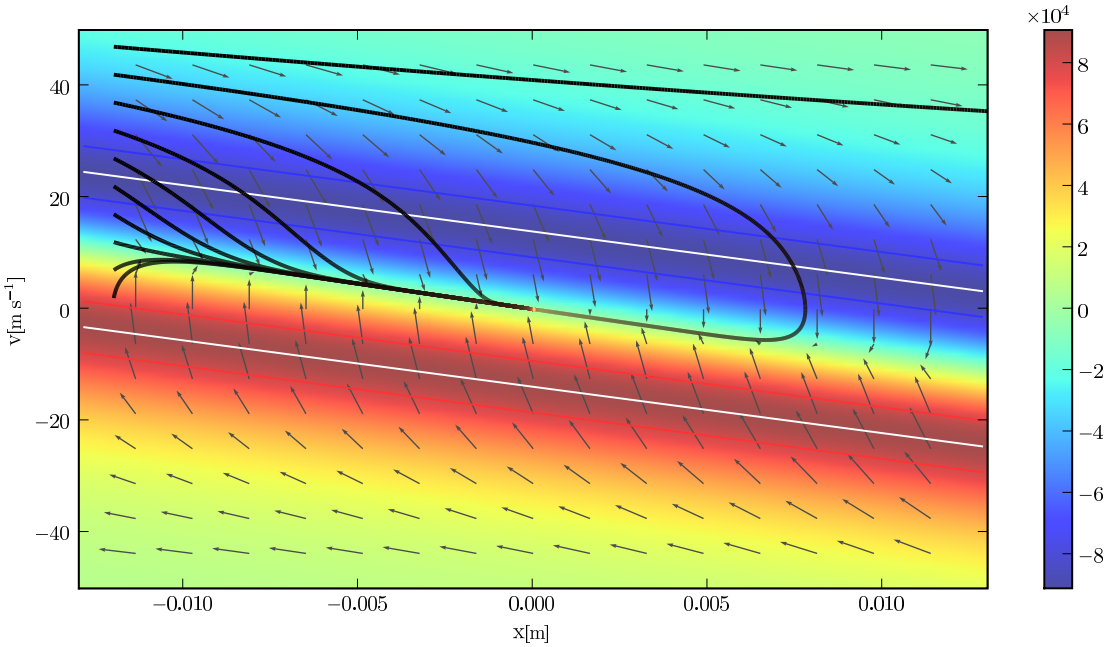

FIGURE V.10 – **High-saturation-parameter capture process in a MOT**
For a description of the different elements of this figure, see caption page 124.
For atoms near the capture velocity, the capture process happens in two steps. First the atom is brought to the line of zero detuning, where the Zeeman effect compensates the Doppler shift, then the atom follows this line, $v \sim \frac{v_0}{x_0} x$.

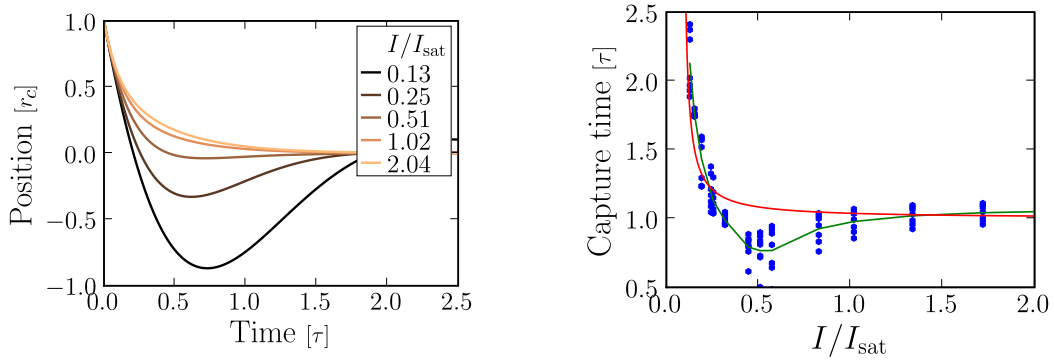

FIGURE V.11 – **(a) Capture trajectories for varying saturation parameter**
The initial velocity was taken at v_c.
(b) Capture time as a function of saturation parameter
The capture time is defined as one fourth of the time required for the position to settled down to 1% of the capture radius. Results from numerical integration of trajectories with different initial velocities are plotted with blue dots, and a green line serves as a guide to the eye. Our estimation is plotted in red and matches reasonably the numerical calculations.

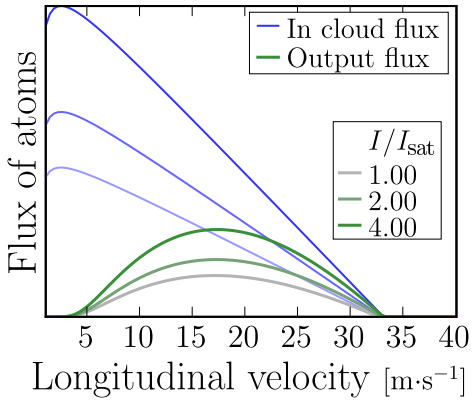

Figure V.12 – **Output flux for various intensities**

The variation of the intra-cloud flux with intensity is due both to the variation of the capture velocity, which increases the slope of the tail, and the variation of the capture time, which pushes the velocity distribution to higher velocities. The tube transfer function (not represented) is not modified. The output velocity distribution reflects the cloud velocity distribution with the atoms filtered by the tube removed.

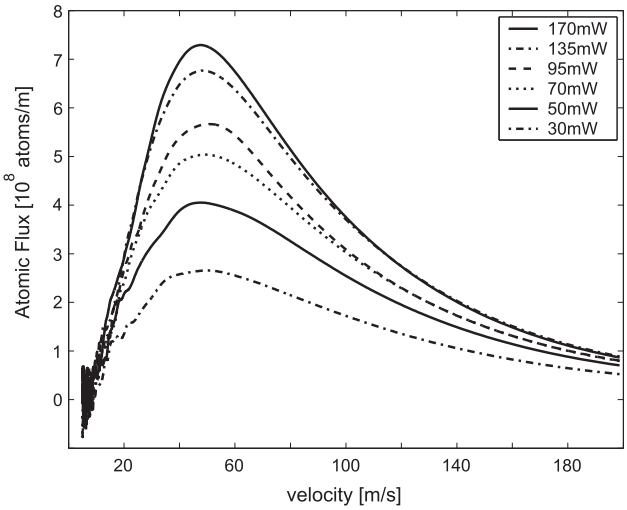

Figure V.13 – **Output flux for various intensity, data from Schoser *et al.* [151]**

The larger mean-velocity in this experimental data than on Figure V.12 can be explained by the long (90 mm) cooling region. The long tail of velocity distribution is not explained by our model, as we only consider atoms that have been completely captured by the 2D-MOT. For the central part of the velocity distribution, the model agrees well with this experimental data.

Given these considerations, and that for high saturation parameter the capture time goes to τ, we can model the dependence of the capture time on saturation parameter as:

$$t_c(s) \sim \tau + \frac{2\,t_0}{s - s_{\text{crit}}} \tag{V.16}$$

Numerical simulations (see Figure V.11(b)) confirm this scaling law.

Variation of the output velocity distribution Using the expression of t_c given by equation V.16 in equation V.8, or its simplified version V.9, taking in account the limited acceptance of the output tube and gravity, we can make an estimation of the velocity distribution of the output jet:

$$\Phi(v_z) = v_c^3\, r_c\, n\left(v_z - \frac{l}{\tau + \frac{t_0}{s - s_{\text{crit}}}}\right) T(v_z) \tag{V.17}$$

As we vary intensity, the flux and its velocity distribution vary because of the increased lateral capture velocity and the reduced capture time. The increase in the lateral capture velocity increases the total number of atoms captured in the lateral Doppler cooling for a given longitudinal velocity class. The decrease in capture time increases

the number of longitudinal velocity classes that can be captured and thus a higher output flux (see Figure V.12).

1.2.3 Results from the model

Although the toy model for the 2D-MOT developed in the previous paragraphs can hardly be considered as an adequate description of the experimental situation, it gives insight on the collimation mechanism:

- The number of atoms in the 2D-MOT cloud is determined by the ratio of the trapping time and the length of the cooling region. As this number goes up, the mean velocity in the cloud goes up, but the number of slow atoms is always greater than the number of fast atoms.
- The divergence of the output beam is given by the Doppler-limited transverse velocity distribution in the cloud, and is mostly independent of experimental parameters.
- The output flux is limited by the exit tube, mostly by the loss of low velocity atoms, due to their divergence and deflections.

1.3 Experimental implementation and operation

We have not measured the output velocity distribution of our atomic beam. Detecting an output beam requires setting up a probing beam and a camera. As the atomic density in the output beam is very low, the detection has to be very sensitive. The easiest way for us to detect the output flux is to capture the atoms in the 3D-MOT. This is not a measure of the total output flux, but only of the number of atoms below the capture velocity of the 3D-MOT. This is the only relevant parameter for our purposes, but not having access to the parameters describing the atomic beam limits our understanding of the 2D-MOT.

3D-MOT performance

Our model predicts an output flux for the 2D-MOT mostly below the capture velocity of the 3D-MOT(see Figure V.5 and V.12). We can suppose that only the atoms in the thermal background, those not captured in the 2D-MOT cloud, are too fast to be captured by the 3D-MOT. As our model for the 2D-MOT does not take these atoms in account, all the atoms of the output beam accounted for are captured by the 3D-MOT with our experimental parameters.

A large MOT cloud is optically dense. If the laser intensity at the center of the beams, where the cloud is located, is not above saturation intensity, the steady-state number of atoms in the MOT will be quickly limited by the optical thickness of the cloud. Experimentally, we find that the optimal $1/e^2$ diameter for our beams depends

Table V.1 – **Experimental parameters for our 2D-MOT**

cooling region length	50 mm
capture radius	5 mm
output acceptance	30 mrad
output hole size	1 mm
saturation parameter	$0.5 - 1.5$

The cooling region is actually made of two successive 25 mm-long cooling regions. Their lateral capture is not as efficient as that for a 50 mm-long regions. To account for this we have used a value of 40 mm when plotting graphs. The output acceptance is limited by the size of the 3D-MOT capture region, not by the output hole of the tube The saturation parameter varies depending on the state of our laser sources.

on available laser power. For large laser power, we use a $1/e^2$ diameter of 16.5 mm to maximize the intensity on the edge of the beam; for low laser power we have to reduce the $1/e^2$ diameter to 10.2 mm in order to have a intensity at the center of at least I_{sat}.

2D-MOT Performance

The atomic cloud We have measured the near-resonance absorption of the 2D-MOT cloud in the longitudinal direction with a probe beam going through the exit tube. The absorption spectrum shows peaks around 20 MHz wide, which reveals the longitudinal velocity selection in the capture process. Deriving a velocity distribution out of these spectrums is however difficult, as the probe laser, although very weak, strongly perturbs the cloud when near resonance. We have measured a total absorption at resonance of 25%. This corresponds to a density of approximately $2{\cdot}10^7 \text{at}{\cdot}\text{cm}^{-3}$ in the cloud.

Pusher beam We use a fifth, low power[11], 2 mm $1/e^2$-diameter, beam, propagating along the longitudinal direction, to push the atoms in the output tube. This accelerates atoms in the cloud with a low velocity and gives them enough velocity to avoid the dip of the tube's transfer function. As the cloud velocity distribution is maximum at these low velocities, the increase in flux can be significant. With low power in the lateral Doppler-cooling beams, the pusher beam plays an important role

[11] 0.8 – 1.1 mW, i.e. a saturation parameter of $s_0 \sim 1.5$.

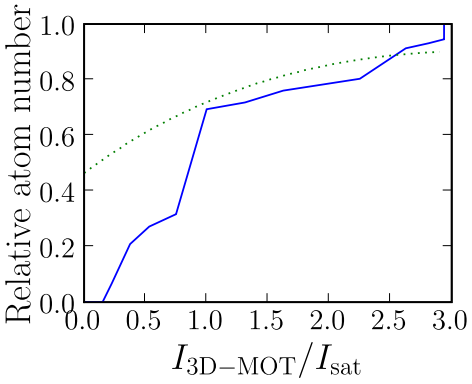

Figure V.14 – **Number of atoms as a function of 3D-MOT intensity**

The arbitrary units given by the model were scaled to match the measured number of atom. The predictions of the model fit reasonably well to the experimental data above saturation intensity, however it completely breaks down below saturation intensity.
The errors on the measurements of number of atoms are large, as they were done with a probe laser with frequency fluctuations with excursion on the order of the linewidth of the transition.

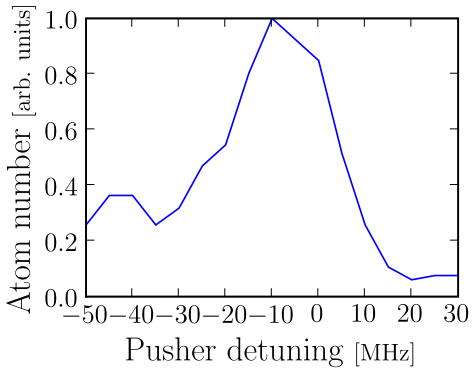

FIGURE V.15 – **Number of atoms as a function of pusher detuning**

in achieving good loading rate of the 3D-MOT. We believe that, at low saturation parameter, the cloud velocity distribution is largely below the cut-off due to the filtering of the output tube (see Figure V.12). With increased optical power in the beams, we have observed that the pusher alignment and frequency beam plays a very little role. We do not use repumping light in the pusher beam. Once the atoms are outside the cooling region they are no longer repumped by the lateral cooling lasers, and do not undergo spontaneous emission cycles in the output tube.

We detune the pusher beam to the blue of the laser-cooling transition by a few megaHertz[12]. Atoms moving away from the pusher beam with a velocity of a few meters per second are resonant with the laser. The radiation pressure thus pushes the velocity distribution in the output beam up until the exiting atoms are no longer resonant. Good optimization of the pusher frequency can increase the flux by a factor up to ten (see Figure V.15).

Intensity limits atomic flux Experimentally we have observed a strong dependence of the number of atoms over the laser power in the 2D-MOT. For saturation parameters below 1 the 2D-MOT is mostly inefficient (see V.16). This is most probably due to the reduced capture efficiency. Indeed, deflections larger than the effect of gravity taken in account in our model would dig a large hole in the low velocity end of the output velocity distribution. For the 2D-MOT to deliver a high flux, the

[12]The exact optimum value of the detuning varies from day to day. The reason is not yet understood.

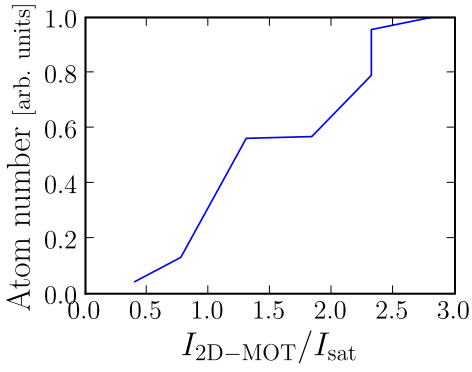

FIGURE V.16 – **Number of atoms as a function of 2D-MOT intensity**

intensity has to be large enough for the cloud velocity distribution to extend past the cut-off of the tube transfer function.

We have increased the total optical power for the 2D-MOT, partly at the expense of laser power for the 3D-MOT, with a new layout of our laser system (see §IV.3.2). As our model suggests we are not limited by the capture velocity of our 3D-MOT, even at very low saturation parameter, we preferred to optimize the atom flux from the 2D-MOT rather than the capture velocity of the 3D-MOT. Moreover, we have doubled the intensities on the atoms by retro-reflecting the transverse laser beams[13]. This has resulted in an increase of the number of trapped atoms in the 3D-MOT of a factor of three.

Magnetic field inhomogeneities The two dimensional magnetic field gradient is created by finite sized wires: a pair of elongated racetrack coils. This creates a gradient in the longitudinal direction which impedes laser cooling at both ends of the coils. The trapping region is therefore reduced, and, as it ends further away from the exit hole, the effective acceptance of the exit hole is reduced. We use coils wound around the longitudinal axis of the 2D-MOT at both ends to compensate for this gradient. This increases the flux by a factor of three.

We typically load $2 \cdot 10^7$ *atoms in the 3D-MOT in* 4 *s. After a phase of compressed MOT and optical molasses we reach a density of* 10^{12} *At*$\cdot$ cm^{-3} *at* $60\,\mu K$*. The number of atoms collected is small compared to laser-cooled clouds commonly used to achieve Bose-Einstein condensation, but numerical simulations suggest that we can reach BEC with these initial conditions. We believe that this number is limited by the flux of our 2D-MOT, itself limited both by the low rubidium vapor pressure and the small acceptance of the exit tube, due to the large distance between the 2D-MOT and the 3D-MOT, and the small diameter of the tube. Using high intensities on the 2D-MOT alleviates this last limitation as it increases collimation of the atomic jet before the output tube.*

2 A compressible optical dipole trap

Resonant light is not the proper tool to manipulate ultra-cold atoms, as photon diffusion creates a random-walk in momentum space and limits the temperature of the atomic sample. We use a far-detuned optical-dipole trap to perform evaporative cooling of the Doppler-cooled sample of atoms. For efficient loading and rapid evaporation we use a crossed dipole trap geometry with a variable size.

[13]Unlike a 3D-MOT, a 2D-MOT is not optically dense, it is thus very advantageous to retro-reflect the beams.

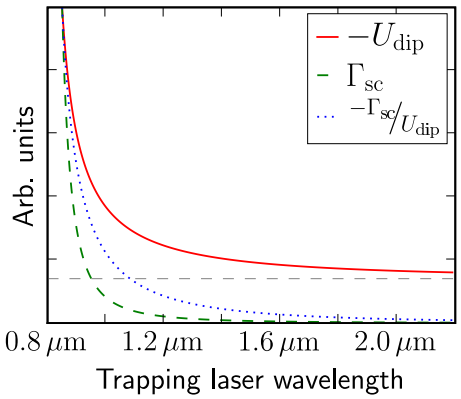

FIGURE V.17 – **Trap depth and scattering rate for ^{87}Rb ^{5}S$_{1/2}$**

The ^{5}S$_{1/2}$ rubidium energy level is the ground state of the D2 transitions, at 780 nm. In the 780 nm – 1.2 μm range its dipolar shift and photon scattering rate decrease fast (as $1/\delta$). Past 1.2 μm, the dipolar shift levels off as the quasi-static regime is reached (shown on the plot as a gray dashed line); gain in scattering rate per constant trap depth is small as the detuning increases.
The calculation of the light-shift, in particular the transitions taken in account, are detailed in §VI.1.1

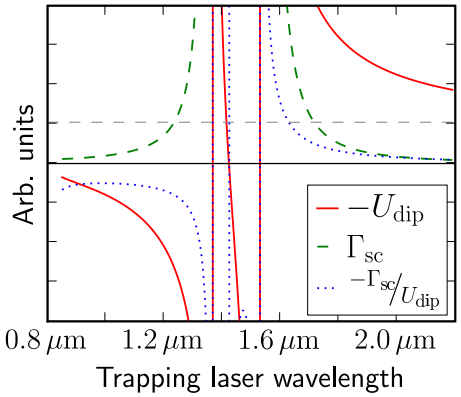

FIGURE V.18 – **Trap depth and scattering rate for ^{87}Rb ^{5}P$_{3/2}$**

^{5}P$_{3/2}$ is the excited state of the D2 transitions, at 780 nm. But it also is the lower state level of transitions at 1529 nm and 1367 nm. The quasi-static regime is reached only at wavelengths above 2 μm. In the 780 nm – 2 μm range, the polarizability is governed by the various resonances.
The calculation of the light-shift, in particular the transitions taken in account, are detailed in §VI.1.1 The arbitrary units have the same scale than Figure V.17

2.1 The far-off-resonance laser

Choice of the trapping wavelength To achieve very large trapping depths and volumes, and capture a Doppler-cooled sample of atoms, high laser intensities are needed. Heating by scattered photons is avoided by choosing a laser frequency very far from the relevant atomic transitions. For a laser field detuned far from atomic resonance ($\delta \gg \Gamma$, with δ the detuning to resonance, and Γ the line-width of the transition), the resonant interaction is negligible compared to the dipolar energy shift. For a given laser intensity of I, the depth of an optical dipole trap scales as $U_{\mathrm{dip}} \propto I/\delta$, while the scattering rate scales as $\Gamma_{\mathrm{sc}} \propto I/\delta^2$.

For rubidium atoms, Nd:YAG lasers ($\lambda \sim 1\,\mu$m) and CO_2 lasers ($\lambda \sim 10\,\mu$m) have been successfully used to achieve Bose-Einstein condensation in conservative optical dipole traps. At these very large detunings, the rotating-wave approximation (see e.g. Grimm *et al.* [155], Cohen-Tannoudji *et al.* [156]) is no longer valid, and the trap depth and scattering rate scale as:

$$U_{\mathrm{dip}} \propto I\left(\frac{\Gamma}{\omega_0-\omega}+\frac{\Gamma}{\omega_0+\omega}\right) \tag{V.18}$$

$$\Gamma_{\mathrm{sc}} \propto I\left(\frac{\omega}{\omega_0}\right)^3\left(\frac{\Gamma}{\omega_0-\omega}+\frac{\Gamma}{\omega_0+\omega}\right)^2 \tag{V.19}$$

where ω_0 is the atomic transition angular frequency, ω the laser angular frequency. At very large red detunings the trap depth becomes independent of frequency, the quasi-

static limit. For the ground state of the rubidium D2 transition ($|g\rangle$), the quasi-static regime starts at approximately 1.5 μm (see Figure V.17). As this is the atomic level in which BECs are made, the achievable trap depth for this atomic level is most relevant. However, optical manipulations of rubidium atoms (laser cooling, one or two photon transitions) are most often performed on the D2 transition, and populate the excited state $|e\rangle$ of the transition. For trapping lasers between 780 nm and 1530 nm, $|g\rangle$ and $|e\rangle$ cannot be trapped simultaneously, as the laser is to the red of the transitions departing for $|g\rangle$ but to the blue of transitions departing from $|e\rangle$. Trapping lasers with wavelengths longer than 1530 nm create red-detuned dipole traps for both states (see Figure V.17 and Figure V.18). This is why CO_2 laser ($\lambda \sim 10\,\mu$m) have been very successfully used to create dipole traps loaded from optical molasses and cooled to quantum degeneracy. However these far infra-red lasers require special viewports (ZnSe glass) and are inconvenient to work with. The recent availability of high-power fiber lasers in the $1-2\,\mu$m range opens new possibilities for laser sources used for dipole traps.

We chose to work with a 1565 nm fiber laser, just to the red of the 1529 nm transition of the excited state. While laser light at this wavelength traps strongly the rubidium excited level, it can also shift the D2 transition out of resonance from the Doppler cooling lasers and inhibit laser cooling (this is studied in detail §VI.1). We use an erbium fiber laser[14] as a turn-key solution for 50 W of laser light at 1565 nm. It has a spectral width of a fraction of a nanometer, but has negligible intensity noise[15]. For a simple Gaussian beam geometry with a waist of 50 μm, the trap depth for rubidium atoms is approximately 2 mK.

Control of the intensity During the evaporation ramp, the depth of the trap is reduced by lowering laser intensity. Similarly, to perform time-of-flight sequences, the trap is suddenly turned off. Precise and fast control of the laser intensity is thus required. In order not to perturb the ballistic flights of atoms during time-of-flight sequences, the residual trap depth must be small compared to the kinetic energy of the atoms (typically a few hundred nanoKelvins). We need extinction ratios better than 0.1%, with cut-off speeds larger than the inverse trap frequencies, i.e. milliseconds.

Both AOMs and Electro-Optical Modulators (EOMs) used as intensity modulators are suitable for our needs. We choose a custom-made EOM[16] (CONOPTICS) as EOMs have higher efficiencies than AOMs in terms of laser intensity. AOMs are

[14] IPG ELR-50 series, with linear polarization option.

[15] Intensity noise of a spectral density of S in the trapping laser will heat the trapped atom by a rate of $\dot{E} = \frac{\pi}{2} m\omega^4 S(\omega)$, where ω is the trap frequency. A low-intensity-noise laser at frequencies up to a few kilohertz is paramount for creating a good dipole trap for ultra-cold atoms.

[16] Conoptics provides off-the-shelf EOM with similar specifications, however building an EOM that provides full $\lambda/2$ range for 1.5 μm light, with driving frequencies of kilohertz at such high fluxes is a technical challenge. The difficulty comes from the fact that at such long wavelengths creating a $\lambda/2$ phase difference requires both a long electro-optical crystal and very a strong polarizing electric field. As the crystal is long, creating strong fields over its entire length would require excessively high voltage. The field is thus created transversally, and the optical diameter instead of the length is limited by the constraint on the driving voltage. It follows that the crystal is of small optical diameter and subject to high optical intensities. Under high optical intensities, impurities in the

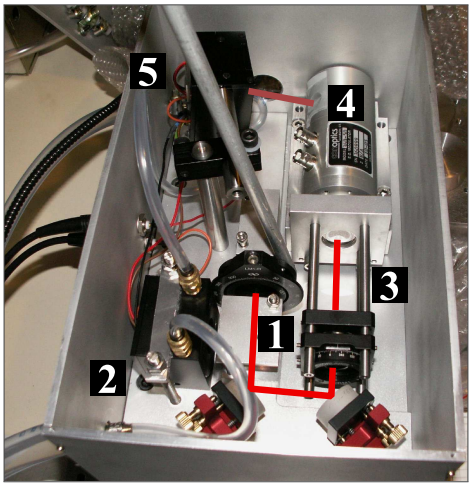

FIGURE V.19 – **Intensity-control apparatus**
The intensity of the fiber laser is reduced and controlled in a protected enclosure, under clean air over-pressure. The fiber laser first goes through a half-wave plate and a thin film plate polarizer (CVI) (1). The half-wave plate can be rotated by a long rod that is accessible outside the enclosure. The reflected beam is sent to a water-cooled power-meter head[a] (2). The main laser path is injected in the OEM (4) via a 2:1 confocal telescope and a half-wave plate. The OEM has a Glan polarizer mounted at 45° to its axes, at its output. The reflected beam is sent to another power meter head (5) and the other beam exits the enclosure.

[a]Ophir, 150W-A.1-Y

specified at 80% diffraction efficiency; we reach at least 90% transmission with our EOM. Another major drawback of AOMs is that they strongly degrade the beam shape and would therefore prevent us from achieving tight traps (see §V.2.2). Due to the high optical intensities on the input and output surfaces of the EOM, the intensity-control apparatus was mounted in a small duraluminium enclosure with a clean air over-pressure and holes just large enough for the lasers beams, the control cables, and the fiber (see Figure V.19). Working with high-power 1.5 μm lasers is tedious as neither cameras nor high-flux power meters can be used at low power, and alignment must be performed at low power and checked at full power. We use water-cooled power-meter thermal heads at each output port of our optical system and we align the system continuously checking for unexpected losses in the optical components (at 50 W a 5% loss is sufficient to permanently damage components).

We have up to now achieved extinction ratios of 2% with the EOM. The modulator is specified for extinction ratios of 0.5%. We suspect that either the injection polarization is not very linear[17], or we are not injecting the EOM well along it axis. We have recently received a more sensitive power meter that will allow better diagnostics. Alternatively, the output Glan polarizer may not have a high enough extinction ratio. At high power, it seems to warm up and the refractive indexes change. The total internal reflection ceases to be total and a small portion of the beam is diffracted in the output port of the EOM. This stray beam cannot be extinguished. However it propagates in a direction different from that of the main beam and is of no concern to us.

crystal heat up and damage the EOM, therefore a large impurity-free sample is required.

The driver is a standard M302 also from Conoptics, with a maximum drive frequency of 250 kHz

[17]The thin film polarizer is specified to polarize to 1%, but it has to be hit by the beam with the right Brewster incidence angle for this. We are considering adding a Glan polarizer after it.

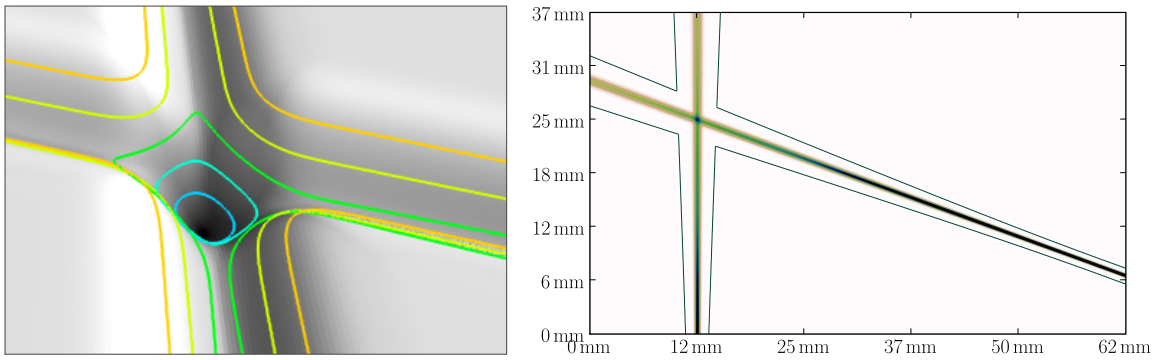

Figure V.20 – **(a) Crossed dipole trap potential, 3D view**

(b) Intersecting expanding Gaussian beams, 2D view
Due to their expansion, the beams have a larger width at their intersection point than at the focal point, if the two points do not coincide.

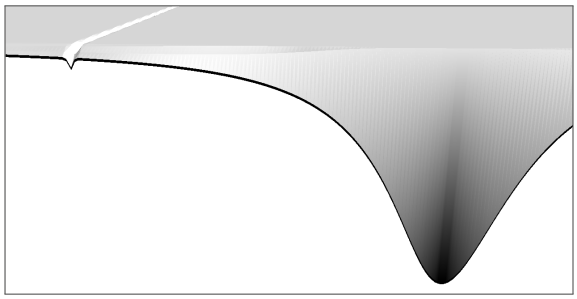

Figure V.21 – **Cut of the potential along the axis of a Gaussian beam**
The absolute minimum is located at the focal point of the Gaussian beam, but there is a local minimum at the intersection point of the two beams. This figure is a cut of a surface representation of the potential along the axis of one of the beams; the second beam creates a "canyon" that can be seen perpendicular to the cut axis, and the upper left of the figure.

2.2 Optical design for varying trap size

We control the size of the trap by physically moving an optical element, thus deforming the intensity distribution in the vacuum chamber.

Crossed Gaussian geometry

Trapping region In red-detuned dipole traps, atoms are trapped near maxima of laser light intensity. Our trap is made of two intersecting Gaussian beams. The intersection of the beams creates a local maximum and defines the trapping region (see Figure V.20(a)). The size of the trapping region is given by the diameter of the lasers at the intersection point. The half width at half maximum of a Gaussian beam goes as

$$w(z) = w_0\sqrt{1+\left(\frac{z}{Z_R}\right)^2} \tag{V.20}$$

where z is the distance to the focal point along the propagation axis, Z_R is the Rayleigh range, and w_0 is the waist of the beam at the focal point. By having the two beams intersect far from their focal point we can control the diameter of the trapping region

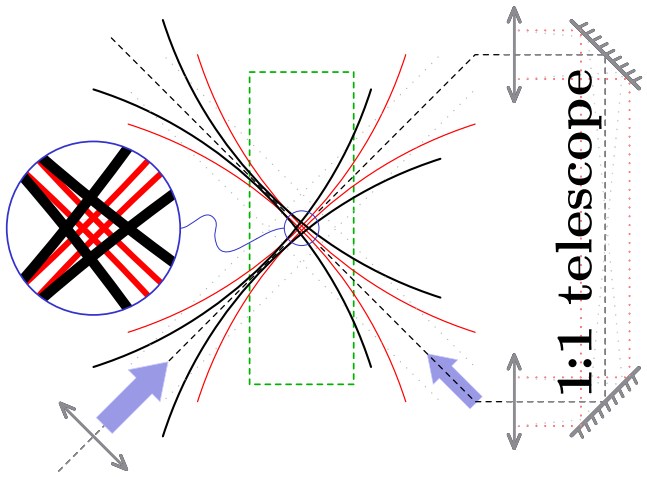

FIGURE V.22 – **Diagram of the beam path for the recirculating crossed dipole trap**
The trapping beam is focused in the vacuum chamber (dashed green line) and reinjected in the vacuum chamber after a 1:1 confocal telescope. The confocal telescope acts as an image transport and when the input beam is displaced, the displacement is imaged identically in the reinjected beam. The intersection of the beams (the trapping region) is always located at the center of the chamber.

(see Figure V.20). If the intersection point is far from both focal points, the absolute maximum of intensity (minimum of potential) is located at the focal points and not at the intersection point, as can be seen in Figure V.21.

Recirculating the power To achieve a larger trap volume with a given amount of laser power, we pass the trapping laser beam twice through the vacuum chamber, at 70° angle. The first pass is focused into the chamber. It expands while leaving the chamber. It is next collimated and refocused in the chamber by a 1:1 confocal telescope. This optical system behaves as an image-transport system; it copies the intensity distribution of its object plane to its image plan (see Figure V.22). Thus any displacement of the beam in the first pass is reproduced identically on the second pass. By moving the focal point of the input beam, we displace both beams while keeping their intersection at the center of the vacuum chamber.

If the recirculation length is not loner than the coherence length of the laser, interference patterns can modulate the potential. While this modulation is not by itself a problem, small mechanical vibrations shake the resulting lattice and heat the atoms. Although the linewidth of our laser is large, we have observed such heating, most probably due to a fine structure in the emission spectrum. One solution to suppress interferences patterns is to use perpendicular polarizations on both beams.

The mechanical zoom optics

The incoming beam is focused in the vacuum chamber through an optical system with a lens mounted on a translation stage to move the position of the focal point inside the chamber.

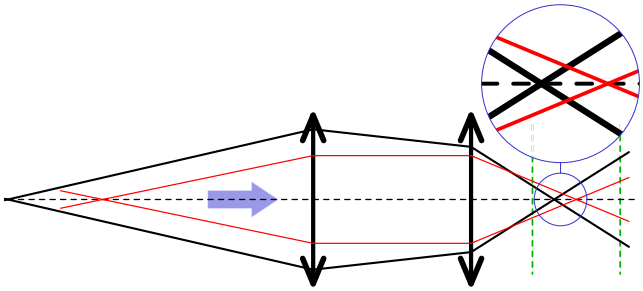

Figure V.23 – **Zoom for the compressible dipole trap**
A first focal point is created by a lens not shown on this figure. The movement of the input focal point is imaged in the vacuum chamber with a longitudinal magnification of $4:1$. The focal length of the first lens is $500\,\text{mm}$, that of the second lens $250\,\text{mm}$. The two lenses are separated by $100\,\text{mm}$, and the center of the vacuum chamber (the trapping region) is at the focal point of the second lens.

Choice of the numerical aperture to minimize focal-point size The laser beam exits the EOM with a beam diameter of 1.9 mm. The fiber laser has a good $\text{TEM}_{0,0}$ beam profile as it is propagated in a single mode fiber. In order to achieve tight confinement of the atoms in the optical dipole trap, the beam is focused down to a narrow waist in the chamber. For diffraction-limited optics, the waist w achieved through an imaging system of an output Numerical Aperture (NA) α is given by[18]

$$w \sim \frac{\lambda}{2\,\alpha} \tag{V.21}$$

A stigmatic optical system refocuses rays originating from one source point into an object point by compensating for free-propagation path-length differences, using, for instance, lenses. The diffraction limit cannot be achieved when the difference in path length for the various rays going through the optical system is above $\lambda/4$. With high NA optical systems, this condition is technically hard to meet, as light rays propagate with large angles and the non-linearities of the deflection at lens interfaces are no longer negligible. This creates aberrations which deform and broaden the waist at the focal point. Aberrations typically increase very fast with α; the so-called spherical aberration goes as α^3, for instance. Engineering optical systems to cancel the various aberrations at large numerical aperture and working distance is a technical challenge. For a given cost and engineering effort, the best strategy to achieve a tight focus is not to seek the largest numerical aperture; the numerical aperture that minimizes the waist at the focal point is reached when aberrations enlarge the focus as much as the diffraction limit. For our dipole trap we chose to use a NA of 0.1, that is a diffraction limit of $10\,\mu\text{m}$, and a target value for the waist of $20\,\mu\text{m}$. In terms of optical engineering, a NA of 0.1 corresponds to an f-number of 5, an aperture at which singlet lenses begin to show significant aberrations.

[18] This minimal waist value is achieved for a Gaussian beam filling only half of the optics. The beam profile is then close enough to a Gaussian to apply Gaussian-beam optics formulas.

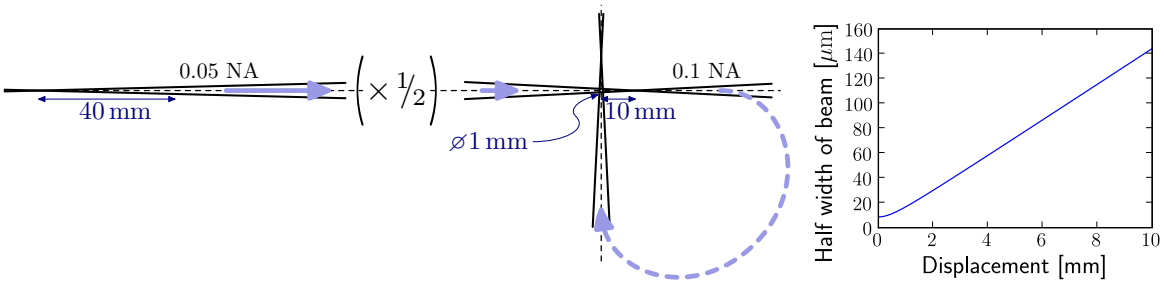

FIGURE V.24 – **(a) Displacement of the different focal points**
A displacement of 40 mm of the input focal point before the 2 : 1 optical system corresponds to a displacement of 10 mm in the chamber. As the beams have a numerical aperture of 0.1, the diameter of the beams defocused by 10 mm is 1 mm.
(b) Waist at the intersection of the beams in the vacuum chamber as a function of the displacement of the input focal point
This calculation was performed using the ABCD matrix formalism.

Moving the focal point For more flexibility and to be able to move the focal point, we keep all our optics outside the vacuum chamber. The lens nearest to the vacuum chamber is therefore at a distance of at least 200 mm. The 1.9 mm-diameter beam coming out of the fiber-laser is not large enough to achieve the target NA at this working distance. We create a first focal point outside the vacuum chamber using a short-focal-length lens, and we image it in the chamber through an optical system of numerical aperture large enough to reach the desired diffraction limit (see Figure V.23). The short-focal-length lens creating the first focus is mounted on a high-precision, low-vibration, computer-controlled translation stage[19]. By moving the focal point outside the chamber, the imaged focal point moves and we have control over the trapping volume. Defocusing a 0.1 NA Gaussian beam by a distance of x yields a beam of $0.1\,x$ full width at half maximum. To have a trap size of the order of magnitude of a MOT (~ 1 mm), we need to move the focal point inside the vacuum chamber by 10 mm (see Figure V.24(a)).

Limiting the aberrations To limit the number of high NA lenses[20], we use an optical system with a magnification of 2:1. The longitudinal magnification is then 4:1 (see Figure V.23) and the displacement range of the input waist 40 nm. The two converging lenses of the confocal telescope introduce positive spherical aberration that can be partly compensated by using a diverging lens (introducing negative spherical aberration) to create the input waist. In addition, the converging beam enters the chamber with a 35° angle to the normal of the viewport (see Figure V.22). It passes through a 13 mm-thick Kodial viewport that introduces higher order aberrations such as astigmatism. A tilted, 23 mm-thick, silica plate is added in the beam before the confocal telescope to compensate for the astigmatism. Experimental characterization of the first generation optical system described in Figure V.23 reveals a minimal waist

[19] Aerotech ANT-50L

[20] The output NA (vacuum-chamber side) is fixed at 0.1, the input NA is given by the magnification and the output NA, with a magnification of 2:1 it is 0.05.

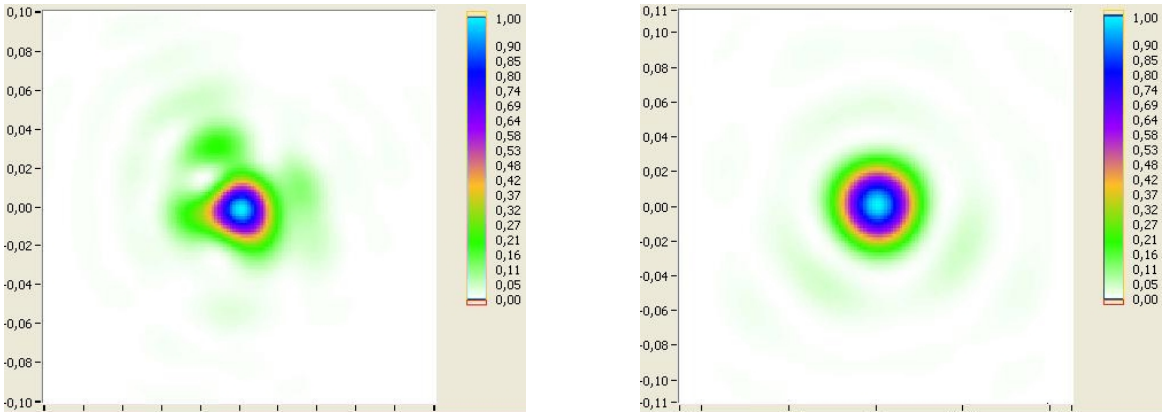

Figure V.25 – **Spot shape at the focal point**
Left – spot shape without the compensation for astigmatism.
Right – spot shape with the compensating silica plate.
These images are reconstructions of the minimal diameter spot obtained by a Shack-Hartmann wavefront analyzer. Astigmatism appears as asymmetries in the spot shape and spherical aberration as circular ripples. In the compensated spot almost no astigmatism and very little spherical aberration are present. The waist at the focal point is measured to be $30\,\mu$m.

of $30\,\mu$m (see Figure V.25). This resolution is limited by the spherical aberrations induced by the last lens: a plano-convex singlet lens working at infinite conjugate with an f-number of 5. As the spherical aberration grows as α^3, the contribution of the other lens is small compared to this last lens. A second generation system uses a doublet lens. It has been experimentally shown to yield a $15\,\mu$m waist and is planned for installation on the experiment.

Using the erbium fiber laser and the mechanical zoom apparatus we can create a crossed dipole trap of dimension ranging from $1\,mm$ *to* $30\,\mu m$ *and of a well controlled depth. At a diameter of* $0.3\,mm$ *the maximum trap depth in the crossed Gaussian beam is* $100\,\mu K \times k_B$*, which is slightly above the temperature achieved in optical molasses. We can load the trap from the optical molasses in this configuration and progressively switch to a very tightly focused trap, favorable for evaporation.*

3 A large homogeneous magnetic field

We plan to control interactions, either intraspecies or interspecies, between potassium and rubidium, with a homogeneous magnetic field via magnetically-tunable Feshbach resonances. This section describes the coils that were built for this purpose.

3.1 Magnetic-control of the collisional-shift in interferometers

Improving accuracy and precision of inertial sensors As discussed in §I.1.3.2, interactions in BECs lead to a reduced coherence length. As a result, the collimation of the cloud is limited. In addition, the collisional phase shifts introduced by interactions can lead to systematic errors in the measurement. Collisions can thus limit the precision or the accuracy of the measurement when their contribution to the phase shift is on the same order of magnitude as the experimental resolution of the measurement of this phase-shift, typically $2\pi \cdot 10^{-2}$ rad, limited by quantum-projection noise or technical noise.

The phase-shift introduced by collisions is, in the mean-field approximation (see Witthaut *et al.* [157]):

$$\Delta\phi_{\text{coll}} = 4\pi \frac{\hbar\, a}{m} n\, T \tag{V.22}$$

where a is the scattering length, m the mass of the atom, n the density of the sample, and T the interrogation time. Typically[21], $n \sim 10^{13}\,\text{at} \cdot \text{cm}^{-3}$. For 1 s interrogation times[22], the scattering length should be below $7 \cdot 10^{-13}\,\text{m} = 0.013\, a_0$ for the collisional shift to be below the error on the measurement.

Controlling interactions in a potassium-rubidium mixture Magnetic control of interactions can be used to fully cancel them and produce a diffraction-limited, non-interacting, atomic source using a non-interacting Bose gas (Cornish *et al.* [55]). The bosonic isotope of potassium, ^{39}K, is a good candidate for such a source, as it has a broad zero-point resonance at 350 G that can be used to precisely cancel its self-scattering length. Fattori *et al.* [54] have recently demonstrated a large increase in coherence by tuning the scattering length to zero in a condensed gas of ^{39}K, although they have not demonstrated the absence of interaction shift, wich would be an important feature of a non-interacting BEC important in high-precision atom-interferometry. The coherence time achieved on their experiment is limited by imperfect control of the interactions across the sample due to the inhomogeneity of the field (G. Modugno, private communication).

The wide Feshbach resonance used to cancel the interaction in the ^{39}K sample is such that a change of one Gauss in magnetic field corresponds to a change of $0.55\, a_0$ in scattering length. Using this zero-point resonance, a scattering-length difference of $7 \cdot 10^{-13}$ m corresponds to a change in magnetic field of 24 mGauss, that is 70 ppm (parts per million) at 350 G. For the collisional shift to be controlled well-enough to be negligible after long interrogation times, the constraints on the homogeneity and

[21] This order of magnitude holds for trapped samples. As the cloud is released from the trap it expands, and the density is quickly reduced. However, its would be interesting to be able to perform high-precision interferometric measurements using guided atom-interferometry, thus with a dense trapped sample. This is why we use this order of magnitude here.

[22] Inertial sensing on freely-falling atoms with 1 s interrogation time is not possible in a gravity field, but it is possible using atom interferometry with guided atoms (Wu *et al.* [158]) or with atoms bouncing from Raman pulses (Impens *et al.* [159]).

Feshbach resonances

atoms	B(G)	ΔB(G)	ref.
^{87}Rb – ^{87}Rb	1007.6	0.2	[160]
^{40}K – ^{87}Rb	545.4	1.2	[161]
^{39}K – ^{39}K	40	~ 20	[162]*
^{85}Rb – ^{85}Rb	155.0	10.7	[163]

Zero-point resonances

atoms	B(G)	ref.
^{85}Rb – ^{85}Rb	167.8	[163]
^{39}K – ^{39}K	350	[54]

$\star$ Theoretical prediction.

Table V.2 – **Main features of controllable interactions in potassium-rubidium mixtures**

reproducibility of the field are thus stringent. Working with dilute samples can reduce these constraints by several orders of magnitude.

Achieving a good control of the interactions for the various possible potassium–rubidium mixtures requires a precisely-tunable magnetic field up to 1 050 G (see Table V.2), homogeneous over the size of the atomic sample. Taking into account a small safety margin, we have specified our coils to 1 200 G.

3.2 Design of the coils

Dimensions of the coils The field created by a pair of coils is most homogeneous when the coils are positioned in Helmholtz configuration, i.e. the distance between the coils equal to their radius R. This geometry is also the most effective in terms of the magnitude of the field for a given electrical power dissipated in the coils. The magnetic energy stored in the coils is:

$$U = \frac{\pi R^3}{2\mu_0} B^2 \tag{V.23}$$

To produce a strong magnetic field with a limited amount of electrical power it is advantageous to use coils as close as possible to the targeted atoms to reduce R. However curvature increases as the dimensions of the coils are reduced. For an exact Helmholtz configuration, the curvature at the point of symmetry goes with distance as x^4 and scales as R^{-5}, but if we deviate from the perfect Helmholtz geometry, which is inevitable in a real set-up, as wires have a finite thickness, a small x^2 curvature term appears and scales as R^{-3}. Coils with a large radius or additional field-shim coils are thus needed for very homogeneous fields. There is a trade-off between minimizing power requirement by being as close as possible to the atoms and achieving a highly homogeneous field. We use coils with an inner diameter of 205 mm designed to fit around a CF-160 vacuum viewport.

Coil geometry The magnetic field produced by a pair of Helmholtz coils of a given radius is proportional to number of Ampere·turns, $N\,I$:

$$B = \left(\frac{4}{5}\right)^{3/2} \mu_0 \frac{N\,I}{R} \tag{V.24}$$

For a given cross-section of conductor (eg copper) the coils may be arranged in many turns of low-conductance small wires or fewer turns of high-conductance large wires, to achieve the same number of Ampere·turns. The power dissipated P does not depend on the number of turns, but on the total conductance C of the entire section of the coils:

$$P = \frac{2\pi}{\mu_0^2} B^2 \frac{R^3}{C} \left(\frac{5}{4}\right)^3 \tag{V.25}$$

For a given material, this conductance depends only on the total cross-sectional area, thus the available room. Using a cross-section of $10\,\mathrm{cm}^2$ annealed copper, of resistivity of $1.68 \cdot 10^{-8}\Omega \cdot \mathrm{m}$, the coils satisfying our needs would dissipate 1 kW each. To limit the size and weight of the coils, we do not wish to use a larger cross-section of copper to reduce dissipation. The dissipated power must therefore be extracted. This can be done using hollow wire through which water is flown. In long windings, if no compressor is used, the pressure drop limits the flow and the cooling efficiency. Through a tube of length l and diameter d, for a given flow rate Q the pressure drop scales as $l\,d^{-4}\,Q$. For a given coil cross-section, a small number of turns with large hollow wire gives a maximum cooling efficiency as it reduces the hydraulic load[23]. Moreover, the self-inductance of the pair of coils scales as N^2, N being the number of coils. To drive the coils with a fast response time, a low inductance solution, with a high current and a low number of turns, is also preferable. However very high operating currents are more cumbersome to work with, as any unwanted resistance of components such as leads, or IGBTs, creates large voltage drops.

We use 126 turns of $6 \times 6\,\mathrm{mm}$ square wire[24], with a round hole of 3 mm inner diameter. It is wound in a geometry that tightly encircles the vacuum chamber, but leaves a large amount of optical access (see Figure V.27). Before starting the fabrication of the coils, we carried out a numerical simulation of their performance to evaluate the power dissipation and the homogeneity of the field at 1 200 G (see Table V.3). The available cooling power, limited by the water flow at 3 Bar[25], and the pressure drop was also calculated. The electromagnetic calculation was done by summing the exact expression of the magnetic field from an arbitrary current loop

[23]Cooling efficiency scales as d^6, for a given input pressure, for a given total cross-sectional area, as the length of the tube that can be coiled in this cross-section decreases when its diameter increases.

[24]The hollow tubing was ordered from Wolverine Tube, and "Le Guipage Moderne" wrapped it in a double layer of polyester.

[25]We prefer not using a compressor as it is both a source of noise and brings an added risk of leaks.

(Bergeman *et al.* [164]):

$$\mathbf{B}_z = \frac{\mu I}{2\pi} \frac{1}{\left[(R+\rho)^2+(z-A)^2\right]^{1/2}} \left(K(k^2) + \frac{R^2-\rho^2-(z-A)^2}{(R-\rho)^2+(z-A)^2} E(k^2) \right) \quad \text{(V.26)}$$

$$\mathbf{B}_\rho = \frac{\mu I}{2\pi\,\rho} \frac{z-A}{\left[(R+\rho)^2+(z-A)^2\right]^{1/2}} \left(-K(k^2) + \frac{R^2+\rho^2+(z-A)^2}{(R-\rho)^2+(z-A)^2} E(k^2) \right) \quad \text{(V.27)}$$

where E and K are the complete elliptic integrals and:

$$k^2 = \frac{4\,R\,\rho}{(R+\rho)^2+(z-A)^2}$$

3.3 Realization of the magnetic field

Construction of the coils We wound ourselves a first set of coils on a lathe, applying a layer of glue between each layer of wires. We were not satisfied with the mechanical strength of the coils. As we want the magnetic field to be well reproducible, the coils should not deform. Sudden stress is applied on the wires when the magnetic field is rapidly changed. The coils should be robust enough to go through many magnetic field cycles.The strength of our coils is limited by the glue. We subcontracted the construction of a pair of coils to a company specialized in magnetic coils for scientific laboratory and large instruments (SIGMAPHI[26]). These coils are first wound on a lathe, and then inserted into a mould into which glue in injected at high pressure (see Figure V.26). The resulting coils are very robust and the individual wires have no freedom to move.

The real coils perform slightly less satisactorily than our calculations predicted (See Table V.3). The major setback is that the water flow achievable without a compressor

[26]http://www.sigmaphi.fr

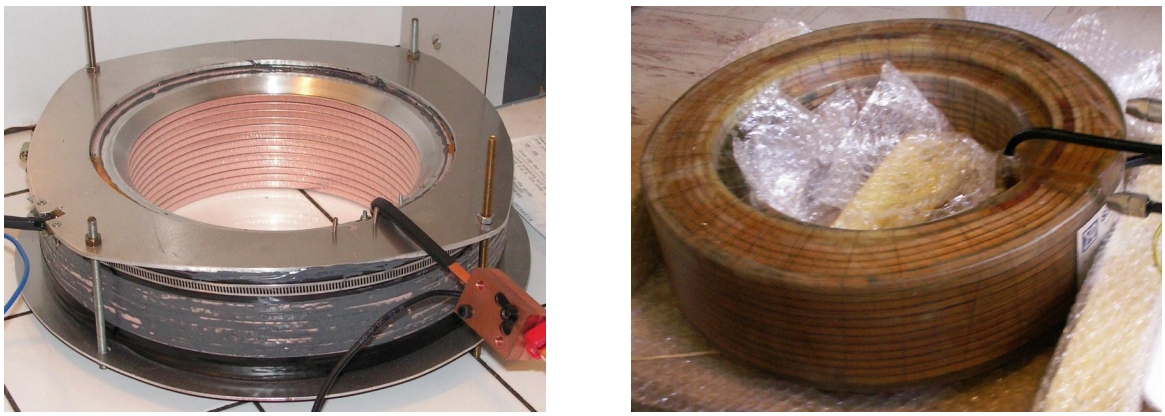

Figure V.26 – **Left – homemade coils** **Right – coils made by SigmaPhi**

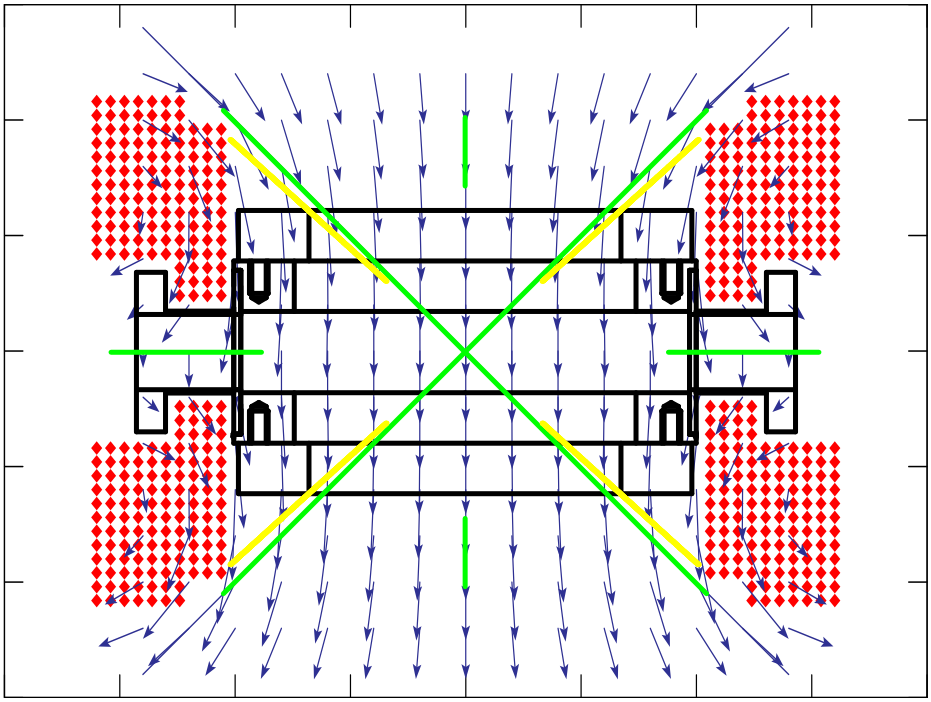

FIGURE V.27 – **Geometry of the coils.**
Each red diamond represents a 6×6 mm square copper wire. Results of the numerical calculation of the field are plotted as blue vectors.
The geometry has been chosen to tightly match the shape of the UHV chamber and leave optical access at 45° through the CF-160 viewport. Technical drawings describing the coiling arrangement of the coils can be found in §E.1, on page 217.

	Calculated	**Measured**
Number of turns	126	
Length of wire (per coil)	105 m	
Value of the field at the center	$8.4\,\mathrm{G}\cdot\mathrm{A}^{-1}$	$8.0\,\mathrm{G}\cdot\mathrm{A}^{-1}$
Resistance of one coil at 20°C	0.082 Ω	0.067 Ω
Inductance of the pair, in dipole configuration	< 12 mH	4.7 mH
Water flow in one coil under a pressure of 3 Bar	$4.3\,\mathrm{L}\cdot\mathrm{min}^{-1}$	$0.48\,\mathrm{L}\cdot\mathrm{min}^{-1}$
At 1 200 G:		
Current	142 A	150 A
Voltage drop trough one coil	11.6 V	10.0 V
Power dissipated in one coil	1 656 W	1 500 W
Water flow required to operate continuously[a]	$0.47\,\mathrm{L}\cdot\mathrm{min}^{-1}$	

[a] In the calculations we tolerated an increase in water temperature of 25°

TABLE V.3 – **Characteristics of the coils**
The inductance was estimated by taking the maximum value of the field, and multiplying it by the sum of the areas of the current loops, it is therefore not surprising that the calculations are above the measured value by a factor of three.
The large discrepancy between the calculated and the measured value of the flow is most probably due to the sharp bends of the tubes that where not taken in account.

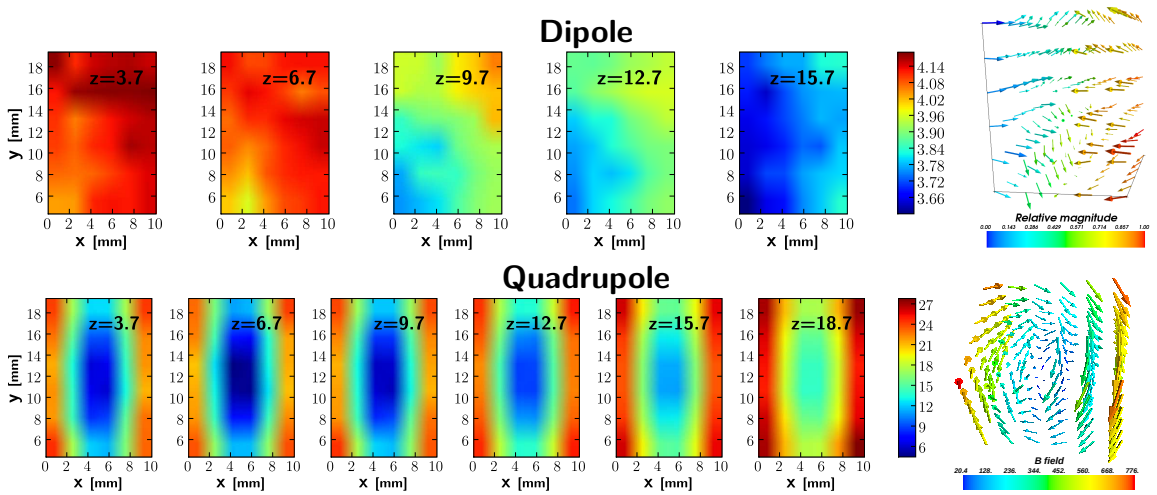

Figure V.28 – **Field magnitude measured in dipole and quadrupole configuration**

Positions are in millimeters, magnetic field in Gauss. The current in the coils is 40 A. The values represented for the dipole configuration are the variations around a mean value of 317 G (on the 3D-plot, the vectors represent the variation to the direction of the field, and their color the variation to the magnitude).

A small gradient can be seen in the z direction in the dipole configuration. A bias in the z direction can also be seen in quadrupole configuration. As the variation in direction is symmetrical (as can be seen on the 3D-plot), we believe this is not due to the coils, but to an external field.

In quadrupole configuration, the coils produce a gradient of $0.75\,\mathrm{G}\cdot\mathrm{cm}^{-1}\cdot\mathrm{A}^{-1}$.

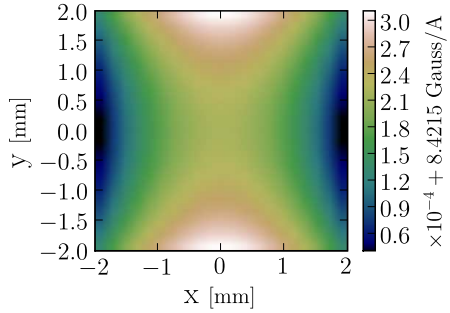

Figure V.29 – **Homogeneity predicted for the dipole field**

Using our simulations we evaluate the homogeneity of the field over the $4\,\mathrm{mm}^2$ area at the center (field in Gauss/A, distance in mm):

$$|\mathbf{B}| \sim 8.421721 + 0.000023\cdot x^2 - 0.000045\cdot y^2$$

gives us no safety margin relative to the flow that we estimated was required to run the coils continuously at full power. This does not set a limit as the fraction of the experimental cycle during which we need to run the coils at full power[27] should not exceed $\frac{1}{4}$. If needed, we can add a compressor to increase the flow: the water circuit has been leak-tested up to 30 Bar.

Our measurement of the field in dipole configuration (see Figure V.28) reveals a homogeneity worse than the predicted value (see Figure V.29). The residual gradient could be due either to an external field, or a differing numbers of Ampere-turns in

[27] As long as the atoms are above 100 nK, their interactions cannot be controlled via magnetic fields. The coils will be used in quadrupole configuration during the magneto-optical trap phases, but it will not be run at full power. They will be turned off and switched back to dipole configuration during the early stages of evaporation. They can be run at full power during the end of the evaporation and during an experimental sequence with the degenerate gas.

each coil. As the measurement was not performed with the coils in their final position, it may not reflect the field the atoms will actually experience.

Power supply An ultra-precise current-regulated power supply is required for control of interactions during precision measurements. We use a custom Danfyzik Magnet Power Supply 858 that provides a maximum current of 150 A and a maximum voltage of 32 V. It is designed to control magnets in particle accelerators and claims 3ppm stability in current. We have adapted its 18bit digital servo to be directly digitally-controlled by our time-sequencing electronics, to be able to drive it to its full precision.

Rapid switching of the magnetic field A voltage $U \sim L\,I/t$ is required to switch the current in an inductor L from a value I to 0 in a time t. To perform our experimental sequences we need to turn on or off the coils in a millisecond. We therefore need voltages in the kilovolt range. The switching is performed by a circuit similar to that described in Fauquembergue *et al.* [165]. Briefly, the large required voltage is stored in a capacitor; to rapidly establish the current in the coils the capacitor is suddenly connected to the coils via an IGBT. The LC circuit thus formed is left to undergo a quarter of an oscillation, during which the energy is transferred from the capacitor to the coils. The power supply then takes over. To switch off the magnetic field, a discharge capacitor limits overvoltage. We have measured switching times of ~ 1 ms from 120 A to zero. A remaining magnetic field due to eddy currents in the copper gaskets of the CF160 viewports of an amplitude of 20% of the initial field takes another millisecond to decay.

This switching time may be too long to perform time of flight sequences with imaging in zero field starting from high-fields. However, we can perform in-field imaging, as the field homogeneity is large-enough and shifts uniformly the energy levels of the atoms over a region explored by a time-of-flight sequence.

We have designed coils that can sustain fields up to 1 000 *G continuously. The field produced has a theoretical homogeneity of* 30 *ppm (parts per million) over a* 4 mm^2 *region at their center. We have verified that the experimental homogeneity is better than* 180 *ppm. This homogeneity is sufficient to perform high-precision guided-atom-interferometry experiment with separation between the wave packets of several millimeters and interrogation time up to the second. Using capacitors for the required high-voltage we can switch the field off in* ~ 1 *ms. We also use these large coils for large magnetic gradients in compressed MOT sequences (see VI.1.2), which would not be possible with normal MOT coils.*

4 The atom-optics apparatus: compact, yet versatile

In order to pave the way for transportable coherent atom-interferometric inertial sensors we have designed a compact experiment. Yet we kept a large freedom to implement new techniques and change technical choices. This apparatus is not an engineering prototype, but a laboratory experiment. Having to design the experiment with compactness in mind forced us to explore new layouts that can be used for a next-generation, smaller and lighter apparatus, that can be used to perform experiments in the Zero-G Airbus. By measuring the requirements of the current experiment, the next prototype can establish more precisely-defined specifications and avoid over-, or under-, engineering.

We choose to limit the dimensions of the atomic-physics apparatus to $1200 \times 900 \times 900$ mm. We paid no attention to the volume of the control electronics and semiconductor laser sources, as techniques to miniaturize these are well-known and beyond the scope of an atomic-physics laboratory.

4.1 Vacuum system

We designed the apparatus by starting from the different requirements set by our experimental goals, specifying the optical and mechanical access needed for the beams and coils. The science chamber was designed to accommodate these constraints. Specifically we need:

- 0.1 NA optical access for both the input and the output of the dipole trap beams, in two different directions separated by 70° to 90°.
- Mechanical access for the large coils. The coils themselves are designed to leave enough access for the different beams.
- Optical access for 25 mm diameter MOT beams, along six orthogonal directions, one of them aligned with the axis of the coils.
- Optical access for a small-diameter optical-pumping beam, very well aligned with the axis of the coils, to be able to shine σ-polarized light on the atoms.
- Optical access for an imaging beam and a lens at the output of the beam. Ideally the lens should be as close as possible to the atoms and have a large numerical aperture for a good diffraction limit on the imaging resolution.
- Optical access for vertical Raman-pulse beams for a light-pulse gravimeter.
- One or more vacuum ports with a good conductance for pumps.
- An input for the slow atomic beam.

Design of the science chamber A glass cell provides full optical access and can be small enough to position the coils close to the atoms, but as the glass is not anti-reflection coated on the inside of the cell, it is incompatible with the high-power laser we use for the dipole trap. Our science chamber provides large optical access through two CF160 viewports positioned as close as possible to each other in an octagonal configuration (see Figure V.30). This opens two 90° angle cones of optical access to the atoms, which we use for the crossed dipole trap beams, with an angle of 70° between each other, and a NA of 0.1.

The coils are wound around the octagon and the chamber has been designed to leave as much room as possible close to the atoms (the lateral flanges have been moved away from the central cylinder and the coils fit in the resulting gap). In order not to obstruct the access at 45° of their axis for the dipole trap beam, the coils are not exactly in Helmholtz configuration. This introduces a slight second-order curvature, but the effect of this curvature is limited by the size of the coils compared to the size of the region explored by the atoms (see §V.3.2).

Allocation of the different ports The potential created by the crossed dipole trap is steeper in the direction orthogonal to both beams. We use this steep potential gradient to compensate gravity, but want a weaker confinement along the horizontal plane. We therefore propagate both beams in the horizontal plane. The octagon is standing on its side, with the two CF160 viewports serving as access for the dipole trap beams.

Gravity deflects the slow atomic beams and can lead to a loss of atoms in the beam transferring from the collection chamber to the science chamber; the tube connecting the two should be as vertical as possible. However, in the long run, optical access along the vertical direction will be required to add Raman beams for a light-pulse gravimeter. To leave vertical access for the Raman beams we connected the collection chamber at a 45° angle from the vertical. The MOT beams must propagate along three orthogonal directions, one of them being along the axis of the coils. We use the optical access for the Raman beams for one of the other counter-propagating beam pairs. The remaining pair are sent along the horizontal direction. The MOT beams along the axis of the field have a small angle (5°) with the axis of the magnetic field to leave access for a small optical pumping beam well-aligned with the field to produce well polarized σ light. Indeed the MOT is not very sensitive to a slight mis-alignment whereas the quality of optical pumping is strongly reduced by improperly polarized light. The imaging beam is sent along the remaining axis with optical access, the diagonal opposite to the collection chamber. The imaging optics and the camera are positioned as low as possible on the optical breadboard to limit vibrations in the imaging system[28].

[28]BECs are imaged with coherent light and stray reflections on optical surfaces introduce fringes in the images. These fringes are suppressed by a differential measurement, namely dividing two images, one with the atoms, another without. Movements of the optics between the acquisition of the two images displace the fringes and they are no longer canceled by the image division. Vibration of the imaging system is one of the important factors that limits imaging BECs.

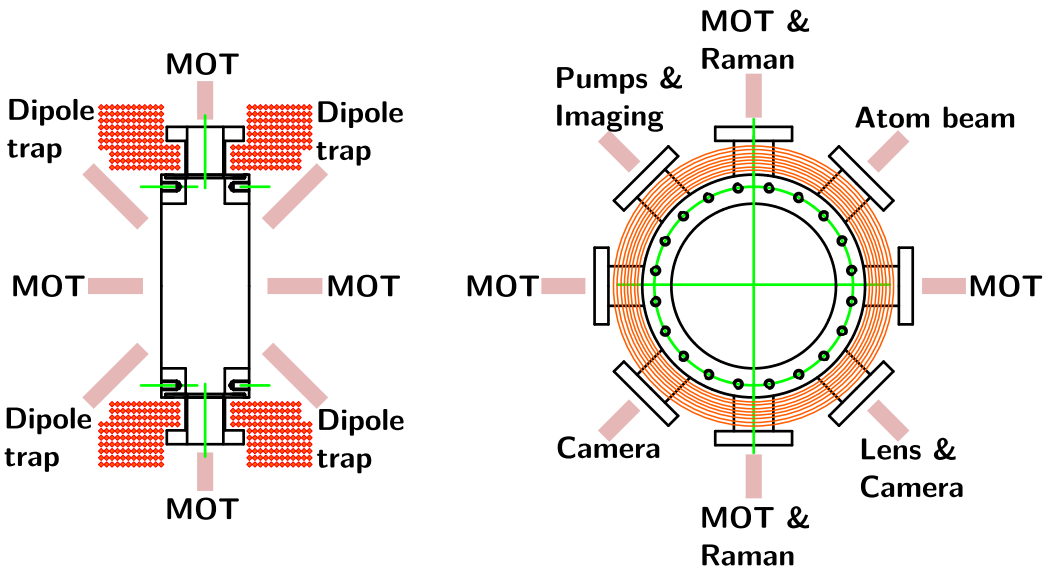

Figure V.30 – **Beam configuration around the science chamber**
The science chamber has two large CF160 ports for optical access at 45°, and eight CF40 ports for various optical and vacuum access. The coils wound around the chamber do not hinder the optical access.

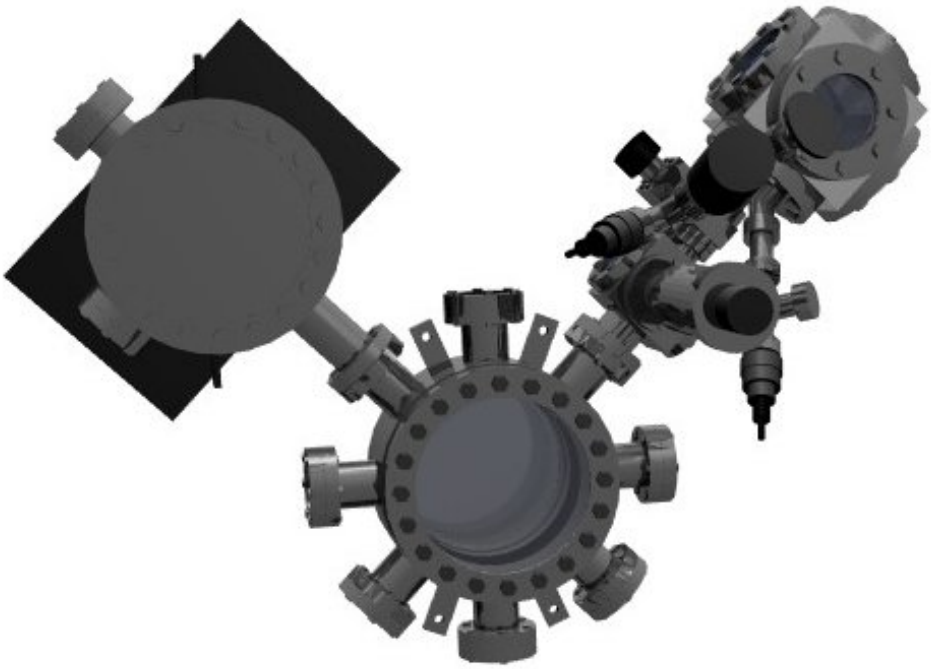

Figure V.31 – **The vacuum system**
The pumps (an ion pump with a titanium sublimation pump in the same chamber) are on the top left, connected to the science chamber, in the center. The collection chamber is on the top right. It is separated from the science chamber by a gate valve and an activated-alloy getter pump (SAES Sorbac st-707) to keep a large vacuum difference between the two chambers.

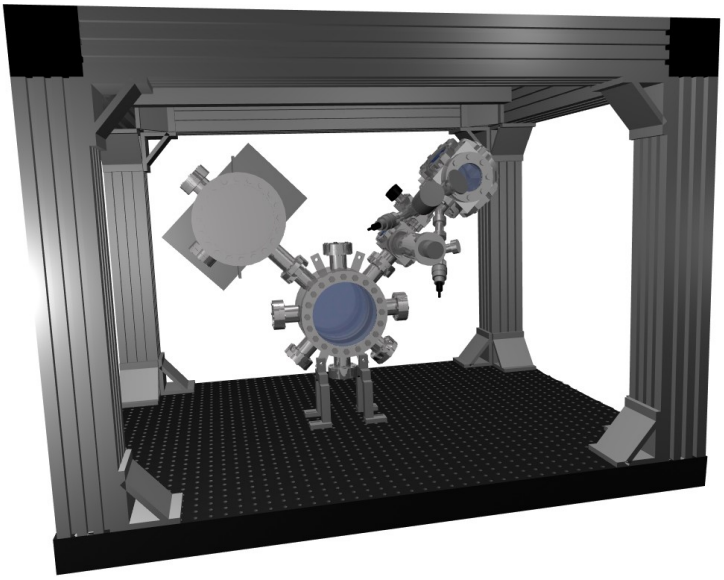

FIGURE V.32 – **The rigid frame enclosing the apparatus**

Finally, the pumps are connected on the last port going upward (see Figure V.31), both to keep the footprint of the system as small as possible, and to keep the science chamber as close as possible to the optical breadboard, in order to reduce the mechanical vibrations in the optics sending the beam in the chamber[29].

We have measured MOT lifetimes of 10 s. This corresponds to a vacuum slightly higher than 10^{-10} mBar which is good enough for our needs.

Support of the vacuum system The vacuum system has been designed to limit its footprint by extending in the vertical direction rather than along the horizontal plane. In order to leave as much as possible the optical breadboard below the vacuum system free to be used for optical setups, we supported the vacuum system from a rigid frame enclosing the apparatus (see Figure V.32). This frame was built from robust optical rails[30]. The frame provides a support to explore the third dimension for much more equipment than the vacuum system itself and helps limit the footprint of the apparatus.

[29]Vibrations in the dipole trap laser at the trapping frequency heat the trapped cloud of atoms (Gehm *et al.* [166]). Previous experience in the group has shown that optics mounted on long rods vibrate and that servo-locking the position of the beam with high enough bandwidth was a lot of work. The best solution to avoid vibrations is either to use large, heavy damped stands, or to avoid tall stands.

[30]Newport T100 series. These rails are both very robust and compatible with standard components such as those provided by ITEM (http://www.itemamerica.com) and machined to optical precision, unlike ITEM components which are extruded. They are no longer manufactured and no real equivalent can be found. We bought the last parts in stock and use ITEM components to complete the setup.

To attach the vacuum chamber to the frame, we used high-strength slings[31]. The vacuum system is attached on the optical breadboard from its lowest point with stainless steel mounts. Other end points of the vacuum system are firmly help in several directions by slings. In order to prevent mechanical deformations of the apparatus if it is transported, we use turnbuckles[32] to control the tension of the slings pulling in different directions and pre-stress the slings. We slowly increase the tension on the slings while monitoring the position of the vacuum chamber with a workshop's micrometer. Ideally, the vacuum system should not be suspended from the frame, but also pulled down with slings to pre-stress it in the vertical direction. We have not installed enough slings for this purpose and plan to do so only if the set-up is really used as a transportable gravimeter, e.g. in the Zero-G airbus.

High-tech exotic fiber slings are stronger and easier to work with than steel cables or chains. However they very slowly relax and the forces can become unbalanced. Moreover they cannot withstand high temperatures and need to be air cooled during bake out of the vacuum system.

4.2 Experimental setup for the 3D-MOT

Splitting into six beams The laser light for the rubidium MOT is expanded from an optical fiber into a 30 mm $1/e^2$-diameter beam. Both frequencies (trapping and repumping lasers) are coupled in the same fiber. Immediately after the fiber we impose the polarization axis with a Polarcor polarizer. Polarization fluctuations due to drift of the birefringence of the fiber are transformed in intensity fluctuations. The beam is then divided into six through five non-polarizing beam-splitting cubes and sent to the science chamber.

The beam path of the four horizontal MOT beams is such that they travel roughly the same distance before entering the vacuum chamber. This way the repumper can be injected via the back of the dividing beam-splitting cube and a hole in the repumping beam can be imaged onto the cloud, thus forming a dark MOT (Ketterle *et al.* [167], see also Le Coq [141] for a possible layout). This future enhancement may prove important to enhance the number of Potassium atoms (K. Sengstock, private communication).

Beam path The optics for beam expansion and splitting are mounted on a 600×600 mm light aluminum breadboard positioned above the science chamber, at the top of the frame enclosing the apparatus (see Figure V.33). Positioning this breadboard on the top of the apparatus avoids using space on the large breadboard

[31] Mountain climbing slings made of Dyneema. Dyneema has a Young's modulus greater than that of steel, and is well suited for the pre-stressing of structures. It is used for this purpose in high performance sailing.

[32] Turnbuckles are a standard piece of equipment used in pre-stressed constructions with ropes or cables such as bridges or ship rigs. Turnbuckles of adequate dimensions for our purposes can be bought in shipchandlers such as ACMO (http://www.acmo.fr/).

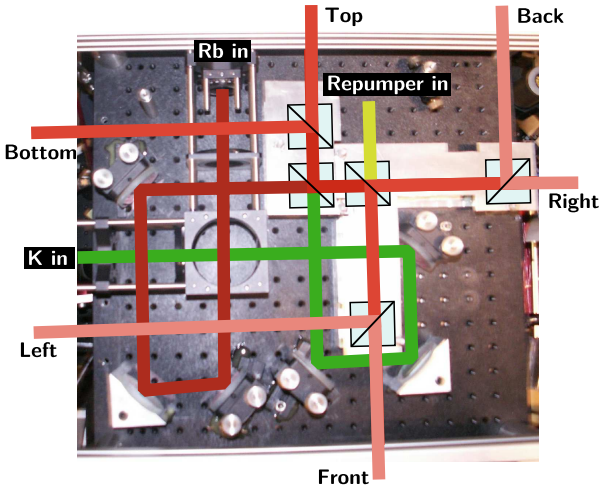

FIGURE V.33 – **Expansion and splitting of the MOT beams**
There are three possible inputs, two for rubidium and potassium light, and one for a repumper beam in which a small mask can be imaged in the center of the chamber. The entry port of the repumper is located above the MOT cloud. The beam path is symmetrical for the four horizontal beams to ensure equal distance to the target. Optical setups with 30 mm diameter beams are bulky, but the layout has been optimized to fit on a 600×600 mm breadboard. The various beam-splitting cubes are glued on a precisely-machined support and clamped by a large plate.

forming the baseplate of the apparatus. We allot this space for beams for which vibration control is critical. The drawback of this arrangement is that the MOT beams have to be periscoped down to the chamber over a large distance ($\sim$ 800 mm, see Figure V.34). While this provides a large dog-leg very convenient for beam alignment, this beam alignment can easily drift, as the frame deforms due to temperature changes. In an air-conditioned laboratory, this is not a problem, but if the experiment is to be transported, or installed in a more hostile environment it will probably be necessary to servo-lock the temperature of the frame above room temperature with heating elements. A MOT, by itself, is not very sensitive to alignment[33], and misalignment observed in the lab has always been due to human intervention. The lower mirror-mount of the periscope is mounted on a 25 mm post, bolted and glued on the breadboard. Just after the mirror, the beam goes thought a diaphragm before entering the chamber. After leaving the chamber it passes a second diaphragm, that of the counter-propagating beam. These two diaphragms have been carefully adjusted and are solidly clamped and glued in place. They define the optimum beam alignment for the MOT and make re-alignment an easier task.

Power balance and polarization of the beams We use solely non-polarizing beam-splitting cubes. Using polarizing beam-splitters would force us to use a combination of bi-chromatic wave-plates to rotate both the potassium 767 nm laser-cooling light and the rubidium 780 nm light. We were not able to buy non-polarizing cubes with the intensity balanced between the two ports to better than 4%. This power imbalance is later turned into a net loss in power as we reduce the excess power to equalize the power in counter-propagating beam pairs. The last optical element before a beam enters the vacuum chamber is a quarter-wave plate glued on a Polarcor polarizer to form a well-controlled circular polarizer. The angle between the polarizer and the quarter-wave plate has been adjusted separately by zeroing the return

[33]When loading a small trap from a MOT, the loading process can be very sensitive to MOT alignment, but the performance of a MOT by itself is not.

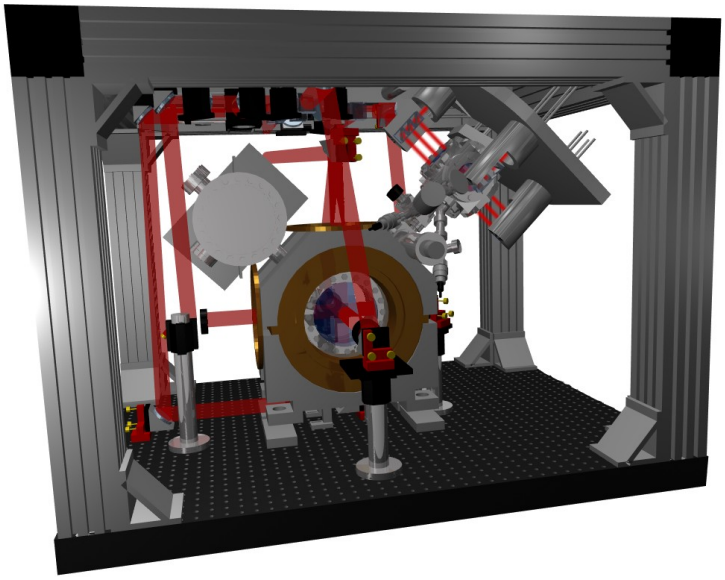

Figure V.34 – **The beam paths of the 3D-MOT**
The MOT beams are expanded from fibers at the top of the apparatus, on a breadboard[a] and mirror-mounts attached to the rigid frame. They are sent to the science chamber via periscopes going around the chamber.

[a]This breadboard is not shown on this figure, but the optical parts that it supports are.

power of a beam retro-reflected through both components. The power balance between the beams is tuned by rotating the circular polarizer relatively to the incoming linearly-polarized light. The benefit of working with non-polarizing beam-splitters and circular polarizers is that both the power balance and the polarization are very stable. After balancing the power in each beam, we adjust the balance of the molasses forces by monitoring the expansion of the cloud on a CCD camera and fine-tuning the position of the zero of magnetic field gradient with compensation coils. We work with currents of a few Amperes and low-resistance compensation coils, to use the current-limited power supplies in a regime where they are most stable. We seldom re-balance magnetic field or beam intensity.

It should be noted that the beam-path after the expansion of the fiber brings along heavy power losses. First of all, the beam-splitting cubes and polarcor have a large absorption, second the expanded beam is larger than the optics, as we want to achieve high intensities on the edge of the beam. All in all, we loose approximately half of the total power from the fiber to the chamber.

4.3 Operation of the 2D-MOT

Producing a dilute vapor of ^{87}Rb and ^{40}K

We use alkali-metal dispensers[34] to release an atomic vapor in our collection cell. The dispensers are made of a small vessel, containing an alkali salt as well as a reducing agent, connected to electrically conducting leads. Running a electrical current in the dispensers triggers a chemical reduction of the alkali salt, and pure alkali vapor is released. For natural-isotopical-abundance alkalis, dispensers are available commercially[35].

The fermionic isotope of potassium is ^{40}K. Its natural isotopical abundance is 0.012%. Although the cooling and collimating process of the 2D-MOT is isotope-selective, and therefore an enrichment process, it is preferable to start from an enriched vapor, as the output flux is, as long as collisions can be neglected, proportional to the partial pressure of the target isotope. Isotopically-enriched potassium dispensers can be built from enriched[36] KCl and calcium (Demarco [128]). This operation requires a clean-box setup and we have a collaboration with J. Thywissen in Toronto to use his installation and knowledge to build our dispensers.

At the time of the writing, we have not yet used enriched sources. In our collection chamber, we have two rubidium dispensers and two potassium dispensers. We estimate one rubidium dispenser with a current of 5.2 A yields a pressure of approximately 10^{-6} mBar. On a day to day basis, we run the dispensers at 4.0 A as this gives us enough flux and insures a lifetime of the dispensers of at least one year. We have enough room and electrical connections in the vacuum chamber for four dispensers. We currently have two rubidium and two natural-isotopical-abundance potassium dispensers.

2D-MOT layout

Vacuum and optics Our design for the 2D-MOT is a prototype of a future compact layout. The vacuum chamber is a $113 \times 113 \times 113$ mm cube with six CF-60 ports. The racetrack-shaped coils creating the 2D magnetic field gradient are mounted in the vacuum chamber. The former on which they are wound is also the mechanical part in which the exit hole is bored. This insures that the output tube is oriented along the axis of the 2D magnetic field gradient.

The optics for the transverse Doppler cooling are mounted on a large stand-alone mechanical structure that we can pre-align in the absence of the vacuum chamber. For a compact design, we use two sets of counter-propagating beams rather than elongated beams. This avoids having to expand the beams to a large transverse waist, a bulky operation.

[34] Experimental procedures to use dispensers in cold atoms experiments can be found in Rapol *et al.* [149].

[35] We buy our dispensers from SAES getters

[36] Currently KCl enriched only to 7% in ^{40}K is available at reasonable prices.

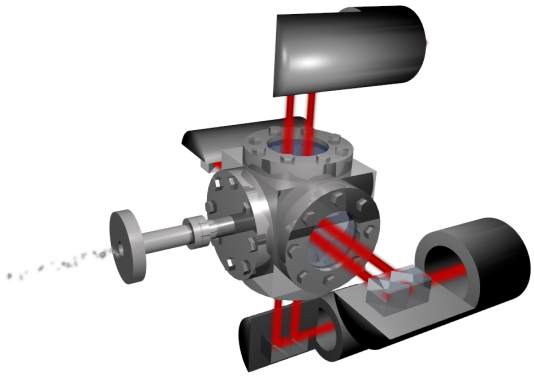

Figure V.35 – **Optics and vacuum system for the 2D-MOT**
The transverse cooling is performed by two sets of counter-propagating lasers mounted one after the other, and separated by non polarizing beam-splitting cubes.
This view shows the original setup, without retro-reflection.

The laser light arrives from the laser sources through two separate fibers. One for each direction. All frequencies (repumper and trapper, for both species) have been mixed in the laser source, and are already injected in the same fiber. The fiber is out-coupled to free space in an "optical cage"[37], without any collimation lens. While the beam is small, it passes through a quarter-wave plate for control of polarization. It is then collimated to a $\sim 15\,\mathrm{mm}$ $1/e^2$-diameter beam by a lens centered on the cage. The beam is divided in two by a non-polarizing beam-splitting cube and the deflected beam is sent to the vacuum system (see Figure V.35). The non-deflected beam is, in its turn, deflected by an internal reflection prism and sent to the chamber. As the internal reflection introduces a π shift between the TE and TM polarization compared to a reflection on a dielectric surface, a half-wave plate is glued to the output of the internal reflection prism, to compensate for the relative shift and achieve the same circular polarization in both beams. Each of these elements has a limited efficiency. In particular, large blocks of glass used for the beam-splitters and the prisms absorb a fraction of the infrared light. In addition, part of the power is lost when the beam is diaphragmed through a limiting aperture[38]. The beam is retro-reflected using a 2" mirror on a kinematic mount behind a 3" quarter-wave plate.

A fifth beam is used to push the atoms longitudinally in the output tube. It is mounted directly on the outer rigid frame and two mirrors are used to inject it through the viewport at the back of the 2D-MOT chamber.

Although the mechanical structure was designed and built with precise alignment in mind, the positioning of the optical elements is not good enough for the counter-propagating beams to be aligned by construction. If two counter-propagating beams do not overlap well, an imbalance in the force is created at the edge of the beams, just before the entrance of the exit tube. This deflects the output jet and crops the low velocity end of the output beam velocity distribution (see V.1.2.2). The collimation lenses are mounted on translation stages to control the propagation direction of the

[37] Thorlabs cage component

[38] The solution to this problem may not to make the $1/e^2$ diameter of the beam smaller, as we are not trying to maximize intensity, but capture velocity, and capture velocity is maximized for a maximum local intensity on the edge of the beam.

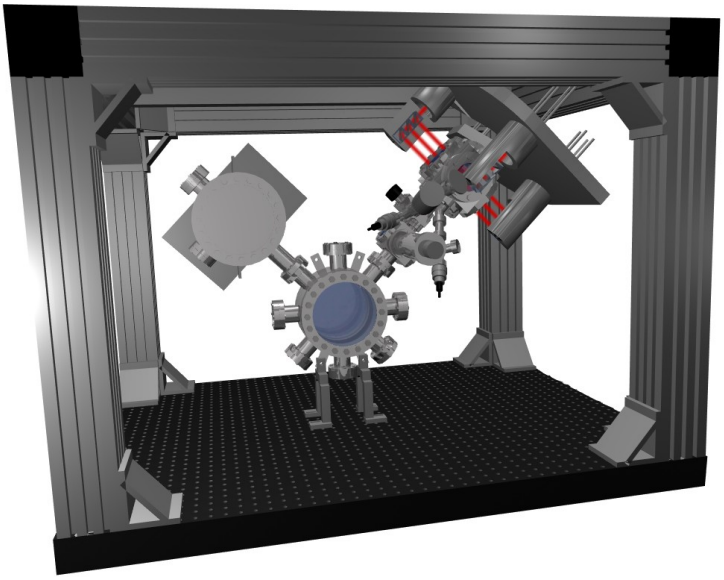

FIGURE V.36 – **The 2D-MOT mechanics mounted on the vacuum system**

beam. As the beam-splitter cube and the total internal reflection prism are not perfectly parallel, the two successive pairs of beams are not parallel either. We optimize the beams just before the output tube, as these are critical. Similarly, as we have no control over the power balance between two successive beams, we balance the power in the beams before the exit, by fine tuning power distribution between the different fibers in the laser source, and leave a small imbalance in the second pair.

Connecting the 2D-MOT to the apparatus To alleviate the deflection due to gravity, the 2D-MOT is mounted above the apparatus, with an exit direction of 45° to vertical (see Figure V.36). The mechanical structure holding the optics is mounted on the outer frame using standard rigid construction items. Compensation coils to shift the zero of the magnetic field gradient are mounted on this structure; we use up to 0.5 G of compensation fields. We use coils wound around the exit tube to compensate for the magnetic field created by the large coils of the 3D-MOT.

Adjusting the 2D-MOT

Adjusting the 2D-MOT to optimize the output flux can be done by optimizing loading time of the 3D-MOT. To do this, the 3D-MOT is switched on and off once per second and the different parameters of the 2D-MOT are tuned.

We balance powers before hand, as a power imbalance cannot be distinguished from a magnetic field offset by the atom's behavior. We geometrically align counter-propagating beams by super-imposing the focused spot of one beam on the fiber tip of its opposite match. Using a circular analyzer, we adjust the quarter wave plate for good circular polarization. Compensation coils are set to optimize the output flux. Next, polarization of each beam is fine-tuned to optimize flux. Finally, polarization,

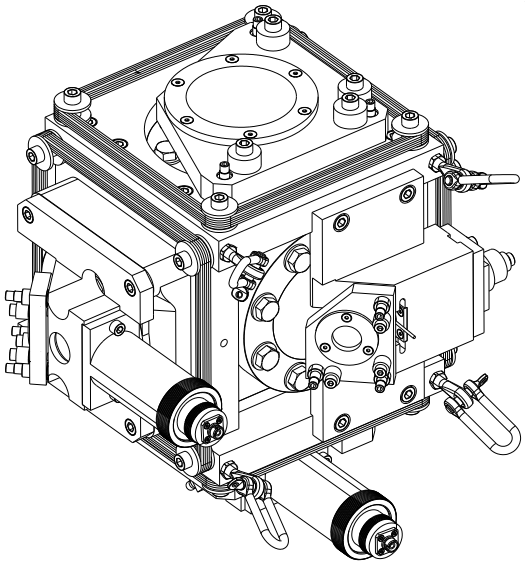

Figure V.37 – **Second-generation mechanics for the 2D-MOT**
The mechanical structure is directly assembled on the vacuum chamber. Two custom-made collimation tubes (left and bottom) serve for beam expansion out of the fiber. The beam-splitter cube is mounted inside the structure. A mirror is mounted on an separate adjustable part. The two beams pass through the chamber and are retro-reflected by an adjustable 3" mirror, with a quarter-wave positioned just before. Compensation coils are winded on the mechanical structure. Slings supporting the vacuum system are directly attached to the mechanical structure via carabiners screwed in its back. The structure itself holds the vacuum chamber by clamping it between a limited number of point contacts. A small collimation tube and an adjustable mirror are mounted at the back for a pusher beam.
Drawing and mechanical design by P.Fournier.

frequency, and alignment of the pusher beam is optimized, also by monitoring the output flux.

Second-generation design

Higher intensities A second-generation design of the 2D-MOT mechanical setup has been has been built and awaits assembling (see Figure V.37). It uses elliptical beams to increase intensity in the central region.

Improving mid-term stability Apart from drift of the total laser power (see §IV.3.1), the main source of instability in our atomic beam is the drift in polarization due to thermal drift of the fibers[39]. A small change in polarization of one arm is very detrimental to the performance of the 2D-MOT as it induces an imbalance in the Doppler-cooling process, and a deviation of the beam coming out of the trapped cloud. By switching to retro-reflected beams, we hope to that the change in polarization will have a less drastic effect, as it will affect similarly both counter-propagating beams.

The second source of instability is mechanical drift of the beams. First of all, the translation mounts used to move the collimation lens and to adjust the lateral beams, have poor long term thermal stability. The new design replaces translation stages by kinematic mounts which have a better stability. Second, due to the pointing drift of the pusher beam, mounted on the outer frame, a realignment of the beam can be necessary on a near weekly basis. The new layout uses a compact design for the pusher beam-path, minimizing the length of mechanical part liable to drift.

[39]We use polarization-maintaining fibers but it seems that their axis changes slightly over a period of one month, and the input polarization must be re-adjusted to match one of the axis. As we don't have an ellipsometer, this is a lengthy process.

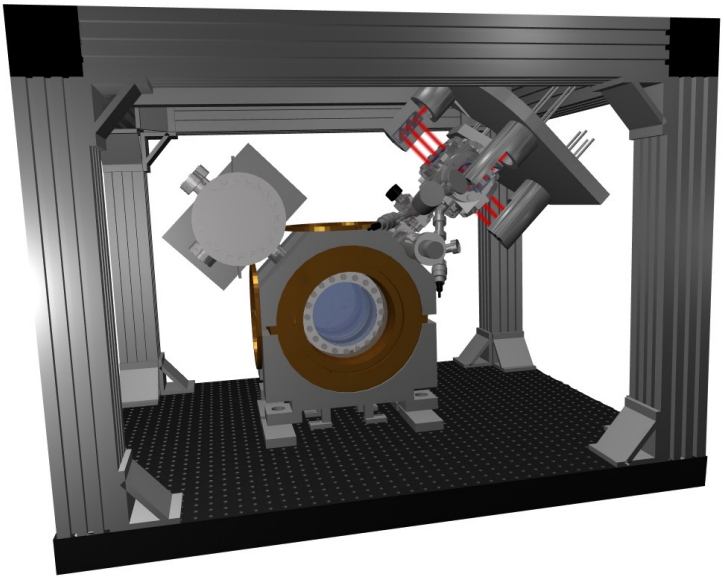

FIGURE V.38 – **The coils and their mounts assembled around the chamber**

Overall, the second-generation mechanics uses the experience acquired from the first generation to build a very compact and, we hope, stable layout.

4.4 Mounting the Feshbach-resonance coils

The coils for the Feshbach-resonance-inducing dipolar magnetic field weigh 25 kg each and occupy a central position in the apparatus: the immediate surroundings of the science chamber. Although they have been designed to closely fit to the vacuum chamber, proper mounting mechanics are required. Indeed to achieve a stability of the magnetic field to the part per million, the accuracy of our power-supply, the coils should be well fixed in position and not move when subjected to changing electromagnetic forces while switching.

Large two-part circular duraluminium "V-mounts" (see Figure V.38) have been machined for this purpose. They are supported by M-30 stainless steel threaded rods, for control of their height, bolted in stainless steel base-plates, themselves bolted in the breadboard via eight M-6 screws. The two mounts face each other, with the coils separated by the vacuum chamber between them. Threaded rods connect the opposite mounts together and are fastened to robustly clamp the coils in the lateral direction. Well-dimensioned spacers are inserted between the pair of coils, to avoid applying pressure on the chamber.

The coils and their mounts completely occupy the useful volume around the chamber. The mounts are laden with threaded holes used to mount optics, sensors, and the compensation coils for the MOT.

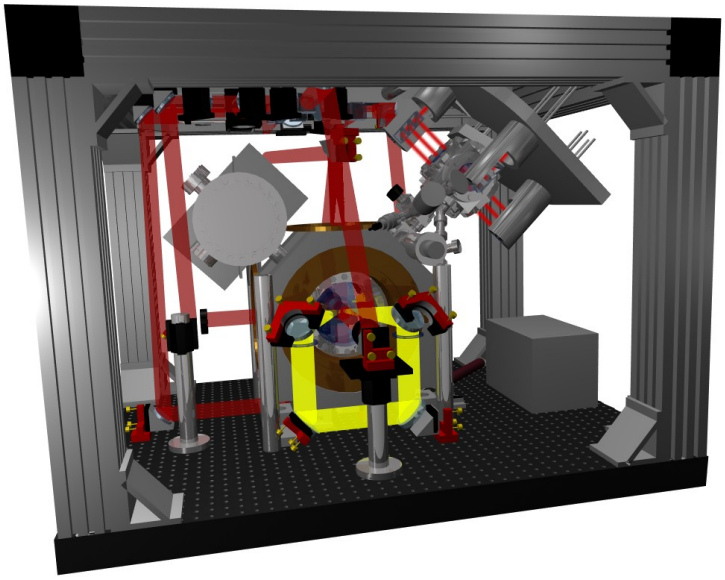

Figure V.39 – **The crossed dipole-trap setup**
The dipole trap beam is represented in yellow. This view shows the $1:1$ confocal telescope used to re-inject the beam in the chamber for recirculating the power. The rail for the mechanical zoom is not shown.

4.5 Beam path for the crossed dipole trap

The optical setup for the recirculating, compressible, crossed-optical dipole trap should both fit in the volume of the apparatus, and take advantage of the optical access of the science chamber while leaving access for existing, and future, beams to manipulate the atoms.

Precise alignment of the different optical components is important for the optical quality of the beam. Lenses should be well centered, and perpendicular to the beam, to work on axis, with low angles. A mechanical rail setup has been designed to hold as much as possible optics for the mechanical zoom in a well-controlled straight line, but the last lens has to be close to the vacuum chamber for a large image-side NA; it is held on a separate mount.

Most of the optics are mounted as close as possible to the optical breadboard to avoid vibrations. The beam enters and exits the chamber four times for the crossed dipole trap. Each time it is raised 200 mm to the chamber by a periscope. The last element before the chamber is a dichroic mirror that reflects the 1 565 nm dipole trap, but is transparent to 780 nm. This leaves optical access for beams for atomic manipulation (see Figure V.39). The large NA lenses for focusing the beam in the chamber are positioned on five-axis kinematic mounts, just before the dichroic mirror, in the middle of the periscope.

4.6 Imaging

We image the trapped cloud of atoms by absorption imaging[40]. Briefly, the cloud is released from the trap and, eventually after an expansion period, a beam of collimated resonant light is shone onto the atoms. An optical system collects the light after the cloud and images on a CCD camera the shadow cast by the cloud in the beam. For high-resolution imaging, the requirements on the imaging optical system are similar to those on the dipole trap optics: high NA and good control of aberrations to image small details at the diffraction limit. Requirements specific to imaging add to this: the magnification of the optical system should be well known; its luminosity should be constant over the working field; in other words, vignetting should be reduced as much as possible[41].

As we want to work with long free-flight times to investigate long-interrogation-time atom interferometry, we want good imaging over a large volume. This means that the optical quality of the system should be preserved in the lateral field. As for the longitudinal depth of field, it is limited by the large NA. It is difficult to calibrate the imaging system magnification in situ[42], as we do not know a priori the size of the features observed on the atomic cloud. BEC experiments often resort to optical systems where the dependence of magnification on the working distance is small. In optical engineering terms, these system are doubly-telecentric optical systems. A frequently used layout is a 1 : 1 confocal telescope, to make an image of the BEC out of the chamber, and a short-working-distance microscope objective lens to enlarge this virtual object on a CCD camera.

Designing a high quality objective lens to image the cloud out of the chamber is a complex task. The resulting system is likely to be expensive, due to the cost of both non-mass-produced lenses and the precision mechanics required to hold the optics in place. It is not to hard to design a system with a good on-axis resolution, as only the spherical aberration needs to be canceled out. Most BEC groups assemble their own. However, due to imperfections in the alignment, lenses always work slightly off-axis. Moreover the resolution of a naively-designed imaging system quickly drops in the lateral field. Finally, due to our compact apparatus, we cannot propagate the beam long enough to use the often-used confocal telescope setup.

Industrial machine-vision objective lenses offer a low cost, compact, and high-quality alternative to custom-made systems. Telecentric objective lenses are used for metrology purposes on assembly lines, or in medical imaging. Our vacuum chamber limits the NA at 0.13 (ie a diffraction limited resolution of $\sim 6\,\mu$m with 780 nm wavelength light) and imposes a working distance of at least 160 mm. Zeiss and Schneider optics are the two companies producing high-NA, diffraction-limited, telecentric lenses

[40] see e.g. Ketterle *et al.* [168] for a discussion of absorption imaging.

[41] With absorption imaging this is actually not critical, as the imaging sequence uses a comparison between images with and without atoms that cancels out intensity differences. However vignetting also induces field aberrations

[42] Magnification can be estimated by measuring the acceleration of a free-falling cold atomic cloud, but it is difficult to have a precise measurement.

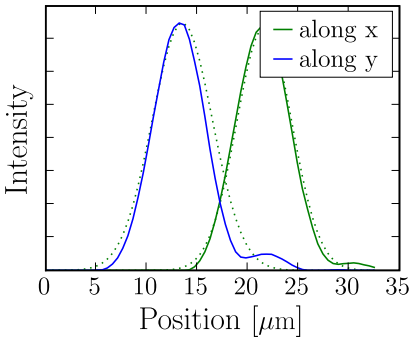

Figure V.40 – **Point spread function of the imaging lens**
The half width at half maximum of a Gaussian fitted to the curves is 6 μm.

with large working distances[43]. Only one objective lens on their catalog meets our requirements, the Xenoplan 1:3 by Schneider. Testing the lens on a Zygo interferometer confirmed the advertized resolution: diffraction limit both on axis, and at an angle of 2°. We also tested the objective lens at 780 nm by using a bare fiber as a point source, and recording the resulting image on a CCD camera with a microscope objective. This setup simulates our imaging procedure. The core of the fiber used was smaller than the diffraction limit, the resulting bell-shaped curve is thus the point spread function of our optical system. The microscope objective used has a higher NA than the telecentric lens. The measurement shows that the resulting imaging system is indeed at the diffraction-limited resolution of the telecentric lens (see Figure V.40).

The imaging lens is too long to fit on the apparatus at the required position: the beam path is going downward and runs for only 150 mm outside the chamber before it hits the breadboard. Adding a mirror to deflect the beam while keeping the full numerical aperture of the viewport would double the working distance, and no telecentric lens is commercially available with such a long working distance. We modified the Xenoplan telecentric lens to add an angle between its input and its output. Doubly-telecentric lenses are most often made from a symmetrical optical layout and, although the manufacturer would not provide us with details of the inner parts of the lens, we guessed that it would be made of two separate barrels holding complex lens assemblies, with an adjustable diaphragm in between. We carefully cut apart the lens and retrieved the two barrels. A precision, single-block, mount for the barrels and a mirror deflecting the beam, was designed and precision-machined to reconstruct a well-aligned beam path with a 60° angle. The resulting mount holds the objective lens and is positioned on the breadboard. At its output, a microscope objective collects the light. It is mounted on an extension tube screwed in the camera's C-mount. The camera itself is positioned on an xyz translation stage. As the objective lens has a good resolution even in its lateral field[44], it does not need to be precisely aligned and is simply glued and clamped to the table.

[43] One can easily buy telecentric microscope lenses with very short working distances, but imaging small details at a large distance is an intrinsically difficult problem that the industry avoids by placing the lens close enough to the object to be inspected. High-NA long-working-distance objective lenses are thus hard to find.

[44] The modified objective lens was examined on the Zygo interferometer and little to no performance drop was observed compared with the measurement on the original objective lens.

We cannot record a point spread function for the resulting imaging system, as the object plane is in the vacuum system, but we suspect that its resolution will be smaller than the one measured on the test system. Indeed, the camera and microscope tube are not held on an optical rail and are most likely mounted with a small angle relatively to the beam propagation. The microscope objective's off-axis aberrations are not known. The real limits of the imaging system are hard to evaluate, as we need a target with very small features in the vacuum chamber[45].

4.7 Automation and control

An experimental run (loading the 3D-MOT, or the dipole trap, performing a time-of-flight sequence...) is made of a sequence of experimental events such as shifting the frequency of a laser, switching a magnetic field, or turning on or off a beam. The timing of the sequence is precisely controlled by a hard-real-time[46] embedded device developed by André Villing, the group's electronics engineer, with a time step of 1 μs. This sequencer is connected via TTL or analog channels to the instruments. Sequences are loaded on this device by the computer that runs the experiment. A computer is required not only to scan parameters from a sequence to another, but also to load, process, and store the images captured by the camera.

For the control software, we adapted to our needs an architecture used by the group on other experiments. We use MatLab as a framework to graphically edit the sequences, to load them on the sequencer, to retrieve the images from the camera, to process them and to display them. The camera is controlled via a low-level C library dynamically loaded in Matlab's memory. Raw access to the camera SDK allows non blocking input/output, specifically not to hang the Matlab engine while the camera waits for a hardware trigger. As Matlab's engine does not allow any parallel execution of operations[47], running an experiment with several computer-controlled instruments driven at the same time requires to interleave non-blocking calls to the instruments. The software sequence that controls the experiment follows:

1. The parameters of the run are saved to a file.

2. The parameters of the camera are set, and the camera is told to wait for the hardware trigger.

3. The sequence is uploaded to the sequencer and the sequencer is given the start signal.

[45] Using tomography of the dipole trap, has discussed in §VI.1.1, we have observed features as small as 12 μm.

[46] Hard real-time, as opposed to soft real-time, means that the timings are guarantied be the design of the system, and not dependent on environment. Computer systems are most often soft real-time devices, and a extra load of calculation can introduce unwanted delays.

[47] The Matlab virtual machine in which the m-language scripts are executed is fundamentally mono-threaded, as it has no memory isolation of the variables, and no notion of locks.

4. The sequencer runs the sequence, trigging the camera once or more during the run.

5. The sequencer calls back, signaling the end of the sequence to the computer.

6. The computer downloads the data from the camera, processes it and displays the results (estimated number of atoms, center of cloud, temperature...).

7. The data is saved to the disk and logged.

Steps 2 and 6 are flexible and the computer actually runs a list of hardware-related operations. In addition to initializing the camera and retrieving the images, we may change set points or program different devices using e.g. the GPIB bus or TCP/IP communication. The translation stage for the compressible dipole trap can be programmed during these steps.

This sequential design shows its limits as it produces code hard to read. Moreover, it would not scale very well if more instruments were to be added in the control loop. An event-based parallel design would be more adapted, but it is impossible with MatLab.

The experimental apparatus for cooling a boson-fermion mixture to quantum degeneracy has to face the challenges brought by the requirements of compactness and robustness on top of the challenges involved in a double specie ultra-cold atomic physic experiment. The resulting design is innovative among cold atoms setups by its extensive use of the third dimension, but also by new semiconductor laser sources, a unique optical layout for the dipole trap, and a chamber with two $90°$ *cones of optical access.*

Chapter VI

Loading laser-cooled atoms in a dipole trap

Le meilleur cheval,
c'est celui qu'on a dans son écurie.
Proverbe moustachu

This chapter presents the first experimental results for the loading of the dipole trap from laser-cooled atoms. In addition, in the second section, I present simple theoretical studies of possible schemes to combine laser cooling and the dipole trap.

Dipole traps used to produce BECs have to be made of far-detuned light, in order to avoid spontaneous emission and therefore heating of the BEC. Far-Off-Resonance Traps (FORTs) used for this purpose enclose a phase-space volume limited by laser power. On the other hand, to achieve BEC via evaporative cooling (and even more to use a BEC to sympathetically cool a Fermi gas to degeneracy) a large number of trapped atoms is required. A large cloud of atoms will rapidly suffer severe loss due to free evaporation if the trap depth is not several times its temperature[1]. A trap also has to match the spatial extent of the atomic cloud loaded in the trap, to be able to capture it with a reasonable efficiency. All in all, this leads to the conclusion that the phase-space volume of a conservative trap is larger than the phase-space volume covered by the atoms it can capture. Therefore to capture a large volume of atoms at a given phase-space density, a large trap is inevitable. This led us to the acquisition of a powerful laser, 50 W of light at 1565 nm.

We load directly the dipole trap from the MOT. Using a mechanical zoom to control the trap size, evaporation in a dipole trap can be achieved quicker than in a large magnetic trap (Kinoshita *et al.* [169]). Moreover, the optical trap will allow us to use magnetically-tunable Feschbach resonances to avoid the drop in K-Rb collision cross-section at 100 μK (Aubin *et al.* [170]).

[1] A common estimate is that free evaporation starts to be insignificant for trap depth around 5 times the cloud temperature.

Our dipole trap has two interesting features seldom encountered in ultracold-atom experiments: first, its size can be dynamically adjusted, second, the light shifts it produces on the D2 transitions of the rubidium atom (used for Doppler cooling and for absorption imaging) are much larger than the linewidth of the transition.

1 From the MOT to the dipole trap

The dipole trap is first mode-matched to the MOT making its size as large as possible with the available power while keeping its depth on scale with the temperatures of a MOT. A mechanical zoom enables us to go from this configuration, favorable for loading, to a tighter configuration, more favorable for rapid evaporation. In this section we discuss the first experimental results of the transfer of the atoms from the MOT to the dipole trap, in particular the choice of the of the optimal trap size, as well as the possible causes of atom loss during the loading.

1.1 A diagnostic tool: tomography of the dipole trap

Light shift of the D2 transitions

The temperature of a dense laser-cooled sample of rubidium is on the order of $50\,\mu$K. In order to capture such a cloud, the depth of the dipole trap must be a few times larger than the energy corresponding to this temperature, that is a depth of around $150\,\mu\mathrm{K}\cdot k_\mathrm{B}$. The light-shift corresponding to this depth is[2] 3 MHz, this means that the rubidium $5s\,^2S_{1/2}$ level, which is the level that we are interested in trapping, will be shifted by 3 MHz to the red inside the trap compared to its energy outside the trap.

The D2 transition, used in Doppler trapping and cooling as well as in imaging, is the $5s\,^2S_{1/2} \rightarrow 5p\,^2P_{3/2}$ transition. The upper level of this transition has a strong light shift in the presence of our 1565 nm far-off-resonance trapping light. Equation V.18 (on page page 139) gives the energy shift of an atomic level for a two-level atom. In the case of a multi-level atom, each possible transition contributes a similar factor, but instead of the lifetime of the excited state, we have to use the Einstein A coefficient, which gives the departure rate of the population of this energy level along this specific transition (Cohen-Tannoudji *et al.* [156], Johnson [171]). The light-shift for an energy level i is thus given by:

$$U_\mathrm{dip} = I_\mathrm{FORT} \sum_{\left\{\substack{\text{All allowed}\\ i\rightarrow j \text{ transitions}}\right\}} \frac{3\pi\,c^2}{2\omega_{i\rightarrow j}^3}\left(\frac{A_{i\rightarrow j}}{\omega_{i\rightarrow j}-\omega_\mathrm{laser}}+\frac{A_{i\rightarrow j}}{\omega_{i\rightarrow j}+\omega_\mathrm{laser}}\right) \qquad \text{(VI.1)}$$

[2] A good order of magnitude to keep in mind when dealing with quantum effects at finite temperature is that $1\,\mathrm{K} \sim 20\,\mathrm{GHz}$.

$\lvert g\rangle$	→	$\lvert l\rangle$	λ_{gl}[nm]	A_{gl}[10^6 rad · s^{-1}]	p_{gl}[m^2 s]
$5s\,^2S_{1/2}$	→	$5p\,^2P_{1/2}$	794.979	36.1	$-1.3075{\cdot}10^{-36}$
"	→	$5p\,^2P_{3/2}$	780.241	38.1	$-1.2643{\cdot}10^{-36}$
"	→	$6p\,^2P_{1/2}$	421.671	1.50	$-3.4405{\cdot}10^{-39}$
"	→	$6p\,^2P_{3/2}$	420.298	1.77	$-4.00519{\cdot}10^{-39}$
"	→	$7p\,^2P_{1/2}$	359.259	0.289	$-3.4193{\cdot}10^{-40}$
"	→	$7p\,^2P_{3/2}$	358.807	0.396	$-4.6612{\cdot}10^{-40}$
"	→	$8p\,^2P_{1/2}$	335.177	0.0891	$-7.93006{\cdot}10^{-41}$
"	→	$8p\,^2P_{3/2}$	334.966	0.137	$-1.21618{\cdot}10^{-40}$
$5s\,^2S_{1/2}$	→	all			$-2.58031{\cdot}10^{-36}$

TABLE VI.1 – **Transitions used to compute polarizability for the ground state**
Data from the NIST atomic-spectra database (http://physics.nist.gov/PhysRefData/ASD/index.html).

$\lvert e\rangle$	→	$\lvert l\rangle$	λ_{el}[nm]	A_{el}[10^6 rad · s^{-1}]	p_{el}[m^2 s]
$5p\,^2P_{3/2}$	→	$5p\,^2S_{1/2}$	780.241	38.1	$1.2643{\cdot}10^{-36}$
"	→	$6s\,^2S_{1/2}$	1366.875	9.5618	$-9.46910{\cdot}10^{-36}$
"	→	$7s\,^2S_{1/2}$	741.021	3.0339	$-7.93382{\cdot}10^{-38}$
"	→	$8s\,^2S_{1/2}$	616.133	1.4555	$-1.67017{\cdot}10^{-38}$
"	→	$\mathbf{4d\,^2D_{3/2}}$	**1529.261**	**1.774**	$\mathbf{-1.44583{\cdot}10^{-35}}$
"	→	$\mathbf{4d\,^2D_{5/2}}$	**1529.366**	**10.675**	$\mathbf{-8.728031{\cdot}10^{-35}}$
"	→	$5d\,^2D_{3/2}$	776.157	0.67097	$-2.17279{\cdot}10^{-38}$
"	→	$5d\,^2D_{5/2}$	775.978	3.93703	$-1.27355{\cdot}10^{-37}$
"	→	$6d\,^2D_{3/2}$	630.097	0.63045	$-7.979905{\cdot}10^{-39}$
"	→	$6d\,^2D_{5/2}$	630.007	3.71235	$-4.69595{\cdot}10^{-38}$
$5p\,^2P_{3/2}$	→	all			$-1.102435{\cdot}10^{-34}$

TABLE VI.2 – **Transitions used to compute polarizability for the excited state**
Data from the NIST atomic-spectra database (http://physics.nist.gov/PhysRefData/ASD/index.html).

where I_{FORT} is the intensity of the trapping laser, ω_{laser} its angular frequency, and $A_{i\to j}$ and $\omega_{i\to j}$ are the Einstein A coefficient and the angular frequency of the $i \to j$ transition. The Einstein A coefficient $A_{i\to j}$ is the angular frequency corresponding to the departure rate of the atomic level i along the $i \to j$ transition. In the case of a two-level atom, it corresponds to the linewidth Γ of the upper level.

We can see from equation VI.1 that the energy of every atomic level is shifted by an amount proportional to the intensity of the laser: $U_{\mathrm{dip}} = p\, I_{\mathrm{FORT}}$. This ratio is the polarizability of the atomic level, given by the sum in expression VI.1, and differs from one atomic level to the other. For both $\lvert g\rangle$ and $\lvert e\rangle$, the ground and excited

Laser power	25 W
Waist	200 μm
Ground state depth	150 μK
Excited state depth	6 mK
D2 transition detuning	120 MHz $\sim 20\,\Gamma_{\mathrm{Rb}}$

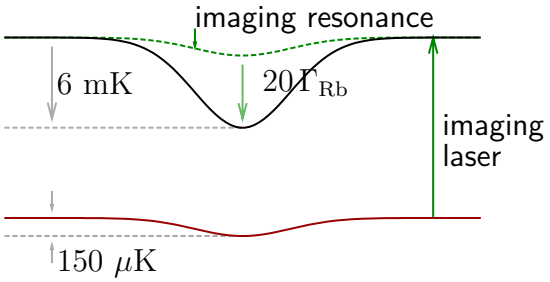

Figure VI.1 – **Light-shift of the upper and lower levels of the D2 transition, and detuning of the imaging laser**

state of the D2 transition, the different terms of the sum over the most important transitions are given in tables VI.1 and VI.2. The excited state of the D2 transition has a couple of transition to a doubly-excited state at 1529 nm. These transitions contribute strongly to the polarizability of this level for a laser at 1565 nm, detuned to the red of these transitions. As a consequence, the excited level is shifted to the red more than the ground state: the ratio of the polarizability is 44.

The D2 transition is thus shifted by 43 times the light shift of the ground state. The light shift of the ground state, imposed by the depth of the trap required to match the cloud temperature, is on the order of 3 MHz. The resulting shift on D2 transition is 120 MHz (see Figure VI.1). Such a large transition shift is unusual in cold-atom experiments. Indeed, choosing laser power and frequency to achieve required trap depth while minimizing photon scattering (see §V.2.1 for a discussion of this choice) limits the maximum light shift in the ground state by leading to the choice of a far off resonance laser. However, in our case, the laser is located close to an excited-level transition, whose photon scattering rate is not important, as it is not populated.

Dipole-trap tomography

This particularity of our system can be exploited to image selectively atoms at a give potential height and provide direct information on the potential landscape and

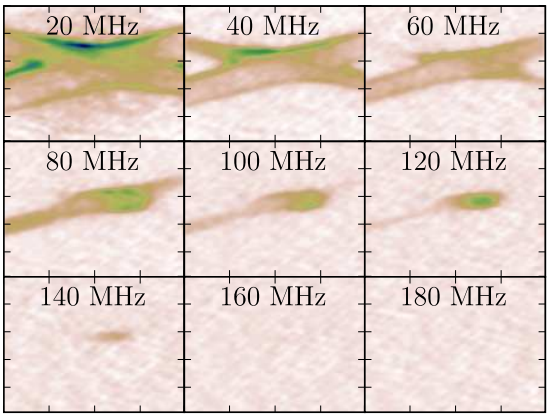

Figure VI.2 – **Tomograms of the cloud in the dipole trap**

Each absorption image addresses selectively atoms at different depths in the dipole trap. Zero detuning (not displayed) corresponds to atoms outside of the trap, while, in this series of images, the bottom of the trap is located at ~ 140 MHz. The images correspond to the visualization of an isosurface of the potential, which is a 3D surface. Thus what is represented is a projection of this atomic population on this surface, and not a cut of this surface along a 2D plane.

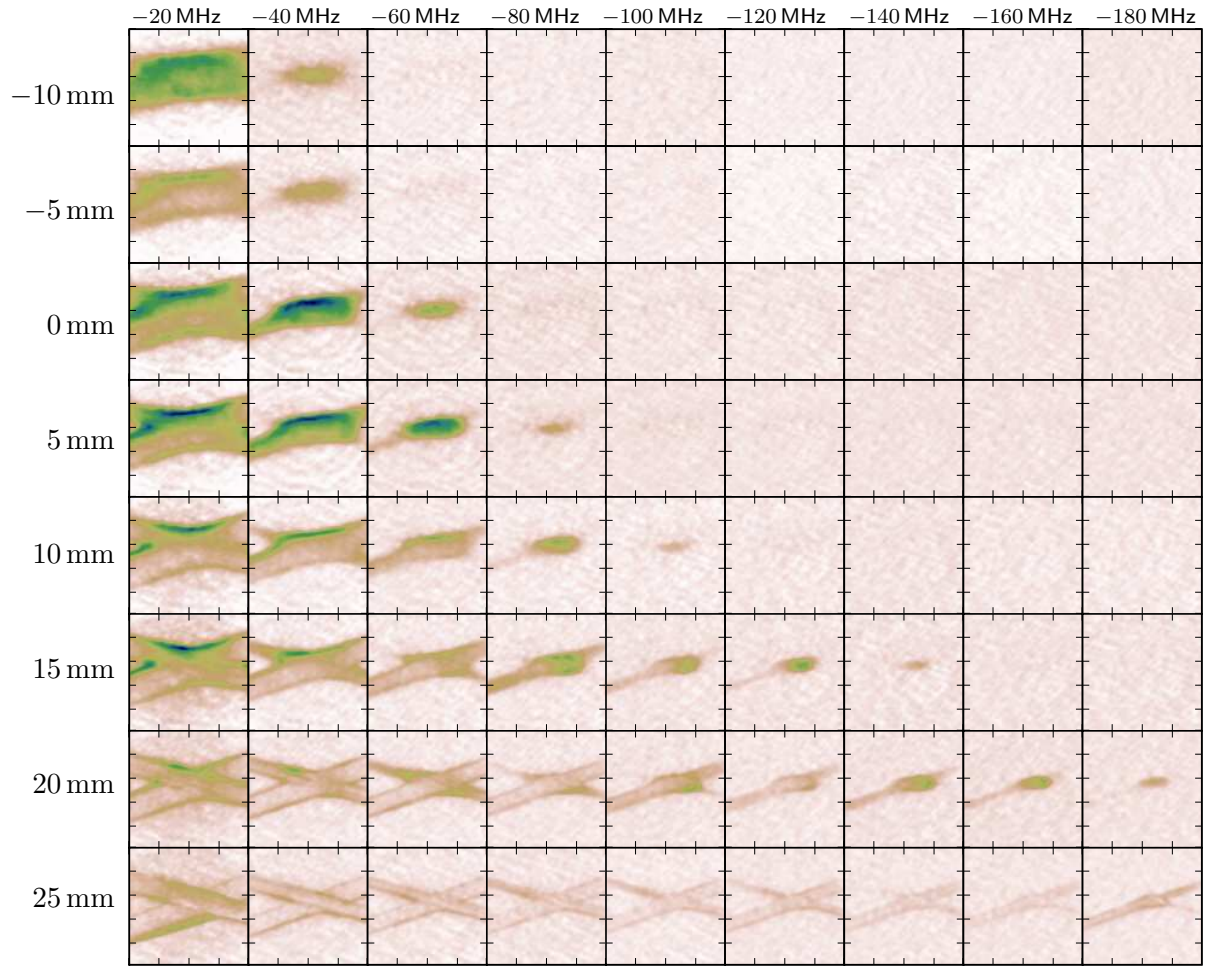

FIGURE VI.3 – **Tomograms of the dipole trap for different positions of the mechanical zoom**

As detailed in §V.2.2, we create our dipole trap by intersecting two focused beams. We control the effective size of the trap by using a mechanical zoom to defocus the beams so that they intersect far from their focal point.

The tomograms of the trap show that we can control the beam size as predicted. These images give access to the actual potential on the atom in spite of poorly-known losses and aberration effects.

Each image corresponds to a 2×2 mm-sized view. The laser power in the first pass used for these data is 28 W.

atomic distribution (as in Salomon *et al.* [172]). Indeed the atomic linewidth, $\Gamma_{\mathrm{Rb}} \sim 6\,\mathrm{MHz}$, is small compared to the detuning of the transition over the complete extent of the trap. By imaging the atoms inside the trap, we can address the different layers of atoms by detuning the imaging laser[3], performing what we call a tomography of the trap, as can be seen in Figure VI.2. We use these *in situ* images to align the dipole trap, to measure the shape and depth of the trapping potential for different positions of the mechanical zoom, and to measure the atomic potential-energy distribution in the trap.

In situ analysis of the beam shape

We would like to compare the size and depth of the dipole trap for which the loading is optimal to the size and temperature of the captured cloud. We can calculate the trap size and depth from our knowledge of the optical setup, but lens focal lengths and positions are only known to a limited precision. Moreover, there are losses and possible aberrations on the viewport of the vacuum chamber. Ideally, it would be necessary to measure the intensity distribution in the vacuum chamber; however, we do not want to break vacuum. To estimate the dimensions and depth of the dipole trap as a function of the position of the lens that we adjust in the mechanical zoom, we can use the tomography images of the dipole trap for different positions of the lens (see Figure VI.3).

Gaussian beam divergence The intensity distribution in a Gaussian beam is given by:

$$I(\mathbf{r}) = \frac{P}{\pi w(z)^2} \exp\left(-\frac{r^2}{2\,w(z)^2}\right) \qquad \text{with} \quad w(z) = w_0\sqrt{1+\left(\frac{z-z_0}{Z_{\mathrm{R}}}\right)^2} \tag{VI.2}$$

Where Z_{R} is the Rayleigh length and w_0 the diffraction-limited waist for the Gaussian beam. Far from the focal point, the beam size ($1/e^2$-radius) increases linearly with a diffraction-limited divergence $\theta = \lambda/(\pi\, w_0)$. We measure the diameter of the trap at half maximum from the tomograms at different positions of the mechanical zoom and infer the value of the waist. We find a divergence of $\theta \sim 27\,\mathrm{mrad}$ (see Figure VI.4),

[3]The imaging laser is locked to a reference laser by beat-note locking (see §IV.1.3). We can thus detune it easily over a wide range of frequencies.

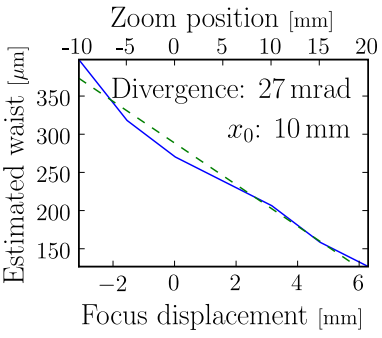

Figure VI.4 – **Divergence of the beam**
We fit the estimate of the waist of the beam to a linear law to extract the divergence and the position of the focal point. The position axis is both given in displacement of the lens we move in the mechanical zoom (top axis) and in the corresponding displacement in the chamber, estimated from the focal lengths of the lenses used (bottom axis).

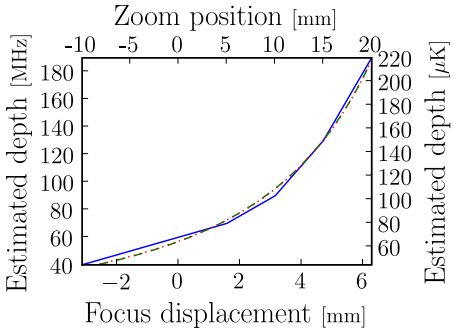

FIGURE VI.5 – **Depth of the dipole trap**
We fit the depth of the trap to formula VI.3 for the depth of a Gaussian beam with the Rayleigh length and the position of the focal point as free parameters. However, a fit to a formula that does not take in account diffraction, $\delta_0/(z-z0)^2$, is indistinguishable from the fit to the more correct formula.

in reasonable agreement with a geometric measurement performed outside the vacuum chamber before the last lens (30 mrad). The w_0 parameter ($1/e^2$-diameter of an aberration-free Gaussian beam) can be compared with the theoretical value: we find 18 μm experimentally, and we expected 15 μm.

Estimate of the beam quality The depth of the trap appears on the tomograms as the largest detuning for which we can still see atoms in the trap. We can measure it more precisely than the width. However, as it is proportional to the laser power that we consider as an unknown, we cannot use it for an independent evalutation of the same beam parameters.

If we neglect diffraction, the diameter of the beam is a linear function of the distance to the focal point, and the maximum trap depth is given by $\delta \propto (z - z_0)^2$. The measured values for the depth fit well this law (see Figure VI.4). However, close-enough to the focal point, the curvature due to diffraction imposes a Lorentzian shape to the depth. The depth of the trap is given by:

$$\delta = \frac{\delta_0}{1 + (\frac{z-z_0}{Z_\mathrm{R}})^2} \tag{VI.3}$$

where δ_0 is the detuning at the focal point. We can extract the value of the Rayleigh length from the measurements of the trap depth in the vicinity of the focal point. We estimate[4] the light-shift at the center of the trap to be on the order of 1.8 GHz. We fit the data to formula VI.3 and find a Rayleigh length of 2.3 mm, which corresponds to a waist at the focal point of $w = 60\,\mu$m ($Z_\mathrm{R} = \pi\, w^2/\lambda$).

This value of the waist is the actual value for the $1/e^2$-diameter at the focal point, including the effects of the aberrations, whereas the value inferred from the divergence of the beam, is the diffraction limited value for an ideal Gaussian beam. The difference between the two can be used to calculate the value of the beam-quality factor: $M = \sqrt{w_\mathrm{measured}/w_\mathrm{ideal}}$. We find $M = 1.8$. This corresponds to the value measured using the Shack-Hartmann wave-front analyzer.

The data points around the focal point are not precise, and we believe this good agreement to be a mere coincidence. However, with more data points this method can

[4] We cannot currently perform tomography at full trapping laser power near the focal point, because the light-shift induced by the laser at full power is too large for the imaging laser. We do have performed such measurements at reduced power.

be used to determine the trap depth and size, robust against ill-controlled aberrations and losses.

1.2 Matching the MOT with the dipole trap

To optimize the number of atoms loaded from the MOT into the dipole trap, the phase-space volume of the dipole trap has to be matched with the distribution of the atoms in the MOT. To do this experimentally, we first align the center of the trap, defined by the intersection of the two focused beams, with the position of the MOT. We then vary the size of the trap using the mechanical zoom to optimize the number of atoms.

Aligning the dipole trap

To align the dipole trap on the MOT cloud we first use the perturbation of the laser-cooling process due to the light shift of the dipole trap as a signature of the dipole trap: we modulate the optical power of the dipole trap at a frequency between 200 Hz and 2000 Hz, and look for signal at this frequency in the fluorescence of the MOT using a lock-in amplifier. After maximizing this signal, the dipole trap is aligned on the MOT well-enough to observe tomography images. We find the focal point of the trapping beam by maximizing the light-shift induced on the atoms (measured by tomography). The second pass is aligned similarly.

The two beams are crossed one with the other by looking at the tomography images: if the beams are not crossed, the potential isosurfaces of the two elongated trap do not intersect, and the projection of the isosurfaces of the dipole trap is the projection of two separate tubular traps. On the contrary, if the beams intersect, the projection is not that of two superimposed tubes, but of a cross:

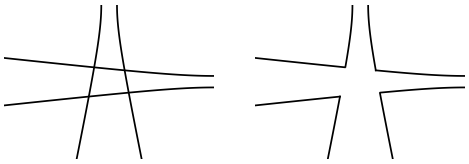

Figure VI.6 – **Tomography of two beams: Left: non-intersecting – Right: intersecting**

When loading a dipole trap made of only one focused beam, the angle between the propagation direction of the beam and the horizontal has to be very small, or the confinement of the trap along its longitudinal direction will not be large-enough to compensate for gravity. When a cloud of atoms is loaded from a trap made by a single focused beam, it expands along the longitudinal direction of the trap, and eventually spills out of the trap by its end if the beam is not perfectly horizontal. As can be seen on Figure VI.7 (b), the initial density of the atomic cloud in the trap is very small. Adding a second trapping beam does not change this loading dynamic unless

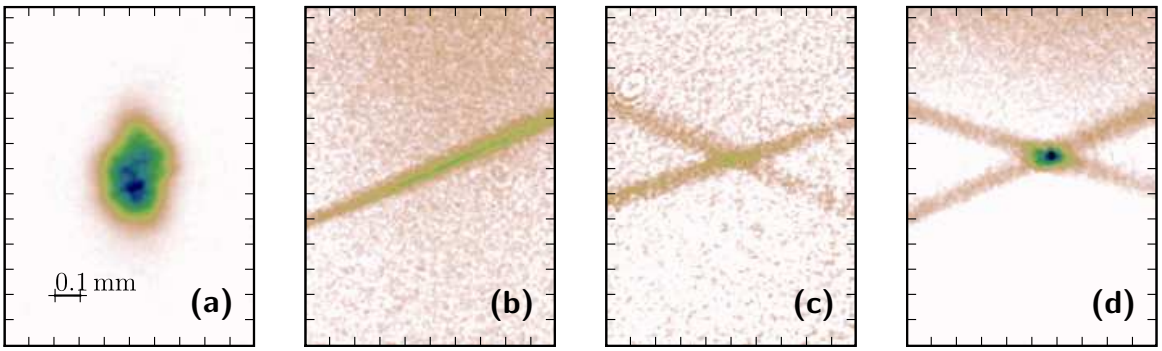

FIGURE VI.7 – **Aligning the optical dipole trap**
(a) Absorption image of the MOT, with negligible free expansion. The perturbation of the atomic levels by the dipole trap can just be seen on the absorption image of the could.
(b) Single pass dipole trap, after 20 ms of expansion of the Doppler-cooled cloud.
(c) Two pass dipole trap, after 20 ms of expansion of the Doppler-cooled cloud.
(d) Crossed dipole trap, after 20 ms of expansion of the Doppler-cooled cloud.
Images (b), (c), and (d) have the same colormap scaling, but not image (a).

the beams are crossed. In this case, the intersection of the beams forms a trap steep in all directions, and a large fraction of the atomic cloud is trapped in this hole and does not expand (see Figure VI.7 (d)). This lack of expansion is another signature of well-crossed beams.

Optimum choice of trap size

We optimize experimentally the position of the mechanical zoom to maximize the number of atoms loaded in the dipole trap. The knowledge of the depth and size of the trap acquired by analysis of the tomograms is useful to deduce the corresponding trap parameters.

Varying the size of the trap Experimentally, when varying the position of the mechanical zoom, we observe that if the trapping beams intersect close to their focal point, the physical size of the trap is too small compared to the MOT to collect efficiently atoms, whereas if we defocus too much the beams, the depth of the trap is too small compared to the temperature of the laser-cooled cloud and the loading is also inefficient.

We have found that, with the low number of atoms in our MOT, the optimum situation to load the dipole trap is with a compressed MOT (Petrich *et al.* [173]): before releasing the atoms from the MOT, we jump the gradient of the magnetic field to $40\,\mathrm{G}\cdot\,\mathrm{cm}^{-1}$. Due to the large capacitors in our ultrastable power supply[5], the magnetic field gradient takes 150 ms to rise. Finally, we jump the detuning of the cooling laser to $8\Gamma_{\mathrm{Rb}}$ for a few milliseconds for sub-Doppler cooling in the compressed MOT. We achieve a cloud of $\sim 300\,\mu$m diameter with a temperature of $\sim 50\,\mu$K.

[5]The excellent stability of the power supply is of no use in a MOT, and we are thinking of using a faster power supply for this part of the experimental sequence.

Phase-space matching between the atomic cloud and the trap In the experimentally-optimal configuration (around a zoom position of 10 mm), the size of the trap, given by the diameter at $1/e$ of the intersection of the two beams, is $\sim 300\,\mu$m, similar to the size of the compressed MOT (we measure $300\,\mu$m half width at $1/e$). The depth of the central part, roughly half the total depth, is around $60\,\mu$K, which corresponds to the temperature of the atomic cloud. The optimal loading geometry seems to lie where the phase-space shape occupied by the atomic cloud is best matched by the phase-space shape of the trap.

1.3 Loading dynamics

1.3.1 Atomic loss processes

The number of trapped atoms decreases quickly with time. As can be seen in Figure VI.9, this decrease is well-described by the sum of two exponentials of time constants $\tau_1 \sim 100$ ms and $\tau_2 \sim 750$ ms. There are thus two different physical processes that lead to a loss of atoms. We will see that the first process corresponds to atoms with an initial energy higher than the depth of the trap leaving the trap along the beams, whereas the second loss process can be due either to rethermalization of the trapped cloud through collisions, or to a heating process.

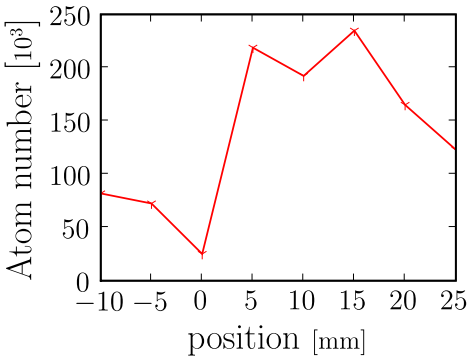

Figure VI.8 – **Number of atoms captured for different zoom positions**
These preliminary results are very noisy, as the number of atoms in the MOT was fluctuating during these measurements. However, they do show the tendency observed when adjusting zoom position to optimize number of trapped atoms: a broad maximum for a zoom position of 10 mm, corresponding to a trap size of $200\,\mu$m (i.e. a waist of the intersecting beams of $\sim 100\,\mu$m).

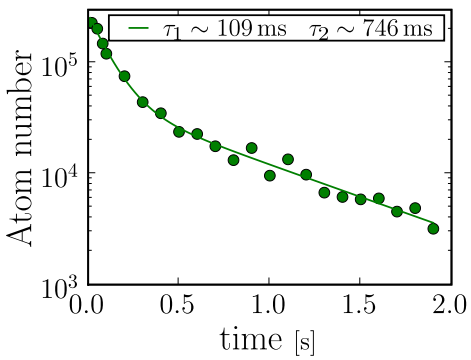

Figure VI.9 – **Number of atoms in the trap as a function of time**
We fit the number of atoms with the sum of two exponentials, of time constant τ_1 and τ_2.

Energetic atoms spilling out of the trap During the first hundred milliseconds, we observe a rapid loss of atoms. However this loss process does not concern all the atoms, as for times large compared to the duration of this process we still observe trapped atoms, whose number decreases with a longer time scale.

We can gain more insight on this loss by using trap tomography to gain information on the atomic distribution after different hold times in the dipole trap (see Figure VI.10). We can see that during the first instants after the MOT has been switched off, the wings of the trap, outside the intersection of the two beams, are populated, but they quickly vanish, and only the atoms in the central part of the trap are left.

Indeed, what appears as wings of the inner trap is the side of a larger trap made by each single beam. Atoms spread in this trap and the local density at the intersection of the beams decreases. Moreover, as the beams are not perfectly horizontal, the atoms can escape through one end of the beam: the longitudinal trapping force is not large-enough to hold atoms against gravity. The time scale for the atoms to propagate along the beam to find the exit point, or the trap minimum, is given by their oscillation frequency.

The longitudinal trap frequency of a single beam, given by $1/(2\pi)\sqrt{2\,U/(m\,Z_{\mathrm{R}}^2)}$ (see Grimm *et al.* [155]), where U is the trap depth, and Z_{R} the Rayleigh length, measured as discussed in the previous paragraph, is $\sim 5\,\mathrm{Hz}$. The time scale for atoms to explore the wings and escape from the trap by the gravity-induced potential minimum in the wing thus matches the time scale of the first loss process. This confirms the analysis of the tomography images: the first loss process is due to atoms with a higher energy than the inner-most part of the crossed-dipole trap, escaping through the wings of the dipole trap.

Thermalization of the trapped cloud The cloud loaded in the trap is out of thermal equilibrium: its initial velocity distribution is far from a Maxwell-Boltzmann and is probably similar to the thermal distribution of the compressed-MOT cloud ($T \sim 50\,\mu\mathrm{K}$), truncated to the depth of the trap, $\sim 60\,\mu\mathrm{K}$. Elastic collisions between

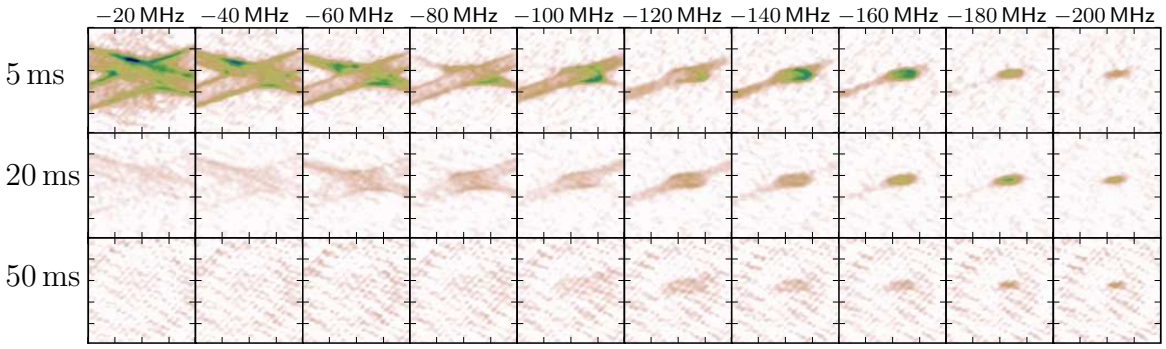

FIGURE VI.10 – **Tomography of the trapped cloud after different hold times in the trap** These images show the evolution of the distribution of atoms in the trap after the loading of the trap.

trapped atoms rethermalize the cloud in a free evaporation process to form a thermal distribution with a temperature equal to a fraction of the trap depth (Granade *et al.* [174]). This process occurs in a time scale corresponding to the time required for a few collisions to take place. The collision rate of atoms in the trap is given by:

$$\Gamma_{\text{col}} \sim n\,\sigma\,\bar{v} \tag{VI.4}$$

where n is the density of trapped atoms, $3{\cdot}10^4$at in $(100\,\mu\text{m})^3$, σ is the collisional cross section, $\sigma = 8\pi\,a^2 \sim= 8\pi\,(5\,\text{nm})^2$, and $\bar{v}$ is the mean thermal velocity, $\bar{v} \sim 0.1\,\text{m}\cdot\,\text{s}^{-1}$. The order of magnitude of the collision rate is thus 2 Hz. The time scale for free evaporation can thus correspond to the second time constant measured on the atom-number decrease. However, the number of atoms does not seem to stabilize to a measurable value. This might indicate that there is a heating mechanism that induces losses on the same time scale. Moreover, preliminary estimates of the temperature in the trap by time of flight measurements do not show a decrease in temperature, but the number of atoms for long hold times is too low to obtain a good evaluation of their temperature.

1.3.2 Compressing the trap

To match the size of the compressed MOT, we use a large dipole trap. As a result, due to our limited total power, the trap is shallow, and cannot hold energetic atoms. In addition, the trap frequencies are small, thus the trapped cloud is dilute, the collision rate is small, and the thermalization is slow. We can use the mechanical zoom to reduce the trap size and increase its depth.

Dynamically increasing the trap depth After a free evaporation period, the temperature of an atomic cloud in a finite depth trap stabilizes at a fraction of the trap depth, usually written as $\eta = k_{\text{B}}\,T_{\text{f}}/U_0$, with T_{f} the final temperature of the cloud, and U_0 the depth of the trap. Depending on trap geometry, η most often lies between 5 and 10. If an out-of-equilibrium cloud is loaded in the trap, the higher its initial temperature compared to $T_{\text{f}} = \eta\,U_0/k_{\text{B}}$, the more atoms will be lost during free evaporation.

If we use the mechanical zoom to reduce adiabatically the trap diameter by a factor x, its depth increases by a factor of x^2. The compression also transfers energy to the cloud, thereby heating it. If the compression is adiabatic, the temperature of the cloud after compression, but before free evaporation, increases as x^2. Thus the temperature increases as fast as the depth of the trap. However, when the trap is very large, it is not very steep. Gravity is then non-negligible and reduces the effective trap depth. For a trap diameter of $400\,\mu$m, the depth of the trap without gravity is $150\,\mu$K and the variation of gravitational energy over the trap height is $k_{\text{B}}\cdot 40\,\mu$K. The optimal trap-loading diameter is thus a diameter for which the trap is very loose and its effective depth is limited by gravity. When we compress the trap, as its size decreases while its depth increases, the importance of gravity becomes negligible.

If we compress the trap during the first loss process, as we increase the depth of the trap more than we communicate energy to the atoms, we can capture atoms that would not be trapped without compression, but that have not found their way to the escape points during the compression. Our preliminary results show that compressing the trap before the first loss process is finished indeed increases the final number of atoms. Using this loading protocol, we have found the optimum initial size of the trap to be larger than the optimum trap size without compression.

Increasing the thermalization rate When compressing the optical dipole trap, as envisaged in the previous paragraph, the density is increased by a factor x^3, but the mean velocity is also increased by adiabatic compression by a factor of x. Using equation VI.4, we find that a reduction by a factor of x of the trap diameter leads to an increase by a factor of x^4 of the collision rate[6]. It is important to have a high collision rate, as collisions are required for evaporative cooling, the next cooling step we plan to use on our road to condensation.

By compressing the optical dipole trap, we can thus hope, not only to reach equilibrium faster, but also to loose fewer atoms in the process. In addition, the scaling laws for forced evaporation are more favorable if the trap size is decreased while its depth is reduced for forced evaporation: the collision rate can be kept constant, near the hydrodynamical regime, whereas if the depth is reduced at a constant trap diameter, the trap frequencies go to zero (see Kinoshita *et al.* [169]).

The first experimental results of the transfer between the MOT and the dipole trap show the importance of matching the diameter and depth of the dipole trap to the size and temperature of the laser-cooled cloud. Tomography is a powerful tool both to inspect the trapping potential and to image the in situ *atomic distribution.*

We observe two atomic loss phenomena during the loading of the dipole trap. The first is due to atoms escaping the trapping along the two individual beams. The second is most likely due to thermalization of the trapped cloud through collisions. By adiabatic compression of the trap we believe that we can reduce these losses as we can increase the trap depth more than the temperature of the cloud.

2 Laser cooling in the dipole trap?

We are limited in the number of atoms we can capture in the dipole trap because a large fraction of the atoms we initially load in the trap have too much energy to

[6] If the collision rate is higher than the trap frequencies, the cloud enters the hydrodynamical regime, and the thermalization is not limited by the collision rate, but by the time required for an atom to explore the potential. The initial oscillation frequencies of the inner trap are around 100 Hz, we are thus far from this regime.

stay trapped and leave. In this section we discuss how we can use laser cooling to add dissipation and increase the number of trapped atoms.

2.1 Adding laser cooling to the loading process

Laser cooling density and temperature limits

We are loading the dipole trap from a laser-cooled cloud, limited in temperature and density by the laser cooling. By adding laser cooling during the trap loading we should not hope for further gains in density or temperature.

The dipole trap is turned on non-adiabatically. Atoms that are not located at the minimum of potential energy acquire a potential energy due to the trapping potential that adds to their kinetic energy. As there are no dissipative processes during the first instants of the loading of the dipole trap (the collisions can be neglected), only the atoms with a total energy (potential and kinetic energy) below the energy of the lowest escape point of the trapping potential are trapped.

The density in the dipole trap after the atoms in the wings have been removed is on the order of $3 \cdot 10^4$ at in $(50\,\mu\text{m})^3$, that is, $3 \cdot 10^8\,\text{at} \cdot \text{cm}^{-3}$, well below the $10^{11}\,\text{at} \cdot \text{cm}^{-3}$ density limit of laser cooling process. In addition, we measure a temperature of the trapped cloud of $\sim 40\,\mu\text{K}$, significantly below the depth of the trap. This means that, unless there is some loss process that we do not understand, the loading of the atoms in the dipole trap is not limited by their initial distribution, and the potential energy contributed by the trap to the atoms inside the trap volume is enough to exclude a large part of the initial density-limited thermal distribution.

Thus laser cooling can in fact lead to a gain in the number of trapped atoms by removing the excess energy communicated during the trap turn-on, and bring the trapped cloud closer to the density limit.

Strategies for laser cooling in a dipole trap

Superimposing optical molasses to the dipole trap Superimposing the dipole trap to optical molasses, or a MOT, is a common way of loading it when working with quasi-electrostatic optical trap in which all atomic levels are shifted similarly by the trapping laser (see e.g. Barrett *et al.* [175], Granade *et al.* [174]). However, when using a trapping light closer to resonance, the light-shift of laser-cooling transition due to the dipole trap interferes with the cooling process. Moreover, in the case of trapping lasers with wavelengths shorter than $1.3\,\mu\text{m}$, such as YAG lasers, for rubidium, the upper state of the laser cooling transition is anti-trapped, and, as it is populated during the laser-cooling process, the effective trapping force is weakened.

Alternating laser cooling and dipolar trapping To alleviate these problems, the laser cooling and the dipole trap can be run in a quickly alternating sequence. As described in Dalibard *et al.* [176], if the two processes are switched at a rate higher than the trap frequencies, the force felt by the atoms is the time-averaged force. It thus combines a steep trapping component due to the dipolar trapping force and a dissipative component due the laser cooling force. The first optical-dipole trap for atoms (Chu *et al.* [177]) was loaded using this scheme. Preliminary results on our experiment show an improvement in number of atoms loaded in the dipole trap by a factor of up to three.

We would like to take advantage of the large trapping potential for the excited state and increase the effective depth of the dipole trap by populating the excited level during the loading of the trap. This hope prompted us to study theoretically the regime with both trapping potential and laser-cooling running simultaneously. In the following sections I describe a model for the force and use it to find the limiting factors on the number of trapped atoms when optical molasses are superimposed to the dipole trap.

2.2 Model of coupled laser-cooling and dipole trapping

When both laser cooling and the dipole force of the FORT act together on an atom, the detuning of the MOT lasers to the atomic transition varies spatially in the trap and is large compared to the linewidth Γ. The resulting force cannot be linearized nor derived from a potential, and the dynamical system describing the motion of the atoms is difficult to study analytically. We have conducted simple numerical simulations by integrating an expression of the force for one atom, neglecting many-body effects and sub-Doppler cooling, in an effort to determine whether the combination of the two effects could lead to a trapped and damped motion.

The near-resonance radiation pressure force We use the simple model of the 2 level atom introduced to describe Doppler-cooling in §V.1, but modify it in order to take in account the detuning $\delta_{\mathrm{FORT}} = (p_e - p_g) I_{\mathrm{FORT}}$ due to the dipole trap, where p_e and p_g are the polarizability of the excited and ground states, calculated at the beginning of this chapter. However we do not expand the expression of the force for small detuning. In a 1D model, the expression of the force is:

$$F_{\mathrm{MOT}} = \frac{\hbar \Gamma_{\mathrm{Rb}} k_{\mathrm{MOT}}}{2} \left(\frac{s_0}{1 + s_0 + \Delta_+^2} - \frac{s_0}{1 + s_0 + \Delta_-^2} \right) \tag{VI.5}$$

$$\text{where:} \quad s_0 = \frac{I_{\mathrm{MOT}}}{I_{\mathrm{sat}}}$$

$$\Delta_\pm = \frac{2}{\Gamma_{\mathrm{Rb}}} \left(\delta_0 + \delta_{\mathrm{FORT}}(x) \right) \pm \frac{x}{x_0} \mp \frac{v}{v_0}$$

with x_0 and v_0 as introduced in §V.1, 123. We have given the expression of this force for a MOT, where there is a magnetic field gradient, but it can also describe Doppler cooling in optical molasses, in which case $x/x_0 = 0$.

The dipolar force of the FORT The light-shift of each individual atomic level is proportional to the intensity of the laser (see equation VI.1). We use a simple 1D model, and the intensity is given by a Gaussian. The atom cycles between the two different levels of the MOT transition. The expression of the radiation pressure of the MOT lasers given in equation VI.5 is valid only if we consider that the atomic populations are always at equilibrium with the laser field (this is a common approximation of the Doppler model). To express the effective force felt by the atom as it cycles between the two dipolar potentials (the ground state and the excited state) we take the population-weighted average of the two forces:

$$F_{\text{FORT}} = \Big(p_g + (p_e - p_g)\,\Pi_e(r,v)\Big)\,\nabla I_{\text{FORT}}(r) \tag{VI.6}$$

where:

- p_g and p_e are the polarizability for the ground and excited states, as calculated in tables VI.1 and VI.2,
- and Π_e is the upper state population, given by the optical Bloch equations:

$$\Pi_e = \frac{1}{2}\frac{s_0}{1+s_0+\Delta_+^2} + \frac{1}{2}\frac{s_0}{1+s_0+\Delta_-^2}$$

The dipolar force of the near-resonance lasers To trap atoms using the dipolar force, a laser field with spatial varying intensity is most often used. The expression of the trapping potential is then[7] (Cohen-Tannoudji *et al.* [156], Dalibard [145]):

$$U_{\text{dip}}(r) = -\frac{\hbar\,\delta}{2}\ln\Big(1+s(r)\Big) \tag{VI.7}$$

A closer look at this expression shows that there is a force (a non-constant potential) if the saturation parameter s varies spatially. If we consider the dipolar potential created by the Doppler-cooling lasers, while addressing the D2 transition, the detuning varies, and therefore s is non-uniform. The given expression of the dipolar potential is no longer valid and following the same method as in Dalibard [145] gives the expression of the dipole force:

$$\begin{aligned} F_{\text{dip,MOT}} &= -\frac{\hbar\,\delta}{2}\frac{\nabla s(r)}{1+s(r)} \\ &= \left(\frac{1}{1-s_0+\Delta_+^2}\,\frac{\Delta_+^2}{1+\Delta_+^2} + \frac{1}{1-s_0+\Delta_-^2}\,\frac{\Delta_-^2}{1+\Delta_-^2}\right)\frac{u_e-u_g}{\pi}\nabla I_{\text{FORT}}(r) \end{aligned} \tag{VI.8}$$

The order of magnitude of this force is the same as that of the FORT force, and both are 100 times smaller than the radiation pressure force at resonance. This force has the same sign as the FORT force, it is a trapping force.

[7] In far off-resonance traps, the saturation parameter s is small and the logarithm is expanded.

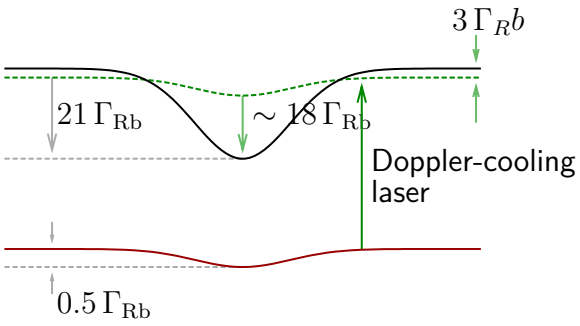

FIGURE VI.11 – **Detuning of the Doppler-cooling transition**
Due to the differential light shift of the ground and excited states of the D2 transition, the Doppler-cooling laser, red-detuned outside the dipole trap, is blue-detuned inside the trap.

2.3 Laser cooling tuned to the bottom of the trap

In this section we consider optical molasses tuned to be effective at the bottom of the dipole trap. The size of the region over which the molasses are effective is small. We numerically integrate atomic trajectories to see if they slow the atom enough to capture it as it crosses the dipole trap.

Necessity to detune the Doppler-cooling lasers

As can be seen in Figure VI.11, the D2 transitions are shifted down in energy by more than a hundred megahertz in the dipole trap. As a result, the Doppler-cooling laser, tuned 12 MHz to the red of an unperturbed D2 transition, will be blue-shifted relative to the same transition inside the dipole trap. This breaks down the Doppler-cooling process, as the previously damping and restoring radiation-pressure force changes sign inside the dipole trap. It now heats and ejects atoms from the trap. Its effect is much larger than the trapping effect of the FORT. Simulations and experiments have confirmed that the combination of laser cooling and dipole trapping does not lead to efficient loading atoms in the trap.

Laser cooling near the bottom of the trap

The Doppler-cooling lasers have to be tuned to the red of the laser-cooling transition over the complete extent of the trap in order not to introduce heating. They can be tuned to the red of the bottom of the trap by a few natural linewidths, in order to yield efficient Doppler cooling at the center of the trap (see Figure VI.12).

The parameters of importance for dissipative loading of a trap are its capture velocity and the ratio of the depth of the trap to the in-trap equilibrium temperature.

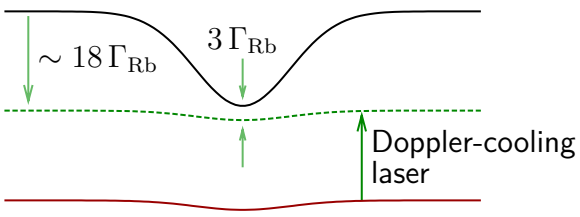

FIGURE VI.12 – **Doppler cooling tuned to the bottom of the trap**

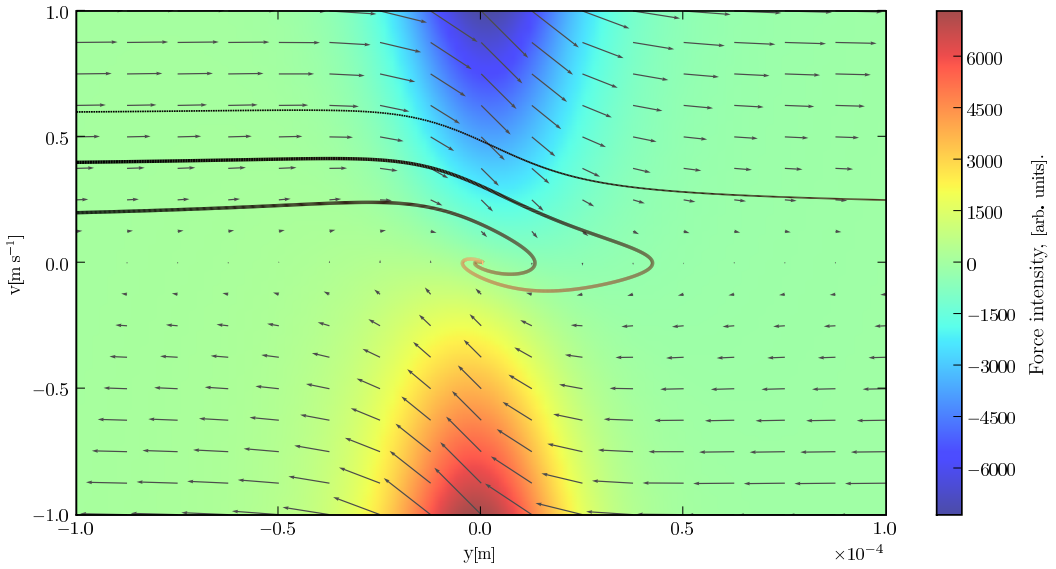

Figure VI.13 – **Phase portrait of some trajectories in the dipole trap, with optical molasses tuned to the bottom of the trap**

This simulation was performed for a trap with a waist of $100\,\mu$m.
Outside the trap, the lasers are far from resonance and the amplitude of the force is very small, appearing in green on the plot. Inside the dipole trap, the molasses slow the atoms down, deflecting phase-space trajectories to the zero-velocity axis of the phase diagram.
Three atomic trajectories, starting outside the trap with initial velocities of 0.2, 0.4 and $0.6\,\mathrm{m}\cdot\mathrm{s}^{-1}$ have been plotted. The one with the highest initial velocity is not captured, and the trajectories escape the trap.
The spiraling motion in a phase-diagram is the canonical signature of a damped oscillator. These atoms are damped and trapped inside the dipole trap.

Capture velocity We have numerically integrated atomic trajectories to evaluate the capture velocity of the Doppler-cooling process limited to the bottom of our dipole trap, using a waist of $100\,\mu$m. As can be seen in Figure VI.13, atoms with a velocity up to a fraction of a meter per second outside the trap are slowed enough by the Doppler-cooling process to be captured in the trap in one oscillation. If the trap is too steep, the Doppler cooling cannot operate on a large-enough distance to stop the atoms; the capture velocity is reduced (it falls to $0.2\,\mathrm{m}\cdot\mathrm{s}^{-1}$ for a waist of $50\,\mu$m).

The mean velocity of the atomic cloud loaded in the dipole trap is $0.1\,\mathrm{m}\cdot\mathrm{s}^{-1}$ (corresponding to a temperature of $50\,\mu$K), below the capture velocity of the Doppler-cooling process in the dipole trap.

Equilibrium temperature The lowest temperature that can be achieved with Doppler cooling is given by the equilibrium between heating by photon scattering and the damping force. In the optimal conditions, this limit is given by $\hbar\Gamma/(2\,k_\mathrm{B})$ (see Phillips [178]), $140\,\mu$K for rubidium. This temperature is higher than the trap depth. Doppler cooling heats the atoms too much to leave them confined in the trap. Fortunately, the initial temperature of the cloud, $50\,\mu$K, is smaller than this temperature, there are thus some sub-Doppler processes at work in the compressed

MOT and we can hope they will also be efficient in the dipole trap[8]. Indeed, the Doppler-cooling laser is red-detuned to the bottom of the trap, and the detuning increases as the atom moves away from the bottom of the trap. This reduces the efficiency of the cooling mechanism, but also reduces the heating by photon scattering.

As a conclusion for this laser-cooling scheme, we can say that the laser cooling is efficient-enough to stop the atoms as they cross the dipole trap for the trap sizes that we use, however the heating due to photon scattering may lead on the long term to a loss of atoms. We think it would be interesting to try to implement this technique for a short amount of time during the loading. Ideally, it might be interesting to ramp the power of the dipole trap up while increasing the detuning of the molasses. This way the molasses would be effective over a large volume[9] in the beginning. The limit to this approach is that while the dipole trap is ramped up, the atomic cloud expands. This ramp should therefore be very short, no longer than the typical duration of optical molasses when loading a magnetic trap.

2.4 Dual-frequency MOT

The main limitation of the cooling and trapping scheme presented above, namely optical molasses tuned to be efficient near the bottom of the dipole trap, comes from the limited zone on which the optical molasses damp the motion of the atoms. This limits the capture volume of the trap and we would like to extend the cooling to outside the dipole trap. To do this, we can add a second Doppler-cooling laser, tuned to be efficient outside the dipole trap, in other words, the non-modified laser light of the MOT. This external laser-cooling can capture atoms and continuously load the dipole trap.

Capture conditions The resulting system can be depicted by three regions. In the first region, outside the dipole trap, the inner-molasses laser light is detuned far to the red of the cooling transition, and the near-resonant light of the MOT dictates the dynamics of the atoms. This region is similar to a normal MOT. In the inner region, near the bottom of the dipole trap, this dynamics is governed by the optical molasses that damp the motion of the atoms, as mentioned in the previous paragraph. In between these two regions, the outer-MOT laser is detuned far to the blue of the laser-cooling transition and the inner-molasses laser far to the red, the two processes compete, one slowing and trapping the atom, the other accelerating and ejecting it, in addition to the dipole trapping forces. We have conducted numerical integrations of

[8] The spatial dependence of the detuning in the dipole trap is likely to hinder sub-Doppler cooling processes, but a similar spatial dependence is present in the compressed MOT, we can thus infer that the limiting temperature in the dipole trap can be as low as the temperature of the compressed MOT.

[9] It might be even more interesting to increase the detuning by starting from a very detuned configuration and compress the dipole trap. This would maximize the volume on which the molasses are initially effective.

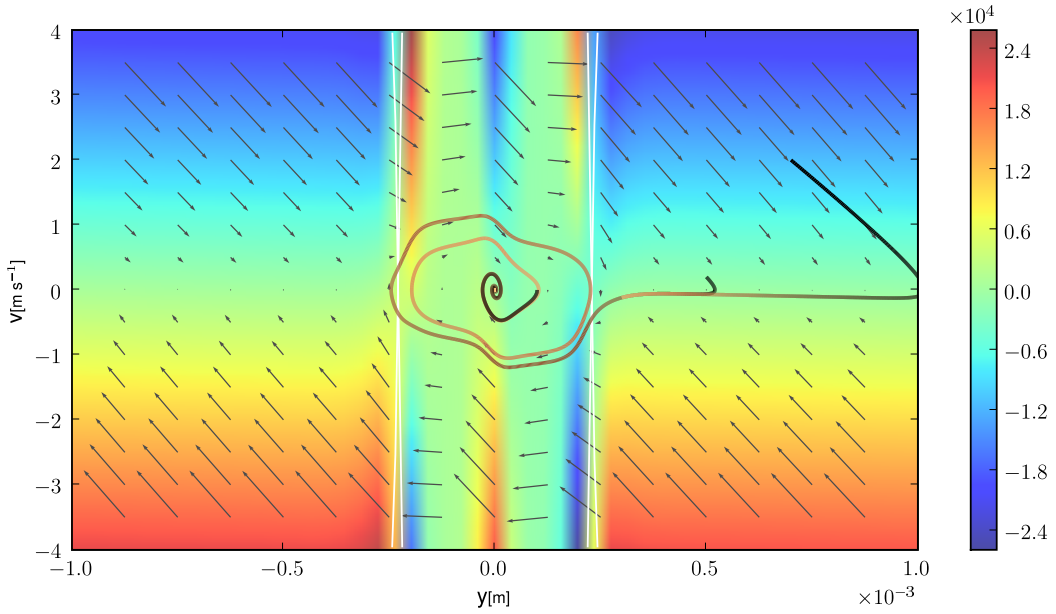

Figure VI.14 – **Phase portrait of some trajectories in the bi-chromatic MOT**
In the external part of the phase diagram, outside the dipole trap, the diagram is similar to that of an unperturbed MOT, such as shown on Figure V.2 on page 124.
The presence of the dipole trap can be seen, as the resonance condition in the (x, v) plane for each laser is no longer a oblique line, but strongly distorted (the resonance lines are drawn in white on the plot). The two resonance lines cross $200\,\mu$m from the center of the trap, where the external MOT becomes blue-detuned.
Inside the trap, there is a phase-space region where both laser-cooling frequencies are far from resonance and the force is small. In the innermost center of the trap, the phase diagram is similar that of the detuned molasses, in Figure VI.13.
Atoms captured by the MOT enter the inner region and are successively accelerated by the blue-detuned laser-cooling process and decelerated by the red-detuned one, until they have lost enough energy to stay in inner part of the trap and be captured by the internal molasses.
These simulations where done with a saturation parameter of 4.5 for the external MOT, and of 1.5 for the internal molasses.

atomic trajectories to find a situation where the damping due to the central molasses is sufficient to capture an atom before it escapes the central region where this damping is efficient. We use a simple model in which we consider that the two frequencies create a separate radiation pressure force, each given by equation VI.5. This is equivalent to neglecting the effect of saturation of the transition by one frequency on the force created by the other.

As can be seen in Figure VI.14, the internal molasses can trap the atom in the dipole trap with a waist of $100\,\mu$m if the corresponding saturation parameter is 1.5 or more. With such laser power in the internal frequency, the atom loses enough energy while going across the dipole trap to compensate for the energy it acquires when on resonance with the external MOT lasers. We have checked that this still holds in a three-dimensional model[10].

[10]In 3D, an atom oscillating in the trapping potential does not necessarily go through the center of the trap. For certain values of the saturation parameters and the trapping diameter, the behavior

Equilibrium temperature and stability zone As has been previously discussed, the equilibrium temperature in a Doppler-cooling process is due to a balance between momentum diffusion, introduced by photon scattering, and the damping force. The momentum diffusion can be pictured as random momentum jumps of amplitude $\hbar k$ at a frequency given by the photon scattering rate, Γ_{scat}. This diffusion process yields an increase in the momentum spread of $\sigma_{\mathbf{p}} = 3\,(\hbar k)^2\,\Gamma_{\text{Rb}}\,t$ (the factor of three comes in because there are three independent diffusion processes, one for each spatial direction). The damping force yields a decrease in velocity $\dot{\mathbf{v}} = -\gamma\,\mathbf{v}$, where γ is the damping coefficient, given by the expansion of the radiation pressure force (VI.5) for small velocities[11]. The equation of motion for $\sigma_{\mathbf{p}}$ is thus:

$$\frac{d}{dt}\sigma_{\mathbf{p}} = 3\,\hbar^2\,k^2\,\Gamma_{\text{scat}} - \frac{\gamma}{2}\,\sigma_{\mathbf{p}} \tag{VI.9}$$

The equilibrium momentum rms width is given by the steady-state solution of this equation. Thus:

$$\sigma_{\mathbf{p}} = \frac{3}{2}\,m\,k_{\text{B}}\,T = 3\,\hbar^2\,k^2\,\frac{\Gamma_{\text{scat}}}{\gamma} \tag{VI.10}$$

Using the equations for photon scattering rate and damping coefficient for a MOT or a optical molasses, we recover[12] the well-known Doppler limit for $s_0 \ll 1$ and $\Delta = 1$.

With the model of the bi-chromatic MOT used for integration of the trajectories we can evaluate the Doppler equilibrium temperature for different places in the dipole trap (see Figure VI.15). Those places for which heating due to the blue-detuned outer MOT is larger than cooling of the inner molasses appear as negative temperatures, as the damping coefficient is negative. There, the system is unstable; atoms are accelerated and ejected.

As we can see in Figure VI.15, only a fraction (approximately half the diameter) of the dipole trap is stable. This means that the trapped cloud is limited to a small volume of the dipole trap. Moreover, about the borderline, the damping coefficient is small: it is likely that the atomic density will be limited below the $10^{11}\,\text{at}\cdot\text{cm}^{-3}$ density limit usually observed in MOTs.

If we suppose that the region in which atoms can remain trapped is $100\,\mu$m, and that the $10^{11}\,\text{at}\cdot\text{cm}^{-3}$ density limit is indeed achieved in this region, we find a limit for the number of atoms in the dipole trap of 10^5.

---

of the atom is unstable and chaotic in 3D, while it is simply oscillating in 1D: the phase-space of the 1D problem does not have enough dimensions to exhibit chaotic behavior.

[11] We do not give the expression of this damping coefficient, as we have not calculated it analytically.

[12] For Doppler-cooling, $\gamma = \dfrac{\hbar k^2}{m}\dfrac{s_0}{1+\Delta^2}\dfrac{4\Delta}{1+\Delta^2}$ and $\Gamma_{\text{scat}} = \dfrac{\Gamma_{\text{Rb}}}{2}\dfrac{s_0}{1+s_0+\Delta^2}$ (VI.11)

As a result, the temperature limit for a Doppler-cooling process is given by:

$$T = \frac{\hbar\,\Gamma_{\text{Rb}}}{4\,k_{\text{B}}}\frac{(1+\Delta^2)^2}{\Delta\,(1+s_0+\Delta^2)} \tag{VI.12}$$

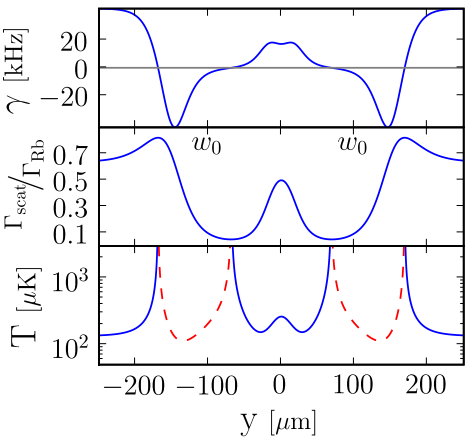

Figure VI.15 – **Heating and damping in the bichromatic MOT**
The heating due to photon scattering is proportional to the scattering rate, while the cooling is given by the damping coefficient of the linearized radiation pressure force.
The Doppler equilibrium temperature is proportional to the ratio of the scattering rate and the damping coefficient (see equation VI.12). For negative damping coefficients, the system is unstable and the temperature appears negative. The absolute value of these negative temperatures is plotted in red, dashed lines.
These curves where plotted with a saturation parameter of 4.5 for the external MOT, and of 1.5 for the internal molasses. The size of the inner stable region depends only weakly on the saturation parameters. Using a saturation parameter of 1.5 for the external MOT, and 4.5 for the internal molasses yields a radius for the stable region of 90 μm.

The Doppler model that we use to calculate the damping coefficient is known to be incorrect for a large detuning where sub-Doppler processes take over; it can lead to cooling in blue-detuned molasses (Boiron *et al.* [179]). The results of this section are thus worst case scenarios, and a more systematic study could be conducted. We do not wish to do so, as our goal is only to give some simple theoretical guidelines for experimental work.

As a conclusion on the bichromatic MOT, the damping process is indeed efficient-enough to slow the atoms down to the center of the trap, but, inside the dipole trap, the competition between the red and blue-detuned lasers creates a large unstable region. As a result, the effective size of the dipole trap is limited. We cannot really expect that this scheme will be very efficient at loading the trap.

We have aligned the dipole trap with the atomic cloud of the MOT and optimized its size and depth for maximum loading efficiency. A novel imaging technique, that we call dipole-trap tomography, gives us a good diagnostic tool for the alignment of the dipole trap and the evolution of the atomic cloud immediately after loading. In addition, we use this new imaging technique to measure the Gaussian-beam parameters, taking into account the effects of uncontrolled aberrations and losses. We currently trap a few percents of the atoms in the MOT, and we believe they undergo a slow evaporation process. We compress the trap dynamically during loading to increase the trap depth.

The first experimental results for the loading of the dipole trap from a laser-cooled cloud have highlighted the need for dissipative process to remove the excess energy communicated by the trap: we lose an order of magnitude an atom number as energetic atoms escape the trap.

- *Laser cooling can be combined with dipole trapping by alternating the two processes at high frequencies. The first experimental attempts to apply this technique to the experiment have been successful.*

- *Laser cooling can also be superimposed with the dipole trap, but it should be tuned to interact with atoms in the bottom of the trap. The limitation of this configuration is that the heating induced by photon scattering gives more energy to the atoms than the depth of the trap in the Doppler regime. The success of this technique will thus depend on the efficiency of the sub-Doppler cooling processes.*

- *Finally, we have investigated a scheme that uses two different laser-cooling frequencies tuned to match both the bottom of the dipole trap, and the outside of the trap, in an effort to capture atoms outside the trap and continuously load the trap. In this situation, the spatial shell surrounding the center of the trap is unstable as the inner cooling process competes with the heating due to the blue detuned external cooling process. The number of trapped atoms is limited by size of the internal stable region. This region can be enlarged by using more power in the optical molasses tuned to the bottom of the trap. We have tried this technique unsuccessfully on an early version of our setup with a single-pass dipole trap, limited power in the inner optical molasses, and limited knowledge of the light-shift.*

The conclusion of this feasibility study is that there is no obviously effective scheme for laser cooling in the trap. More experimental work is required to explore the solutions proposed on theoretical grounds.

The experimental work presented is this chapter is still in early stages. As imperfections in the experimental setup are honed out and alignment is refined, the quality of the experimental data will improve. Dipole-trap tomography is a quantitative tool which enables us to gain more understanding of the dipolar trap and of the loading dynamics.

Conclusion to part II

In this second part, I have described in detail the construction of the apparatus that we use to cool rubidium atoms. The apparatus has been designed with ambitious goals in mind. On the engineering side, it was required that only technology and designs suited for transportation or deployment in rugged environments would be used. For the physics, we wanted an all-optical set-up to cool a rubidium-potassium mixture down to degeneracy, to reduce the evaporation time with a control of the density and the collisions, and to achieve good control of the atomic interactions over a large volume.

The groundwork for the experiment has been completed. Day-to-day work in the lab has shifted from instrumentation-building to aligning, measuring, optimizing... We can start to see the limitations and the errors in the initial design, as well as the more successful features.

- It appears clearly that a 2D-MOT-based setup requires a lot of laser power, as it works better for large beams, and high saturation intensity. In our experiment, the higher the available power, the larger the atom number. Also, retro-reflected 2D-MOT beams are easier to align and yield more atomic flux.

- Similarly, if the 2D-MOT is correctly aligned, it works better with a high background pressure to load from. This implies that to work comfortably with dispensers we would empty them frequently. In order not to be limited by the amount of rubidium available in the vacuum chamber, the system should be designed either for easy replacement of the dispensers, or with large capacity atomic sources.

- It is important to keep the distance between the 2D-MOT and the 3D-MOT as small as possible.

- The external frame has proven very handy both for designing the experiment, but also to add new elements that were not originally planned. We do not believe that it has introduced a source of misalignment in the experiment.

- Moving the atomic-optic part of the apparatus from the old Institute to the new was extremely easy as, due to its compactness, we did not have to take it apart.

- Using a high-quality, off-the-shelf, telecentric objective lense for imaging yields good results for a modest effort in optical design. However, the availability of off-the-shelf objective lenses with high working distances is very limited compared to that for short working distances.

- A crossed dipole trap is much easier to work with than a trap made of a single focused beam as the trap frequencies are higher.

Conclusion

In this thesis, I have described the construction and the first results of two cold-atom sources in the perspective of their use for long-interrogation-time atom-interfero -metric inertial sensing. The particularity of the first source is to be designed for and successfully tested in a microgravity environment, which opens the door to long time of flights in compact apparatuses. The second source aims to produce degenerate atomic gases for a collimated atomic source.

By building and demonstrating a rubidium MOT operated during ballistic flights in a short time frame, we have shown that our technology is suited for the rugged environment of the airplane and that a program of short-development-cycle-driven atom-interferometric experiments can use the ballistic flight to develop high-precision inertial measurements in microgravity. The goal of the next flight campaign, planned in February 2008, is to demonstrate a light-pulse interferometer. In the future, to extend interrogation times, a compact version of the interferometer can be released freely-flying in the cabin. It would then be interesting to acquire noise statistics on the atom-interferometric readings of the acceleration, to see if the acceleration measured is repeatable enough for measurement to be correlated from one free flight to another using a Bayesian estimator. If it is indeed the case, as I believe, an atom-interferometric test of the universality of free fall can be performed in the airplane's reference frame. Precise comparison of the fall trajectories of two atoms with a significantly different mass over 50 m would be a simple and suggestive test of the universality of free fall, that could pave the way to more precise orbital tests. Many challenges remain before such an experiment can be held in an airplane, indeed ground-based high-precision experiments are themselves challenging.

The second atomic source built during my PhD has made good progress toward achieving quantum degeneracy for rubidium atoms. We have designed a compact apparatus with which we prepare a laser-cooled sample of up to $5 \cdot 10^7$at. We load atoms into the dipole trap from which we will perform evaporative cooling. For successful evaporation sequences, transfer from the MOT to the dipole trap should be mastered, as the number of atoms loaded in the trap is currently too low. The resulting atomic source will be used in interferometric schemes to study the impact of interactions and quantum pressure. These effects are best seen for long interaction times, which we cannot access with freely-falling atoms in the Earth gravity field. However we can investigate interferometric schemes where the vertical movement of the atoms is restricted, such as, for instance, by alternating periods of free fall, and Raman pulses acting as mirrors (as suggested in Impens *et al.* [159]). Using a potassium-rubidium mixture this would form an interesting system to study the relative dephasing and spread due to interaction or quantum pressure. Moreover, a proof-of-principal test of the universality of free fall could be implemented in this system.

Progress in atomic sources both in microgravity environments, and in more conventional laboratories, can lead to increased sensitivity for inertial sensors, and the work that has begun along those two axes is complementary. The first applications of new ultra-precise and ultra-accurate inertial sensors are likely to be tests of gravitational theories. A test of the universality of free fall is a promising candidate, both in the laboratory and in the microgravity, because it is a differential measurement of fundamental interest.

My PhD has marked the start of the I.C.E. project. In three years, we have made much progress on both our understanding of the challenges in long-interrogation-time atom interferometry and on the experimental implementations. We have validated all the technological choices for microgravity operation, as well as for producing degenerate atomic sources; we have a clear idea of how to perform full-scale interferometric measurements. Both experiments are now manned by a full-blown team and guarantee a bright future to the I.C.E. project.

Articles published

- R. A. Nyman, G. Varoquaux, B. Villier, D. Sacchet, F. Moron, Y. Le Coq, A. Aspect, and P. Bouyer, *Tapered-amplified AR-coated laser diodes for Potassium and Rubidium atomic-physics experiments*, Review of Scientific Instruments **77**, 033105 (2006)
- R. A. Nyman, G. Varoquaux, F. Lienhart, D. Chambon, S. Boussen, J.F. Clément, T. Muller, G. Santarelli, F. P. Dos Santos, A. Clairon, A. Bresson, A. Landragin, P. Bouyer, *I.C.E.: a Transportable Atomic Inertial Sensor for Test in Microgravity*, Journal of Applied Physics B, **84** 673-681 (2006)
- G. Varoquaux, N. Zahzam, W. Chaibi, J-F. Clement, O. Carraz, J-P. Brantut, R. A. Nyman, F. Pereira Dos Santos, L. Mondin, M. Rouze, Y. Bidel, A. Bresson, A. Landragin, and P. Bouyer, *ICE: an ultra-cold atom source for long-baseline interferometric inertial sensors in reduced gravity*, Proceedings of the international Moriond meetings on gravitational waves and experimental gravity.

Appendices

Appendices

Raman-pulse beam-splitter

1 Beam-splitting process

For beam splitters and mirror, a Raman transition couples two hyperfine levels of an atom with two lasers, via a virtual level located close to a D2 transition.

Raman scattering can be understood as the absorption of one photon in the first beam, and the stimulated emission of a photon in the second beam. During the process, the atom internal state changes, and the atom itself gains the momentum $\hbar k_1$ communicated by one photon in the first beam, and loses the momentum $\hbar k_2$ taken by the escaping photon. The momentum transfer from the laser beams to the atom during the whole process is:

$$\Delta p = \hbar(k_1 - k_2) \qquad \text{(A.1)}$$

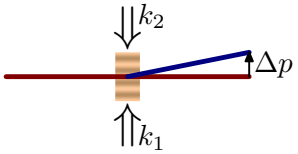

2 Transition probability

The two lasers have a respective angular frequency of ω_1 and ω_2. The frequency difference between them is close to the hyperfine transition frequency (6.8 GHz for ^{87}Rb, 1.2 GHz for ^{40}K), detuned by δ.

Both lasers are detuned from a D2 transition (780 nm for rubidium, 767 nm for potassium), by Δ.

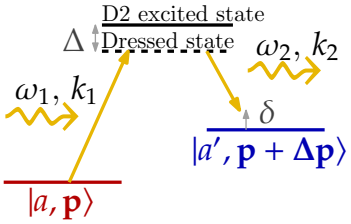

As the two lasers are near a atomic resonance, the transition probability is higher than a simple two-photon transition. This can be calculated using second-order perturbation theory. The calculation is easiest by considering a fully quantum description of the system: quantized atomic level, and quantized laser field (Cohen-Tannoudji *et al.* [156]. Indeed, using this formalism, the perturbation is time independent.

The energy levels without the atom/laser interaction (shown to the right) show explicitly two states, detuned by Δ below the D2 exited state. The Raman transition is a transition between those two states, due to the atom-laser interaction. The perturbation Hamiltonian is the atom-laser interaction.

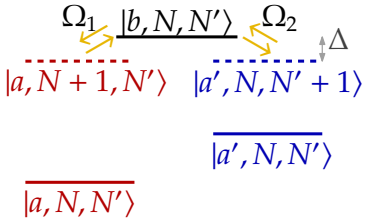

$$H = \underbrace{H_{\text{at}} + H_{\text{laser1}} + H_{\text{laser2}}}_{H_0} + \underbrace{V_{\text{at-laser1}} + V_{\text{at-laser2}}}_{V} \tag{A.1}$$

The base of the unperturbed problem is given by the atomic internal state, the number of photons in the first laser, and the number of photons in the second laser. In the $(|a, N+1, N'\rangle,\ |b, N, N'\rangle,\ |a', N, N'+1\rangle)$ base,

$$H_0 = \hbar \begin{bmatrix} -\Delta & & \\ & 0 & \\ & & -\Delta \end{bmatrix} \qquad \text{and} \qquad V = \hbar \begin{bmatrix} 0 & \Omega_1/2 & 0 \\ \Omega_1/2 & 0 & \Omega_2/2 \\ \Omega_1/2 & 0 & \Omega_2/2 \end{bmatrix} \tag{A.2}$$

where Ω_1 and Ω_2 are the single-photon-transition Rabi frequencies due to the two lasers: $\Omega_{1,2} = \Gamma\sqrt{I_{1,2}/(2\,I_{\text{sat}})}$.

The transition rate from a to a' is zero at first order in V, which is to be expected, as a Raman transition is a two-photon transition. In second order it is given by [180]:

$$r_{a\to a'} = \left| \sum_c \langle a| V |c\rangle \frac{1}{E_a - E_c} \langle c| V |a'\rangle \right|^2 \tag{A.3}$$

The sum reduces to $|b\rangle$: $$r_{a\to a'} = \left| \frac{\Omega_1\Omega_2}{4\Delta} \right|^2 \tag{A.4}$$

The problem is thus equivalent to a normal single-photon transition between two levels with an effective on-resonance Rabi frequency:

$$\Omega_{\text{eff}} = \frac{\Omega_1\Omega_2}{2\Delta} \tag{A.5}$$

However one laser induces a light shift on the transition seen by the other laser. The effective detuning, used in the off-resonance Rabi-oscillation formalism, is therefore:

$$\delta_{\text{eff}} = \delta + \frac{\Omega_2^2}{4\Delta} - \frac{\Omega_1^2}{4\Delta} \tag{A.6}$$

Adapting formulas for the classic single photon Rabi oscillations, the probability for a transition, after a Raman pulse of duration τ is:

$$P(\tau) = \left(\frac{\Omega_{\text{eff}}}{\Omega_{\text{R}}}\right)^2 \sin^2\Big(\frac{\Omega_{\text{R}}}{2}\tau\Big) \qquad \text{with} \qquad \Omega_R = \sqrt{\delta_{\text{eff}}^2 + \Omega_{\text{eff}}^2} \tag{A.7}$$

3 Velocity selection of the transition

For energy conservation, the transition must remove for the atoms the kinetic energy brought by the momentum kick. As the Raman lasers are applied during a finite interaction time, non resonant transitions are possible (Cohen-Tannoudji *et al.* [180]). The lasers have Fourier-limited width of $\Delta\omega = 2\pi/\tau$, resulting in a momentum-width of the transition:

$$\delta p = \frac{2\pi m}{k_{\text{eff}}\tau} \tag{A.8}$$

Appendix B

Conditional probability for the Bayesian estimator

1 Derivation of an analytical expression

To illustrate the how analytical expressions required for the Bayesian estimator can be derived, we give in this appendix the derivation for a simple model that however expresses the difficulties of precision measurements in a test of the universality of free fall.

We use a simplified model where we consider that the fluctuations in contrast for both species are correlated, and we neglect the fluctuations of the background measurement:

$$\begin{cases} m_1 &= A\sin\Big(\Phi + k(\delta x + X)\Big) \\ m_2 &= A\sin\Phi \end{cases} \tag{B.1}$$

where the random variables are written with capital letters. It is very easy to add to the formulas derived here a fluctuating offset noise, giving a more realistic description of the actual measurement: $m_1' = m_1 + B$, as the probability density function of m_1' can be derived from that of m_1 by a simple convolution: $p_x(a+b) = \int p_x(a)p(b)db$. We will not add those extra random variables, to avoid having long expressions.

1.1 Reformulation of the Bayesian estimator algorithm

Bayes' theorem

Bayes' theorem states that:

$$p(a|b) = \frac{p(a)}{p(b)}p(b|a) \tag{B.2}$$

It can be easily derived by calculation the joint probability of a and b: $p(a,b) = p(a|b)\,p(b)$ but also, $p(a,b) = p(b|a)\,p(a)$.

Estimator algorithm using measurement conditional probability

The algorithm for the Bayesian estimator, as presented on §II.2.3.2 makes use of the conditional probability of the parameter we are interested in δx, given the result of the measurements $p(\delta x|m_1, m_2)$. Is it easier to calculate the probability of the measurements, given the parameter, $p(m_1, m_2|\delta x)$, and the estimator algorithm is often presented in these terms (in Stockton *et al.* [112] for instance):

1. Calculate the conditional probability of the n^{th} measurement for the different values of the parameter: $p(m_1, m_2|\delta x)$
2. Compute the un-normalized probability distribution function for δx, using Bayes' theorem:
$$p_n(\delta x) = p(\delta x|m_1(n), m_2(n)) = p(m_1(n), m_2(n)|\delta x)p_{(n-1)}(\delta x)$$
3. Renormalize the resulting $p_n(\delta x)$.
4. Perform a new measurement and recurse the algorithm.

1.2 Derivation of $p(m_1, m_2|\delta x)$

We can reformulate the joint probability in term of less coupled probabilities:

$$\begin{aligned} p(m_1, m_2|\delta x) &= p(m_1|m_2, \delta x)p(m_2|\delta x) \\ &= p(m_1|m_2, \delta x)p(m_2) \qquad \text{as } m_2 \text{ does not depend on } \delta x \end{aligned} \tag{B.3}$$

Let us first calculate $p(m_1|m_2, \delta x)$. We can isolate its dependence on the fluctuating variable ϕ:

$$p(m_1|m_2, \delta x) = \int p(m_1|m_2, \delta x, \phi)p(\phi, m_2, \delta x)d\phi \tag{B.4}$$

The first term can be calculated[1] using $m_1 = \dfrac{m_1}{\sin\phi}\sin\Big(\phi + k(x+\delta x)\Big)$:

$$p(m_1|m_2, \delta x, \phi) = \sum_{\left\{\substack{x \text{ for all} \\ m_1\sin(\phi+k(x+\delta x)) \\ =m_2\sin\phi}\right\}} p(x)\frac{\sin\phi}{m_2\, k|\cos\Big(\phi + k(x+\delta x)\Big)|} \tag{B.5}$$

[1] For $y = f(x)$, the probability distribution function of y can be found by expressing the probabilities, instead of the probability distribution function:

$$p(y)dy = \sum_{\left\{\substack{x \text{ such as} \\ f(x)=y}\right\}} p(x)dx$$

thus, using $dy = f'(x)\,dx$, $$p(y) = \sum_{\left\{\substack{x \text{ such as} \\ f(x)=y}\right\}} \frac{1}{|f'(x)|}p(x)dx$$

For the second term we use Bayes' theorem:

$$p(\phi|m_2) = \frac{p(\phi)}{p(m_2)}\, p(m_2|\phi) \tag{B.6}$$

$$= \frac{p(\phi)}{p(m_2)}\, \sin\phi\, p_a\left(\frac{m_2}{\sin\phi}\right) \qquad \text{as } m_2 = a\, \sin\phi \tag{B.7}$$

Finally, equation B.4 can be written as:

$$p(m_1, m_2|\delta x) = \int \sum_{\left\{\substack{x \text{ for all} \\ m_1 \sin(\phi + k(x+\delta x)) \\ = m_2 \sin^2\phi}\right\}} p(x)\, \frac{\sin^2\phi}{m_1\, k|\cos\Big(\phi + k(x+\delta x)\Big)|} p_a\left(\frac{m_1}{\sin\phi}\right) \frac{p(\phi)}{p(m_2)}\, d\phi \tag{B.8}$$

Using equation B.4, the $p(m_2)$ factors cancel out, and the probability we are looking for is expressed by:

$$p(m_1, m_2|\delta x) = \int \sum_{\left\{\substack{x \text{ for all} \\ m_1 \sin(\phi + k(x+\delta x)) \\ = m_2 \sin^2\phi}\right\}} p(x)\, \frac{\sin^2\phi}{m_1\, k|\cos\Big(\phi + k(x+\delta x)\Big)|} p_a\left(\frac{m_1}{\sin\phi}\right) p(\phi)\, d\phi \tag{B.9}$$

2 Practical implementation of the estimator

Expression B.9 is numerically expensive to evaluate, as it involves finding all the roots of an expression (the equation given the different x in the sum). If it has to be evaluated a large number of time, it can be numerically interesting to precompute the conditional probability on a grid of the plane (m_1, m_2). This can be done by simulating the model with random number generators, and buiding a density estimation on a grid with a histogram of the randomly-generated measurements.

Density estimation

Unless the minimum number of points per histogram bin is much greater than 1, the histogram will suffer from aliasing noise. In the tails of the distribution the density can be very small, compared to the peak density. This condition therefore imposes to take in account a large number of points (for our model, to sample $p(m_1, m_2|\delta x)$ for a given value of δx, we need at least 10 million points). One solution uses a kernel density estimator: each randomly generated data point is given a Gaussian extent, the width of which is calculated as a function of local density (this is similar to a technique employed in the field of computer graphics known as Gaussian splatting). Even though this technique lowers the number of required data points, in the absence of specially optimized implementation of kernel estimators[1], the naive approach of sampling a large number of points is more numerically efficient.

[1]There exist optimized implementations of kernel density estimators, but they are geared toward graphic needs, and are not suitable for our purposes with extra work.

The number of sampling points required is determined by the number of bins, and therefore by the number of measurements and unknown parameters that we are trying to estimate, and not the number of fluctuating variables in the model. This means that this Monte Carlo sampling method is well-adapted to a low dimensionality problem, as ours.

A poor man's alternative to a kernel density estimator is to oversample the density array by calculating the histogram over a fine grid, and to convolve the result with a Gaussian kernel of width corresponding to the desired resolution, this reduces aliasing noise. It is not optimal in terms of number of data points, unlike the real kernel density estimator, but it is very cheap numerically.

Limiting the number of Monte Carlo random variables

As previously mentioned, the contribution of an additional additive random variable, such as $m_1' = m_1 + B$ can be calculated by the convolution of the two probability densities. Convolving two arrays is cheap and is preferable to adding a random variable to the Monte Carlo model.

Dealing with rare events

An experiment has failures, and impossible things can happen, that are impossible events according to the model describing the experiment. In other words, the model is not complete, and never will be. In a Bayesian estimator these impossible events, whether they are really impossible, or just impossible with the actual value of the hidden parameter, greatly hinder the convergence of the estimator, and can even make it impossible. Moreover, the estimation of the conditional probability is imprecise, even if it is implemented with the exact formula, because of numerical errors. In the tails of the distribution these errors are more pronounced. We have observed during numerical simulations that rare events can greatly slow down the convergence of the estimator, and introduce errors in the estimation of the RMS error, although in the long run the estimator does converge to the correct values.

One solution to reduce these worst-case scenarios is to add a constant offset to the probability density function. This offset causes a bias in the finite-time estimation that can easily be limited. It corresponds physically to accepting that any event is possible, whatever the choice of hidden parameter is. With this offset, the estimator is no longer the optimal convergence algorithm for the model, but this offset takes in account the incorrectness of the model due to the finite knowledge of the experimental system.

Test flight equipment

1 Rack 2: control rack

Object	**Height** (U)	**Height** (mm)	**Weight** (Kg)	**Torque** (Kg·mm)	**Dimensions** (mm)
MOT laser doubling	2	98.9	27	2670.3	4Ux500
2x MOT crystal temperature	6	276.7	1.4	387.38	200x150x100
MOT crystal 1U tray	5	232.25	1	232.25	1Ux300
Dispensers and coils power supply	8	365.6	4.5	1645.2	2Ux300
Screen and keyboard	18	810.1	6	4860.6	600x600x50
Keyboard 1U trait	9	410.05	1	410.05	1Ux300
Archos digital recorder	22	987.9	1	987.9	300x100x50
Oscilloscope	25	1121.25	3	3363.75	4Ux200
Thorlabs shutter control		100	2	200	300x150x100
Uniblitz shutter control		100	1.7	170	300x150x100
Diode power supply rack	6	276.7	15	4150.5	3Ux500
Power distributor	8.5	387.825	0.2	77.565	1Ux50
Master laser	13	587.85	13	7642.05	4Ux500
Servo locks	16.5	743.425	5.5	4088.84	3Ux500
Slave lasers	19.5	876.775	7.5	6575.81	3Ux500
Oscilloscope	23	1032.35	3	3097.05	4Ux200
Power distributor	3	143.35	0.5	71.675	1Ux50
5W fiber amplifier	5	232.25	9.6	2229.6	2Ux500
Raman beams doubling stage	8	365.6	20	7312	4Ux500
Hyperfrequency source	14	632.3	17	10749.1	4Ux500
Oscilloscope	16	721.2	13.5	9736.2	160x400x500
Control electronics rack	19.5	876.775	8	7014.2	3Ux300
Oscilloscope	23	1032.35	3	3097.05	4Ux200
Computer	3	143.35	20	2867	4Ux600
Fabry-Perot power supply	5	232.25	2.3	534.175	300x100x70
Power supplies	7	321.15	4.5	1445.17	2Ux300

Thorlabs shutter control	9	410.05	2	820.1	300x100x70
Power distributor	4	187.8	0.2	37.56	1Ux50
Power distributor	11	498.95	0.2	99.79	1Ux50
Sequencer	17.5	787.875	4	3151.5	3Ux300
Fan tray	19.5	876.775	6	5260.65	1Ux500
Power distributor	6	276.7	0.5	138.35	1Ux50
10W fiber amplifier	9	410.05	10	4100.5	2Ux500
AOM controller 1U tray	20	899	2	1798	2Ux400
AOM controller	21	943.45	3	2830.35	300x150x300
Weather station	21	943.45	0.4	377.38	4Ux200
Cables		500	1	500	
Mounting hardware		500	4	2000	
Top profiles		1200	10	12000	
Angle brackets		500	10	5000	
Side profiles		500	8	4000	
Small angle brackets		500	4	2000	
Base-plate (27Kg/m^2)		5	25	125	660x1540x10

2 Rack 3: electrical rack

Object	**Height** (U)	**Height** (mm)	**Weight** (Kg)	**Torque** (Kg·mm)	**Dimensions** (mm)
UPS	1	54.45	31	1687.95	2Ux700
Ion pump power supply	5	232.25	22	5109.5	4Ux400
Reference laser servo box	8	365.6	10	3656	3Ux300
Compensation coils supply	11	498.95	4.5	2245.27	2Ux300
Compensation coils supply	13	587.85	4.5	2645.32	2Ux300
Power delayed distributor	11	498.95	1	498.95	1Ux300
Power distributor	5	232.25	0.5	116.125	1Ux50
Reference laser	8	365.6	7	2559.2	4Ux300
Laser 1U tray	7	321.15	1	321.15	1Ux300
Accelerometer driver	10	454.5	0.8	363.6	300x100x100
+5V power supply	14	632.3	0.5	316.15	100x100x50
Electrical board	14	632.3	4	2529.2	400x500x300
Electrical board 1U tray	14	632.3	2	1264.6	2Ux500
Angle brackets		600	10	6000	
Small angle brackets		350	4	1400	
Side profiles		400	8	3200	
Base plate (27Kg/m^2)		5	12	60	640x640x10

Appendix D

Line-width of an extended-cavity diode laser

The line-width of a laser is limited by the phase diffusion due to spontaneous emission in the cavity. The finite photon lifetime yields a finite correlation time as the laser's dynamics are perturbed by random spontaneous emission. In diode lasers coupled dynamics between the photon population and the charge carrier population increase the impact of these fluctuations. Extended-Cavity Diode Lasers (ECDL) narrow the line-width by increasing photon lifetime with an external reflector.

Calculations of these effects can be found in textbooks (Grynberg *et al.* [181], Chow and Sargent III [137], Petermann [182]), but can be difficult to follow and adapt to ECDLs as they are often immersed in a complex description of the laser dynamics. I give here a simplified approach that yields the correct modified Schawlow-Townes formula for a diode laser line-width and apply this result to ECDLs in order to derive their Schawlow-Townes limit.

1 Modified Schalow-Townes formula

1.1 Schawlow-Townes line-width: phase diffusion due to spontaneous emission

The line-width of an ideal laser is limited by the diffusion of the phase of the intracavity electromagnetic field due to spontaneous emission (see Schawlow and Townes [139] for initial studies, or Grynberg *et al.* [181] for a accessible review).

Spontaneous emission in the cavity mode creates modifications in the the amplitude and the phase of this mode :

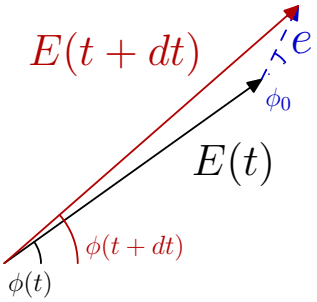

$$E(t+dt)e^{i\phi(t+dt)} = E(t)e^{i\phi(t)} + ee^{i\varphi_0}$$

where e is the quantum of electric field created by a photon emission; and φ_0 is a random phase.

$$\begin{aligned} \text{We have} \quad E(t+dt) &= E(t) + e\cos\phi_0 \\ \text{and} \quad \phi(t+dt) &= \phi(t) + \sin^{-1}\left(\frac{e}{E(t+dt)}\sin\phi_0\right) \end{aligned}$$

If S is the number of intra-cavity photons, and $E = e\,\mathcal{E}$, with $S = |\mathcal{E}|^2$, this can be written as:

$$|\mathcal{E}(t+dt)| = |\mathcal{E}(t)| + \cos\phi_0 \tag{D.1}$$

$$\text{et} \quad \phi(t+dt) = \phi(t) + \sin^{-1}\left(\frac{1}{|\mathcal{E}(t+dt)|}\sin\phi_0\right) \tag{D.2}$$

Gain saturation gives the equilibrium value of S, and, after a spontaneous emission, it will relax toward its equilibrium value. However the phase of the intra-cavity field is arbitrary. It will be modified by each spontaneous emission by a factor of:

$$\delta\phi \sim \frac{1}{\sqrt{S}}\sin\phi_0$$

There is a phase diffusion process due to random jumps of an average amplitude of $\frac{1}{\sqrt{2\,N}}$ with a repetition rate of R_{sp}, the spontaneous emission rate in the cavity mode. The phase RMS width increase as:

$$\sigma\phi(t) = \sqrt{\langle\phi^2\rangle} = \frac{1}{\sqrt{2\,N}}\sqrt{R_{\text{sp}}\,t} \tag{D.3}$$

This phase diffusion can be related to the laser line-width using Wiener-Khintchine theorem that tell us that the spectral density of a signal is given by the Fourrier transform of its correlation function.

Therefore the spectral width of a signal is the inverse of the width of its correlation function, or the inverse of the signal coherence time, given by:

$$\langle\mathcal{E}(t)^\star\mathcal{E}(O)\rangle = |\mathcal{E}(0)|^2 e^{-\frac{|t|}{\tau_{\text{coh}}}}$$

If we neglect the fluctuation of the norm of $\mathcal{E}$ this yields[1]:

$$\langle\mathcal{E}(t)^\star\mathcal{E}(O)\rangle \sim |\mathcal{E}(0)|^2 e^{-\frac{\langle\phi(t)^2\rangle}{2}}$$

[1]This is true only because ϕ is a gaussian random process; as ϕ comes from a diffusion process

$$\text{thus} \qquad \tau_{\text{coh}} = \frac{2t}{\langle \phi(t)^2 \rangle} = \frac{4N}{R_{\text{sp}}}$$

The spectral line-width due to phase diffusion by spontaneous emission is thus given by:

$$\delta\nu = \frac{2}{\tau_{\text{coh}}} = \frac{R_{\text{sp}}}{4\pi S} \tag{D.4}$$

1.2 Henry factor: importance of refractive index fluctuations during spontaneous emission

Optical properties of a semi-conductor medium strongly depend on the charge carrier population. This is why, in a laser diode, the semi-conductor medium becomes transparent only after the upper band population as reached a certain level. After this threshold an inversion of population appears and the medium acts as a gain medium for the electromagnetic wave. The gain appears as a positive imaginary part for the refractive index:

$$E = \mathcal{E}(t)\exp\Big(i(\omega\, t - n\, k_0\, x)\Big)$$

with $k_0 = \dfrac{\omega}{c}$ the vacuum wavevector

$$= \mathcal{E}(t)\exp\Big(i(\omega\, t - n'\, k_0\, x)\Big)\exp(n''\, k_0\, x)$$

with $n = n' + i\, n''$

Below laser threshold, in equilibrium regime, the gain due to the semiconductor medium balance the cavity loss: the total gain average on a cavity round trip is $n'' = 0$ (n is the index of the cavity). The number of charge carriers fluctuates, due to spontaneous emission. This create an index fluctuation, which in turn yields a fluctuation of the gain of the cavity, and of the phase of the field.

The factor α that relates small fluctuation of the real part and the imaginary part of the index is a characteristic of the semiconductor junction, and most often $\alpha \sim 5$.

$$\Delta n = \Delta n' + i\Delta n'' = \Delta n''(\alpha + i) \qquad \text{with} \qquad \alpha = \frac{\Delta n'}{\Delta n''}$$

A modification of $\Delta n''$ of the imaginary part of the index corresponds to a modification of linear gain of[2] $\Delta g = 2k_O\, \Delta n''$, and thus of the gain by unit of time of:

$$\Delta G = \frac{\dot{S}}{S} = 2\omega\frac{v_g}{c}\,\Delta n'' \qquad \text{where } v_g \text{ is the wave's groupe velocity} \tag{D.5}$$

In addition, the fluctuation in the real part of the refractive index yields a phase shift during propagation of:

$$\Delta\phi = \Delta n'\,\frac{\omega}{c}\,x$$

$$\text{Thus, following the wave front} \qquad \Delta\phi = \Delta n'\,\omega\,\frac{v_g}{c}\,t \tag{D.6}$$

[2]The factor of 2 comes from the facts that the gain measures the increase in intensity, and not in electric field.

Thus an electron-hole recombination due to spontaneous emission modifies both the intensity, through the fluctuation of the gain, and the phase. Equations D.5 and D.6 connect intensity and phase modifications:

$$\dot{\Delta\phi} = \frac{\alpha}{2}\frac{\dot{S}}{S} \tag{D.7}$$

For each spontaneous emission of a photon in the cavity mode, the intra-cavity intensity jumps to an out-of-equilibrium value, and the resulting gain modification brings it back to its equilibrium value, after a few relaxation oscillations. During the relaxation oscillations the index fluctuates. A modification of the phase of the electromagnetic field follows. It can be calculated by the integration of equation D.7.

Equation D.1 gives $\delta S \sim 2\sqrt{S}\cos\phi_0$. The phase modification due to the modifications in the number of charge carriers can thus be written[3]:

$$\delta\phi = -\alpha\frac{\cos\phi_0}{\sqrt{S}}$$

Equation D.2 can thus be written taking in account the index modification:

$$\phi(t+dt) = \phi(t) + \frac{1}{\sqrt{S}}\sin\phi_0 + \frac{\alpha}{\sqrt{S}}\cos\phi_0$$

The calculation of the previous section yields the line-width of a diode laser, taking in account the coupled photon–charge carrier dynamics. The resulting formula is often called "modified Schawlow-Townes formula":

$$\delta\nu = \frac{R_{\text{sp}}}{4\pi S}(1+\alpha^2) \tag{D.8}$$

The role of the α^2 factor was first noticed by Henry [142]. A more formal approach can be found in Petermann [182], chap. 7.

2 The effect of the extended cavity

2.1 Calculation of the spontaneous emission rate

The linear gain in the semi-conductor medium is due to radiative stimulated electron-hole recombinations in the laser diode hetero-junction. The rate of spontaneous and stimulated recombinations only depends on the populations of the upper and lower bands of the junction. We can introduce the "inversion factor": $n_{\text{sp}} = r_{\text{sp}}/r_{\text{st}}$, with r_{sp} and r_{st} the spontaneous and stimulated emission rates (see Petermann [182] chap. 2.3). n_{sp} is characteristic of the junction and slowly decrease with injection current. Typically $n_{\text{sp}} \sim 1.5\ldots2.5$ (Petermann [182]).

[3]The minus sign come from the fact that it is a return to equilibrium, the intra-cavity intensity goes from $I + \Delta I$ to I

The gain in photons par time units is equal to the stimulated emission rate minus the cavity losses, R_{sp}, as introduced in the first paragraph. R_{sp} is related to the spontaneous emission rate by a simple geometrical factor Γ_{conf}. Thus:

$$R_{\mathrm{sp}} = \Gamma_{\mathrm{conf}}\, r_{\mathrm{sp}} = \Gamma_{\mathrm{conf}}\, n_{\mathrm{sp}}\, r_{\mathrm{st}}$$

In continuous regime the gain is saturated; the creation of photons by stimulated emission is balanced by the cavity loss:

$$r_{\mathrm{st}} = \frac{1}{\tau_{\mathrm{ph}}} \qquad \text{where } \tau_{\mathrm{ph}} \text{ is the photon lifetime in the cavity.}$$

Thus:

$$R_{\mathrm{sp}} = \frac{\Gamma_{\mathrm{conf}}\, n_{\mathrm{sp}}}{\tau_{\mathrm{ph}}}$$

In addition, the intra-cavity photon number can also be related to the photon lifetime through the out-coupled optical power P_{out} and the losses by absorption or diffusion in the cavity γ_s:

$$\frac{P_{\mathrm{out}}}{\hbar\omega} = S\left(\tau_{\mathrm{ph}}^{-1} - \gamma_s\right)$$

The line-width of a laser diode is thus given by:

$$\delta\nu = \frac{\hbar\omega\, \Gamma_{\mathrm{conf}}\, n_{\mathrm{sp}} (1+\alpha^2)\left(\tau_{\mathrm{ph}}^{-1} - \gamma_s\right)}{4\pi\, \tau_{\mathrm{ph}}\; P_{\mathrm{out}}} \tag{D.9}$$

2.2 Line-width of a laser diode with a linear Fabry-Pérot cavity

Let us describe the cold diode laser (with no injection current) as a Fabry-Pérot cavity with mirrors of reflectivity R_1 and R_2, and an absorbing medium with linear losses of α_s. The optical intensity decreases by a factor of $R_1\, R_2\, e^{-\alpha_s\, 2L}$ for each cavity round trip, that is for a time of $2L/v_g$. The number of intra-cavity photons thus decrease as:

$$S(t) \sim S(0) \exp\left(\left(-\alpha_s\, 2L + \ln(R_1 R_2)\right)\frac{t\, v_g}{2L}\right)$$

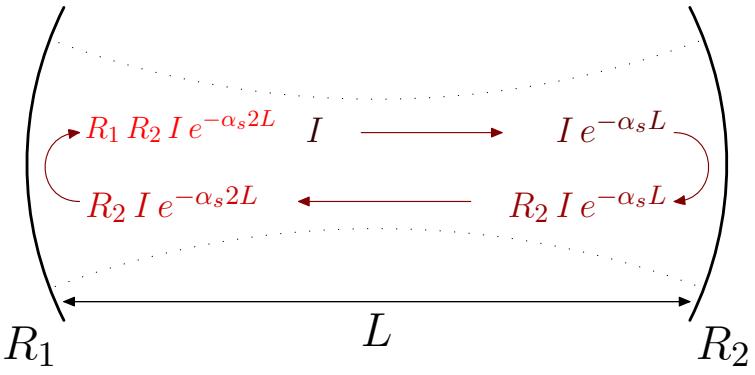

FIGURE D.1 – **Linear cavity, and electro-magnetic field amplitude in the cavity**

Parameter	Symbol	Value
Back face reflectivity	R_1	0.9
Front face reflectivity	R_2	0.06
Confinement factor	Γ_{conf}	0.6
Propagation losses in the medium	α_s	$40\,\text{cm}^{-1}$
Inversion factor	n_{sp}	2.7
Angular frequency	ω	$2\pi \cdot c/780\,\text{nm} \sim 2.42 \cdot 10^{15}\,\text{Hz}$
Henry factor	α	5
Group velocity	v_g	$\frac{c}{4} \sim 75\,000\,000\,\text{m.s}^{-1}$
Output power	P_{out}	20 mW
Cavity length	L	0.1 mm

Table D.1 – **Parameters used to described the laser diode, adapted from Henry [142] to match our experimental situation.**

Photon lifetime in the cavity is thus:

$$\frac{1}{\tau_{\text{ph}}} = v_g\Big(\alpha_s - \frac{1}{2L}\ln(R_1R_2)\Big) \tag{D.10}$$

and the photon loss rate is given by:

$$\gamma_s = v_g\,\alpha_s$$

The line-width of a laser diode can be written:

$$\delta\nu = \frac{\hbar\omega\,\Gamma_{\text{conf}}\,n_{\text{sp}}(1+\alpha^2)v_g^2}{4\pi\,P_{\text{out}}}\Big(\alpha_s - \frac{1}{2L}\ln(R_1R_2)\Big)\,\alpha_s \tag{D.11}$$

Using table D.1 with this formula, one finds a photon lifetime of $\tau_{\text{ph}} \sim 1\,\text{ps}$ and a line-width for an ideal diode laser of:

$$\delta\nu \sim 18\,\text{MHz}$$

2.3 Line-width of an extended-cavity diode laser

As can be seen on equation D.11, a laser diode's line-width decreases as the square of the photons lifetime in the cavity. The addition of an external reflector, as in an Extended Cavity Diode Laser (ECDL) increases the photon lifetime and thus the coherence of the diode.

Let us consider the propagation of a pulse of electrical field E in the coupled cavities to calculate an estimation of the photon life-time in the cavity:

- First the pulse can propagate in the internal cavity, the field decreases as in the last paragraph: $\exp(-t/\tau_{\text{int}})$ where τ_{int} is given by D.10.

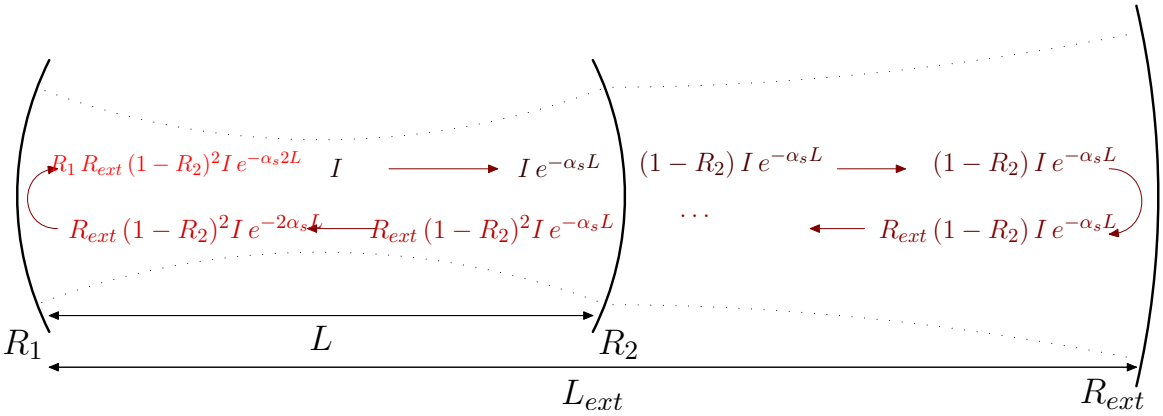

FIGURE D.2 – **Extended cavity, and amplitude of the field in the cavity**

- Additionally, after a time $2\,L_{\text{ext}}/v_g$ corresponding to a round trip in the extended cavity, the pulse comes back with an amplitude of (see Fig. D.2):

$$E\left(\frac{2\,L_{ext}}{v_g}\right) = E(0)\,R_1\,R_{ext}\,(1-R_2)^2 I\,e^{-2\alpha_s L}$$

Supposing that the extended cavity is perfectly tuned, and that the two cavity length are tuned so that the amplitudes of the two paths add up,

$$E\left(\frac{2\,L_{\text{ext}}}{v_g}\right) = E(0)\left(R_1\,R_{ext}\,(1-R_2)^2 e^{-2\alpha_s L} + e^{-\frac{2\,L_{\text{ext}}}{v_g\,\tau_{\text{int}}}}\right)$$

Extrapolating a exponential decrease $\exp(-t/\tau_{\text{ph}})$ from this simple picture, the photon life-time is[4]:

$$\frac{1}{\tau_{\text{ph}}} = -\frac{1}{2\,L_{\text{ext}}}\ln\left((R_1\,R_2)^{\frac{L_{\text{ext}}}{L}} e^{-\alpha_s 2\,L_{\text{ext}}} + R_1\,R_{\text{ext}}(1-R_2)^2 e^{-\alpha_s 2\,L}\right) \tag{D.12}$$

Using equation D.9 with the numbers given in table D.1 and $L_{\text{ext}} = 20\,\text{mm}$ and $R_{\text{ext}} = 0.3$,

$$\tau_{\text{ph}} = 240\,\text{ps}$$

This yields a line-width of

$$\delta\nu \sim 50\,\text{kHz}$$

2.4 Line-width of an AR-coated extended-cavity diode laser

For an anti-reflection coated extended-cavity diode laser, there is no internal cavity. Equation D.10 can be adapted to this situation:

$$\tau_{\text{ph}} = \frac{v_g}{2\,L_{\text{ext}}}\Big(\alpha_s\,2L - \ln(R_1\,R_{\text{ext}})\Big)$$

[4]One should be careful when following the approach found in Petermann [182] that supposes a weak coupling.

Even if the reflectivity of the external reflector is chosen to match the reflectivity of the output facet of a non AR-coated diode laser, the photon lifetime is increased by the increase in cavity length. Using an $R_{\text{ext}} = R_2$, the photon lifetime is $\tau_{\text{ph}} = 100\,\text{ps}$, and the ideal line-width:

$$\delta\nu = 120\,\text{kHz}$$

Appendix E

Production drawings of the Feschbach resonance coils

Figure E.1 – **Next page: Production drawings of the Feshbach resonance coils.**

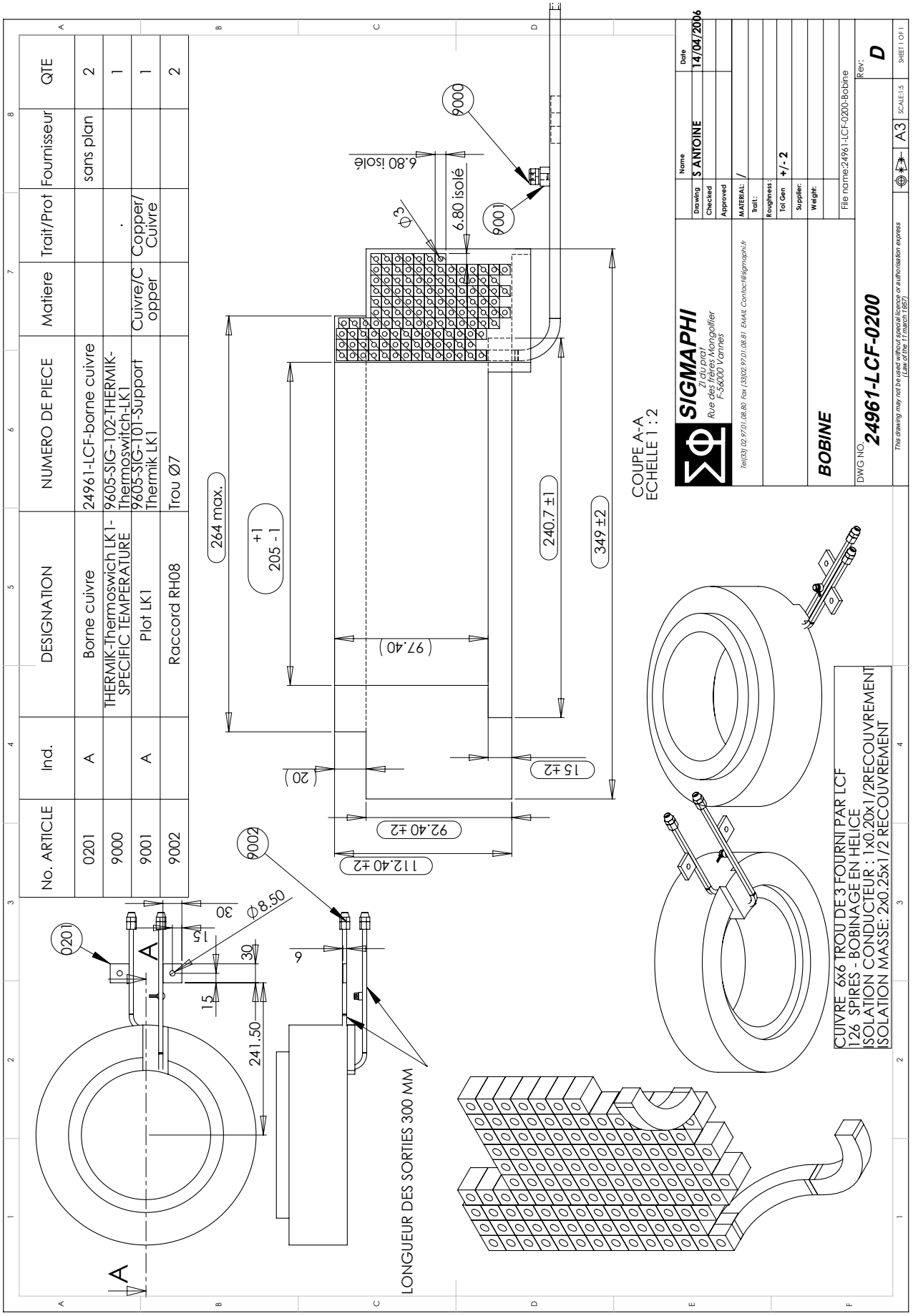
No. ARTICLE | Ind. | DESIGNATION | NUMERO DE PIECE | Matiere | Trait/Prot | Fournisseur | QTE
0201 | A | Borne cuivre | 24961-LCF-borne cuivre | | | sans plan | 2
9000 | | THERMIK-Thermoswich LK1-SPECIFIC TEMPERATURE | 9605-SIG-102-THERMIK-Thermoswitch-LK1 | | . | | 1
9001 | A | Plot LK1 | 9605-SIG-101-Support Thermik LK1 | Cuivre/Copper | Copper/Cuivre | | 1
9002 | | Raccord RH08 | Trou Ø7 | | | | 2
SIGMAPHI
ZI du prat
Rue des frères Montgolfier
F-56000 Vannes
Tel:(33) 02.97.01.08.80 Fax:(33)02.97.01.08.81 EMAIL:Contact@sigmaphi.fr
Drawing S ANTOINE 14/04/2006
Checked
Approved
MATERIAL: /
Trait:
Roughness:
Tol Gen +/- 2
Supplier:
Weight:
BOBINE
DWG NO. 24961-LCF-0200
File name:24961-LCF-0200-Bobine
Rev: D
A3
SCALE:1:5
SHEET 1 OF 1
This drawing may not be used without special licence or authorisation express (Law of the 11 march 1957)
COUPE A-A
ECHELLE 1 : 2
264 max.
205 +1 -1
97.40
240.7 ±1
349 ±2
112.40 ±2
92.40 ±2
15 ±2
20
6.80 isolé
Ø8.50
30
15
241.50
6
LONGUEUR DES SORTIES 300 MM
CUIVRE 6x6 TROU DE 3 FOURNI PAR LCF
126 SPIRES - BOBINAGE EN HELICE
ISOLATION CONDUCTEUR : 1x0.20x1/2RECOUVREMENT
ISOLATION MASSE: 2x0.25x1/2 RECOUVREMENT

Appendix F

Rubidium and potassium atomic levels

1 Rubidium

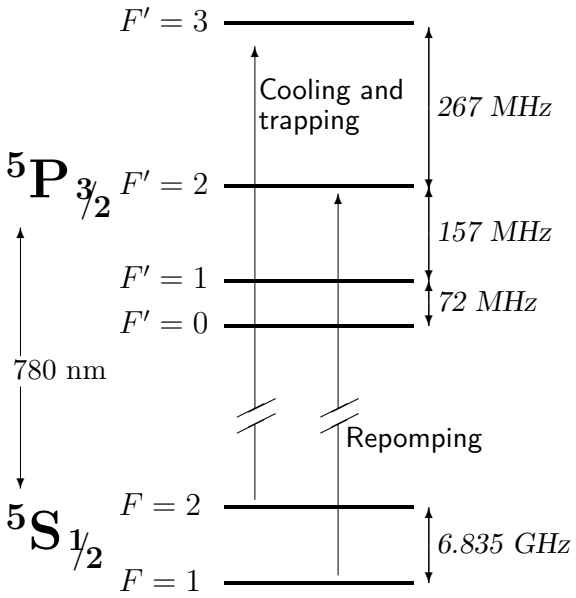

Figure F.1 – **Hyperfine sublevels of rubidium 87**

2 Potassium

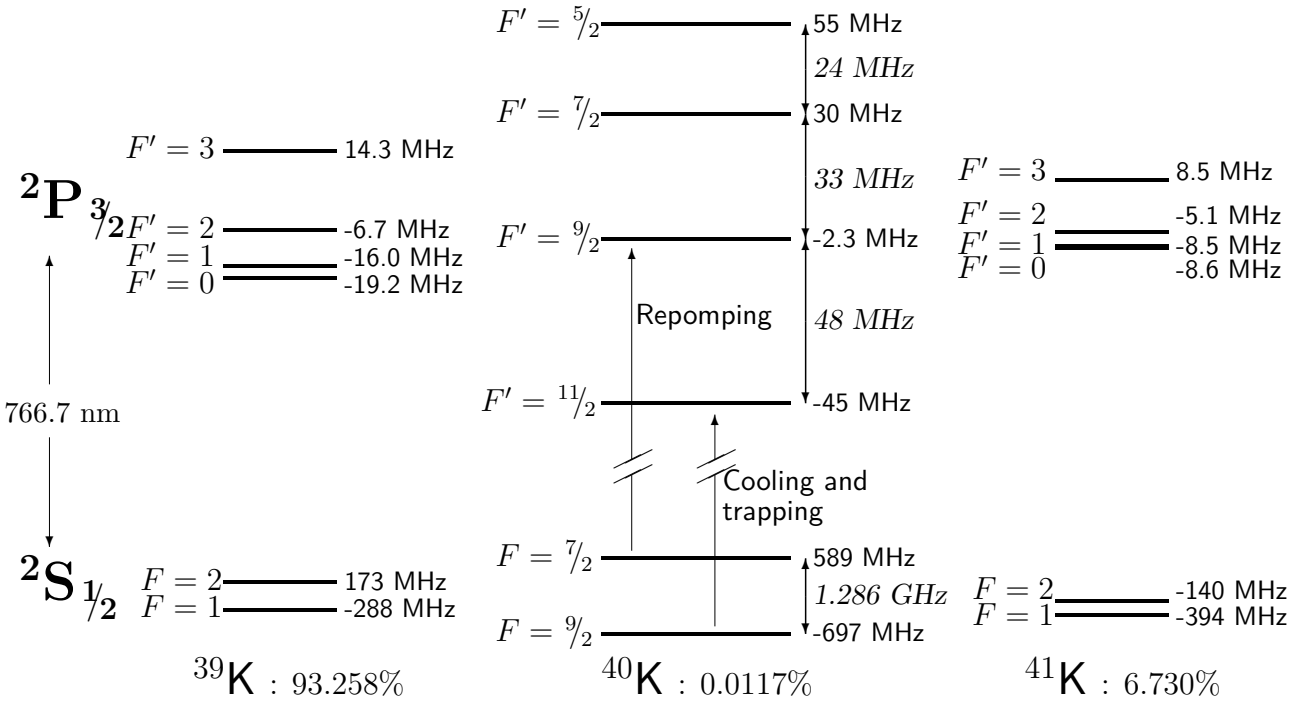

Figure F.2 – **Hyperfine sub-levels of the different isotopes of potassium (data from Williamson [121]).**

Bibliography

[1] L. de Broglie, Recherches sur la théorie des Quanta. Ph.D. thesis, http://tel.archives-ouvertes.fr/tel-00006807/fr (1924).

[2] M. H. Anderson, J. R. Ensher, M. R. Matthews, C. E. Wieman, and E. A. Cornell, Observation of Bose-Einstein condensation in a dilute atomic vapor. *Science* **269**(0), 198 (Jul. 1995).

[3] M. A. Kasevich, E. Riis, S. Chu, and R. G. DeVoe, RF spectroscopy in an atomic fountain. *Phys. Rev. Lett.* **63**(6), 612 (Aug 1989).

[4] M. R. Andrews, C. G. Townsend, H.-J. Miesner, D. S. Durfee, D. M. Kurn, and W. Ketterle, Observation of interference between two Bose-Einstein condensates. *Science* **275**(0), 637 (Jan. 1997).

[5] K. B. Davis, M.-O. Mewes, M. R. Andrews, N. J. van Druten, D. S. Durfee, D. M. Kurn, and W. Ketterle, Bose-Einstein condensation in a gas of sodium atoms. *Phys. Rev. Lett.* **75**(22), 3969 (Nov. 1995).

[6] A. Abramovici, W. E. Althouse, R. W. P. Drever, Y. Gursel, S. Kawamura, F. J. Raab, D. Shoemaker, L. Sievers, R. E. Spero, and K. S. Thorne, LIGO - The Laser Interferometer Gravitational-Wave Observatory. *Science* **256**, 325 (Apr. 1992).

[7] J. E. Zimmerman and J. Mercereau, Compton wavelength of superconducting electrons. *Phys. Rev. Lett* **14**, 887 (1965).

[8] D. M. Greenberger, The neutron interferometer as a device for illustrating the strange behavior of quantum systems. *Reviews of Modern Physics* **55**, 875 (Oct. 1983).

[9] H. Rauch, W. Treimer, and U. Bonse, Test of a single crystal neutron interferometer. *Physics Letters A* **47**, 369 (Apr. 1974).

[10] F. Riehle, T. Kisters, A. Witte, J. Helmcke, and C. J. Bordé, Optical Ramsey spectroscopy in a rotating frame - Sagnac effect in a matter-wave interferometer. *Physical Review Letters* **67**, 177 (Jul. 1991).

[11] M. Kasevich and S. Chu, Atomic interferometry using stimulated Raman transitions. *Physical Review Letters* **67**, 181 (Jul. 1991).

[12] D. W. Keith, C. R. Ekstrom, Q. A. Turchette, and D. E. Pritchard, An interferometer for atoms. *Phys. Rev. Lett.* **66**(21), 2693 (May 1991).

[13] F. Hasselbach and M. Nicklaus, Sagnac experiment with electrons: Observation of the rotational phase shift of electron waves in vacuum. *Phys. Rev. A* **48**, 143 (Jul. 1993).

[14] A. Peters, K. Y. Chung, and S. Chu, High-precision gravity measurements using atom interferometry. *Metrologia* **38**, 25 (2001).

[15] B. Canuel, F. Leduc, D. Holleville, A. Gauguet, J. Fils, A. Virdis, A. Clairon, N. Dimarcq, C. J. Bordé, A. Landragin, and P. Bouyer, Six-Axis Inertial Sensor Using Cold-Atom Interferometry. *Physical Review Letters* **97**(1), 010402 (Jul. 2006).

[16] J. M. McGuirk, G. T. Foster, J. B. Fixler, M. J. Snadden, and M. A. Kasevich, Sensitive absolute-gravity gradiometry using atom interferometry. *Phys. Rev. A* **65**(3), 033608 (Feb 2002).

[17] T. L. Gustavson, A. Landragin, and M. A. Kasevich, Rotation sensing with a dual atom-interferometer Sagnac gyroscope . *Classical and Quantum Gravity* **17**, 2385 (Jun. 2000).

[18] G. Geneves, P. Gournay, A. Gosset, M. Lecollinet, F. Villar, P. Pinot, P. Juncar, A. Clairon, A. Landragin, D. Holleville, F. Dos Santos, J. David, M. Besbes, F. Alves, L. Chassagne, and S. Topcu, The bnm watt balance project. *Instrumentation and Measurement, IEEE Transactions on* **54**(2), 850 (April 2005), ISSN 0018-9456.

[19] A. Peters, K. Y. Chung, B. Young, J. Hensley, and S. Chu, Precision Atom Interferometry. *Royal Society of London Proceedings Series A* **355**, 2223 (Dec. 1997).

[20] J. Stuhler, M. Fattori, T. Petelski, and G. M. Tino, MAGIA - using atom interferometry to determine the Newtonian gravitational constant. *Journal of Optics B: Quantum and Semiclassical Optics* **5**, 75 (Apr. 2003).

[21] N. Yu, J. M. Kohel, J. R. Kellogg, and L. Maleki, Development of an atom-interferometer gravity gradiometer for gravity measurement from space. *Applied Physics B: Lasers and Optics* **84**, 647 (Sep. 2006).

[22] R. A. Nyman, G. Varoquaux, F. Lienhart, D. Chambon, S. Boussen, J.-F. Clément, T. Müller, G. Santarelli, F. Pereira Dos Santos, A. Clairon, A. Bresson, A. Landragin, and P. Bouyer, I.C.E.: a transportable atomic inertial sensor for test in microgravity. *Applied Physics B: Lasers and Optics* **84**, 673 (Sep. 2006).

[23] T. Wendrich, M. Gilowski, T. Muller, W. Herr, C. Schubert, E. Rasel, and W. Ertmer, Cold atom sagnac interferometer. *Frequency Control Symposium, 2007 Joint with the 21st European Frequency and Time Forum. IEEE International* pp. 647–647 (May 29 2007-June 1 2007), ISSN 1075-6787.

[24] A. Clairon, C. Salomon, S. Guellati, and W. D. Phillips, Ramsey resonance in a Zacharias fountain. *Europhysics Letters* **16**, 165 (Sep. 1991).

[25] N. F. R. Daniel Kleppner, Robert F. C. Vessot, An orbiting clock experiment to determine the gravitational red shift. *Astrophysics and Space Science* **6**(1), 13 (1970).

[26] P. Laurent, M. Abgrall, C. Jentsch, P. Lemonde, G. Santarelli, A. Clairon, I. Maksimovic, S. Bize, C. Salomon, D. Blonde, J. F. Vega, O. Grosjean, F. Picard, M. Saccoccio, M. Chaubet, N. Ladiette, L. Guillet, I. Zenone, C. Delaroche, and C. Sirmain, Design of the cold atom PHARAO space clock and initial test results. *App. Phys. B* **84**, 683 (Sep. 2006).

[27] P. Laurent, P. Lemonde, E. Simon, G. Santarelli, A. Clairon, N. Dimarcq, P. Petit, C. Audoin, and C. Salomon, A cold atom clock in absence of gravity. *European Physical Journal D* **3**, 201 (1998).

[28] J. S. Bell, On the einstein-podolsky-rosen paradox. *Physics* **4**(1), 195 (1968).

[29] A. Aspect, Bell's theorem : the naive view of an experimentalist. In R. A. Bertlmann and A. Zeilinger, eds., Quantum [Un]speakables – From Bell to Quantum information, Springer (2002), quant-ph/0402001.

[30] O. Penrose and L. Onsager, Bose-einstein condensation and liquid helium. *Phys. Rev.* **104**(3), 576 (Nov 1956).

[31] G. Magyar and L. Mandel, Interference Fringes Produced by Superposition of Two Independent Maser Light Beams. *Nature* **198**, 255 (Apr. 1963).

[32] R. Hanbury Brown and R. Q. Twiss, A test of a new type of stellar interferometer on Sirius. *Nature* **178**, 1046 (1956).

[33] R. J. Glauber, The quantum theory of optical coherence. *Phys. Rev.* **131**(6), 2529 (Jun. 1963).

[34] P. A. M. Dirac, The principles of quantum mechanics. The International Series of Monographs on Physics, Oxford: Clarendon Press, 1947 (1947).

[35] Z. Y. Ou, Multi-photon interference and temporal distinguishability of photons. quant-ph:0708.0077 (2007).

[36] L. Mandel and E. Wolf, Optical coherence and quantum optics. Cambridge: Cambridge University Press, |c1995 (1995).

[37] E. Collett and E. Wolf, Is complete spatial coherence necessary for the generation of highly directional light beams? *Optics Letters* **2**, 27 (Feb. 1978).

[38] Q. Shen, X-ray flux, brilliance and coherence of the proposed cornell energy-recovery synchrotron source. http://erl.chess.cornell.edu/papers/2001/ERLPub01_4.pdf (2001).

[39] F. Gerbier, J. H. Thywissen, S. Richard, M. Hugbart, P. Bouyer, and A. Aspect, Momentum distribution and correlation function of quasicondensates in elongated traps. *Phys. Rev. A* **67**, 051602(R) (May 2003).

[40] T. Donner, S. Ritter, T. Bourdel, A. Öttl, M. Köhl, and T. Esslinger, Critical Behavior of a Trapped Interacting Bose Gas. *Science* **315**, 1556 (Mar. 2007).

[41] Y. Le Coq, J. H. Thywissen, S. A. Rangwala, F. Gerbier, S. Richard, G. Delannoy, P. Bouyer, and A. Aspect, Atom laser divergence. *Phys. Rev. Lett.* **87**(17), 170403 (Oct. 2001).

[42] D. A. Butts and D. S. Rokhsar, Trapped fermi gases. *Phys. Rev. A* **55**(6), 4346 (Jun 1997).

[43] F. Dalfovo, S. Giorgini, L. P. Pitaevskii, and S. Stringari, Theory of Bose-Einstein condensation in trapped gases. *Rev. Mod. Phys.* **71**(3), 463 (Apr. 1999).

[44] K. Gibble and S. Chu, Laser-cooled Cs frequency standard and a measurement of the frequency shift due to ultracold collisions. *Phys. Rev. Lett.* **70**(12), 1771 (Mar. 1993).

[45] Y. Sortais, S. Bize, C. Nicolas, A. Clairon, C. Salomon, and C. Williams, Cold collision frequency shifts in a ^{87}Rb atomic fountain. *Phys. Rev. Lett.* **85**(15), 3117 (Oct 2000).

[46] F. Pereira Dos Santos, H. Marion, S. Bize, Y. Sortais, A. Clairon, and C. Salomon, Controlling the cold collision shift in high precision atomic interferometry. *Phys. Rev. Lett.* **89**(23), 233004 (Nov 2002).

[47] Y. Le Coq, J. A. Retter, S. Richard, A. Aspect, and P. Bouyer, Coherent matter wave inertial sensors for precision measurements in space. *Applied Physics B: Lasers and Optics* **84**, 627 (Sep. 2006).

[48] Y. Castin and J. Dalibard, Relative phase of two Bose-Einstein condensates. *Phys. Rev. A* **55**(6), 4330 (Jun. 1997).

[49] G.-B. Jo, Y. Shin, S. Will, T. A. Pasquini, M. Saba, W. Ketterle, D. E. Pritchard, M. Vengalattore, and M. Prentiss, Long Phase Coherence Time and Number Squeezing of Two Bose-Einstein Condensates on an Atom Chip. *Physical Review Letters* **98**(3), 030407 (Jan. 2007).

[50] S. Gupta, Z. Hadzibabic, M. W. Zwierlein, C. A. Stan, K. Dieckmann, C. H. Schunck, E. G. M. van Kempen, B. J. Verhaar, and W. Ketterle, Radio-frequency spectroscopy of ultracold fermions. *Science* **300**, 1723 (Jun. 2003).

[51] G. Roati, E. de Mirandes, F. Ferlaino, H. Ott, G. Modugno, and M. Inguscio, Atom Interferometry with Trapped Fermi Gases. *Physical Review Letters* **92**(23), 230402 (Jun. 2004).

[52] D. J. Wineland, J. J. Bollinger, W. M. Itano, F. L. Moore, and D. J. Heinzen, Spin squeezing and reduced quantum noise in spectroscopy. *Phys. Rev. A* **46**, 6797 (Dec. 1992).

[53] G. Santarelli, P. Laurent, P. Lemonde, A. Clairon, A. G. Mann, S. Chang, A. N. Luiten, and C. Salomon, Quantum Projection Noise in an Atomic Fountain: A High Stability Cesium Frequency Standard. *Physical Review Letters* **82**, 4619 (Jun. 1999).

[54] M. Fattori, C. D'Errico, G. Roati, M. Zaccanti, M. Jona-Lasinio, M. Modugno, M. Inguscio, and G. Modugno, Atom interferometry with a weakly-interacting bose einstein condensate. condmat/0710.5131 (2007).

[55] S. L. Cornish, N. R. Claussen, J. L. Roberts, E. A. Cornell, and C. E. Wieman, Stable ^{85}Rb Bose-Einstein condensates with widely tunable interactions. *Phys. Rev. Lett.* **85**(9), 1795 (Aug. 2000).

[56] S. Chu, The manipulation of neutral particles. *Rev. Mod. Phys.* **70**(3), 685 (Jul. 1998).

[57] C. N. Cohen-Tannoudji, Manipulating atoms with photons. *Rev. Mod. Phys.* **70**(3), 707 (Jul. 1998).

[58] W. D. Phillips, Laser cooling and trapping of neutral atoms. *Rev. Mod. Phys.* **70**(3), 721 (Jul. 1998).

[59] H. F. Hess, Evaporative cooling of magnetically trapped and compressed spin-polarized hydrogen. *Phys. Rev. B* **34**(5), 3476 (Sep. 1986).

[60] H. Metcalf and P. van der Straten, Laser Cooling and Trapping. Springer, New York (1999).

[61] T. Mukaiyama, H. Katori, T. Ido, Y. Li, and M. Kuwata-Gonokami, Recoil-limited laser cooling of ^{87}Sr atoms near the Fermi temperature. *Phys. Rev. Lett.* **90**(11), 113002 (Mar 2003).

[62] P. Bouyer and M. A. Kasevich, Heisenberg-limited spectroscopy with degenerate Bose-Einstein gases. *Phys. Rev. A* **56**, 1083 (Aug. 1997).

[63] C. J. Bordé, Propagation of laser beams and of atomic systems. In J. Dalibard, J.-M. Raimond, and J. Zinn-Justin, eds., Fundamental Systems in Quantum Optics, Elsevier Science Publishers (1991).

[64] P. Wolf and P. Tourrenc, Gravimetry using atom interferometers: Some systematic effects. *Physics Letters A* **251**, 241 (Jan. 1999).

[65] L. Vitushkin, Measurement standards in absolute gravimetry and comparisons of absolute gravimeters at the BIPM. http://space.cv.nctu.edu.tw/SG/5_LV_presentation_Taipei_March-2007.pdf (2007).

[66] T. L. Gustavson, P. Bouyer, and M. A. Kasevich, Precision Rotation Measurements with an Atom Interferometer Gyroscope. *Physical Review Letters* **78**, 2046 (Mar. 1997).

[67] P. Storey and C. Cohen-Tannoudji, The Feynman path integral approach to atomic interferometry. Atutorial. *Journal de Physique II* **4**, 1999 (Nov. 1994).

[68] C. J. Bordé, Atomic interferometry with internal state labeling. *Phys. Lett. A* (1989).

[69] K. Moler, D. S. Weiss, M. Kasevich, and S. Chu, Theoretical analysis of velocity-selective Raman transitions. *Phys. Rev. A* **45**, 342 (Jan. 1992).

[70] C. Antoine and C. J. Bordé, Quantum theory of atomic clocks and gravito-inertial sensors: an update. *Journal of Optics B* **5**, 1999 (Apr. 2003).

[71] E. J. Post, Sagnac effect. *Rev. Mod. Phys.* **39**(2), 475 (Apr 1967).

[72] D. M. Greenberger and A. W. Overhauser, Coherence effects in neutron diffraction and gravity experiments. *Rev. Mod. Phys.* **51**(1), 43 (Jan 1979).

[73] C. Antoine, Rotating matter-wave beam splitters and consequences for atom gyrometers. *Physical Review A (Atomic, Molecular, and Optical Physics)* **76**(3), 033609 (2007).

[74] P. Langevin, Theorie de l'experience de sagnac. *C. R. Acad. Sc (Paris)* **173**, 821 (1921).

[75] L. Silberstein, The Propagation of Light in Rotating Systems. *Journal of the Optical Society of America (1917-1983)* **5**, 291 (Jul. 1921).

[76] J. Anandan, Sagnac effect in relativistic and non-relativistic physics. *Phys. Rev. D* **24**, 338 (Jul. 1981).

[77] C. J. Bordé, Theoretical tools for atom optics and interferometry. *Comptes Rendus de l'Académie des Sciences, t. 2* **IV**, 509 (2001).

[78] O. Avenel, Y. Mukharsky, and E. Varoquaux, Superfluid gryometers. *Journal of Low Temperature Physics* **135**, 745 (2004).

[79] E. Varoquaux and G. Varoquaux, The Sagnac effect in superfluids. arXiv:0707.0270v1 (Jul. 2007), accepted in Uspekhi Fizicheskikh Nauk.

[80] H. J. Arditty and H. C. Lefevre, Sagnac effect in fiber gyroscopes. *Optics Letters* **6**, 401 (Aug. 1981).

[81] N. Ashby and D. W. Allan, Coordinate time on and near the earth. *Phys. Rev. Lett* **53**(19), 1858 (1984).

[82] G. B. Malykin, The Sagnac effect: correct and incorrect explanations. *Uspekhi Fizicheskikh Nauk* **43**, 1229 (Dec. 2000).

[83] K. K. Nandi and Y.-Z. Zhang, General relativistic effects on quantum interference and the principle of equivalence. *Phys. Rev. D* **66**(6), 063005 (Sep. 2002).

[84] G. Rizzi and M. L. Ruggiero, A Direct Kinematical Derivation of the Relativistic Sagnac Effect for Light or Matter Beams. *General Relativity and Gravitation* **35**, 2129 (Dec. 2003), see also *Relativity in Rotating Frames*, (Kluwer Academic Publishers, Dordrecht, 2004) http://diglander.libero.it/solciclos/, p. 179.

[85] G. Stedman, R. Hurst, and K. Schreiber, On the potential of large ring lasers. *Optics Communications* **279** (2007).

[86] G. Varoquaux, N. Zahzam, W. Chaibi, J.-F. Clément, O. Carraz, J.-P. Brantut, R. A. Nyman, F. Pereira Dos Santos, L. Mondin, M. Rouzé, Y. Bidel, A. Bresson, A. Landragin, and P. Bouyer, I.C.E.: An Ultra-Cold Atom Source for Long-Baseline Interferometric Inertial Sensors in Reduced Gravity. In Proceedings of Rencontres de Moriond on Gravitational Waves and Experimental Gravity (2007).

[87] A. Vogel, M. Schmidt, K. Sengstock, K. Bongs, W. Lewoczko, T. Schuldt, A. Peters, T. van Zoest, W. Ertmer, E. Rasel, T. Steinmetz, J. Reichel, T. Könemann, W. Brinkmann, E. Göklü, C. Lämmerzahl, H. J. Dittus, G. Nandi, W. P. Schleich, and R. Walser, Bose Einstein condensates in microgravity. *Applied Physics B: Lasers and Optics* **84**, 663 (Sep. 2006).

[88] D. W. Allan, Statistics of atomic frequency standards, pp. 466–+. Precision Measurement and Calibration (Jun. 1972).

[89] J. D. Anderson, P. A. Laing, E. L. Lau, A. S. Liu, M. M. Nieto, and S. G. Turyshev, Study of the anomalous acceleration of Pioneer 10 and 11. *Phys. Rev. D* **65**(8), 082004 (Apr. 2002).

[90] S. Buchman, C. W. F. Everitt, B. Parkinson, J. P. Turneaure, D. Debra, D. Bardas, W. Bencze, R. Brumley, D. Gill, G. Gutt, D. H. Gwo, G. M. Keiser, J. Lipa, J. Lockhart, J. Mester, B. Muhlfelder, M. Taber, S. Wang, Y. Xiao, and P. Zhou, The Gravity Probe B Relativity Mission. *Advances in Space Research* **25**, 1177 (2000).

[91] H. Dittus, C. Laämmerzhal, and S. Turyshev, eds., Lasers, Clocks, and Drag-Free: Exploration of Relativistic Gravity in Space. Springer (2007).

[92] L. D. Landau and E. M. Lifshitz, Field theory. Course of theoretical physics, Oxford: Pergamon Press, 1965 (1965).

[93] R. Bingham *et al.*, HYPER Hyper-Precision Cold Atom Interferometry in Space Assessment Study Report, vol. 10. ESA-SCI (2000).

[94] M.-C. Angonin, P. Tourrenc, and P. Delva, Cold atom interferometer in a satellite: orders of magnitude of the tidal effect. *Applied Physics B: Lasers and Optics* **84**, 579 (Sep. 2006).

[95] S. Dimopoulos, P. W. Graham, J. M. Hogan, and M. A. Kasevich, Testing general relativity with atom interferometry. *Physical Review Letters* **98**(11), 111102 (2007).

[96] A. Einstein, On the relativity principle and the conclusions drawn from it. In The collected papers of Albert Einstein. Vol. 2 : The Swiss years: writings, 1900–1909, Princeton University Press, Princeton, NJ (1907), anna Beck translator.

[97] A. Harvey, ed., On Einstein's Path, essays in honor of Engelbert Schucking (1999).

[98] M. W. Clifford, The confrontation between general relativity and experiment. *Living Rev. Relativity* **9**, 3 (2006), http://www.livingreviews.org/lrr-2006-3.

[99] R. H. Dicke, Experimental relativity. In C. M. DeWitt and B. S. DeWitt, eds., Relativity, Groups and Topology. Relativité, Groupes et Topologie, pp. 165–313, Gordon and Breach, New York, U.S.A. (1964).

[100] L. I. Schiff, On Experimental Tests of the General Theory of Relativity. *American Journal of Physics* **28**, 340 (Apr. 1960).

[101] C. Lämmerzahl, The search for quantum gravity effects I. *Applied Physics B: Lasers and Optics* **84**, 551 (Sep. 2006).

[102] C. Lämmerzahl, The search for quantum gravity effects II: Specific predictions. *Applied Physics B: Lasers and Optics* **84**, 563 (Sep. 2006).

[103] R. Chhun, M. Rodrigues, and P. Touboul, Microscope mission and performance. *Nuclear Physics B Proceedings Supplements* **113**, 277 (2002).

[104] T. J. Sumner, J. Anderson, J.-P. Blaser, A. M. Cruise, T. Damour, H. Dittus, C. W. F. Everitt, B. Foulon, Y. Jafry, B. J. Kent, N. Lockerbie, F. Loeffler, G. Mann, J. Mester, C. Pegrum, R. Reinhardt, M. Sandford, A. Scheicher, C. C. Speake, R. Torii, S. Theil, P. Touboul, S. Vitale, W. Vodel, and P. W. Worden, STEP (satellite test of the equivalence principle). *Advances in Space Research* **39**, 254 (2007).

[105] P. Wolf, F. Chapelet, S. Bize, and A. Clairon, Cold Atom Clock Test of Lorentz Invariance in the Matter Sector. *Physical Review Letters* **96**(6), 060801 (Feb. 2006).

[106] L. Cacciapuoti, N. Dimarcq, G. Santarelli, P. Laurent, P. Lemonde, A. Clairon, P. Berthoud, A. Jornod, F. Reina, S. Feltham, and C. Salomon, Atomic Clock Ensemble in Space: Scientific Objectives and Mission Status. *Nuclear Physics B Proceedings Supplements* **166**, 303 (Apr. 2007).

[107] S. Fray, C. A. Diez, T. W. Hänsch, and M. Weitz, Atomic Interferometer with Amplitude Gratings of Light and Its Applications to Atom Based Tests of the Equivalence Principle. *Physical Review Letters* **93**(24), 240404 (Dec. 2004).

[108] F. Yver-Leduc, P. Cheinet, J. Fils, A. Clairon, N. Dimarcq, D. Holleville, P. Bouyer, and A. Landragin, Reaching the quantum noise limit in a high-sensitivity cold-atom inertial sensor. *Journal of Optics B* **5**, 136 (Apr. 2003).

[109] P. Cheinet, B. Canuel, F. Pereira Dos Santos, A. Gauguet, F. Leduc, and A. Landragin, Measurement of the sensitivity function in time-domain atomic interferometer. *ArXiv Physics e-prints* (Oct. 2005).

[110] J. Le Gouet, P. Cheinet, J. Kim, D. Holleville, A. Clairon, A. Landragin, and F. P. D. Santos, Influence of lasers propagation delay on the sensitivity of atom interferometers (2007).

[111] G. T. Foster, J. B. Fixler, J. M. McGuirk, and M. A. Kasevich, Method of phase extraction between coupled atom interferometers using ellipse-specific fitting. *Optics Letters* **27**, 951 (Jun. 2002).

[112] J. K. Stockton, X. Wu, and M. A. Kasevich, Bayesian estimation of differential interferometer phase. *Physical Review A (Atomic, Molecular, and Optical Physics)* **76**(3), 033613 (2007).

[113] F. Lienhart, S. Boussen, O. Carraz, N. Zahzam, Y. Bidel, and A. Bresson, Compact and robust laser system for rubidium laser cooling based on the frequency doubling of a fiber bench at 1560 nm. *Applied Physics B: Lasers and Optics* pp. 290–+ (Sep. 2007).

[114] F. Lienhart, Etude d'un gravimètre à atomes froids embarquable. Ph.D. thesis, Université de Paris VII (2007).

[115] R. J. Thompson, M. Tu, D. C. Aveline, N. Lundblad, and L. Maleki, High power single frequency 780nm laser source generated from frequency doubling of a seeded fiber amplifier in a cascade of PPLN crystals. *Optics Express* **11**, 1709 (Jul. 2003).

[116] R. Besson and M. Mourey. In Proc. of the 11th European Frequency and Time Forum, p. 227, Neuchatel, Switzerland (1997).

[117] P. Worden, R. Torii, J. C. Mester, and C. W. F. Everitt, The STEP Payload and Experiment. *Advances in Space Research* **25**, 1205 (2000).

[118] R. A. Nyman, G. Varoquaux, B. Villier, D. Sacchet, F. Moron, Y. Le Coq, A. Aspect, and P. Bouyer, Tapered-amplified antireflection-coated laser diodes for potassium and rubidium atomic-physics experiments. *Review of Scientific Instruments* **77**, 3105 (Mar. 2006).

[119] B. Sheehy, S.-Q. Shang, R. Watts, S. Hatamian, and H. Metcalf, Diode-laser deceleration and collimation of a rubidium beam. *J. Opt. Soc. Am. B* **6**, 2165 (1989).

[120] R. S. Williamson and T. Walker, Magneto-optical trapping and ultracold collisions of potassium atoms. *Journal of the Optical Society of America B: Optical Physics* **12**(8), 1393 (1995).

[121] R. S. Williamson, Magneto-optical trapping of potassium isotopes. Ph.D. thesis, University of Wisconsin - Madison (1997).

[122] C. E. Wieman and L. Hollberg, Using diode lasers for atomics physics. *Rev. Sci. Instrum.* **62**, 1 (1991).

[123] A. S. Arnold, J. S. Wilson, and M. G. Boshier, A simple extended-cavity diode laser. *Rev. Sci. Instrum.* **69**, 1236 (1998).

[124] M. G. Littmann and H. J. Metcalf, Spectrally narrowed pulsed due laser without beam expander. *Applied Optics* **17**, 2224 (1978).

[125] S. Aubin, M. H. T. Extavour, S. Myrskog, L. J. LeBlanc, J. Esteve, S. Singh, P. Scrutton, D. McKay, R. McKenzie, I. D. Leroux, A. Stummer, and J. H. Thywissen, Trapping fermionic ^{40}K and bosonic ^{87}Rb on a chip. *Journal of Low Temperature Physics* **140**, 377 (2005).

[126] F. S. Cataliotti, E. A. Cornell, C. Fort, M. Inguscio, F. Marin, M. Prevedelli, L. Ricci, and G. M. Tino, Magneto-optical trapping of fermionic potassium atoms. *Phys. Rev. A* **57**(2), 1136 (Feb. 1998).

[127] M. Prevedelli, F. S. Cataliotti, E. A. Cornell, J. R. Ensher, C. Fort, L. Ricci, G. M. Tino, and M. Inguscio, Trapping and cooling of potassium isotopes in a double-magneto-optical-trap apparatus. *Phys. Rev. A* **59**(1), 886 (Jan. 1999).

[128] B. Demarco, Quantum Behavior of an atomic fermi gas. Ph.D. thesis, University of Colorado (2001).

[129] C. S. Fletcher and J. D. Close, Extended temperature tuning of an external cavity diode laser. *Applied Physics B: Lasers and Optics* **78**, 305 (2004).

[130] I. Shvarchuck, K. Dieckmann, M. Zielonkowski, and J. T. M. Walraven, Broad-area diode-laser system for a rubidium Bose-Einstein condensation experiment. *Appl. Phys. B* **71**, 475 (2000).

[131] D. Voigt, E. C. Schilder, R. J. C. Spreeuw, and H. B. van Linden van den Heuvell, Characterization of a high-power tapered semiconductor amplifier system. *Appl. Phys. B* **72**, 279 (2001).

[132] J. Goldwin, S. B. Papp, B. DeMarco, and D. S. Jin, Two-species magneto-optical trap with ^{40}K and ^{87}Rb. *Phys. Rev. A* **65**, 021402 (2002).

[133] J. Catani, P. Maioli, L. de Sarlo, F. Minardi, and M. Inguscio, Intense slow beams of bosonic potassium isotopes. *Phys. Rev. A* **73**(3), 033415 (Mar. 2006).

[134] D. Cassettari, E. Arimondo, and P. Verkerk, External-cavity broad-arealaser diode operating on the D1 line of cesium. *Optics Letters* **23**, 1135 (Jul. 1998).

[135] C. Aussibal, Réalisation d'un condesat de Bose-Einstein sur une microstructure. Ph.D. thesis, Laboratoire Charles Fabry de l'Institut d'Optique, Université de Paris Sud XI (2003).

[136] J. Sacher, D. Baums, P. Panknin, W. Elsässer, and E. O. Göbel, Intensity instabilities of semiconductor lasers under current modulation, external light injection, and delayed feedback. *Phys. Rev. A* **45**(3), 1893 (Feb. 1992).

[137] S. K. W. W. Chow and M. Sargent III, Semiconductor-Laser Physics. Springer, Berlin (1994).

[138] L. Hildebrandt, R. Knispel, S. Stry, J. R. Sacher, and F. Schael, Antireflection-coated blue gaN laser diodes in an external cavity and doppler-free indium absorption spectroscopy. *Applied Optics* **42**(12), 2110 (2003).

[139] A. L. Schawlow and C. H. Townes, Infrared and optical masers. *Phys. Rev.* **112**(6), 1940 (1958).

[140] M. S. Santos, P. Nussenzveig, L. G. Marcassa, K. Helmerson, J. Flemming, S. C. Zilio, and V. S. Bagnato, Simultaneous trapping of two different atomic species in a vapor-cell magneto-optical trap. *Phys. Rev. A* **52**(6), R4340 (Dec. 1995).

[141] Y. Le Coq, Condensat de Bose-Einstein et Lasers á Atomes. Ph.D. thesis, Laboratoire Charles Fabry de l'Institut d'Optique, Université de Paris Sud XI (2002).

[142] C. H. Henry, Theory of the linewidth of semiconductor lasers. *IEEE J. Quant. Electron.* **QE-18**(2), 259 (1982).

[143] G. Ferrari, M.-O. Mewes, F. Schreck, and C. Salomon, High-power multiple-frequency narrow-linewidth laser source based on a semiconductor tapered amplifier. *Optics Letters* **24**(3), 151 (1999).

[144] K. Dieckmann, R. J. C. Spreeuw, M. Weidemüller, and J. T. M. Walraven, Two-dimensional magneto-optical trap as a source of slow atoms. *Phys. Rev. A* **58**(5), 3891 (Nov. 1998).

[145] J. Dalibard, Cours de DEA: Atomes ultras-froids. http://www.phys.ens.fr/~dalibard/Notes_de_cours/DEA_atomes_froids.pdf (2006).

[146] K. Lindquist, M. Stephens, and C. Wieman, Experimental and theoretical study of the vapor-cell Zeeman optical trap. *Phys. Rev. A* **46**(7), 4082 (1992).

[147] S. R. Muniz, K. M. F. M. aes, P. W. Courteille, M. A. Perez, L. G. Marcassa, and V. S. Bagnato, Measurements of capture velocity in a magneto-optical trap for a broad range of light intensities. *Phys. Rev. A* **65**(1), 015402 (Dec. 2001).

[148] S. Aubin, E. Gomez, L. A. Orozco, and G. D. Sprouse, High efficiency magneto-optical trap for unstable isotopes. *Review of Scientific Instruments* **74**(10), 4342 (2003).

[149] U. D. Rapol, A. Wasan, and V. Natarajan, Loading of a Rb magneto-optic trap from a getter source. *Phys. Rev. A* **64**(2), 023402 (Jun. 2001).

[150] V. S. Bagnato, L. G. Marcassa, S. G. Miranda, S. R. Muniz, and A. L. de Oliveira, Measuring the capture velocity of atoms in a magneto-optical trap as a function of laser intensity. *Phys. Rev. A* **62**(1), 013404 (Jun. 2000).

[151] J. Schoser, A. Batär, R. Löw, V. Schweikhard, A. Grabowski, Y. B. Ovchinnikov, and T. Pfau, An intense source of cold Rb atoms from a pure 2D-MOT. *Phys. Rev. A* **66**, 023410 (Jan. 2002).

[152] V. Schweikhard, Ultracold Atoms in a Far Detuned Optical Lattice. Master's thesis, Universität Stuttgart (2001), diplomarbeit.

[153] T. Petelski, Atom interferometers for precision gravity measurements. Ph.D. thesis, Université de Paris 6 (2005).

[154] S. Chaudhuri, S. Roy, and C. S. Unnikrishnan, Realization of an intense cold Rb atomic beam based on a two-dimensional magneto-optical trap: Experiments and comparison with simulations. *Phys. Rev. A* **74**(2), 023406 (Aug. 2006).

[155] R. Grimm, M. Weidemüller, and Y. B. Ovchinnikov, Optical dipole traps for neutral atoms. *Adv. At. Mol. Opt. Phys.* **42**, 95 (2000).

[156] C. Cohen-Tannoudji, J. Dupont-Roc, and G. Grynberg, Processus d'interaction entre photons et atomes. InterEditions, Editions du CNRS (1988).

[157] D. Witthaut, M. Werder, S. Mossmann, and H. Korsh, Bloch oscillations of bose-einstein condensates: Breakdown and revival. *Phys. Rev. E* **71**, 036625 (2005).

[158] S. Wu, E. Su, and M. Pretiss, Demonstration of an area-enclosing guided-atom interferometer for rotation sensing. *Phys. Rev. L* **99**, 173201 (2007).

[159] F. Impens, P. Bouyer, and C. J. Bordé, Matter-wave cavity gravimeter. *Applied Physics B: Lasers and Optics* **84**, 603 (Sep. 2006).

[160] T. Volz, S. Dürr, S. Ernst, A. Marte, and G. Rempe, Characterization of elastic scattering near a feshbach resonance in ^{87}Rb. *Phys. Rev. A* **68**(1), 010702 (Jul. 2003).

[161] F. Ferlaino, C. D'Errico, G. Roati, M. Zaccanti, M. Inguscio, G. Modugno, and A. Simoni, Feshbach spectroscopy of a K-Rb atomic mixture. *Physical Review A (Atomic, Molecular, and Optical Physics)* **73**(4), 040702 (2006).

[162] J. L. Bohn, J. P. Burke, C. H. Greene, H. Wang, P. L. Gould, and W. C. Stwalley, Collisional properties of ultracold potassium: Consequences for degenerate Bose and Fermi gases. *Phys. Rev. A* **59**(5), 3660 (May 1999).

[163] N. R. Claussen, S. J. J. M. F. Kokkelmans, S. T. Thompson, E. A. Donley, E. Hodby, and C. E. Wieman, Very-high-precision bound-state spectroscopy near a ^{85}Rb feshbach resonance. *Phys. Rev. A* **67**(6), 060701 (Jun. 2003).

[164] T. Bergeman, G. Erez, and H. J. Metcalf, Magnetostatic trapping fields for neutral atoms. *Phys. Rev. A* **35**(4), 1535 (Feb. 1987).

[165] M. Fauquembergue, J.-F. Riou, W. Guerin, S. Rangwala, F. Moron, A. Villing, Y. L. Coq, P. Bouyer, A. Aspect, and M. Lecrivain, Partially ferromagnetic electromagnet for trapping and cooling neutral atoms to quantum degeneracy. *Review of Scientific Instruments* **76**(10), 103104 (2005).

[166] M. E. Gehm, K. M. O'Hara, T. A. Savard, and J. E. Thomas, Dynamics of noise-induced heating in atom traps. *Phys. Rev. A* **58**(5), 3914 (Nov. 1998).

[167] W. Ketterle, K. B. Davis, M. A. Joffe, A. Martin, and D. E. Pritchard, High densities of cold atoms in a *dark* spontaneous-force optical trap. *Phys. Rev. Lett.* **70**(15), 2253 (Apr. 1993).

[168] W. Ketterle, D. S. Durfee, and D. M. Stamper-Kurn, Making, probing and understanding Bose-Einstein condensates. In M. Inguscio, S. Stringari, and C. E. Wieman, eds., Proceedings of the International School of Physics - Enrico Fermi, p. 67, IOS Press (1999).

[169] T. Kinoshita, T. Wenger, and D. S. Weiss, All optical Bose-Einstein condensation using a compressible crossed dipole trap. *Phys. Rev. A* **71**, 011602 (2005).

[170] S. Aubin, S. Myrskog, M. H. T. Extavour, L. J. LeBlanc, D. McKay, A. Stummer, and J. H. Thywissen, Rapid sympathetic cooling to fermi degeneracy on a chip. *Nature Physics* **2**, 384 (2006).

[171] W. R. Johnson, Atomic Structure Theory: Lectures on Atomic Physics. Spring (2007).

[172] C. Salomon, J. Dalibard, A. Aspect, H. Metcalf, and C. Cohen-Tannoudji, Channeling atoms in a laser standing wave. *Phys. Rev. Lett.* **59**(15), 1659 (Oct 1987).

[173] W. Petrich, M. H. Anderson, J. R. Ensher, and E. A. Cornell, Behavior of atoms in a compressed magneto-optical trap. *J. Opt. Soc. Am. B* **11**(8), 1332 (Aug. 1994).

[174] S. R. Granade, M. E. Gehm, K. M. O'Hara, and J. E. Thomas, All-optical production of a degenerate Fermi gas. *Phys. Rev. Lett.* **88**(12), 120405 (Mar. 2002).

[175] M. D. Barrett, J. A. Sauer, and M. S. Chapman, All-optical formation of an atomic Bose-Einstein condensate. *Phys. Rev. Lett.* **87**(1), 010404 (Jul. 2001).

[176] J. Dalibard, S. Reynaud, and C. Cohen-Tannoudji, Proposals of stable optical traps for neutral atoms. *Optics Communications* **47**, 395 (Oct. 1983).

[177] S. Chu, J. E. Bjorkholm, A. Ashkin, and A. Cable, Experimental observation of optically trapped atoms. *Phys. Rev. Lett.* **57**(3), 314 (Jul. 1986).

[178] W. D. Phillips, Laser cooling of neutral atoms. In W. D. Phillips and A. Aspect, eds., Proceedings of the International School of Physics - Enrico Fermi, IOS Press (1991).

[179] D. Boiron, A. Michaud, P. Lemonde, Y. Castin, C. Salomon, S. Weyers, K. Szymaniec, L. Cognet, and A. Clairon, Laser cooling of cesium atoms in gray optical molasses down to 1.1 μk. *Phys. Rev. A* **53**(6), R3734 (Jun 1996).

[180] C. Cohen-Tannoudji, B. Diu, and F. Laloë, Quantum Mechanics. Wiley (1977).

[181] G. Grynberg, A. Aspect, and C. Fabre, Introduction aux Lasers et à l'Optique quantique. Ellipses (1997).

[182] K. Petermann, Laser Diode Modulation and Noise. Kluwer Academic Publishers (1991).

Index

Résumé

Dans ce mémoire nous présentons une étude sur les sources atomiques pour des senseurs atomiques à long temps de vol ainsi que la construction de deux sources atomiques. Dans un premier temps nous montrons que les propriétés de collimation et de cohérence nécessaires à l'interférometrie atomique à long temps de vol peuvent être fournies par les gaz atomiques dégénérés et nous explicitons le lien entre le facteur d'échelle du senseur inertiel et la géométrie de l'interféromètre. Puis, nous étudions la possibilité de conduire des expériences de senseurs inertiels par interférométrie atomique en chute libre dans un avion. La microgravité ainsi créée peut permettre d'accéder à 4 secondes de temps d'interrogation, et nous explicitons un protocole pour tester le principe d'équivalence par interférométrie atomique pendant cette période de chute libre. Nous décrivons la source d'atomes froids que nous avons construit et testé en microgravité. Enfin, nous consacrons une part importante de ce mémoire à la description d'un nouveau montage expérimental dont le but est de produire un mélange bosons-fermions dégénéré. Nous décrivons et caractérisons les technologies développées, telles que les nouveaux lasers semiconducteurs accordables et le piège optique compressible. Nous présentons les premiers résultats de chargement d'atomes froids dans une pince optique utilisant un laser inédit pour le piégeage atomique, un laser à fibre à 1560nm. Nous utilisons le fort décalage lumineux, unique à notre système, pour développer une nouvelle technique d'imagerie, sélective en énergie potentielle.

Abstract

In this thesis, we report on the study of atomic sources for long-time-of-flight inertial sensing, as well as the experimental realization of two of such sources. First, we show that the collimation and coherence properties required by long-interrogation-time can be achieved using degenerate atomic gases and we explicit the relationship between scale factor of the interferometer, and geometry of the interferometer. Then we conduct a feasibility study for atom-interferometric inertial-sensing experiments conducted in a freely-falling airplane. The resulting microgravity opens the door to up to 4 seconds of interrogation time. We detail a protocol for an atom-interferometric test of the equivalence principle during this free fall period. We describe the cold-atom source that we built and tested in microgravity. Finally, the second part of the thesis is devoted to the description of a new experimental setup designed to cool a boson-fermion mixture to quantum degeneracy. We expose and characterize the technologies developed, such as new tunable semiconductor lasers or the compressible optical trap. We present the first results of cold atoms loading in optical tweezers using a fiber laser at 1560nm. We use the large light shift, unique to our system, to develop a new imaging technique, selective in potential energy.